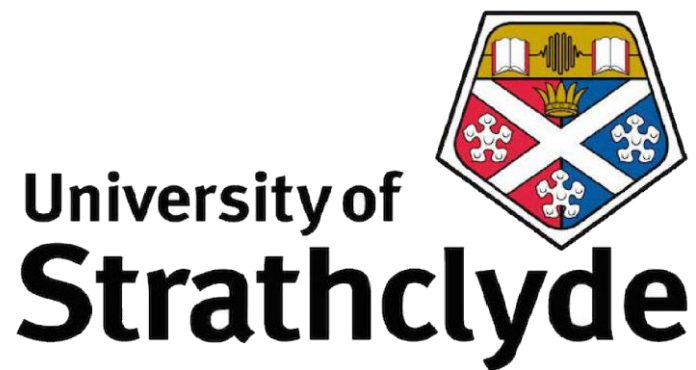


# Continuous Crystallisation and Form Control in a Meso-Scale Oscillatory Baffled Reactor



A thesis presented for the degree of Doctor of Philosophy in the Faculty of  
Science of the University of Strathclyde

by

Stephanie Yerdelen

Strathclyde Institute of Pharmacy and Biomedical Sciences

26 January 2019

## **Declaration of author's rights**

This thesis is the result of the author's original research. It has been composed by the author and has not been previously submitted for examination which has led to the award of a degree.

The copyright of this thesis belongs to the author under the terms of the United Kingdom Copyright Acts as qualified by University of Strathclyde Regulation 3.50. Due acknowledgement must always be made of the use of any material contained in, or derived from, this thesis.

Signed:

Date:

# Abstract

Continuous crystallisation offers a number of benefits over traditional batch processing including reduced variability and consistent quality. This is of particular importance in pharmaceutical manufacturing where ensuring safety, efficacy and quality is essential. The motivation for this work has been to develop a novel meso-scale (internal diameter 10 mm) Continuous Oscillatory Baffled Reactor (COBR) and develop processes that can easily control polymorphic form. Alpha lipoic acid (ALA) is a poorly water soluble compound with challenging physical and chemical properties and is used as a model active pharmaceutical ingredient (API).

Chapters 1, 2 and 3 of this thesis details a literature review, overall aims and objectives of the project and the materials and methods used throughout this work, respectively. Chapter 4 focuses on developing a novel crystal engineering approach to produce the metastable form, form II, of ALA. This was achieved using nicotinamide (NIC) as a solution phase additive. NIC is a widely investigated co-crystal former that is also a hydrotrope. Hydrotropic solubilisation of ALA and the impact on polymorphic outcome with respect to hydrotrope concentration has been investigated. The crystal structure of the new metastable form, ALA II, has been determined and the process conditions for achieving this form defined.

To gain further insight into the crystallisation of ALA II, the process was scaled up to 1 L in a Stirred Tank Reactor (STR) using Process Analytical Technologies (PAT) (Chapter 5). FBRM enables onset of nucleation and growth of ALA crystals to be studied. The crystallisation of ALA II in the required concentration ranges was shown to be influenced by temperature and cooling rate. Evidence of solution-mediated phase transformation after 12 hours was obtained. The results suggested that continuous crystallisation could offer some opportunities to achieve dynamic control over polymorphic form that would be harder to achieve in batch. This was examined in detail (Chapter 6) which describes the design, development and characterisation of a meso scale COBR. Residence time distribution (RTD) studies at a variety of mixing conditions were completed and a model predictive temperature control system developed. The

novel 10 mm ID platform established can deliver near plug flow operation with accurate temperature control, well suited to control of crystallisation processes. In Chapter 7 the development of a continuous crystallisation process for ALA polymorphs is described. The small scale batch crystallisation conditions investigated in Chapters 4 and 5 were converted into an unseeded cooling CC process. The polymorphic form of ALA was controlled by exploiting the hydrotropic effect of NIC and the ability to rapidly change process conditions in a continuous environment.

# Acknowledgements

It has to be said that without my supervisor, Prof Alastair J. Florence and his group, this thesis would not have materialised. Some of this work is based on the initial research carried out by the late Dr Lihua Zhao, whom I never had the chance to meet, but would like to take this opportunity to express my appreciation for her meticulous notes. I am eternally indebted to Dr Cameron J. Brown, Dr Humera Siddique, Dr Thomas McGlone and Vishal Raval as their help throughout has been indispensable.

I would like to express my gratitude to the Doctoral Training Centre in Continuous Manufacturing and Crystallisation (Grant Ref: EP/K503289/1), the EPSRC Centre for Innovation Manufacturing in Continuous Manufacturing and Crystallisation (Grant Ref EP/I033459/1), the technical staff in the Future Continuous Manufacturing and Advanced Crystallisation Research Hub (Grant Ref EP/P006965/1), CMAC National Facility supported by UKRPIF (Grant Ref: HH13054), Dr Nuno Reis at the University of Bath for the opportunity to collaborate, Dr Murray Robertson for automating very complicated mathematical calculations, Dr Iain Ostwald and Lauren Conner for their help with single crystal structure analysis.

I would particularly like to mention Raaz's constant support both in and outside of the lab. His positive outlook on life, keen eye for detail and excellent computer skills have kept me sane throughout this time. Special thanks to CDT cohort 2013 and fellow students who made my PhD experience a pretty huge deal!

A massive thank you to Aniq, Aisha, Maria, Francesca, Meliha and Saba who have all been a phone call away. Cheers for the moral support Dr John Robertson, Dr Murray Robertson, Dr Antony Vassileiou and Andrew Dunn.

Cheers to the coffee cart for supplying the caffeine, Maddison's for lunch and Sainsbury's for the snacks and the sparkling water!

I would particularly like to thank my family, both near and far, for their support and encouragement. However, this thesis, submitted on the year of her 47<sup>th</sup> birthday, is dedicated to Özlem Çapar, my dear aunt who departed too soon.

Stephanie

# Contents

<b>1 INTRODUCTION.....</b>	<b>1</b>
1.1 CONTINUOUS MANUFACTURING AND CRYSTALLISATION IN THE PHARMACEUTICAL INDUSTRY .....	2
1.2 CONTINUOUS CRYSTALLISATION TECHNOLOGIES.....	5
1.3 FUNDAMENTAL PROCESS PARAMETERS.....	7
1.3.1 <i>Solubility</i> .....	7
1.3.2 <i>Nucleation Kinetics</i> .....	10
1.3.3 <i>Growth Kinetics</i> .....	14
1.4 DESIRABLE PARTICLE ATTRIBUTES .....	15
1.4.1 <i>Polymorphic Form</i> .....	16
1.4.2 <i>Crystal Size Distribution</i> .....	18
1.4.3 <i>Crystal Shape</i> .....	20
1.5 METHODS OF CRYSTALLISATION AND MOVING FROM BATCH TO CONTINUOUS	23
1.5.1 <i>Cooling Crystallisation</i> .....	23
1.5.2 <i>Anti-solvent Crystallisation</i> .....	24
1.5.3 <i>Evaporative Crystallisation</i> .....	24
1.5.4 <i>Crystallisation Techniques</i> .....	25
1.6 PROCESS ANALYTICAL TECHNOLOGIES .....	27
1.6.1 <i>UV Spectroscopy</i> .....	28
1.6.2 <i>Focused Beam Reflective Measurement</i> .....	28
1.6.3 <i>Fourier Transformed InfraRed</i> .....	29
1.6.4 <i>Powder Diffraction</i> .....	30
1.6.5 <i>Particle Vision and Measurement</i> .....	30

1.6.6 Scanning Electron Microscopy .....	31
1.6.7 Dynamic Light Scattering .....	31
1.6.8 Gas Adsorption .....	31
1.6.9 Differential Scanning Calorimetry.....	32
1.6.10 Particle Size Analysis .....	32
1.6.11 IR Spectroscopy.....	32
1.6.12 Raman Spectroscopy.....	33
1.6.13 Optical Microscopy .....	33
1.7 OBRs: BACKGROUND AND OPERATING PRINCIPLES .....	34
1.7.1 Oscillatory Baffled Reactor.....	34
1.7.2 Mixing.....	35
1.7.3 Fluid Mechanics .....	36
1.7.4 Operational Parameters .....	40
1.7.5 Dimensionless Group.....	41
1.7.6 Applications of OBR's.....	43
<b>2 AIMS AND OBJECTIVES .....</b>	<b>44</b>
2.1 AIMS .....	45
2.2 OBJECTIVES .....	46
<b>3 MATERIAL AND METHODS.....</b>	<b>47</b>
3.1 MATERIALS .....	48
3.2 METHODS.....	48
3.2.1 Process Analytical Technologies.....	48

<b>4 DISCOVERY AND CHARACTERISATION OF FORM II ALPHA LIPOIC ACID .....</b>	<b>52</b>
4.1 INTRODUCTION .....	53
4.1.1 <i>Lipoic Acid</i> .....	54
4.1.2 <i>Hydrotropes and Crystallisation</i> .....	55
4.2 EXPERIMENTAL.....	65
4.2.1 <i>Preparation, Structure Solution and Solid state Characterisation of ALA II</i> . 65	
4.2.2 <i>Hydrotropic Effect of Nicotinamide on ALA</i> .....	66
4.2.3 <i>Effect of Nicotinamide on Polymorphic Outcome of ALA</i> .....	68
4.2.4 <i>Ex-Situ Transformation Measurements Using XRPD</i> .....	68
4.2.5 <i>Dynamic Light Scattering</i> .....	68
4.2.6 <i>Solubility Measurements</i> .....	69
4.2.7 <i>Solid State Stability</i> .....	69
4.2.8 <i>Microscopy</i> .....	69
4.3 RESULTS AND DISCUSSION .....	70
4.3.1 <i>Preparation, Structure Solution and Solid State Characterisation of ALA II</i> 70	
4.3.2 <i>Solubility</i> .....	76
4.3.3 <i>Concentration of NIC Effect on Polymorphic Form of ALA</i> .....	77
4.3.4 <i>Determination of Hydrotropic Effect of Nicotinamide on ALA</i> .....	80
4.3.5 <i>Stability of ALA II in Solution</i> .....	82
4.3.6 <i>Dynamic Light Scattering</i> .....	83
4.3.7 <i>Nucleation of ALA II</i> .....	89
4.3.8 <i>Solid state Stability</i> .....	94
4.4 SUMMARY .....	95



<b>5 SCALE-UP OF CRYSTALLISING ALPHA LIPOIC ACID FORM II</b> .....	<b>96</b>
5.1 INTRODUCTION .....	97
5.2 MATERIALS AND METHOD.....	99
5.2.1 <i>Small Scale Controlled Crystallisation Experiments</i> .....	102
5.2.2 <i>Initial Scale Up (100 mL)</i> .....	104
5.2.3 <i>Final Scale Up (1000 mL)</i> .....	104
5.2.4 <i>Experimental Conditions for Scale Up Experiments</i> .....	105
5.2.5 <i>Experimental Set-Up and Procedure (100 mL)</i> .....	107
5.2.6 <i>Experimental Set-Up and Procedure (1000mL)</i> .....	108
5.2.7 <i>Physical Characterisation</i> .....	109
5.3 RESULTS AND DISCUSSION .....	110
5.3.1 <i>Small Scale Controlled Crystallisation Experiments</i> .....	110
5.3.2 <i>Initial Scale Up (100 mL)</i> .....	115
5.3.3 <i>Final Scale Up (1000 mL)</i> .....	118
5.3.4 <i>Physical Characterisation</i> .....	121
5.4 SUMMARY .....	128
<b>6 DESIGN, DEVELOPMENT AND CHARACTERISATION OF A NOVEL CONTINUOUS OSCILLATORY BAFFLED REACTOR</b> .....	<b>129</b>
6.1 INTRODUCTION .....	130
6.1.1 <i>Mesoscale Oscillatory Baffled Reactor</i> .....	134
6.1.2 <i>Characterisation Methods</i> .....	137
6.1.3 <i>Crystallisation Control Strategies</i> .....	140
6.2 MATERIALS AND METHOD.....	141
6.2.1 <i>Baffle Design</i> .....	141

6.2.2 Assessment of Oscillatory Conditions for Particle Suspension .....	143
6.2.3 Residence Time Distribution Study of Meso scale SPC OBR.....	144
6.2.4 Model Predictive Temperature Control .....	146
6.2.5 CFD Analysis.....	148
6.3 RESULTS AND DISCUSSION .....	149
6.3.1 Baffle Design.....	149
6.3.2 Development of Reactor .....	152
6.3.3 Assessment of Oscillatory Conditions for Particle Suspension .....	158
6.3.4 RTD.....	158
6.3.5 CFD Analysis.....	170
6.3.6 Model Predictive Temperature Control .....	173
6.4 SUMMARY .....	177
<b>7 CONTINUOUS CRYSTALLISATION OF ALA POLYMORPHS .....</b>	<b>178</b>
7.1 INTRODUCTION .....	179
7.1.1 Technology Transfer between Crystallisers.....	179
7.1.2 Experimental Considerations.....	182
7.2 EXPERIMENTAL.....	185
7.2.1 Materials.....	185
7.2.2 Experimental Method .....	185
7.3 RESULTS & DISCUSSION .....	196
7.3.1 Batch Cooling Crystallisation Experiment.....	196
7.3.2 Continuous Crystallisation Experiments of ALA Polymorphs.....	198
7.3.3 Continuous Crystallisation Experiments of ALA-NIC Co-crystal.....	206
7.4 CHALLENGES .....	212

7.4.1 <i>Temperature Control</i> .....	212
7.4.2 <i>Flow and Concentration Adjustment</i> .....	213
7.4.3 <i>Isolation and Wash Step</i> .....	213
7.5 SUMMARY .....	214
<b>8 CONCLUSIONS AND FUTURE WORK</b> .....	<b>215</b>
8.1 CONCLUSIONS.....	216
8.1.1 <i>Chapter 4</i> .....	216
8.1.2 <i>Chapter 5</i> .....	217
8.1.3 <i>Chapter 6</i> .....	217
8.1.4 <i>Chapter 7</i> .....	218
8.2 RECOMMENDATIONS FOR FUTURE WORK .....	219
8.2.1 <i>Hydrotropes and Crystallisation</i> .....	219
8.2.2 <i>Lipoic Acid and Hydrotropes</i> .....	219
8.2.3 <i>Platform and Predictive Capabilities</i> .....	220
8.2.4 <i>Continuous Processing</i> .....	221
<b>9 PUBLICATIONS</b> .....	<b>222</b>
<b>10 REFERENCES</b> .....	<b>224</b>
10.1 REFERENCES.....	225

# List of Abbreviations

AFM	Atomic Force Microscope
ALA	Alpha Lipoic Acid
API	Active Pharmaceutical Ingredient
BET	Bruauer–Emmett–Teller
CLD	Chord Length Distribution
CQA	Critical Quality Attributes
CFD	Computational Fluid Dynamics
CC	Continuous Crystallisation
CM	Continuous Manufacturing
COBR	Continuous Oscillatory Baffled Reactor
CSD	Crystal Size Distribution
CSTR	Continuous Stirred Tanked Reactor
CZ	Cooling Zone
D	Dispersion
EMA	European Medicines Agency
FBRM	Focused Beam Reflection Measurement
FDA	Food and Drug Administration
G	Growth Rate
H	Enthalpy
HAp	Hydroxyapatite
I.D	Internal Diameter

ICH	International Council for Harmonisation
IPA	Isopropyl Alcohol
J	Rate of Nucleation
M	Mass of tracer
MPC	Model predictive controller
MSMPR	Mixed Suspension Mixed Product Removal
MSZW	Metastable Zone Width
NIC	Nicotinamide
OBR	Oscillatory Baffled Reactor
PAT	Process Analytical Technologies
Pe	Peclet Number
PFR	Plug Flow Reactor
PVC	Poly-vinyl chloride
QbD	Quality by Design
ReN	Net Flow Reynolds Number
ReO	Oscillatory Reynolds Number
RPM	Rate per minute
RTD	Residence Time Distribution
S	Entropy
S <sub>s</sub>	Supersaturation
SEM	Scanning Electron Microscope
SEPC	Sharp Edged Periodic Constrictions
SMPT	Solution Mediated Phase Transformation
SPC	Smooth periodic constrictions

St	Strouhal Number
STR	Stirred Tank Reactor
Tf	Transfer Function
T <sub>sol</sub>	Solubilisation temperature
T <sub>nuc</sub>	Nucleation temperature
TiS	Tanks in series
XRPD	Powder X-ray Diffraction
PVM	Particle Vision and Measurement

# List of Nomenclature

$\alpha$	Baffle Open Area Ratio
$x_o$	Oscillation Amplitude
$\text{\AA}$	Angstrom
$\delta$	Baffle Thickness
$\gamma$	Interfacial Tension
$L$	Baffle Length
$d_o$	Baffle Constriction
$f$	Oscillatory Frequency
$\Psi$	Velocity Ratio
$\rho$	Density
$\mu$	Viscosity
$\tau$	Mean Residence Time
$v$	Fluid velocity
$\lambda$	Wavelength

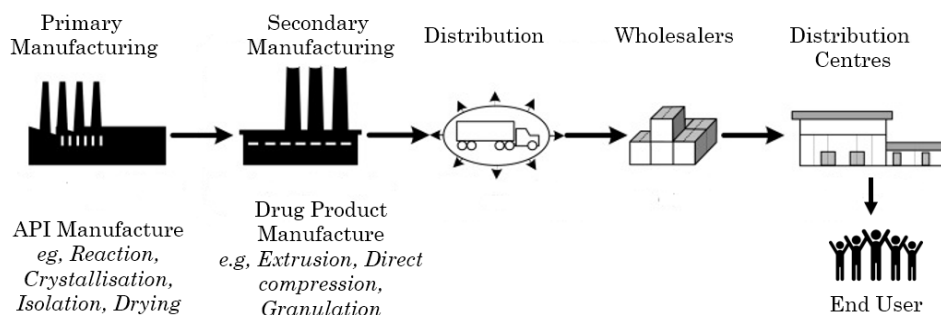
# Chapter 1 Introduction



## 1.1 Continuous Manufacturing and Crystallisation in the Pharmaceutical Industry

Continuous manufacturing (CM) is a relatively novel concept within the pharmaceutical industry and is receiving significant amount of research. One definition for CM is that it is a vision where processes are integrated, based on a systems approach, with model-based control whilst making use of flow<sup>1</sup>. Hence, CM, in its fullest implementation covers all aspects of a process and the distinction between primary and secondary processes are eliminated. CM offers many benefits including; control, consistency over a process, reduced operational costs and contribution to a 'greener' environment<sup>2, 3</sup>. Changing patient demographics, increased development and manufacturing costs are some of the driving forces behind the need for more flexible, reactive and cost-efficient production facilities contributing to a lean, demand-lead supply chain model. The potential economical benefits of continuous manufacturing in addition to better product quality allows it to be a viable option for the pharmaceutical industry to adopt to make considerable savings in cost, energy and product quality and consistency.

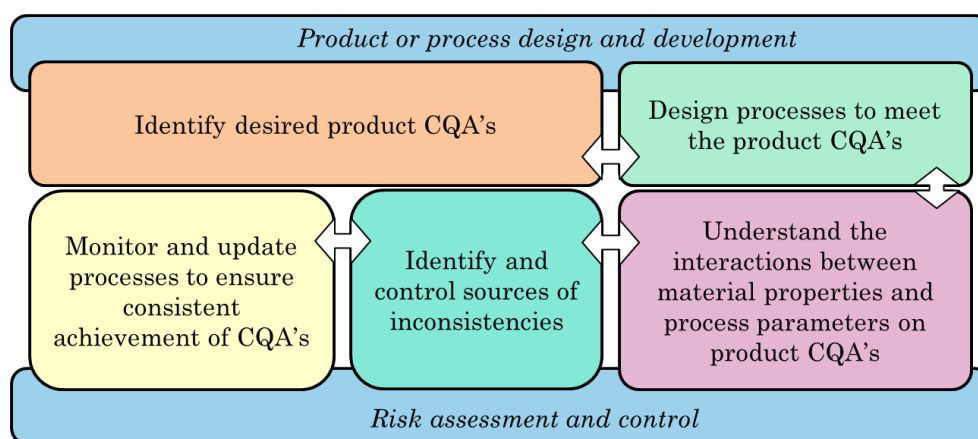
Continuous manufacturing of pharmaceuticals involves bridging the three main stages; primary, secondary processes and supply chain networks. The primary stage involves the manufacture of the active pharmaceutical ingredients (API) and excipients, followed by processes such as, crystallisation, drying and size reduction. The secondary stage involves formulating the API with excipients to provide a final product (Figure 1.1).



**Figure 1.1** A schematic of the processes involved in a pharmaceutical manufacturing (figure adapted from reference 4).

There are tools which can support the development and manufacture of pharmaceuticals and these can be collectively termed as Process Analytical Technologies (PAT). CM utilises PAT to design, evaluate, monitor and control processes. PAT can be applied to ensure final products meet the specifications and if they do not, serve as a method of developing risk mitigation strategies for final product attributes<sup>5</sup>. This can be complemented with automation of hardware (e.g. pumps, heater/chillers), allowing the system to be less labor intensive.

There is a need to fully understand the interactions between process parameters, material properties and Critical Quality Attributes (CQA) to develop and operate CM processes. This is termed Quality by Design (QbD) and is a move towards process and product development that is based on a scientific understanding of the key factors (Figure 1.2).



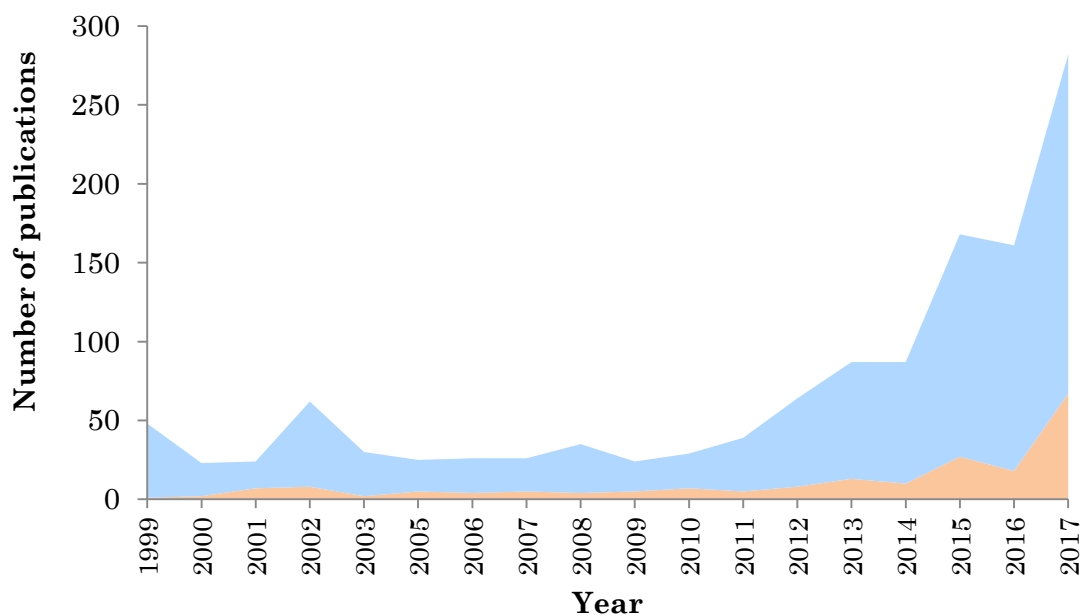
**Figure 1.2** Schematic of QbD (figure adapted from reference 6).

Although CM has been adopted across numerous industries (e.g. oil refining<sup>7</sup>), the uptake by the pharmaceutical industry has been slow. The delay in implementation of CM to pharmaceuticals manufacturing has been attributed to the high initial investment costs as well as challenges associated with introducing innovation within a highly regulated pharmaceutical approval system<sup>8</sup>. A perceived risk for pharmaceutical companies changing from batch to continuous processing is that the industry is subject to very stringent regulations. The regulation covers all aspects of manufacturing including; raw materials, plant design, test standards used to determine safety/efficacy of pharmaceutical ingredients and packaging. Therefore, the pharmaceutical

companies must satisfy the Food and Drug Administration (FDA) in the US and the European Medicines Agency (EMA) in Europe. However, recently the FDA has approved lumacaftor/ivacaftor, a new cystic fibrosis drug and an antiretroviral medication named Darunavir<sup>9</sup>, both of which have incorporated CM to their manufacturing processes. These two examples signify a milestone in integrating continuous processes into commercial pharmaceuticals.

Studies have evaluated the likely benefits of continuous manufacturing with respect to batch processing<sup>8, 10-13</sup>. A continuous twin screw granulation and drying process has been successfully transferred from batch to continuous process<sup>8</sup> which demonstrated reduced manufacturing time and reproducibility of results but highlighted challenges around control of crystal size.

Traditionally pharmaceutical manufacturing has been synonymous with batch processing and as a result continuous crystallisation has gained a significant amount of interest only in the last 20 years (Figure 1.3).



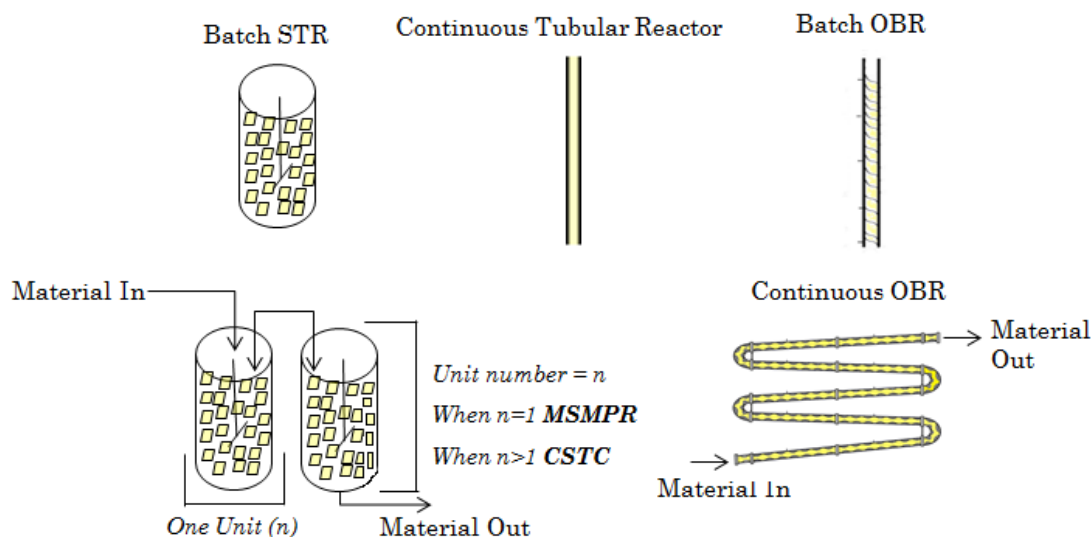
**Figure 1.3** Number of publications for continuous manufacturing (blue) and continuous crystallisation of pharmaceuticals (orange) between the years 1999 and 2017.

Benefits of continuous manufacturing with respect to crystallisation can be recognised in: reduction in solvent use, waste production, energy and footprint consumption, more control and automation of reactions, safer and more

economical scale up possibilities<sup>2, 14-16</sup>. An investigation into the continuous crystallisation of an API indicated that a continuous process offered significant advantages over batch production in terms of operation and costs with a reduction in process time of over 90%<sup>10</sup>. Further to this, a mathematical modelling framework transferring a Mixed Suspension Mixed Product Removal (MSMPR) crystalliser from batch to continuous was developed<sup>13</sup>. It was observed that continuous mode of operation achieved higher throughput with a shorter mean residence time and comparable yield to the previously examined batch process. However, not all processes may be suitable for continuous processes, for example low yields in the production of chiral crystals from continuous crystallisation has been highlighted<sup>17</sup>. Therefore, appropriate analysis of process and optimisation of batch process should be carried out prior to making a decision.

## 1.2 Continuous Crystallisation Technologies

There are a range of continuous crystallisers that have been demonstrated including MSMPR or Continuous Stirred Tank Cascade (CSTC) depending on the number of vessels as well as plug flow reactors (PFR) (Figure 1.4).



**Figure 1.4** Some commonly used crystalliser types (figure adapted from reference 108).

PFRs can be subdivided into three categories namely; segmented flow reactor, tubular reactors with static mixers and oscillatory baffled reactor (OBR). A

second generation of OBR's has also been developed referred to as meso (milliliter) scale OBR's that enable processes to be operated at lower scale in development or for small volume manufacture. There are different process platforms available and the aim of development is to identify the most suitable process conditions to achieve the desired product. Part of this is to look at process understanding and control approaches. Some of the differences and similarities between platforms is shown in Table 1.1. PFR offer some potential benefits for crystallisation due their excellent heat and mass transfer capabilities though must be adequately designed to accommodate required solids loadings or longer residence times for slower processes.

**Table 1.1** A summary of the main differences and suitabilities of static mixer based crystallisers and PFR's (Table adapted from reference 18).

Attribute	CSTR	PFR
Handling of Solids	√ (higher than PFR)	√
Quickness to steady state	X	√
Narrow residence time	X	√
Operational complexity	X	√
Ease of scale-up	X	√
Enhanced heat and mass transfer	X	√

Within the OBR good mixing is also achieved, an important factor affecting crystal properties allowing a uniform experience for the particles as they progress through the process conditions. OBRs have the advantage that they can be modular to respond to changes in demand levels. However, a pressure drop associated with increasing the number of sections can be a limitation. It is perhaps simpler to add another cascade to form a series of cascades to convert a batch static mixer based crystalliser to continuous mode. Furthermore, depending on the initial solid loading needed for a process, CSTR may be more suitable as it is capable of handling higher solid content. Another point to consider would be the residence time needed for the reaction. PFR's have narrow residence time profiles compared to MSMPR which have a wider residence time profile. As a result, the requirements of the system can also influence crystalliser choice.

A study which investigated the crystallisation of paracetamol within an OBR and STR highlighted the OBR to be more effective than the latter in producing particles of smaller sizes, smoother surface with less crystalline imperfections<sup>19</sup>. Comparisons from crystallisations in batch stirred tank and continuous MSMPR reactors have also been studied<sup>20</sup>. The findings from this study indicated narrower size distributions (spans of 1.5 - 2 and 4 - 8, respectively) and lower yields (e.g. 20 - 50% and 30 - 70%, respectively) in the Continuous Oscillatory Baffled Reactor (COBR) compared to the MSMPR for l-Glutamic acid. The COBR demonstrated limited operating conditions (e.g. due to blocking of the reactor), whilst the MSMPR reactor was identified as being more versatile and was operated for up to 70 hours compared to several hours for the continuous OBR. Lastly, the outcome of the examination of the effect of mixing on enantiopurity of seeded crystallisation of sodium chlorate in STR and OBR has been investigated<sup>21</sup>. These findings provided further insight into the nucleation mechanism in the OBR and suggested that an alternative mechanism to that in the STC was observed which is significance is that it can affect CQA.

In conclusion, there are several reasons why one crystallisation technology might be more suitable over the other and the process and outcomes need to be considered as a whole. Lastly, analyses of new continuous crystalliser platforms to determine; e.g. robustness, cleaning, mixing performance are needed to fully understand their application in pharmaceutical manufacturing and their suitability for the process, product requirements.

### **1.3 Fundamental Process Parameters**

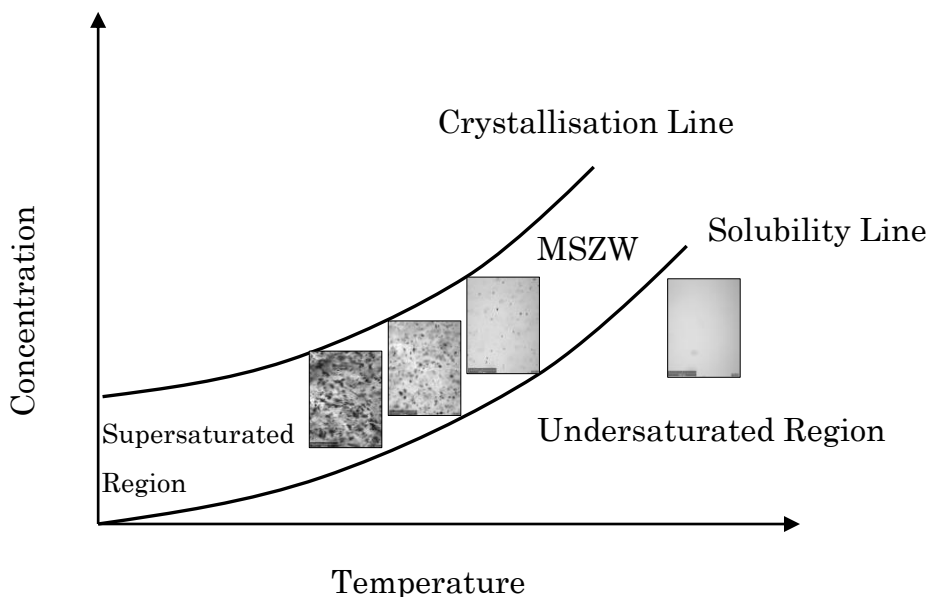
#### **1.3.1 Solubility**

Solubility, is a thermodynamic quantity that defines the maximum amount of solute which can be dissolved in a particular solvent at a given temperature and pressure. In other words, when the chemical potentials of the solid ( $\mu_{\text{solid}}$ ) and the solute in solution ( $\mu_{\text{solution}}$ ) are equal, the solution will be in equilibrium and can be described as saturated ( $\Delta\mu = 0$ ), at constant temperature and pressure.

$$\Delta\mu = \mu_{\text{solution}} - \mu_{\text{solid}}$$

**Equation 1.1**

Solubility of the solute in the respective solvent system is one of the first steps in designing a crystallisation process. Figure 1.5 is a representative solubility diagram, showing the undersaturated area, metastable zone width (MSZW) and supersaturated region. Below the solubility line, i.e. the undersaturated region, crystallisation cannot occur due to dissolution. Within the MSZ, crystallisation is not expected to occur spontaneously; however, factors such as seeding can be introduced to encourage nucleation and growth. Above the crystallisation line, spontaneous crystallisation can occur.



**Figure 1.5** Graphical presentation of the relationship between concentration, solubility and supersaturation. The images above represent initially a clear solution as the solution is undersaturated (Far right). Sequence of images (from right to left) within the MSZW; represent growth of crystals as the solution temperature decreases.

Although the main function affecting solubility is temperature, this is also influenced by the purity of starting material and should be taken into consideration. If the solubility profile of the impurities is also known, better solvent purification estimation can be made. Solubility provides a starting point, however, it is supersaturation which is the driving force behind crystallisation processes. Supersaturation ( $S_s$ ) is a dimensionless difference in the chemical potential of an API between solubility and the supersaturated point<sup>22</sup> and can be expressed in different ways (Equation 1.2 and Equation 1.3). In literature

supersaturation is commonly denoted as  $S$ , however, throughout this thesis it will be denoted as  $S_s$  to differentiate from  $S$  (entropy).

$$S_s = \frac{C_{\text{solute}}}{S_{\text{solute}}} \quad \text{Equation 1.2}$$

$$\text{Relative } S_s = \frac{C_{\text{solute}} - S_{\text{solute}}}{S_{\text{solute}}} \quad \text{Equation 1.3}$$

where  $S_s$  is supersaturation,  $C_{\text{solute}}$  = solution concentration and  $S_{\text{solute}}$  = equilibrium solution concentration.

Supersaturation can be generated by e.g. cooling, evaporation or addition of anti-solvent. However, cooling and anti-solvent addition are the preferred two methods as greater control over the conditions and yield can be achieved. The supersaturation level generated during the process has a direct and major impact on crystal properties including size, morphology, purity and polymorphic outcome<sup>23-25</sup>. Knowledge of solubility data, leads to information about the MSZW which is the supersaturated region at which spontaneous nucleation does not occur and as a result in the absence of any seed crystals the solution would remain crystal free for an extended period of time. MSZW can be identified as the temperature difference between point of solubilisation ( $T_{\text{sol}}$ ) and at which solid material begins to form ( $T_{\text{nuc}}$ )<sup>26</sup>.

$$\text{MSZW} = T_{\text{sol}} - T_{\text{nuc}} \quad \text{Equation 1.4}$$

MSZW is an important process parameter to investigate as it indicates experimental boundaries after which spontaneous nucleation can happen. Thus keeping within this region is of paramount importance allowing more control over process and outcomes. MSZW is a kinetic parameter and depends on several process factors e.g. cooling rate, solvent choice and stirring rate<sup>27-29</sup>; hence, it needs to be defined for each crystallisation process. MSZW can be quantified using the polythermal method, where a saturated solution is cooled at



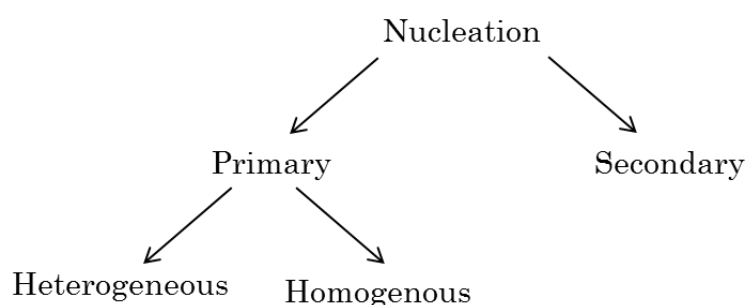
a known rate until nucleation is detected<sup>26</sup> using for example; turbidity<sup>30, 31</sup>, electrical conductivity<sup>32</sup>, bulk video imaging<sup>33</sup> and focused beam reflectance measurement<sup>26</sup>.

### 1.3.2 Nucleation Kinetics

The formation of new crystalline particles from solution is termed nucleation. Creation of nuclei through the continuous increase of supersaturation creates a new phase which results in a more organised structure with a lower free energy<sup>34</sup>. Although the mechanism by which nucleation takes place is not completely clear, currently mechanism of nucleation can be divided into two: primary and secondary which are covered below.

#### 1.3.2.1 Primary Nucleation

Primary nucleation is the formation of nuclei which form and grow from a clear solution and can be further subcategorised as homogenous and heterogeneous (Figure 1.6).

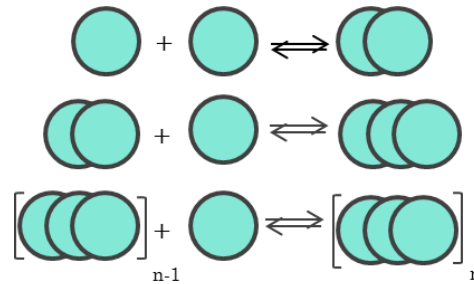


**Figure 1.6** Mechanisms of nucleation

Homogenous nucleation can be defined as a system which is initially in a state of equilibrium which then becomes metastable as a result of substantial supersaturation deliberately being created for example by cooling, and foreign materials (e.g. dust or wall of crystalliser)<sup>34</sup> do not play a role. Heterogeneous nucleation is generally regarded as the process of most practical relevance to industrial processes which involves the formation of the new solid phase due to the presence of other particulates. The presence of foreign material (heteronuclei) between 0.1 – 1 $\mu\text{m}$ <sup>35</sup> has been suggested to be the most

influential. Heteronuclei present in a supersaturated solution has been reported to reduce the energy needed for nucleation, meaning the energy barrier for heterogeneous nucleation is lower than that for homogenous nucleation. In practice, this means lower supersaturations would be needed for heterogeneous nucleation.

Figure 1.7 provides an illustration where there is the addition of structures until a critical cluster size is attained which is more stable and energetically favourable to grow. These mechanisms form the basis of Classical Nucleation Theory (CNT) which is the most widely used theory to describe the nucleation process<sup>36</sup>.



**Figure 1.7** Diagram showing sequential addition molecules to form critical cluster which will result in nucleation (figure adapted from reference 35).

The net free energy barrier required for cluster formation is  $\Delta G$ , which is a balance between an increase in surface energy (favouring dissolution of nuclei) and a decrease in bulk energy (favouring growth of nuclei).<sup>37</sup> The free energy change needed for the formation of a spherical cluster with a radius  $r$  is given by Equation 1.5.

$$\Delta G = \Delta G_s + \Delta G_v = 4\pi r^2 \gamma + \frac{4\pi}{3} r^3 \Delta G_v \quad \text{Equation 1.5}$$

where  $\Delta G_s$  is the surface excess free energy,  $\Delta G_v$  is the volume excess free energy given by the volume of the droplet and  $\gamma$  is the interfacial tension.

For each solute-solvent system there is a definite critical cluster size ( $r_c^2$ ) and amount of energy needed ( $\Delta G_{crit}$ ) to reach that point can be expressed in the following way.

$$\Delta G_{crit} = \frac{4}{3} \pi \gamma r_c^2 \quad \text{Equation 1.6}$$

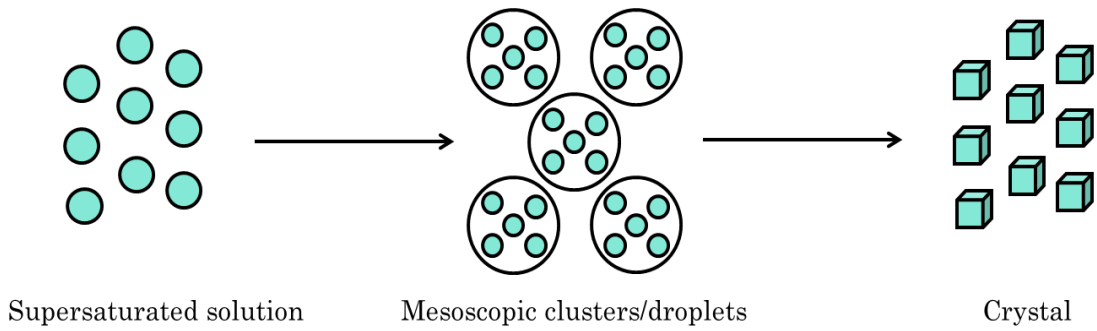
The rate of nucleation ( $J$ ), the number of nuclei formed per unit time/volume, is governed by; temperature ( $T$ ), supersaturation level ( $S$ ), interfacial tension ( $\gamma$ ) where  $v$  is molecular volume,  $A$  is the pre-exponential factor and  $k$  is the Boltzmann constant (Equation 1.7 and Equation 1.8).

$$J_{homogenous} = A \exp \left[ -\frac{16\pi v^2 \gamma^3}{3k^3 T^3 (\ln S)^2} \right] \quad \text{Equation 1.7}$$

$$J_{heterogenous} = kb_{het} \exp \left[ -\frac{16\pi v^2 \gamma^3 f(\varphi)}{3k^3 T^3 (\ln S)^2} \right] \quad \text{Equation 1.8}$$

where  $kb_{het}$  is the homogeneous nucleation rate constant and the factor  $f(\varphi)$  accounts for the decreased energy barrier to nucleation due to the presence of foreign solid particles.

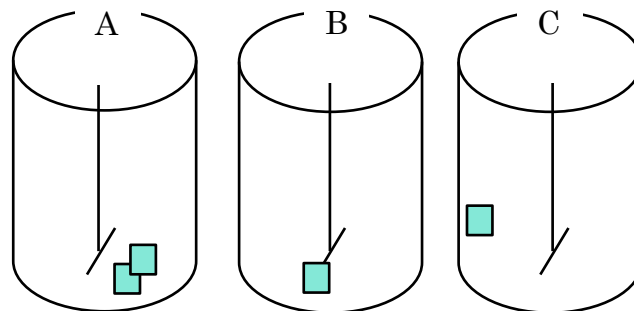
Whilst CNT has offered a starting point for explaining nucleation, it makes several assumptions<sup>38</sup>. The assumptions are: the nuclei are considered as spherical droplets, the formation of nuclei is by single addition of solute monomers, the nuclei formed have the same structure as the final crystal and the size of the nuclei is the only factor used to determine whether a formed nuclei is stable or unstable. Due to the several assumptions made by CNT and because it does not consider the influence of process conditions or impurities, this theory of nucleation has been reconsidered<sup>38</sup>. One suggested theory is the two-step nucleation theory<sup>34</sup> also referred to as multi-step nucleation<sup>39</sup>. In two-step nucleation, dense clusters of solute molecules are produced (“pre-nucleation clusters”) and once an intermediate size is reached, the clusters restructure themselves to an organised crystalline nucleus within this droplet<sup>40</sup> (Figure 1.8).



**Figure 1.8** Simplified schematic of a proposed mechanism of two step nucleation mechanism (Figure adapted from reference 38).

### 1.3.2.2 Secondary Nucleation

Whilst formation of the first nuclei from a supersaturated solution occurs via primary nucleation (whether homogeneous or heterogeneous), induction of nucleation via crystal-crystal, crystal-impeller or crystal-wall interactions is referred to as secondary nucleation which is broadly grouped as “contact nucleation”<sup>35</sup> (Figure 1.9).



**Figure 1.9** Schematic of the three main mechanisms of secondary nucleation: crystal – crystal collision (A), crystal – impeller (B) and crystal – wall (C).

Contact nucleation is generally problematic to forecast and hard to prevent and may be the dominant nucleation process in some crystallisation processes. Uncontrolled secondary nucleation is in most cases an undesirable event and it can cause problems in product quality. Crystal-crystal collisions in liquid medium can cause fractures resulting in smaller crystals and an alteration in the material properties of the parent crystal. This leads to a reduction in the

original volume of crystals therefore affecting final crystal product and size distribution with the increased generation of fines.

Crystal-impeller collisions have been shown to be the most prominent mechanism with the geometry and position of the impeller having some effect on secondary nucleation rates<sup>41</sup>. Conversely, crystals containing defects are prone to internal stress and this can also result in fragmentation generating secondary nuclei. Although secondary nucleation is generally an unwanted event, “seeding”, where crystals are intentionally added to exploit secondary nucleation is a method often used with the aim of producing a final product with a specific particle size/particle size distribution or polymorphic form. However, the effect of seeding is linked to the percentage of seeds added and the addition temperature and, therefore, needs to be examined to identify the suitable conditions.

### 1.3.3 Growth Kinetics

Once nuclei of sufficient size have formed in a supersaturated solution, growth of crystals can begin by attracting solute molecules to the surface of the nucleus<sup>22</sup>. The two main stages involved are: mass transport from bulk solution to the interface between crystal and solution followed by addition of growth units through surface integration steps<sup>42</sup> where the slowest step is the rate-limiting step for crystal growth. This is the foundation of the crystal growth theory based on the growth units binding in a consecutive manner in a supersaturated solution<sup>43</sup>. Other growth theories have also been reported<sup>43</sup>.

Growth rate ( $G$ ) in its basic form can be represented by the change in crystal size ( $x$ ) over time ( $t$ )<sup>37</sup>. This assumes that small crystals and large crystals have the same linear rate of growth (i.e. size independent).

$$G = \frac{dx}{dt} \qquad \text{Equation 1.9}$$

$G$  can be quantified as a function of supersaturation which can be represented by the following equation.

$$G = kS^g$$

**Equation 1.10**

where  $k$  is overall crystal growth coefficient,  $S$  is supersaturation and  $g$  is order of the overall crystal growth.

One way of expressing crystal growth rates as a function of crystal size is shown in Equation 1.11<sup>44</sup>. However, other models for size-dependant growth rate have also been developed<sup>44</sup>.

$$G = kS^g(1 + \gamma L)^b$$

**Equation 1.11**

where  $k$  is overall crystal growth coefficient,  $S$  is supersaturation,  $g$  is order of the overall crystal growth,  $\gamma L$  is dimensionless factor and  $b$  is exponent parameter.

Aside from diffusion and surface integration steps one other process which may affect crystal growth and consequently the crystal size distribution is Ostwald ripening which can be viewed as an instability of the system which will only resolve when free energy has reached its lowest value<sup>42</sup>. Small crystals which are more unstable will dissolve, reducing the number of crystals present overall and larger crystals will continue to grow, increasing the crystal size distribution<sup>45</sup>.

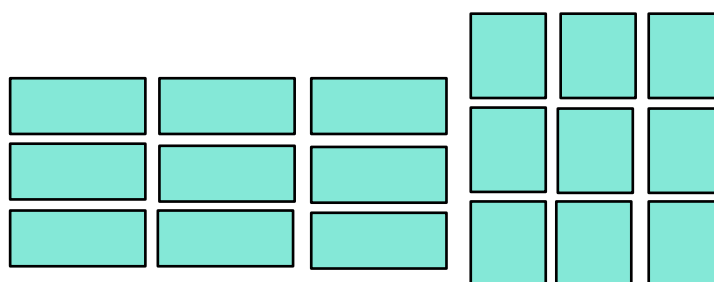
## 1.4 Desirable Particle Attributes

Crystallisation is a unit operation with the ultimate aim of delivering an API in a form suitable for human use. Since crystallisation is a method of purification, the level of impurities in the crystallisation process or in the final product is pivotal. Impurities in the crystallisation medium can influence the nucleation and growth rates, crystalline form, morphology, habit and crystal size distribution<sup>46, 47</sup> which can impact in-vivo performance. Consequently, purity remains the most important outcome to control. Other crystal features can affect downstream secondary manufacturing processes leading to operational

difficulties but these physical properties of the API can often be controlled in the final crystallisation step<sup>48</sup> and as a result are secondary in terms of prominence.

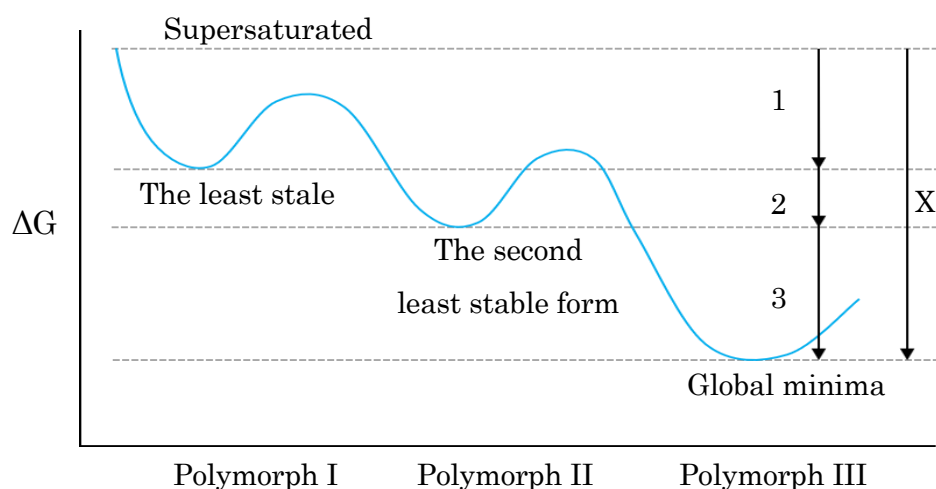
### 1.4.1 Polymorphic Form

Polymorphism is the existence of more than one crystalline form of a compound<sup>22</sup> as even though chemically they may be identical, the molecules are arranged differently within the lattice (Figure 1.10).



**Figure 1.10** Illustration of different packing arrangements within the crystal lattice which leads to polymorphism.

Different polymorphs can have altered properties such as stability, solubility and bioavailability as a result studying a wide range of experimental conditions to discover and identify possible polymorphs is vital. According to the Ostwald's rule of stages, all metastable forms will form and transform until the form with the lowest free energy is reached (Figure 1.11).



**Figure 1.11** Hypothetical energy changes observed for an API with three different polymorphs which will continue until the lowest energy level is reached (figure adapted from reference 49).

An example of the significance of polymorphism with respect to in-vivo performance is chloramphenicol palmitate which has three known polymorphic forms (the stable form A, the metastable forms B and C). Polymorph A is thermodynamically stable, but its absorption in humans is significantly lower than that of polymorph B. The metastable forms of chloramphenicol palmitate shows a higher dissolution rate than form A leading to higher solubility even when the same dose was administered<sup>50</sup>. Although metastable polymorphs have generally an increase in solubility<sup>51</sup>, due to their instability, stable polymorphs are preferred for manufacture. Other types of polymorphism which can be observed during the discovery of new solid state forms. The definitions as accepted by FDA<sup>52</sup> and some reported examples can be seen below (Table 1.2).

**Table 1.2** Definition and examples of pseudopolymorphism.

Type	Definition
Co-crystal	Solids that are crystalline materials composed of two or more molecules in the same crystal lattice (neutral guest molecules) e.g. Alpha Lipoic Acid-Nicotinamide Co-crystal <sup>53</sup> , Urea-Barbuturic Acid <sup>54</sup>
Salt	Compounds that result from replacement of part or all of the acid hydrogen of an acid by a metal/radical acting like a metal; an ionic or electrovalent crystalline compound. e.g. the antimalarial agent $\alpha$ -(2-piperidyl)-3,6-bis(trifluoromethyl)-9-phenanthrene methanol hydrochloride <sup>55</sup>
Solvate/Hydrate	Multiple component crystals where the guest molecule is a solvent or water, respectively. e.g. Carbamazepine Hydrate <sup>56</sup>

Polymorphism is a double-edged sword, whilst an undesired polymorphic conversion can compromise regulatory success, in some cases solubility/bioavailability issues can be addressed. Thus, the pharmaceutical industry must judiciously assess the experimental space for polymorphism for



every drug during the development stage to tighten the experimental conditions which yield the desired form.

#### **1.4.2 Crystal Size Distribution**

Crystal size distribution (CSD) provides size information or span of size for a given sample. Secondary processes, for example filtration and drying, and product efficacy (such as bioavailability and stability) can be affected by CSD, thus tight control over this attribute is critical<sup>57</sup>.

The balance between benefits and adverse side effects of API's can depend on the dissolution rate which is affected by CSD<sup>58</sup>. Control of CSD can enable the optimisation of the dissolution rate to maximize the benefit whilst lessening the undesirable side effects<sup>59</sup>. A broad CSD can also affect storage of the final drug product; large particles will travel towards the bottom and very fine particles can grow together to form lumps of crystals leading to caked powders<sup>60</sup>.

Whilst smaller particles are preferred due to quicker dissolution profile, larger particles are preferred from a manufacturing perspective. CSD is determined by crystal growth, primary nucleation and secondary nucleation, agglomeration and supersaturation. Formation of a high number of nuclei results in smaller crystals with broad distribution and the agitation rate, mass of seed crystals, as well as temperature profile are important parameters that strongly influence the CSD of products<sup>59</sup>. Thus, to minimise secondary processes, experimental conditions should be optimised. More recently, however, a methodology that allows finding regions of attainable particle sizes in crystallisation processes has been reported which uses crystallisation kinetics and defined process start and end points<sup>61</sup>. This in turn allows experimentalists to assess if the desired particle size specifications can be met and if so, under which conditions and equipment.

Secondary processes may still be needed to reduce particle size even after optimisation of experimental conditions or if a further reduction is needed for delivery of the API to specific organ (such as pulmonary delivery). Post-processing of crystals to reach desirable crystal size can be carried out in several ways (Table 1.3.)

**Table 1.3** Pharmaceutical particle engineering techniques available to reduce particle size.

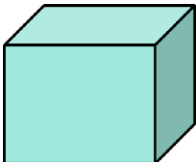

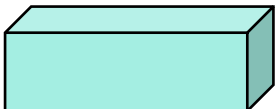


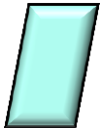
	<b>Fluid Energy Milling</b>	<b>Ball Milling</b>	<b>Media Milling</b>	<b>Microfluidisation</b>
Achievable particle size	1-30 $\mu\text{m}^{62}$	<200 $\text{nm}^{62}$	350 $\text{nm}^{63}$	1-15 $\mu\text{m}^{64}$

An example of particle size reduction has been demonstrated for danazol, an API used in the treatment of a variety of conditions including cystic fibrosis and endometriosis. In this example, the average particle size of 10  $\mu\text{m}$  was reduced to 169  $\text{nm}$  which displayed around 59-fold increase in specific surface area and consequently bioavailability<sup>65</sup>. Another application of particle manipulation is to produce crystals suitable for aerosol delivery to nasal cavity or pulmonary area (particle size less than 1000  $\text{nm}^{62}$ ) and this has recently been demonstrated for paracetamol<sup>66</sup>. As a result, a narrow CSD with a tight control over the mean particle size is necessary.

### 1.4.3 Crystal Shape

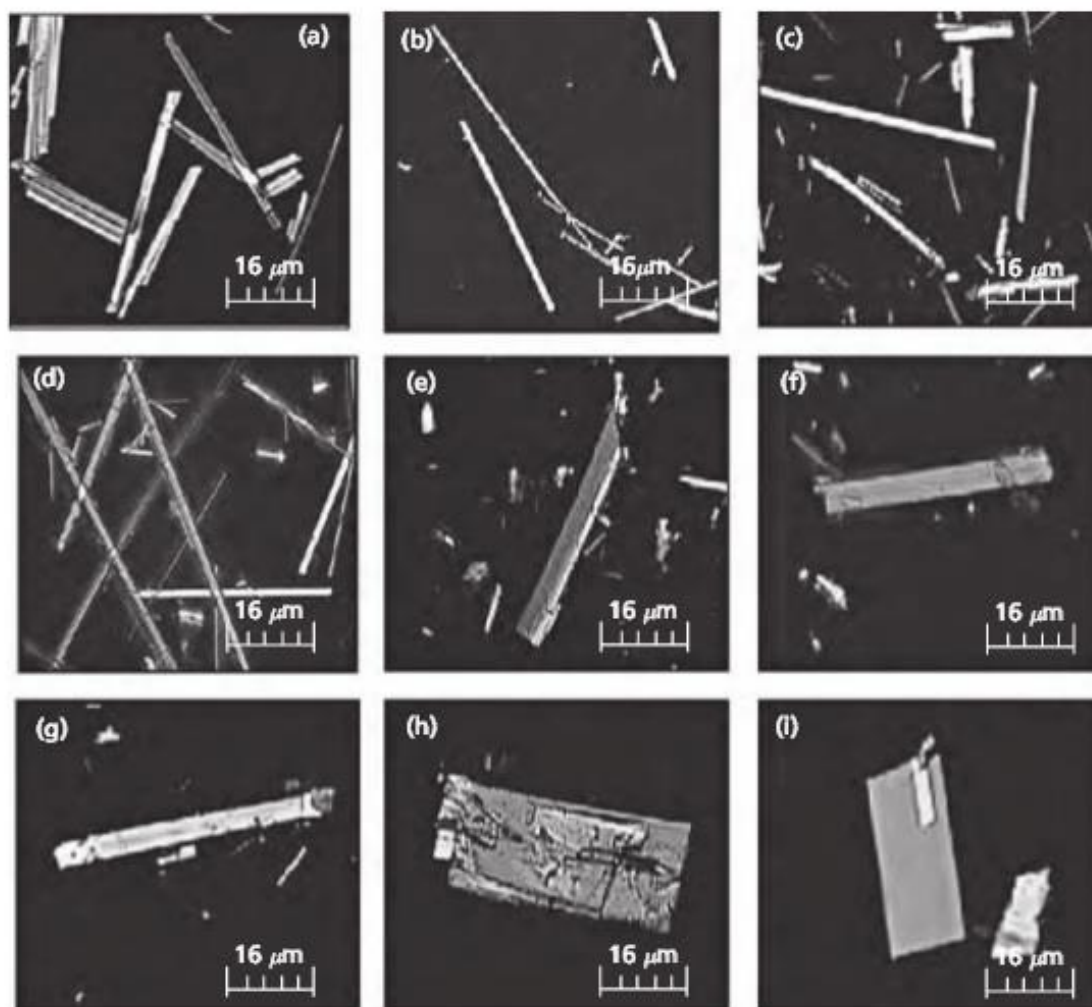
Crystal shape plays a role in the quality and effectiveness of an API as crystals. Different shapes can have different bioavailabilities as the degree of adsorption is determined by the dissolution rates of different crystal faces. As a result, it is a parameter which needs to be controlled and monitored<sup>58</sup>. There are numerous shapes which can form from a crystallisation process and these have been shown below in (Table 1.4).

**Table 1.4** Commonly observed particle shapes (adapted from reference 67).

Particle Shape Name	Shape	Shape Description
Equant		Particles of similar length, width and thickness
Acicular		Slender, needle-like
Columnar		Long, thin particles (width and thickness greater than needle-like particles)
Lath		Long, thin, blade-like particles
Flake		Thin, flat particles, similar length and width
Plate		Flat particles (similar length and width but thicker than flakes)

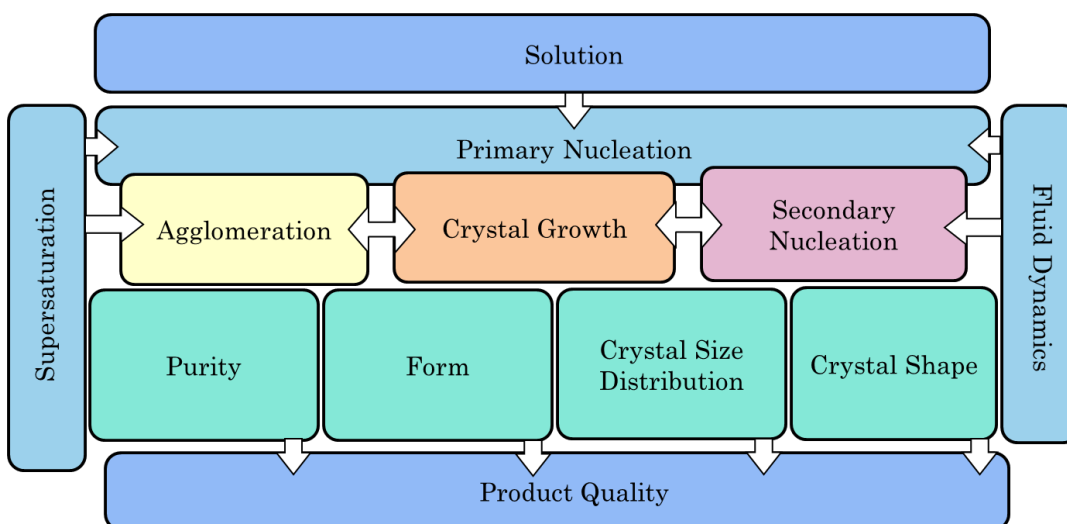
The shape of a crystal is determined by both internal and external factors such as solvent type, impurity/additive concentrations, solution temperature and supersaturation<sup>48, 68</sup>. The impact of solvent choice and experimental conditions has been demonstrated for the crystallisation of phenytoin where crystallisation in alcohols resulted in needle shape crystals and rhombic obtained from acetone<sup>69</sup>. A further example can be seen in Figure 1.12 which displays the

crystals that were obtained for the crystallisation of celecobix in various solvents and through different experimental conditions. These results are supported by other literature examples<sup>70-72</sup>.



**Figure 1.12** Polarised photomicrographs (a) pure drug (celecobix); (b) recrystallised from ethanol, (c) recrystallised from methanol, (d) recrystallised from butanol, (e) recrystallised from toluene at 25°C, (f) recrystallised from chloroform at 25°C, (g) recrystallised from carbon tetrachloride, (h) recrystallised from toluene at 60°C, (i) recrystallised from chloroform 60°C (images from reference 73).

Needle-like crystals can block the filter, increasing the time required for filtration. Needles and flake like crystals are difficult to dry, handle in powder form, formulate and tablet<sup>48, 73</sup>. As well as manufacturing challenges brought about by crystal shape, a variation in in-vitro/in-vivo performance can also be observed. This has been reported for rod-shaped and spherical nanocrystals of an API<sup>74</sup>. Comparison of their dissolution and bioavailability reported rod shaped crystals to have performed better in both instances. The difference was attributed to larger surface area and a smaller diffusion layer provided by the rod shaped crystals compared to the spherical crystals. A similar case has been demonstrated for ibuprofen, where high-aspect ratio rods were obtained from non-polar hydrocarbon solvents, such as hexane or heptane. However, in the presence of more polar solvent (e.g. methanol), equant, low-aspect ratio crystals were formed. The resulting crystals had a better dissolution profile as well as enhanced processing properties relative to the rods grown from non-polar solvents<sup>71</sup>. A change in crystal shape can also be due to a change in polymorphism hence any change in crystal shape needs to be further examined. In conclusion, crystallisation is a multifaceted, intricate process with numerous outcomes to control and monitor. A summary of the events which take place during crystallisation and the CQAs which they can influence is shown in (Figure 1.13).



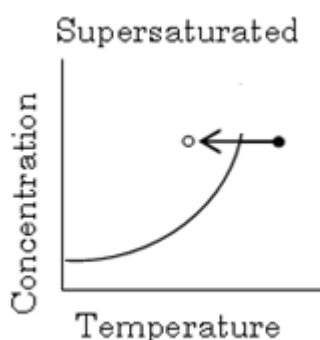
**Figure 1.13** A schematic of the interaction between process parameters and product quality (figure adapted from reference 60).

## 1.5 Methods of Crystallisation and Moving from Batch to Continuous

The method of crystallisation may be specific to the process and, therefore, must be designed to suit the desired outcomes of the process such as polymorphic form, crystal shape, size distribution, scale of operation and future manufacturing plans. There are a number of methods of crystallisation and main techniques used in pharmaceutical industry. However, supersaturation is the driving force of crystallisation and this is generated through different ways which can influence the crystallisation method selected.

### 1.5.1 Cooling Crystallisation

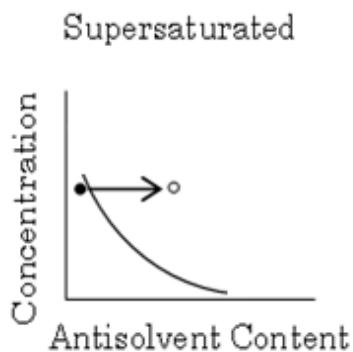
Cooling crystallisation can be selected if the solubility of the API shows strong temperature dependence. This means when the temperature of a suspension is reduced, supersaturation is created, resulting in nucleation and growth (Figure 1.14). Once the MSZW is determined, it is then possible to drive the system where it is cooled to the supersaturated region to induce nucleation and then kept within the MSZW to promote crystal growth and reduce uncontrolled primary nucleation. Since system parameters such as cooling rate can be controlled, the relationship between system parameters and product specifications can be determined. Consequently, the crystallisation process can be optimised to deliver the desired crystal attributes.



**Figure 1.14** Mechanism of supersaturation formation during a cooling crystallisation (figure adapted from reference 60).

### 1.5.2 Anti-solvent Crystallisation

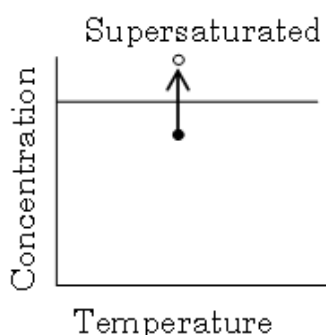
As a means of generating supersaturation, typically a second solvent (anti-solvent) (which the API has a substantially lower solubility) is added to the solution causing a reduction in the solubility of the API in the resultant solvent composition<sup>60</sup> (Figure 1.15).



**Figure 1.15** Mechanism of supersaturation formation during an anti-solvent crystallisation (figure adapted from reference 60).

### 1.5.3 Evaporative Crystallisation

Evaporative crystallisation is the process by which solvent is removed by evaporation over time and chosen if the solubility of API does not show strong temperature dependence. Upon evaporation, the solute concentration rises, increasing the supersaturation which, in turn, is consumed by the newly formed crystals<sup>60</sup> (Figure 1.16).



**Figure 1.16** Mechanism of supersaturation formation during evaporative crystallisation (figure adapted from reference 60).

This process will continue until solution volume is sufficiently reduced. Depending on the solvent's evaporation rate, the temperature can be adjusted

which may also affect the crystal properties. Large scale operation of evaporative crystallisation has been demonstrated in the commodity chemicals sector industry<sup>75, 76</sup>. However, in the pharmaceutical industry, evaporative crystallisation has largely been used for small scale discovery of new chemical forms or compositions. The findings from evaporative experiments have been transformed to a cooling crystallisation which still makes this a valid method within the pharmaceutical sector<sup>54</sup>.

#### **1.5.4 Crystallisation Techniques**

There are numerous crystallisation methods which may be API/process specific. Furthermore, change of crystallisation methods has been shown to alter the properties of final drug product and despite there being many crystallisation methods, cooling and anti-solvent crystallisation are the most commonly used in pharmaceutical industry<sup>77</sup>. Cooling crystallisation can be chosen if the solubility shows a strong dependence on the temperature, greater than 0.005 g/g °C, and if the solubility at the lowest possible temperature is sufficiently low so as to ensure a sufficient yield<sup>78</sup>. This technique has several advantages including: constant solvent composition, easiness of control over process conditions and monitoring and reversibility (temperature cycling)<sup>79</sup>. Despite cooling crystallisation being one of the most commonly deployed methods used in the pharmaceutical industry, it can deliver low yield<sup>80</sup> which from an economical aspect may be undesirable. However, this can be rectified by combining cooling crystallisation with antisolvent crystallisation.

If temperature dependence or solubility is an issue, anti-solvent crystallisation may be of advantage. Anti-solvent crystallisation is suitable if the API is heat sensitive or unstable in high temperatures as crystallisation is carried out at constant temperature. Another advantage is that the solvent activity also changes significantly, hence this approach can have more profound effect on the crystal morphology or polymorphic form than in the case of the cooling crystallisation<sup>81</sup>. Anti-solvent crystallisation heavily involves mixing of process streams. This mixing usually results in high local supersaturation close to the inlet points. Therefore, locally at the flow inlets nucleation occurs after which the crystals grow out upon suspension in the bulk solution. Due to these mixing



effects and local variations in process variables, it is difficult to control such processes<sup>60</sup>. That said both methods (cooling and antisolvent) have often been applied concurrently to purify APIs<sup>81-83</sup>. Some other considerations to design a crystallisation are detailed in Table 1.5.

**Table 1.5** Crystallisation design parameters.

Parameter	Definition
Material Balance	Material (mass) balance considers the quantity of starting materials needed and the quantity of the product. Material balances are useful in studying the efficiency of the operation, calculating yield and for troubleshooting.
Energy Balance	Energy balance is calculated to determine the energy required for a process to be operated. Energy balance aids in designing crystallisation processes and selection of heat exchangers.
Population Balance	The population balance describes the material balance that accounts for the distribution of different size crystals in the crystalliser mainly by considering the nucleation and growth kinetics of the system.

## 1.6 Process Analytical Technologies

Process Analytical Technology (PAT) is the design and control of manufacturing processes through real-time measurements with the goal of ensuring predefined product quality<sup>5</sup> thereby avoiding failed batches through active manipulation of the process. There are a variety of PAT tools and techniques available which have been briefly discussed in Table 1.6.

**Table 1.6** Examples of PAT available within a laboratory environment.

PAT Category	Description	Time Scale for Results	Sample Preparation
In-line	Often probe based techniques which are in direct contact with process fluid e.g. monitoring of temperature using thermocouples.	Instantaneous	No
On-line	Measurement where sample is removed from reaction vessel for analysis, and may be returned to the reaction vessel e.g. FTIR	Instantaneous	No
At-line	With at-line measurements, sample is removed, isolated and analysed in close proximity to the process stream e.g. XRPD analysis or DLS	Minutes	Yes
Off-line	Sample removed and analysed away from process stream. e.g. HPLC	Less than one hour	Yes

At-line and on-line PAT methods present particular limitations. With these methods, sample needs to be removed for analysis and a change in environmental conditions such as temperature can alter the crystal properties such as polymorphic form and may not be a true representation of process fluid.

There is a risk of that during the isolation of material in preparation for further analysis, the material can undergo changes e.g. material can agglomerate changing the CSD or convert to another polymorph. This would result in the data collected not being representative of the product prior to isolation. Such risks can be minimised by utilising in-line PAT probes alongside such analytical tools. Such PAT probes can analyse the process fluids, thereby reducing errors associated with sample preparation and transportation. The time in which PAT data is available needs to be considered as it is necessary for the data to be available in a suitable time-frame to enable real-time decision making. The major advantage of this technology is the capacity to monitor and control the process directly in situ providing a wealth of real-time data e.g. with spectroscopic probes. In situ monitoring is essential to have better understanding of the process and to obtain accurate kinetic and physicochemical parameter estimates for model-based control. In summary, the importance and role of PAT tools have been demonstrated extensively and a summary of the techniques available is provided below.

### **1.6.1 UV Spectroscopy**

Analysis of the solution phase using attenuated total reflection ultraviolet (ATR-UV) spectroscopy is a potential technique for monitoring a crystallisation process. Within crystallisation, the main role of UV, when used in absorbance mode, is to quantitatively determine concentration using the Beer-Lambert law (Equation 1.12).

$$A = \epsilon c l$$

**Equation 1.12**

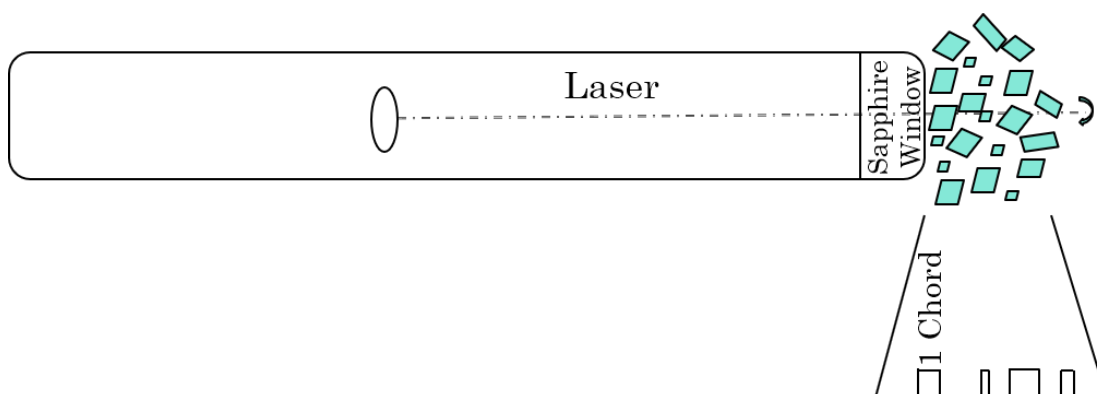
where  $l$  is the path length,  $c$  is the solution concentration, and  $\epsilon$  is a constant which relates chemical properties and experimental conditions.

### **1.6.2 Focused Beam Reflective Measurement**

Focused Beam Reflective Measurement (FBRM) consists of a focused laser beam rotating at a constant rate whilst scanning the particles which enter the

scanning zone. When the light emitted by the laser hits a crystal, a sensor records and analyses the backscattered signal (Figure 1.17).

The data collected, called a chord length, is defined as the distance of the path followed by the beam as it moves across the crystal from one edge to another. As the velocity of the beam is known, the size of the crystal can be calculated by multiplying the rotating speed of the laser by the period of time during which the backscattered signal is received.



**Figure 1.17** Schematic illustrating chord length measurements taken with a FBRM probe.

This data is called the Chord Length Distribution (CLD) which is statistically related to the Crystal Size Distribution (CSD) giving a description of the real crystal population. Whilst FBRM is not particularly well suited to accurately describe large aspect ratio particles (e.g. needle shaped crystals), its ability to carry out real-time measurements without the need for sample removal or calibration has made FBRM an invaluable technique for nucleation/dissolution kinetics<sup>26, 84</sup>, polymorphic transformation detection<sup>85</sup> and particle chord counts and length distribution<sup>86</sup>.

### 1.6.3 Fourier Transformed InfraRed

Offline Fourier transform infrared spectroscopy (FTIR) is a technique whereby an infrared spectrum of a solid or liquid can be obtained very quickly and without damaging the material. With this method data can be obtained over a wide spectral range therefore making it suitable for an array of compounds. This technique can be used in conjunction with other techniques for polymorphic identification e.g. DSC or XRPD.

#### **1.6.4 Powder Diffraction**

Powder diffraction (XRPD) is a commonly accepted technique for identification of polymorph materials including solvate and hydrate determination. Polymorphic forms of an API can have specific physicochemical properties possible influencing: melting point<sup>87</sup>, solubility<sup>50</sup> and morphology<sup>88</sup> yielding this as an important parameter in the pharmaceutical industry. XRPD allows identification, differentiation and quantification between polymorphic forms. However, one consideration is that sensitivity of XRPD has been reported to have a 5 weight percentage lower boundary of detection<sup>89</sup> and that is only suitable for solid, powdered material and other techniques are needed for single crystals or solutions. Furthermore, preferential orientation can pose a problem, where if particles are not randomly orientated, some changes in the presence or intensity of peaks may be observed. However, it is a non-destructive and definitive technique and the sample can be recovered which may be particularly important in the early stages of drug development.

#### **1.6.5 Particle Vision and Measurement**

Particle Vision and Measurement (PVM) represents a supporting tool to the FBRM and UV as it monitors process conditions during the crystallisation process using imaging. Since it is capturing images of the crystal slurry in real time, it provides not only quantitative information like CSD for spherical and non-spherical particles but also qualitative information like change in morphological form during nucleation<sup>86</sup> (whilst this does not unambiguously infer a change in polymorphism it would warrant further investigation). A potential disadvantage of this method can be if the probe window is partially/fully coated with particles, which can reduce the resolution of images. However, despite this potential issue, this technique represents a positive approach that encourages the continuation of this method allowing monitoring of crystallisation processes. The application of this technique within this research was mainly to detect onset of nucleation and gain further information about the crystallisation system under investigation<sup>26</sup>.

### 1.6.6 Scanning Electron Microscopy

Scanning Electron Microscopy (SEM) is a microscope based technique whereby the region of interest is scanned with focused beam of electrons at great magnifications (up to 200,000 times magnification) to identify crystal properties e.g. surface characteristics. SEM offers a powerful imaging capability to investigate from micron scale to a few nanometers<sup>90</sup>.

### 1.6.7 Dynamic Light Scattering

Dynamic Light Scattering (DLS) is an established experimental technique for studying dispersions with nanoscale species as small as 0.3 – 10.0 microns<sup>91, 92</sup>. This method is based on the hypothesis that small particles, when suspended, will move in an unsystematic, random manner, known as Brownian motion<sup>93</sup>. When a laser light is directed to the moving particles, the light will scatter and its intensity will alter with smaller particles having a higher velocity than the larger particles<sup>92, 94, 95</sup>. Consequently, as there is a difference in the shift in the light frequency this technique allows information about the size to be extracted. The diameter is referred to as the hydrodynamic diameter<sup>91</sup> and can be converted into particle size using the Stokes-Einstein equation<sup>96</sup> (Equation 1.13).

$$d_H = \frac{kT}{3\pi\mu D}$$

**Equation 1.13**

where  $d_H$  = hydrodynamic diameter,  $k$  is Boltzmann's constant,  $T$  is absolute temperature,  $\mu$  is viscosity and  $D$  = diffusion coefficient.

### 1.6.8 Gas Adsorption

Gas adsorption is an offline technique of choice to examine and confirm surface characteristics such as porosity observed for solid materials. The technique specifically determines the amount of gas adsorbed, providing information regarding type of porosity, specific surface area and pore size distribution and has been used in literature for this purpose<sup>97-99</sup>. Different gases such as N<sub>2</sub>, Ar, and CO<sub>2</sub> can be used as adsorptives (adsorbable gas), depending on the material

under investigation. However, N<sub>2</sub> adsorption at 77 K and over a wide range of pressures has been used routinely<sup>100</sup>. Qualitative and quantitative information can be derived from this method. Surface area can be calculated using the Bruauer-Emmett-Teller (BET) method, deriving a wide range of information by plotting the changes in weight over a range of relative pressures.

### **1.6.9 Differential Scanning Calorimetry**

Differential Scanning Calorimetry (DSC) is a type of thermal analysis in which the quantity of heat released or absorbed by the sample is measured against temperature. The temperature profile can include heating and cooling cycles at a fixed rate of temperature change<sup>101</sup>. DSC has become an indispensable technique for drug development<sup>102</sup> and pharmaceutical manufacturing as thermal analysis is used to measure physical and chemical properties such as melting point, decomposition, changes between crystalline phases and solvate and hydrate detection.

### **1.6.10 Particle Size Analysis**

Morphologi G3 is a static automated microscopy based imaging technique able to provide data on transparency, size and shape distribution of the sample. The lower and upper limits of detection are 0.5 – 1000 micron. It is able to provide a wealth of information on each particle or entire sample examined including, but not limited to, circle equivalent diameter, length, width and aspect ratio, circularity, convexity and elongation. Its application within pharmaceutically relevant work has been demonstrated<sup>103-106</sup>. This is an at-line method, requiring some sample preparation; however it is easy to use and highly sensitive. The technique is frequently used along with a laser diffraction particle sizing method to gain a better understanding of product or process.

### **1.6.11 IR Spectroscopy**

In-situ IR spectroscopy has demonstrated its suitability for concentration monitoring during crystallisation processes<sup>107, 108</sup>. Whilst this technique requires a concentration calibration to be carried out, concentration monitoring is

essential to have better understanding of the process and to obtain accurate kinetic parameter estimates for model based control. The availability of the concentration measurements along with the CSD measurements can give better insight in to the process and allow model predictive control measures to be employed.

#### **1.6.12 Raman Spectroscopy**

Raman spectroscopy is a complementary technique to XRPD, which probes the vibrational modes of a molecule, relying on changes in the molecular polarisability<sup>109</sup>. Similarly to XRPD, raman scattering provides fingerprint information on samples by investigating peak positions and comparing them to references samples. Furthermore, in-site raman spectroscopy has been used to monitor both the solid and liquid phase of a suspension allowing differentiation between polymorphs and SMPT to be detected which may occur during a crystallisation process<sup>108</sup>. Thus, an in-situ raman probe represents an easy, fast and sensitive tool to detect quantities of different polymorphic fractions in suspension.

#### **1.6.13 Optical Microscopy**

Optical microscopy is a useful supporting tool to other analytical techniques used in solid state chemistry. An optical microscope can be used to determine the crystallinity and the crystal morphology of a sample. In contrast to SEM where a very specific area of the crystal is examined, optical microscopy can be used to examine a wider area and as such can provide a broader picture.

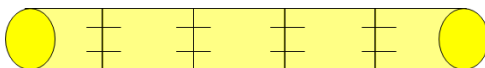


## 1.7 OBRs: Background and Operating Principles

This section of the literature survey begins with an introduction to the Oscillatory Baffled Reactor (OBR) model including; its mixing mechanism, fluid mechanics and applications within industry. This is followed by a review of the applications of OBRs in the crystallisation of APIs.

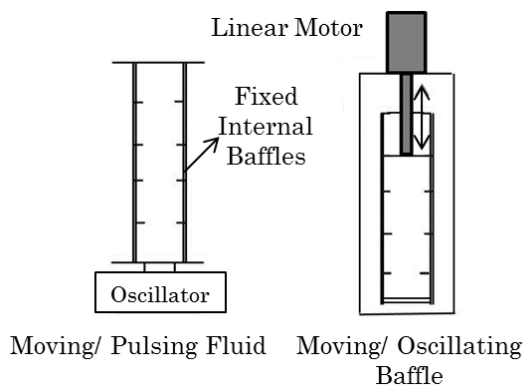
### 1.7.1 Oscillatory Baffled Reactor

An oscillatory baffled reactor (OBR) can be described as a tubular reactor with the presence of periodically spaced baffles (Figure 1.18). The image below is a single orifice design although multi-orifice designs have also been used<sup>110</sup>.



**Figure 1.18** Single orifice OBR with equally spaced baffles.

The fluid mixing within an OBR is classified as oscillatory flow mixing which has been investigated for at least three decades as a novel way of achieving efficient and controlled mixing in baffled tubes<sup>111, 112</sup>.



**Figure 1.19** Schematic of the two oscillating mechanisms (figure adapted from reference 115).

OBR has a number of advantages but of particular interest is the reactor's ability to reduce long reaction times, good mixing, efficient heat and mass transfer rates and near plug flow mode of operation. Oscillation is provided by an oscillator and can be via two mechanisms; moving/pulsing fluid or moving/oscillating baffle as displayed in Figure 1.19. Mixing within a moving

fluid system is achieved by the use of for example: hydraulic, pneumatic or electro-mechanical devices and is designed such that the internal structures remain stationary. Whereas for a moving baffle set up, the mixing can be achieved by using a diaphragm or piston and involves the periodic motion of the internal baffles. Within such systems mixing is an additive effect, as the oscillatory motion of the fluid is superimposed upon the net flow of the fluid<sup>113</sup>.

### 1.7.2 Mixing

Mixing within an OBR is achieved by the generation and cessation of eddies (a whirling motion of fluid within flow) which are generated by interaction of the fluid with periodically spaced baffles. As this is repeated throughout the entire length of the reactor, the strong radial motions created provide uniform mixing in each restricted zone and all the way along the reactor. When the process fluid goes through the reactor, eddies are created around the constrictions (i.e. baffles), enabling significant radial motion. On a down stroke, eddies are created on the opposite side. Intensity of eddy formation and cessation can be controlled accurately, enabling great control over mixing and the ability to alter flow regime. There are a number of scales of mixing and flows which can be observed within a system Table 1.7<sup>114</sup> and Table 1.8<sup>115</sup>.

**Table 1.7** Length scales of mixing.

Type of mixing	Description
Macro	This is mixing on the largest scales of the fluid flow, i.e. the mixing within a vessel and occurs by convection.
Meso	Smaller length scale than the vessel but larger than the smallest mixing scale. it is associated with turbulent diffusion of material into the surrounding fluid.
Micro	This is the smallest scale of fluid flow and includes diffusion. This leads to mixing on the molecular level and can consequently affect fast chemical reactions.

**Table 1.8** Types of flow which can be present within a reactor.

Flow type	Description
Plug Flow	Plug-flow is defined as a systematic flow of fluid through a reactor, and the key aspects are (i) all fluid elements travel at the same speed in the direction of flow, (ii) perfect mixing in the radial direction, and (iii) all flow elements reside for the same length of time.
Laminar Flow	In laminar flow, the speed at the centre of the tube is equal to that of the incoming flow, whilst the velocity at the wall decreases due to drag forces. As a consequence, the fluid at the centre would leave first and fluid travelling along the wall later on, leading to a wide variation in the residence time of fluids.
Turbulent Flow	In turbulent flow, direction of flow is irregular, random and local fluctuations of flow velocity is observed. Due to the random movement of elements within turbulent flow, mixing is enhanced compared to laminar flow.

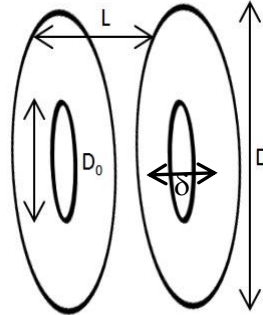
The type of mixing generated within a crystalliser can be determined by Residence Time Distribution studies, is discussed further in Chapter 6.

### 1.7.3 Fluid Mechanics

The periodically formed vortices can be controlled by a combination of geometrical and operational parameters including: baffle diameter, baffle spacing, oscillation frequency and amplitude. In addition to this information, there are also several additional factors that are needed for the operation of an OBR which are summarised in Table 1.11. These can be broadly categorized as *baffle design parameters*, *operational parameters* and the *dimensionless group* and will be examined in the following sections.

### 1.7.3.1 Baffle Design Parameters

Within this section, geometrical parameters relating to OBRs are discussed. The design features which will be considered are: baffle spacing (or length) ( $L$ ), baffle thickness ( $\delta$ ) and baffle open area ratio ( $\alpha$ ) (Figure 1.20).



**Figure 1.20** Baffle design parameters important for OBR design.

#### 1.7.3.1.1 Baffle Spacing

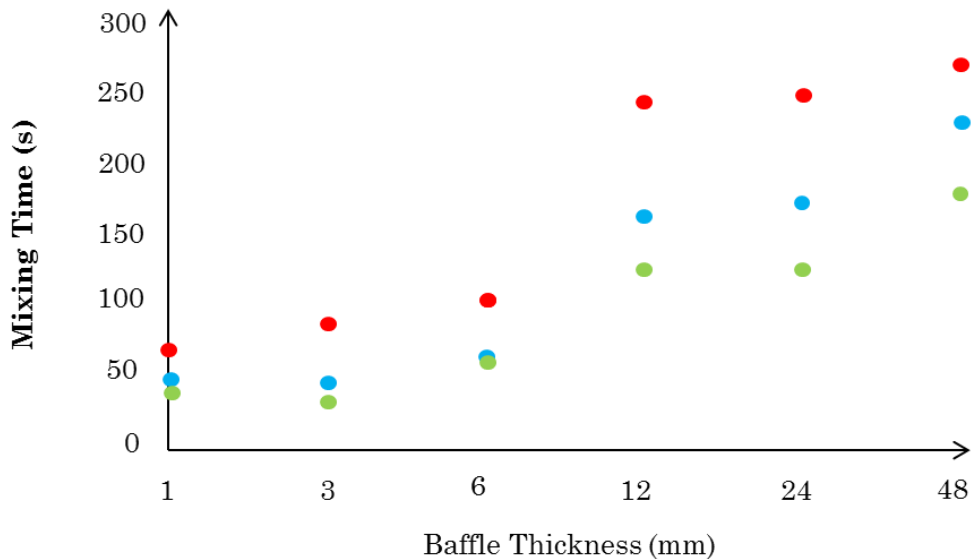
Baffle spacing (or length) ( $L$ ) is the distance between each baffle and it influences the shape and length of vortices formed<sup>116</sup>. To achieve uniform and ideal mixing,  $L$ , should allow the vortices to fully expand and travel throughout all the baffles within the reactor. Short  $L$  distances suppress full vortex formation since vortices formed can collide with the baffle leading to a reduction in the much desired radial dispersion, inhibiting the key mechanism involved in transfer of fluid from the wall to the centre of the reactor. On the other hand, long baffle distances lead to vortices that do not spread throughout the full length of the reactor, producing areas of poor mixing.

The effect of altering the baffle spacing on the efficiency of mixing at a range of distances has been investigated<sup>117</sup> where one and a half the internal diameter ( $1.5D$ ) was demonstrated as the most effective baffle spacing. However, studies by Ni *et al*<sup>118</sup> found baffle spacing of  $2D$  in the lowest mixing time and was recommended as the optimal baffle spacing. However, baffle lengths of  $1.8D$  have also been suggested<sup>119</sup>. Typically, a baffle spacing between  $1D$  and  $3D$  is used with  $1.5D$  being the most commonly used baffle length for OBR based on studies carried out by Brunold *et al*<sup>117</sup>.

### 1.7.3.1.2 Baffle Thickness

Baffle thickness ( $\delta$ ) and its influence on mixing has been investigated<sup>118, 120</sup>. In this study six baffle thicknesses were investigated ranging from 1 to 48 mm and the results suggested that the thinner baffles were favorable for vortex generation, which promote good mixing (Figure 1.21).

One possible explanation given for this was that the eddies formed require a surface to adhere to and if the time needed for adhesion is too long, the shape of the eddies formed can be distorted, affecting mixing time. Therefore, for the purposes of good mixing, baffle thickness of 2 to 3 mm was identified as the optimal value. The importance of baffle thickness and its impact on mixing performance has recently been highlighted in other studies<sup>121</sup>.



**Figure 1.21** Effect of baffle thickness on mixing time at three different frequencies: 1 Hz (red), 2 Hz (blue) and 3 Hz (green). (Figure plotted with data from reference 118).

### 1.7.3.1.3 Baffle Open Area Ratio

Baffle open area ( $\alpha$ ) relates the internal diameter of the baffle ( $D$ ) to the constriction diameter ( $D_0$ ) (Equation 1.14) and is an indication of the width of the vortices formed.

$$\alpha = \left(\frac{D_0}{D}\right)^2 \quad \text{Equation 1.14}$$

Studies considered the effect of  $\alpha$  on mixing time or axial dispersion. Ni *et al*<sup>118</sup> studied the effect of  $\alpha$  (ranging from 0.11 to 0.51) on mixing time and found that the lowest value of  $\alpha$  (0.11) displayed the best mixing and, therefore, required shorter mixing times. This has been supported by oil-water dispersion studies<sup>122</sup>, where the smallest orifice diameter (0.22) achieved complete dispersion at lower minimum oscillation frequencies. This was attributed to more power being applied to the system resulting in more intense mixing.

Experiments carried out by Gough *et al*<sup>123</sup> compared a number of orifice diameters and its effect on flow patterns. At the smallest orifice diameter of 13 mm ( $\alpha = 0.26$ ) small symmetrical eddies were formed at the sharp edges of the baffle but these did not cover the entire column cross-section, nor the complete length of the inner baffle region, and stagnant regions indicative of bad mixing were identified between the eddies.

When the orifice diameter was increased to 16.2 mm ( $\alpha = 0.32$ ) eddies extended to the walls of the reactor and covered a greater area of the inter-baffle zone. An orifice diameter of 31.5 mm ( $\alpha = 0.40$ ), resulted in loss of the symmetry (indicative of plug flow) and intensive interaction between eddies lead to chaotic mixing. The orifice diameter was increased to 34.5 mm ( $\alpha = 0.48$ ) and the formation of eddies was destroyed and little mixing could take place. Typically, a baffle open area between 0.2-0.5 is selected<sup>124</sup>.

### 1.7.4 Operational Parameters

Operational parameters refer to the settings which can be adjusted by the experimentalist depending on the crystallisation process and platform used (Table 1.9).

**Table 1.9** Experimental settings applicable in OBR.

Operational Considerations	
Amplitude & Frequency	The unique mixing effect generated by oscillation is generally achieved across typical ranges of 0.5–20 Hz (frequency, $f$ ) and 1–100 mm (centre-to-peak amplitude, $x_0$ ) <sup>115</sup> . Amplitude should be kept minimal to enhance radial mixing and minimise axial mixing.
Flow Rate	Flow rate can be determined by the required residence time for the crystallisation process. It can also be used to determine effect of net flow Reynolds number which consequently influences mixing.

### 1.7.5 Dimensionless Group

OBR's can be characterised by a number of dimensionless numbers (Table 1.10). These allow the system to be categorised and allow identification of factors which can be altered to achieve the desired flow/mixing conditions<sup>125</sup>. Dimensionless numbers are also important for scale up as they can inform of the conditions required for particle product or process outcomes.

**Table 1.10** Dimensionless group, definitions and formulae.

Dimensionless Value and Definition		Formula
Oscillatory Reynolds Number ( $Re_o$ ): Intensity of mixing	$Re_o = \frac{2\pi f x_o \rho d}{\mu}$	$f$ : oscillation frequency (Hz) $x_o$ : centre to peak amplitude (m) $\rho$ : density of fluid ( $\text{kg m}^{-3}$ ) $d$ : diameter (m) $\mu$ : net flow velocity ( $\text{ms}^{-1}$ )
Net Flow Reynolds Number: The externally imposed net flow	$Re_n = \frac{\rho d u}{\mu}$	$\rho$ : fluid density ( $\text{kgm}^{-3}$ ) $d$ : tube diameter (m) $u$ : superficial fluid velocity ( $\text{ms}^{-1}$ ) $\mu$ : viscosity (Pa s)
Strouhal Number: The eddy propagation	$St = \frac{d}{4\pi x_o}$	$d$ : diameter (m) $x_o$ : amplitude (m)
Velocity Ratio: Ratio of oscillatory Reynolds number to net flow Reynolds number	$\psi = \frac{Re_o}{Re_n}$	$Re_o$ : Oscillatory Reynolds Number $Re_n$ : Net flow Reynolds Number



**Table 1.11** Summary of the operational and geometrical parameters required for the operation of an OBR.

Parameter	Unit	Symbol
Baffle Spacing	mm	L
Constriction Diameter	mm	$D_0$
Baffle Open Area Ratio	-	$\alpha$
Baffle Thickness	mm	$\delta$
Amplitude	mm	$x_0$
Oscillation Frequency	Hz	f
Flow Rate	$\text{ml min}^{-1}$	-
Oscillatory Reynolds Number	-	$Re_o$
Net Flow Reynolds Number	-	$Re_n$
Strouhal Number	-	St
Velocity Ratio	-	$\psi$

### 1.7.6 Applications of OBR's

The enhanced processing aspects with regards to mass and energy transfer, effective mixing, narrow RTD profile and wide range of operating (amplitude and frequency) window have led to various applications of the OBR. This technology has been utilised for the purposes of crystallisation and some examples can be seen (Table 1.12).

**Table 1.12** Examples of variety of OBR reported in literature used for crystallisation.

Internal Diameter	API	Reference
69 mm – Multiorifice (Cooling)	Lactose	107
15 mm – Single orifice (Cooling)	Beta L-Glutamic Acid	126
16 mm – Single orifice (Cooling/Multi-component)	Lipoic Acid - Nicotinamide	53
15 mm – Single orifice (Anti-solvent)	Salicyclic Acid	127
25 mm – Single orifice (Cooling)	API	10
35 mm - Single orifice (Cooling)	Urea	128
50 mm - Single orifice (Cooling)	L-glutamic acid	129
15 mm - Single orifice (Cooling/Multi-component)	Paracetamol	130

OBR's within literature have so far successfully been utilised as crystallisers at a conventional scale (<10 mm I.D). However, these tend to require a significant amount of starting materials, solvent and human resources<sup>115</sup>. This has led to a new avenue within OBR technology to overcome some of the difficulties associated with the previous generation of OBRs, the meso-scale OBR<sup>285</sup>. Majority of literature surrounding meso scale OBR's have been limited to inorganic chemistry and, thus, further work is required to fully assess its suitability for pharmaceutical crystallisation processes. The next few chapters will deal with the development and application of a meso scale OBR with particular focus on polymorphic control of a pharmaceutically relevant compound.

## **Chapter 2 Aims and Objectives**

## 2.1 Aims

An aim of this project was to design, develop and demonstrate a novel scaled down (meso scale) continuous crystallisation platform which can be utilised for the robust, versatile and reproducible operation of crystallisation processes. This is desirable as it allows development using smaller amounts of materials than conventional platforms require. The constructed crystalliser was designed to deliver accurate control over critical quality attributes (e.g. purity, form, shape and size) and to be capable of extended operation at steady state and afford opportunities for real time monitoring and control.

The second main aim was to develop a crystallisation process that was able to switch control between polymorphic forms of an API. The model compound  $\alpha$  Lipoic Acid (ALA) was selected and the crystallisation process investigated to provide the required information to develop the continuous process in the meso COBR. The goal is to take an API from early discovery stage and solid form selection to a continuous crystallisation process with specific control over polymorphic form that could be readily scaled to meet production demands.

The following research questions were identified arising from these research aims:

**Research Question 1:** Can the COBR be successfully scaled down to 10 mm internal diameter whilst maintaining the advantages in mixing and heat transfer in addition to optimal management of solids in flow?

**Research Question 2:** What is the optimal baffle geometry design for a 10mm internal diameter COBR to support continuous crystallisation and ensure adequate particle suspension?

**Research Question 3:** Can the production of a metastable form of Alpha Lipoic Acid in the presence of a hydrotrope be scaled up from small scale (10mL) to 1000 mL in a STR?

**Research Question 4:** Can a batch crystallisation process for controlled formation of metastable ALA polymorph be converted from batch to continuous in a meso COBR?

## 2.2 Objectives

**2.2.1** Design a meso scale OBR to minimise well documented problems associated with baffled crystallisers specifically suboptimal mixing and solid entrapment<sup>115, 118</sup>.

- i. Develop several prototypes to assess the optimal baffle design within a 10 mm COBR by identifying the oscillatory conditions needed to achieve uniform particle suspension.

**2.2.2** Construct, characterise and develop the novel COBR based on the optimal baffle design identified previously.

- i. Characterise the flow performance under a wide design space of operating conditions and determine residence time distributions (RTDs).
- ii. Integrate model predictive temperature control to allow automated control over reactor temperature for process control.

**2.2.3** Investigate the role of Nicotinamide in controlling the polymorphism of Alpha Lipoic Acid by studying the hydrotropic effect of Nicotinamide on Alpha Lipoic Acid and identifying the conditions for polymorphic selection at scales up to 1000 mL.

- i. Carry out small scale experiments to understand the role of Nicotinamide in the crystallisation of Alpha Lipoic Acid.
- ii. Carry out small scale experiments under controlled experimental conditions to identify the conditions at which the metastable form of Alpha Lipoic Acid crystallised.
- iii. Scale-up from 5 mL to 1000 mL using a STR and PAT to illustrate crystallisation of the metastable form of Alpha Lipoic Acid.

**2.2.4** Develop a continuous crystallisation process in the DN10 platform to control the polymorphic form of Alpha Lipoic Acid through the hydrotropic effect of NIC.

- i. Design a platform to allow kinetic information to be translated from batch STR to a batch OBR crystalliser.
- ii. Transfer from batch OBR to continuous meso scale COBR to achieve control of the polymorphic form of Alpha Lipoic Acid.

## **Chapter 3 Material and Methods**

### 3.1 Materials

Alpha Lipoic Acid ( $C_8H_{14}O_2S_2$ , Form I, CAS Number: 1077-28-7, 98%) and Nicotinamide ( $C_6H_6N_2O$ , Form I, CAS Number: 98-92-0, 98.5%) were obtained from *Sigma Aldrich*. Isopropanol alcohol was obtained from VWR. Double distilled water was available in laboratory from a Millipore water purification unit. The purchased ALA and NIC were confirmed as Form I by X-ray powder diffraction and no further purification steps were taken. All solvent used were used as received.

### 3.2 Methods

Analytical techniques that were used for process analysis was carried out using a variety of in-line and off-line techniques. For process monitoring and control, UV spectroscopy, FBRM and PVM were used. Offline analyses included XRPD, SEM, DSC, DLS, FTIR and BET.

#### 3.2.1 Process Analytical Technologies

##### 3.2.1.1 UV spectroscopy

UV-vis optical transmission spectroscopy was performed in-line using a 6mm ATR probe connected to a *Carl Zeiss MCS 600 UV*<sup>131</sup> spectrometer equipped with a CLD 500 deuterium lamp (190 – 2200 nm).

##### 3.2.1.2 Focused Beam Reflective Measurement (FBRM)

FBRM data were acquired using a *Mettler Toledo FBRM G400*<sup>132</sup> probe attached to a control computer. FBRM data were analysed using *iC FBRM* software.

##### 3.2.1.3 Fourier Transformed InfraRed (FTIR)

ATR-FTIR spectra were collected off-line using *Bruker Tensor II IR*<sup>133</sup> spectrophotometer equipped with diode laser, KBr beamsplitter and a Digitech detector. Data analysis was carried out with *OPUS* software version 7.5.

#### **3.2.1.4 Differential Scanning Calorimetry (DSC)**

DSC measurement was carried out in *Netzsch DSC214 Polyma*<sup>134</sup> instrument. The thermal analysis was carried out with *Netzsch Proteus Analysis* software version 7.0.1.

#### **3.2.1.5 SEM (Scanning Electron Microscopy)**

SEM analysis was carried out on a *Keysight FE-SEM8500B*<sup>135</sup>.

#### **3.2.1.6 Dynamic Light Scattering (DLS)**

DLS measurements were carried out using *Malvern ZetaSizer ZS 3600*<sup>136</sup> equipped with 632.8 nm laser. Solutions of known concentration were prepared and analysed in triplicate. The *Zetasizer* software was allowed to automatically determine the attenuator and measurement position for each sample. An attenuator is used to fine-tune the intensity of the laser source which is adjusted depending on the scattered light (derived from particle size and concentration)<sup>137</sup>. The measurement position is changed by moving the focusing lens to adjust the scattering and flaring from the sample which is generated at that particular attenuator position<sup>137</sup>. The Z-average value was used to determine the average size of clusters within solution which is an intensity based measurement based on the mean value obtained<sup>96</sup>. Data were analysed using the *Zetasizer* software version 7.12.

#### **3.2.1.7 Gas Absorption**

The analysis was carried out in a Quantachrome, autosorb iQ and ASiQwin Model 6<sup>138</sup>. The process involved weighing out just over 1 g of material and degassing for 18 hours to remove any moisture or air.

#### **3.2.1.8 Microscopy**

Optical images were acquired using a *Leica DM6000 FS*<sup>139</sup> series microscope equipped with 5x, 10x, 50x and 100x magnification objective lenses. Images were visualised using *LAS-AF* version 2.6.0.



### 3.2.1.9 Powder Diffraction (XRPD)

Solid materials for structural solution were characterised off-line on a *Bruker D8 Advance*<sup>140</sup> equipped  $\theta/\theta$  geometry, primary monochromatic radiation (Cu  $K_{\alpha 1\lambda} = 1.54060 \text{ \AA}$ ), a Braun 1D position sensitive detector using transmission capillary geometry in an 0.7 mm borosilicate glass capillary.

Powder data collected for phase identification were collected on a *Bruker D2 Phaser*<sup>141</sup> diffractometer with  $2\theta/\theta$  geometry; Cu  $K_{\alpha 1,2}$  source radiation ( $K_{\alpha 1} 1.56060 \text{ \AA}$  and  $K_{\alpha 2} 1.54439 \text{ \AA}$  ratio of each not 50:50) -  $1.54060 \text{ \AA}$  with a LynxEye1D Detector. All powder patterns were analysed using *DIFFRAC EVA version 1*.

### 3.2.1.10 Easymax & Optimax

The Easymax and Optimax are STR with a total working volume of 100 mL and 1000 mL, respectively provided by *Mettler Toledo*<sup>142</sup>. They offers precise heating, cooling (-40 °C to 180 °C) and stirring capabilities. PAT tools including FBRM, IR and PVM can be easily added to the experimental set-up and synchronised for start-up. All data and trends can be captured for evaluation through *IControl*.

### 3.2.1.11 Crystalline

The Crystalline holds up to 8 glass vials with a working volume of 8 mL and is provided by *Technobis*<sup>143</sup>. Each reactor can be independently controlled for temperature and stirrer speed and type (overhead or magnetic). Real-time measurements, using turbidity and particle images, can be acquired to enhance process understanding and development.

### 3.2.1.12 Crystal 16

This device has 16 wells each designed to hold HPLC glass vials of total volume of 1.8 mL and is provided by *Technobis*<sup>143</sup>. The reactor can be magnetically stirred at a certain speed and are divided into four blocks that can be individually heated and cooled. Real-time measurements are acquired using a turbidity probe.

### **3.2.1.13 PVM**

In situ images of slurry were acquired using Particle Vision Measurement (PVM) probes provided by *Mettler Toledo* V819 series<sup>144</sup>. Images were acquired every 1 minute.

# **Chapter 4** Discovery and Characterisation of Form II Alpha Lipoic Acid

## 4.1 Introduction

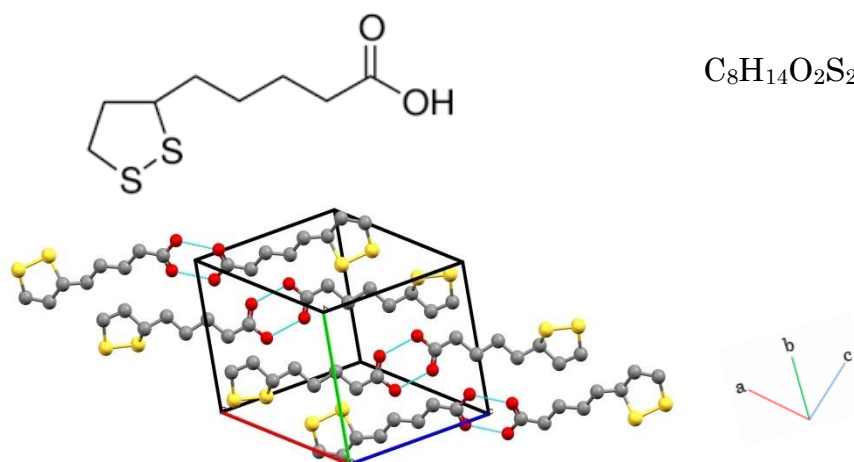
Crystal engineering is the design of molecular solids using the accessible molecular interactions, to formulate APIs with the desired physical and chemical properties<sup>145</sup> and can be used to improve the solubility, dissolution rate and bioavailability<sup>146</sup> by; crystal size and habit modification<sup>65, 73, 74</sup>, polymorphism<sup>50, 147, 148</sup> and co-crystal formation<sup>53, 54</sup>.

The ability to engineer APIs with suitable in-vivo characteristics, with optimum physical and chemical properties for stable and robust solids, provides a strong incentive for the exploitation of crystal engineering. One approach for crystal engineering is to use additives to modify the crystallisation process. These can include specific additives such as polymers<sup>149</sup>, impurities<sup>150</sup> or hydrotropes<sup>151</sup>. However, there are still gaps in the fundamental understanding of the important factors that contribute to the crystallisation of different solid-state forms of a compound in the presence of additives. As a result, the experimental challenge still lies in the selection of physical form with optimal solid-state properties for a given application and which can be produced reliably.

The work presented here examines the application of a hydrotropic additive to control the crystallisation of Alpha Lipoic Acid (ALA) and aims to develop an understanding around the mechanism through which hydrotropes exert their effect. This has led to the discovery of a new form of ALA when crystallised in the presence of a hydrotrope. The conditions under which the metastable form of ALA can be accessed were examined to find out whether the specific interaction between the hydrotrope and ALA contributed to the formation of the metastable ALA. Also, the new polymorph's crystal structure is solved and reported.

### 4.1.1 Lipoic Acid

ALA, also known as thioctic acid, 5-(1,2-dithiolan-3-yl) pentanoic acid, 6,8-thioctic acid, 6,8-dithiooctane acid and 1,2-dithiol-3-valeric acid, is a naturally occurring strong antioxidant<sup>152, 153</sup> which has also demonstrated benefits in the treatment of diabetes<sup>154, 155</sup> and cancer<sup>153, 156, 157</sup>. Despite there being research into the biological mechanism it has mainly been limited to cell activity<sup>158</sup> and anti-inflammatory properties<sup>159, 160</sup> with limited work on crystallisation and material properties. To date, one crystal form of ALA has been reported<sup>161</sup> (Figure 4.1) along with a ALA-Nicotinamide (NIC) co-crystal<sup>53</sup> and an ALA- $\beta$ -cyclodextrin inclusion complex<sup>162</sup>.



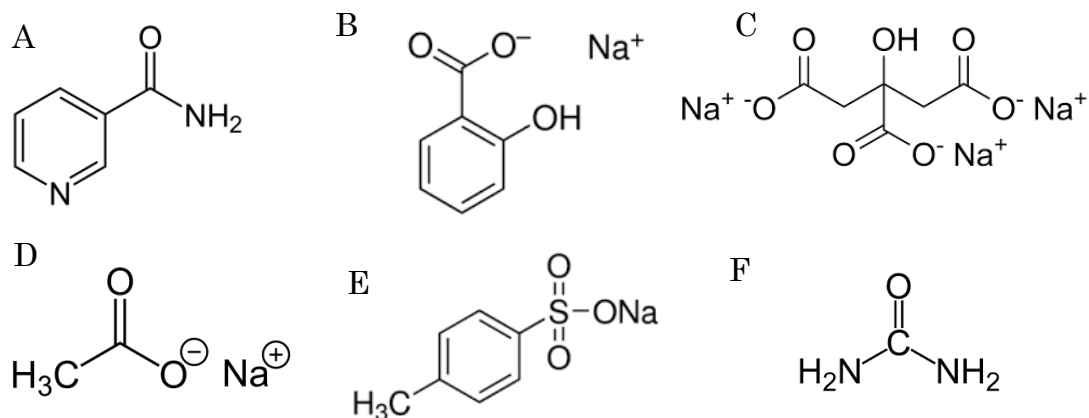
**Figure 4.1** Chemical structure and formula of ALA I (top) and crystal packing of ALA Form I (bottom).

The behaviour of ALA in solution has been studied by following changes in the UV absorption of the solution over a 54-hour period<sup>163</sup>. This revealed that when solution containing ALA was exposed to light, slow changes in the UV spectrum, characterised by decreasing absorption at 330 nm and increase absorption in the 250 nm were observed. This does not occur in solution which was protected from light<sup>163</sup>. ALA has also been shown to polymerise, producing a sticky, colourless material when exposed to heat<sup>164</sup>. Efforts to stabilise the system by complex formation with cyclodextrins<sup>165, 166</sup> and co-crystallisation with nicotinamide<sup>53</sup> are reported. The solubility of ALA in a number of mixed solvents (cyclohexane/ethyl acetate, heptane/ethyl acetate, and hexane/ethyl acetate), has also been determined<sup>167</sup> and in pure ipa<sup>53</sup> and water<sup>53</sup>. In the mixed solvent systems, the solubility of ALA increased with increasing ethyl acetate ratio, indicating that

ALA has a higher solubility in pure ethyl acetate. Amongst the three different mixed solvent systems, at constant solvent ratio to ethyl acetate, the solubility decreased in the order of hexane > heptane > cyclohexane. The crystallisation of ALA has not been widely studied – with the exception of the work exploring the discovery and scale-up of ALA-NIC co-crystal process<sup>53</sup>. Evidence for a metastable polymorph, ALA II, was obtained during the development of the ALA-NIC co-crystal; however, no details on its preparation or crystal structure have been reported to date. These aspects are explored in more detail in this chapter.

#### 4.1.2 Hydrotropes and Crystallisation

Hydrotrope (also referred to as cosurfactant and solvosurfactant<sup>168</sup>) is the term referred to a diverse class of water-soluble, not highly surface-active substances that increase the solubility of a solute<sup>169</sup>. Compounds including nicotinamide, sodium acetate, sodium salicylate, sodium *p*-toluene sulfonate and sodium citrate have been found to enhance the solubility of a variety of drug substances as shown in Figure 4.2<sup>170-172</sup>. Other terminology, which describes similar solubilisation mechanisms have been detailed in Table 4.1.



**Figure 4.2** Chemical structures of some known hydrotropes: A: Nicotinamide, B: Sodium Salicylate, C: Sodium Citrate, D: Sodium Acetate, E: Sodium *p*-toluene sulfonate and F: Urea.

In recent years, there have been examples leading to the discovery of new polymorphs from failed co-crystallisation trials. For example, metastable form of Olanzapine (Form IV<sup>151</sup>) was obtained from a failed co-crystallisation attempt

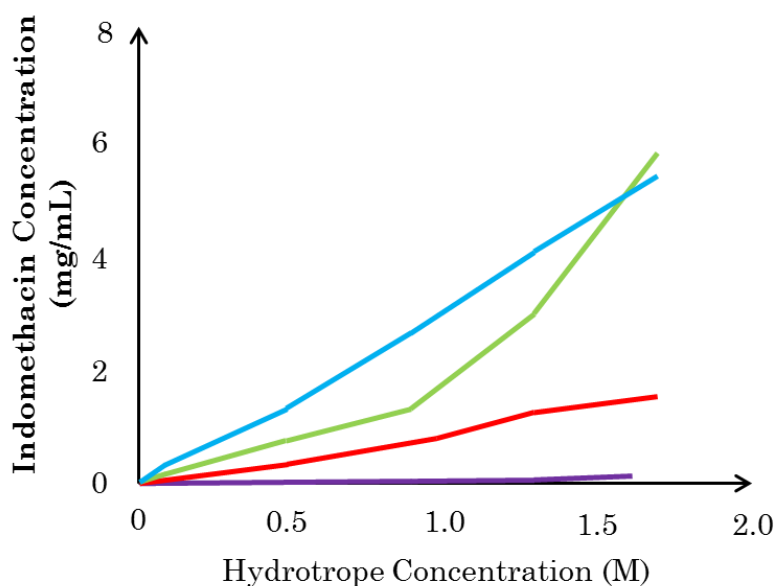
with NIC. In this report, solute and co-former molecules were proposed to be involved in specific interactions which favoured the formation of the metastable polymorphs. It was also observed that when crystallised under identical conditions, only in the presence of NIC was ALA II obtained. NIC, Vitamin B<sub>3</sub>, is a substance well documented to demonstrate hydrotropic solubilisation<sup>171-179</sup>. Based on its low toxicity and evidence of solubilisation, NIC has demonstrated its value as a solubility enhancer in pharmaceutical formulations<sup>177</sup>.

**Table 4.1** Definitions of similar terminology describing solubilisation mechanism.

Terminology	Description	Reference
Hydrotrope	Freely soluble organic compounds which at a concentration considerably enhance the aqueous solubility of organic substances, otherwise insoluble under normal conditions. These compounds may be anionic, cationic or neutral molecules.	180
Solutrope	Addition of a large amount of a solid solute to any solvent (not limited to water) which causes an increase in the solubility of another slightly soluble solute - restricted to include solids only in order to distinguish solubilisation from cosolvents.	168
Lyotrope	Cations and anions which are ranked along the lyotropic series according to their reduction of protein solubility. These structures do not exhibit hydrophilic-lipophilic sections as seen with hydrotropes.	181

Studies investigating the effect of various hydrotropes on the solubility of well-known API's concluded that the degree of solubilisation changed with the hydrotrope structure<sup>176, 182, 183</sup> (Figure 4.3). Jain *et al*<sup>176</sup> investigated the hydrotropic efficiency of a number of hydrotropes on indomethacin, a non-steroidal anti-inflammatory agent which is practically insoluble in water. The

solubility enhancement of indomethacin by the hydrotropes was in decreasing order of; sodium *p*-hydroxy benzoate > sodium benzoate > nicotinamide > resorcinol > urea. Similar studies investigating zaleplon, a poorly water-soluble non-benzodiazepine hypnotic drug, found the solubility of zaleplon increased between 350 and 2000 fold, respectively, when equimolar amounts of sodium benzoate and resorcinol were used<sup>182</sup>. These results are in agreement with Agrawal *et al*<sup>183</sup> findings; where the solubility enhancement of nimesulide by the hydrotropes was observed in decreasing order as piperazine > sodium ascorbate > sodium salicylate > sodium benzoate > and nicotinamide.



**Figure 4.3** Change in aqueous solubility of indomethacin as a function of hydrotrope concentration (sodium nicotinate (blue), sodium benzoate (green), nicotinamide (red) and sodium *p*-toluenesulfonate (purple) figure drawn with data from reference 184).

The above studies attributed these findings to the hydrotropes' ability to interact with the solute as a result of the large surface area and, if present, an aromatic sextet provided by the benzene ring. These sites would be available for non-bonded and van der Waal's interactions with water and the solute, contributing to the solvation of the solute.

Additionally, the effect of hydrotrope concentration on solubilisation efficiency has also been examined<sup>176, 182, 183</sup>. These indicated that there is a concentration



(which is specific to the hydrotrope – solute system<sup>170</sup>) at which the hydrotrope shows a significant increase in solubility of the solute, termed the Minimum Hydrotropic Concentration (MHC)<sup>185</sup>. When sufficient amounts of hydrotrope are in solution, there is an increase in the hydrotrope-hydrotrope association around the solute as opposed to the bulk solution. It is this accumulation around the drug which has been suggested as the basis of MHC<sup>173, 186, 187</sup>. Whilst MHC is widely accepted, cases where there was a lack of MHC which produced a great increase in solubility has been identified. This led to the suggestion that hydrotropic solubilisation may be a continuous phenomenon<sup>172</sup>.

Features like the presence of both hydrophilic to hydrophobic units, degree of hydrophobicity, the number of aromatic rings, a planar molecular geometry of the solute and the solvent's ability to be both a proton donor and acceptor have been shown to be important<sup>172, 188, 189</sup>. However, finding a suitable hydrotrope for a given API remains empirical only through trial and error. That said, the hydrophobicity and aromatic surface area, hydrogen bonding and other bond capabilities have been put forward as important factors for predictive capabilities<sup>189</sup> and recently the task of selecting an appropriate hydrotrope has been explored through machine learning methods<sup>184</sup>.

The difficulty of explaining hydrotropic mechanisms has arisen from the specificity and the structural diversity of hydrotropes. Despite the belief that the mechanism may vary from system to system or may be a concentration dependant mechanism<sup>183, 190</sup>, a number of possibilities explaining hydrotropic solubilisation behaviour have been put forward. These are summarised in the following sections.

#### **4.1.2.1 Complexation Between The Solute and The Hydrotrope**

A complex has been suggested to form by the interaction between the planar hydrophobic regions of the hydrotropic agent and the solute to reduce the exposure of the hydrophobic regions to water<sup>177</sup>. This can be due to electron donor acceptor interactions, hydrogen bonding and hydrophobic interactions<sup>171, 191</sup>. Complex formation between hydrotrope and solute can be either a 1:1 or a 1:2 complex, whereby the drug is associated with one hydrotrope molecule or located between two hydrotrope molecules, respectively.

Hydrotropic solubilisation of riboflavin was previously reported<sup>191</sup> in the presence of caffeine through complex formation. The solubility of riboflavin in a 0.0927 M solution of caffeine in water was increased by three fold. The formation of a non-fluorescent complex, by the addition of caffeine on the fluorescence of riboflavin in aqueous solutions was demonstrated.

Furthermore, studies by Suzuki et al<sup>171</sup>, investigated the mechanism of solubilisation of nifedipine with NIC, urea and their analogues. Thermodynamic properties for both the 1:1 and 1:2 complex formation of Nifedipine with NIC, indicated that whilst the system became more ordered with complex formation (negative  $\Delta S$ ); the overall  $\Delta G$  was negative signifying thermodynamic favourability and spontaneity towards solvation. The  $\Delta H$  values indicated the involvement of other intermolecular forces as well as hydrogen bonding.

Whilst complex formation has been put forward as a plausible explanation for hydrotropic solubilisation, this theory has been challenged. The degree to which NIC was able to solubilize riboflavin was studied by Coffman *et al*<sup>172</sup>. Over the NIC concentrations studied, a 36-fold increase in riboflavin solubility was noted. However, no significant changes in the UV/vis spectrum of riboflavin indicative of complexation were observed. Also, because NIC and riboflavin are both  $\pi$ -electron acceptors, complexation was ruled out as the method of solubilising riboflavin. However, a number of other studies have proposed complexation to be the main mechanism of solubilisation<sup>171, 175, 177, 192</sup>.

#### **4.1.2.2 Self-aggregation of The Hydrotrope**

The self-aggregation theory, assumes that the self-association of a hydrotrope occurs stepwise, initially through monomer addition. As the concentration of the hydrotrope increases, firstly dimers are formed, followed by trimers resulting in higher order associations through consecutive monomer addition to existing small aggregates in solution<sup>193</sup>.

Compounds structurally similar to NIC, N,N-diethylnicotinamide (DENA) and N,N-dimethylbenzamide (DMBA), were studied for their solubilisation efficiency<sup>189</sup>. Their aggregation behaviour in solution was described by the formation of dimers only, whereas the latter required the presence of dimers, trimers, and tetramers. The higher aggregation tendency of DMBA due to its

more hydrophobic nature was suggested as a reason for its overall higher solubilising ability, compared with DENA. Further studies investigated the solubilisation of paclitaxel with DENA and examined the self-aggregation of DENA using NMR<sup>188</sup>. As the concentration of DENA reached 0.1 M, the chemical shifts of all protons of the nicotinamide ring started to decrease, indicating the self-aggregation of DENA molecules. The MHC value of DENA was estimated to be 0.12 M, which was very close to the concentration of 0.11 M where DENA begins to exhibit solubilisation of paclitaxel. This may allow the suggestion to be made that self-aggregation is necessary for hydrotropic solubilisation, since attainment of MHC has been recognised as an important part of achieving hydrotropic solubilisation<sup>185</sup>. Similar findings have been reported by Das *et al*<sup>194</sup> who concluded that the aggregate formations were driven by the hydrophobic tail of the hydrotrope and that MHC was related to the onset of self-aggregation. Molecular dynamic simulation<sup>194</sup> showed the solute molecules to incorporate inside the core of the clusters of hydrotrope molecules, which increased as the hydrotrope concentration increased. This suggests that hydrophobic solute molecules would prefer to stay in a hydrophobic environment over an aqueous medium. Agreeing with other studies, which concluded that self-aggregation of hydrotrope will allow the separation of the hydrophobic solute from water, easing the energy increase to the system<sup>174</sup>.

Conversely, studies which have demonstrated hydrotropic solubilisation with NIC, indicated the level of self-aggregation undertaken by NIC not to be sufficient enough to be essential to the enhanced solubility<sup>175</sup> and that the self-aggregation may in fact reduce the degree of solubilisation<sup>173</sup>.

#### 4.1.2.3 Breaking of the “Water Structure” by The Hydrotrope

The ordering of water is increased when non-polar solutes are dissolved in water molecules<sup>195</sup> and hydrophobic hydration (clathrate cage and cavity based model) describes the changes of water around a non-polar solute. The clathrate cage describes the association of non-polar solute with the tetrahedral water molecules through van der Waals interactions, to become a five molecule structure. The water cluster forms a partial cage around the non-polar solute leading to an ordering effect on the solvent and to a large decrease in entropy<sup>195</sup>. In the cavity based model, the formation of a cavity in the water to accommodate the solute and the interaction of the solute with the water molecules is considered to lead to the structuring of the solvent, decreasing entropy<sup>196</sup>. To overcome these effects, the non-polar solutes can aggregate within the solution (*the hydrophobic effect*). This will decrease the interaction between water and the non-polar solute increasing the disorder within the system, which is thermodynamically favourable<sup>197</sup>. It is reported that urea and NIC have the ability to reduce hydrophobic bonding through their ability to disrupt the structure of water by providing alternative hydrogen bonding possibilities<sup>195, 198</sup>. Such molecules become associated with the structured water making it easier to produce a cavity in which the non-polar solute can be accommodated. Hydrophobic bonding of the solute becomes thermodynamically less favoured and increases the disorder of the system, promoting solvation<sup>195, 196</sup>.

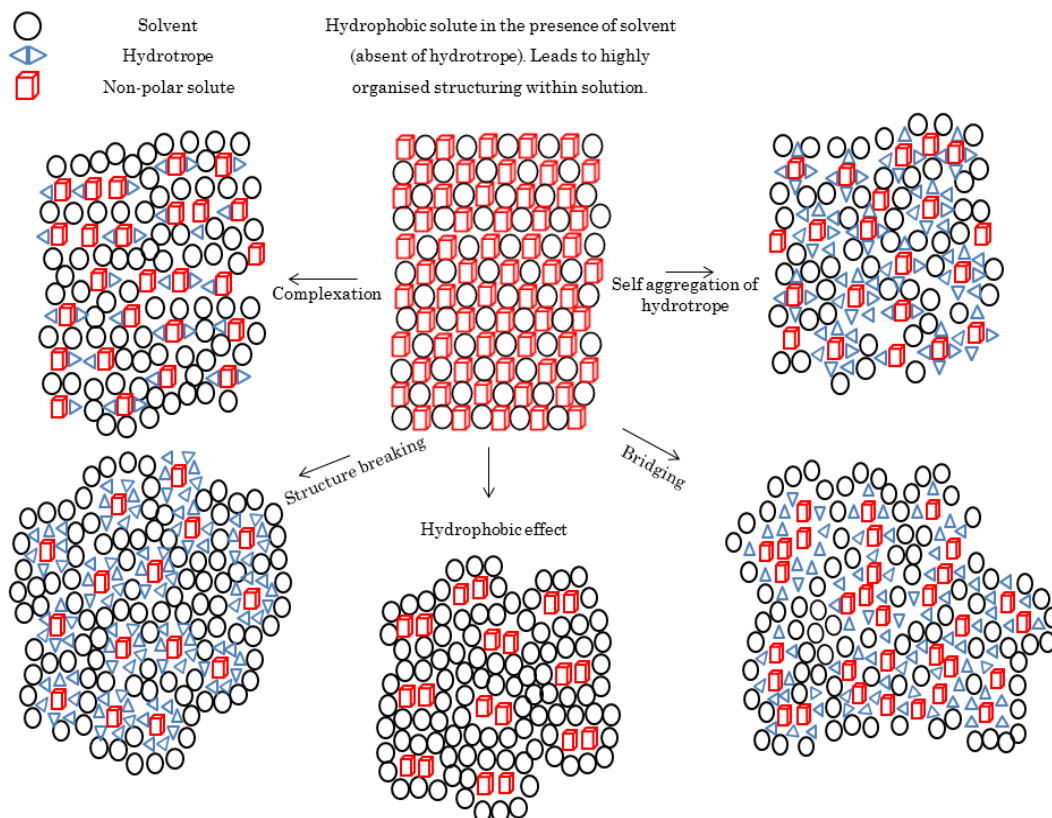
The solvent dependent nature of hydrotropy was examined by assessing the solubilisation efficiency of NIC and urea on riboflavin with a number of solvents (methanol, N-methylformamide, dimethyl sulfoxide, acetone and water)<sup>172</sup>. An examination of solvent properties revealed that the solvent's ability to be both a proton donor and acceptor was important since; in water, methanol, and N-methylformamide, solubility of riboflavin increased with increasing hydrotropes' concentrations but decreased in dimethyl sulfoxide and acetone. This study proposed that hydrotropes may act by altering the solvent's ability to participate in structure formation through intermolecular hydrogen bonding. The solubilisation efficiency of N, N diethylnicotinamide on nifedipine has also been investigated in different solvents and solvent dependant effects were also reported<sup>171</sup>.

Investigations by Booth *et al*<sup>169</sup> assessed the hydrotropic solubilisation of butyl acetate and butyl benzoate with three hydrotropes (urea, sodium benzoate, and sodium salicylate) in the same solvent system (water). If the hydrotrope induced its effect by changing the water structure, both solutes were expected to exhibit a similar degree of solubilisation. The extent of solubilisation of both butyl acetate and butyl benzoate in the same solvent-hydrotrope system was different. Further studies, which include statistical thermodynamics, dismissed changes to water structure as the mechanism of hydrotropic solubilisation and suggested the accumulation of the hydrotrope around the solute and release of water molecules upon preferential interaction between solute and hydrotrope to be the main effects leading to hydrotropic solubilisation<sup>169, 173, 186</sup>.

#### 4.1.2.4 Bridging

Breslow *et al* suggested that molecules such as urea, can directly assist the solvation of non-polar materials in water by acting like a bridge between the polar water and the non-polar solute<sup>197</sup>. This idea stemmed from research which investigated the solubilising efficiency of guanidium chloride (a compound reported to increase the solubility of poorly soluble solutes often reported to act similarly to urea<sup>199</sup>). An increase in the solubility of benzene resulted in an increase in the surface tension (making formation of cavitation energetically more demanding). This allowed the suggestion to be made that this compound was unlikely to exert its effect through structure breaking methods as that would be expected to lead to a reduction in surface tension. A reduction in the Gibbs energy of the system, as a result of the more favourable solvent and additive interaction in relation to the previous solute and solvent interaction was suggested as the reason for the solubility increase<sup>190</sup>. This theory has been supported by the interaction and resultant solubilisation of alkyl-p-hydroxybenzoates and of  $\beta$ -phenylalanine with urea<sup>200</sup>.

Consequently, hydrotropes have been reported to interact with the solute and/or solvent in several ways leading to structural changes in solution. A summary of the, thus far, discussed methods and their respective potential structural changes in solution are shown in Figure 4.4.



**Figure 4.4** Schematic representing the possible ways in which hydrotropes may be interacting with the solute leading to hydrotropic solubilisation.

A number of similarities can be identified between hydrotropes and surfactants (e.g. aggregation, solubilisation, and need for a minimum concentration) and this has led to the suggestion that in some ways hydrotropes do not differ in association behaviour from regular surfactants<sup>201</sup>. However, there are some significant differences and some of these are:

- i. For surfactant the concentration needed generally is in the order of millimolar or less the Critical Micelle Concentration (CMC), however, it is in the molar range for hydrotropes (MHC)<sup>186</sup>.
- ii. The degree of solubilisation exhibited by hydrotropes is generally higher than that observed for surfactants<sup>185</sup>.

- iii. The concentration dependant variation is greater in hydrotropes than surfactants<sup>185</sup>.
- iv. Hydrotropes may have specific effects depending on the solutes whereas surfactants will solubilise a wider range of compounds <sup>185</sup>.
- v. Surfactants have long hydrocarbon chains whereas hydrotropes are characterised by a short, bulky, compact moiety<sup>202</sup>.
- vi. When surfactant concentration is increased above its CMC, surfactant molecules self-aggregate into micelles. Hydrotropes, due to the smaller nature of the hydrophobic region do not form micelles<sup>170</sup>.

Investigations of hydrotrope-solvent mixtures concluded that the solution properties changed as a function of hydrotrope concentration<sup>203</sup>. Such properties describe the solute-solvent interactions, thus, can affect the nucleation process and the crystallisation outcomes. As such, further advances in understanding hydrotropy is required to determine the important factors that contribute to the crystallisation of different solid-state forms of a compound in the presence of an hydrotrope. There is the potential to use modern technologies to enable development of the knowledge base around hydrotropism and therefore extend their application within the pharmaceutical systems.

A hypothesis was made that NIC would interact with ALA and this specific interaction would lead to the crystallisation of ALA II. Although the exact mechanism by which this leads to the metastable form is unknown, the interaction may lead to a number of possibilities:

- i. NIC may be increasing the solubility of ALA I in the solvent system studied, allowing access to a metastable form upon cooling.
- ii. NIC may be interacting with ALA and the NIC-ALA structure could be acting as a molecular template leading to the metastable form.
- iii. NIC may be influencing the nucleation rates of ALA I and ALA II i.e. in the presence of NIC, the nucleation of ALA II may be increased with respect to ALA I.
- iv. If it can be assumed that ALA II may form regardless of the presence of NIC, it may be that NIC is retarding the transformation of ALA II to ALA I.

The initial task would be to identify if NIC acts as a solubiliser. This can be carried out by using a supersaturated solution of ALA which has reached its solubility equilibrium after which NIC would be added and changes in ALA solubility will be monitored. If this is confirmed, the change in solubility can be linked to the presence of NIC. To determine the role of NIC on the crystallisation of ALA II, a series of experiments would be carried out to understand if any differences in the solutions containing NIC can be identified with respect to the solution absent of NIC. Lastly, with the effect of NIC on the solubility of ALA quantitatively determined, this can be used to calculate the supersaturations in which ALA II forms. These experiments would be repeated without NIC to determine if there is any evidence of ALA II forming.

## 4.2 Experimental

### 4.2.1 Preparation, Structure Solution and Solid state Characterisation of ALA II

0.51 g (2.47 mmol) of ALA I and 0.31 g (2.54 mmol) Nicotinamide (NIC) were dissolved in 4.5 mL of ipa and 5 mL of water, respectively. Two solutions were mixed at room temperature and transferred to a freezer at  $-17\text{ }^{\circ}\text{C}$  ( $\pm 0.5$ ) and kept there for 24 hours. The crystals formed were filtered under vacuum, washed with distilled water and dried at room temperature.

Single crystals for structure solution were prepared using the setup described in *Chapter 3 section 3.2.1.11*. Solutions with the above concentrations were prepared and placed isothermally at  $-5\text{ }^{\circ}\text{C}$  without stirring and held for 24 hours. Single crystal X-ray diffraction intensities were collected using a *Bruker D8 Venture* diffractometer with a Cu source ( $\lambda=1.54178\text{ \AA}$ ) at ambient temperature (297K) between  $2\theta$  range  $3.85\text{-}74.23^{\circ}$ . Data were reduced and the cell refined using SAINT as incorporated in the APEX3 software<sup>204</sup>. SADABS was used for the absorption correction<sup>205</sup> as its capable of correcting for errors such as incident beam inhomogeneities. The crystal structure was solved by the intrinsic phasing method in XT and refined using XL in the OLEX2 refinement package<sup>206</sup>. Enhanced rigid bond restraints were applied over all non-hydrogen atoms. The appropriate AFIX constraints were applied to the hydrogen atoms to ride all parent atoms.



#### 4.2.1.1 DSC

The thermal analysis was performed by heating 5 mg of the sample at a scan rate of 10 °C/min in an aluminium pan with pierced lid covered under nitrogen gas flow. The investigation was carried out over the temperature range 20-80 °C using the instrumentation detailed in *Chapter 3 Section 3.2.1.4*). Blank correction was carried out with an empty pan prior to sample analysis.

#### 4.2.1.2 XRPD

Solid materials were characterised off-line via XRPD using a Bruker D8 Advance using transmission capillary as described in *Chapter 3 Section 3.2.1.9*. 2 $\theta$  range and count time were as detailed in Table 4.2.

**Table 4.2** Variable count time scan parameters.

2 $\theta$ -range	Step size	Seconds/step
3° to 30°	0.017°	2s
30° to 43°	0.017°	8s
43° to 56°	0.017°	16s
56° to 70°	0.017°	24s

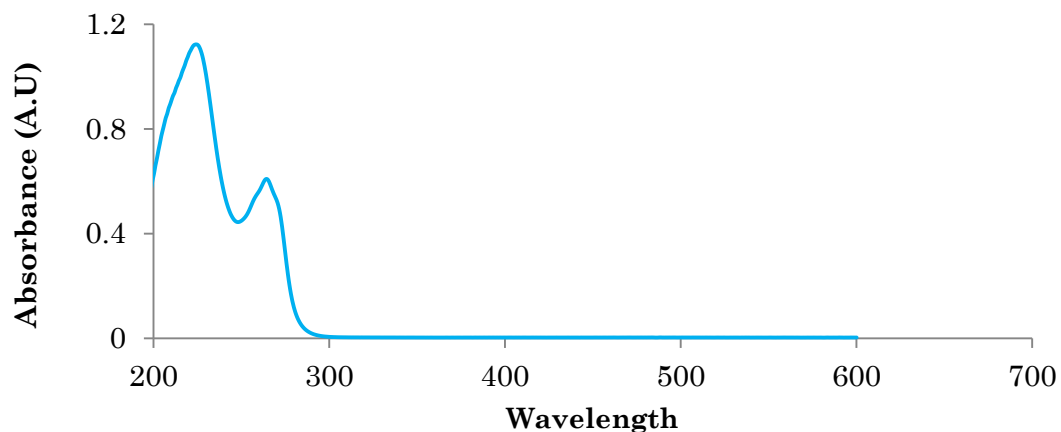
#### 4.2.1.3 IR

IR spectra were recorded on a Bruker Tensor II IR spectrophotometer as detailed in *Chapter 3 Section 3.2.1.3*. Blank reference was taken with air.

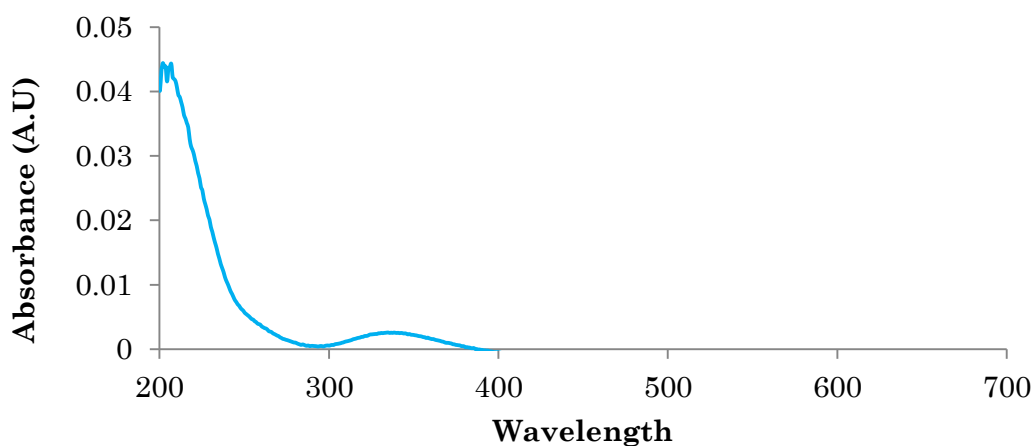
#### 4.2.2 Hydrotropic Effect of Nicotinamide on ALA

A concentration calibration curve for ALA was constructed using known concentrations of ALA I in ipa:water 9:10 v/v at room temperature. Excess ALA was dissolved in ipa:water 9:10 v/v solvent system and stirrer at a constant temperature of 10 °C and 70 rpm until the UV signal stabilised, indicating equilibrium had been reached. Increasing amounts of NIC (as a solid) was added whilst an inline ATR-UV probe took measurements periodically. To record changes in ALA concentration, wavelength 333 nm was selected. NIC's maximum absorbance was recorded at 265 nm (solvent system taken as

reference). Reference measurements for NIC and ALA are shown below in Figure 4.5 and Figure 4.6. Concentration of NIC was increased after 60 minutes. Investigations were carried out in a *Mettler Toledo EasyMax* set up as described in *Chapter 3 Section 3.2.1.10*.



**Figure 4.5** Reference UV measurement for NIC in ipa 9:10 water v/v,  $\lambda_{\max} = 261$  nm.



**Figure 4.6** Reference UV measurement for ALA in ipa 9:10 water v/v,  $\lambda_{\max} = 333$  nm.

### 4.2.3 Effect of Nicotinamide on Polymorphic Outcome of ALA

The influence of NIC concentration on the polymorphic outcome of ALA crystallisation was investigated by carrying out small scale cooling crystallisation experiments. Individual vials containing ALA solutions (0.11 g/mL of ipa) and NIC solutions with concentrations between 0-0.36 g/mL of water were prepared. One vial of ALA solution was then mixed with one vial of NIC solution at 20 °C and this was repeated for all NIC solutions prepared. All solutions were then crash cooled to -10 °C. These experiments were completed using the equipment as detailed in *Chapter 3 Section 3.2.1.11*. The crystals formed were filtered under vacuum, washed with distilled water and air dried.

### 4.2.4 Ex-Situ Transformation Measurements Using XRPD

ALA II stability was assessed by slurring a suspension of ALA II in ipa:water 9:10 v/v was analysed over 24 hours using the *Crystalline* setup (*Chapter 3 Section 3.2.1.11*). The stirring speed was set at 1000 rpm. Each vial was stirred at a constant temperature of -15 °C, -10 °C, 0 °C, 10 °C and 20 °C. At the relevant time interval, an aliquot of solution was removed, filtered, dried and the solid was examined via XRPD.

### 4.2.5 Dynamic Light Scattering

DLS measurements were carried out using a *Malvern ALV/LSE- 5004* instrument using the methodology described in *Chapter 3 Section 3.2.1.6*. Solutions were prepared at room temperature and filtered with a 0.22 micron filter before being placed in a clean, glass sealable vial. Investigations were carried out at constant temperature (25 °C), using a scattering angle  $\theta = 173^\circ$  and laser light wavelength  $\lambda = 632.8$  nm. The size profile within solutions was assessed for six hours at hourly intervals with a final measurement taken at 24 hours. Each sample was analysed three times and the average size detected of the three runs, was plotted and used for comparison.

#### **4.2.6 Solubility Measurements**

The solubilities of ALA II and NIC in ipa water 9:10 v/v mixtures were measured as a function of temperature using the setup described in *Chapter 3 Section 3.2.1.12*. For each well, using the turbidity sensor, the clear point was detected. A stirrer speed of 800 RPM and a heating rate of 0.5 °C/min was selected to investigate solubility of ALA II between 0 - 20 °C.

Excess ALA I was slurred in ipa : water 9:10 v/v solvent system at a range of temperatures (0 °C – 20 °C) for 24 hours using Crystalline setup (*Chapter 3 Section 3.2.1.11*). After 24 hours, the solution was filtered and weighed. Solvent was allowed to evaporate until no more change in weight could be detected.

#### **4.2.7 Solid State Stability**

Solid state stability of ALA II was assessed by storing crystals at -17 °C and at room temperature for up to 12 months. The effect of humidity or light was not taken into consideration. Bruker D2 diffractometer was used to detect any changes in crystalline purity of material using the methodology described in *Chapter 3 Section 3.2.1.9*.

#### **4.2.8 Microscopy**

Optical images were acquired using a Leica DM6000 FS series microscope. Images were visualised using LAS-AF version 2.6.0 (*Chapter 3 section 3.2.1.8*).

### **4.3 Results and Discussion**

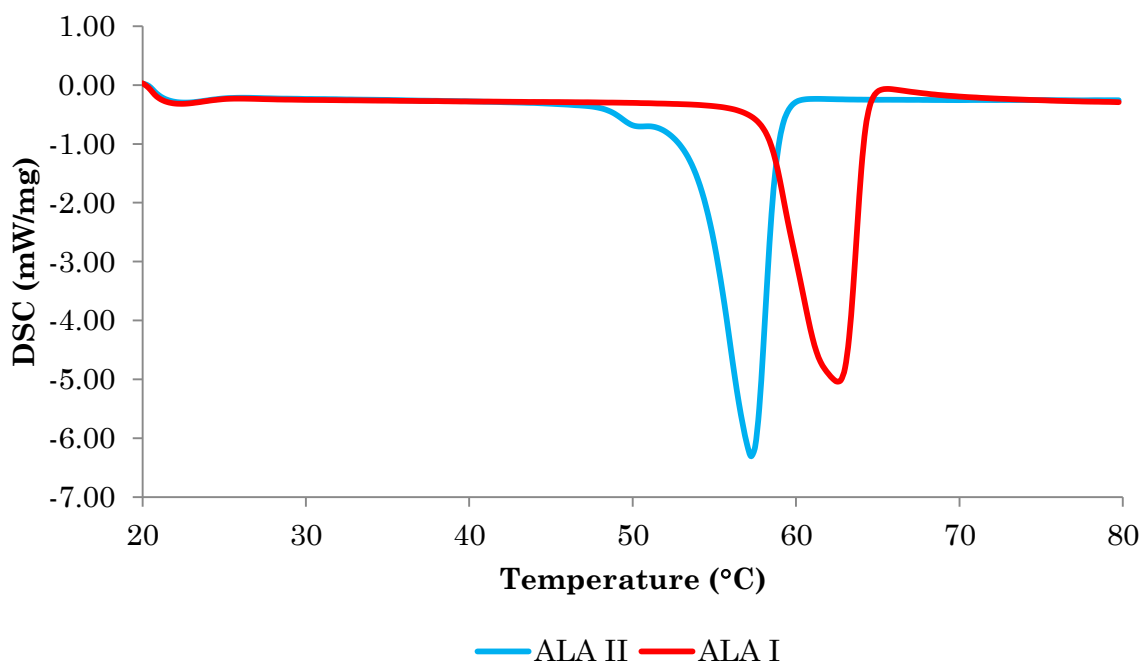
Solid state characterisation of the crystallised product was carried out using DSC, IR, capillary and variable count and variable temperature XRPD. Structure determination of ALA II was also carried out.

#### **4.3.1 Preparation, Structure Solution and Solid State Characterisation of ALA II**

Sample was prepared as described in 4.2.1. The crystals obtained from under these experimental conditions were a different crystalline form than the previously reported form, ALA I.

##### **4.3.1.1 DSC**

DSC analysis showed that ALA II had an onset temperature of melting at 48.4 °C, whilst for ALA I this was slightly higher at 57.6 °C (Figure 4.7). In addition, no mass loss was observed in the TGA, suggesting it to be an anhydrous crystalline phase (not shown here). A single endothermic event, indicating melting, was observed with no further thermal events thereafter. The lower melting temperature, would therefore confirm, ALA II to be the metastable and ALA I to be the stable form. The shoulder at 48.4 °C for ALA II was considered to be due to sample preparation as uneven distribution of sample can lead to such anomalies.

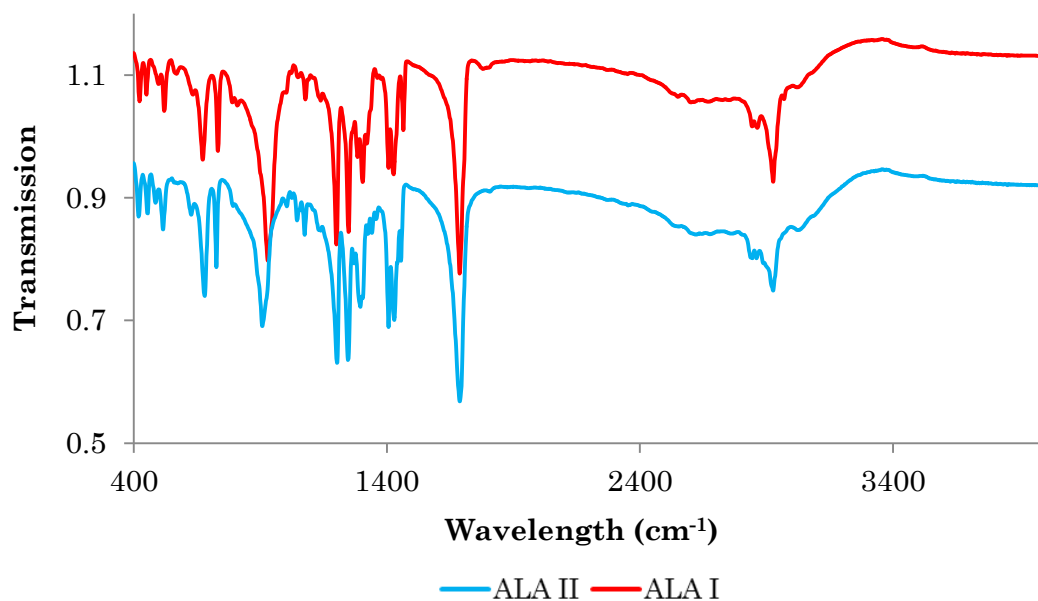


**Figure 4.7** DSC analysis of ALA II (blue) and ALA I (red).

#### 4.3.1.2 IR

The infrared spectra of ALA polymorphs I and II are shown in Figure 4.8. The following modes; 2702  $\text{cm}^{-1}$  corresponding to (C-H), 1712  $\text{cm}^{-1}$  corresponding to (C=O), 1449  $\text{cm}^{-1}$  corresponding to ( $\text{CH}_2$ ), 1414  $\text{cm}^{-1}$  corresponding to ( $\text{CH}_2$  - C=O), 1250  $\text{cm}^{-1}$  corresponding to (C-OH) and 934  $\text{cm}^{-1}$  corresponding to (COOH, dimer) have been reported during the isolation and characterisation of ALA I<sup>207</sup>.

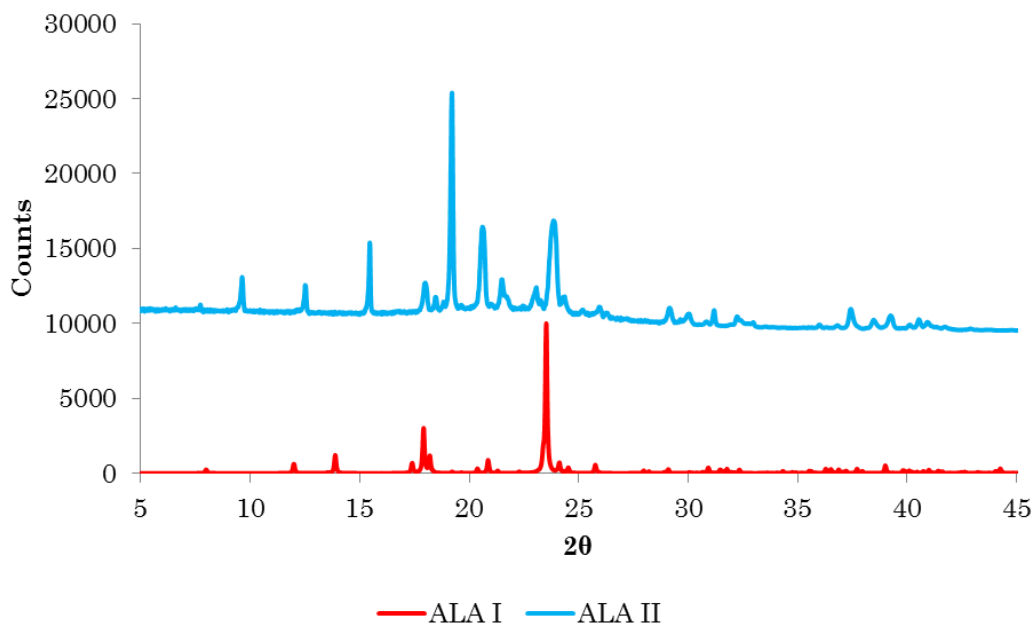
On comparison of the spectrums, the mode corresponding to (C=O) appear to be at similar wavelengths, with a slight broadening for ALA II. No major differences can be seen at 1414  $\text{cm}^{-1}$  corresponding to ( $\text{CH}_2$  - C=O) or 1250  $\text{cm}^{-1}$  corresponding to (C-OH). At around 1450  $\text{cm}^{-1}$  the peak corresponding to ( $\text{CH}_2$ ), is seen to have shifted to the left by 10  $\text{cm}^{-1}$  for ALA II. The peak at round 900-950  $\text{cm}^{-1}$  corresponding to (COOH, dimer) is also seen to have moved to the left by 20  $\text{cm}^{-1}$  for ALA II. This may indicate the packing of the dimers to be different between ALA I and II. The peaks corresponding to ( $\text{CH}_2$ ) and (COOH, dimer) would be useful peaks for polymorph identification. However, with the exceptions noted above, the spectra for ALA I and II are very similar in peak positions across the spectrum with variations of  $<3 \text{ cm}^{-1}$ .



**Figure 4.8** FTIR spectra for ALA I and ALA II.

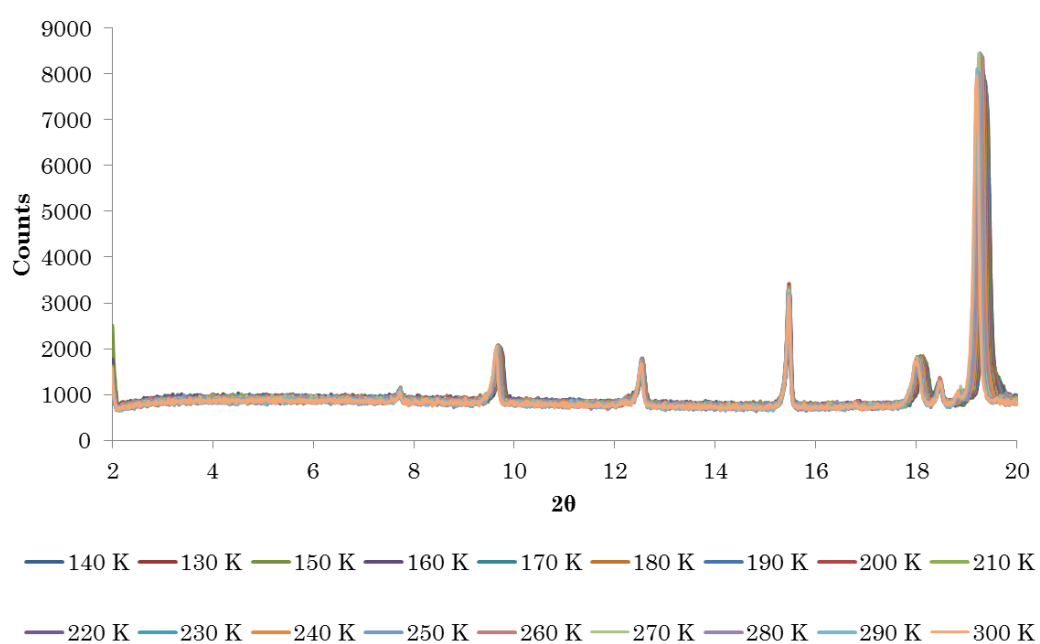
#### 4.3.1.3 XRPD

Capillary powder data was collected for ALA II and is shown alongside the powder pattern for ALA I extracted from CCDC (*Reference THOCAR1*) (Figure 4.9).



**Figure 4.9** Capillary powder pattern for ALA I (top) and ALA II (bottom).

For ALA II some of the characteristic peak positions at  $2\theta$  are as follows:  $7.7356^\circ$ ,  $9.6489^\circ$ ,  $12.5378^\circ$ ,  $15.4527^\circ$ ,  $18.0288^\circ$ ,  $18.4836^\circ$ ,  $18.8496^\circ$ ,  $19.2266^\circ$ ,  $19.4679^\circ$  and  $19.6554^\circ$ . These show numerous differences from the pattern derived from ALA I e.g. at  $2\theta = 9.6489^\circ$  and  $15.4527^\circ$  peaks can be observed for ALA II that are otherwise absent in ALA I. Furthermore, over the temperature range of 100 K to 300 K powder data were also collected to investigate if this would lead to any changes in polymorphism (Figure 4.10). No further changes indicative of solid state transformation could be observed over the temperature range examined. However, a shift in some of the peaks can be seen due to the thermal expansion of the sample rather than a solid form change.

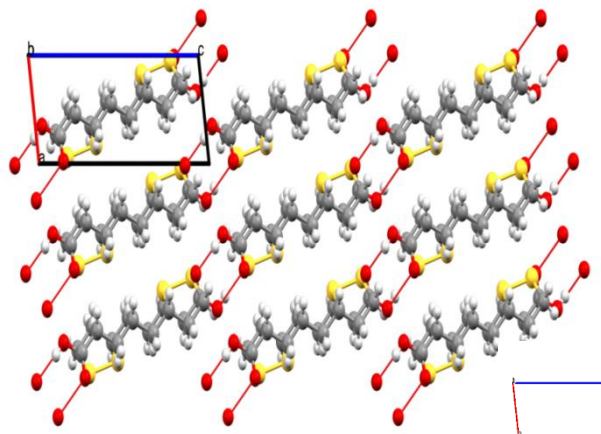


**Figure 4.10** Powder pattern for ALA II at temperatures from 100 K to 300 K.



#### 4.3.1.4 ALA II Crystal Structure

A single crystal sample was obtained as described in *Section 4.2.1* and the crystal structure of ALA II was solved using single crystal diffraction. The diffraction pattern was indexed to a triclinic unit cell with the dimensions in Table 4.3. The crystal packing as viewed down the b-axis is shown in Figure 4.11.



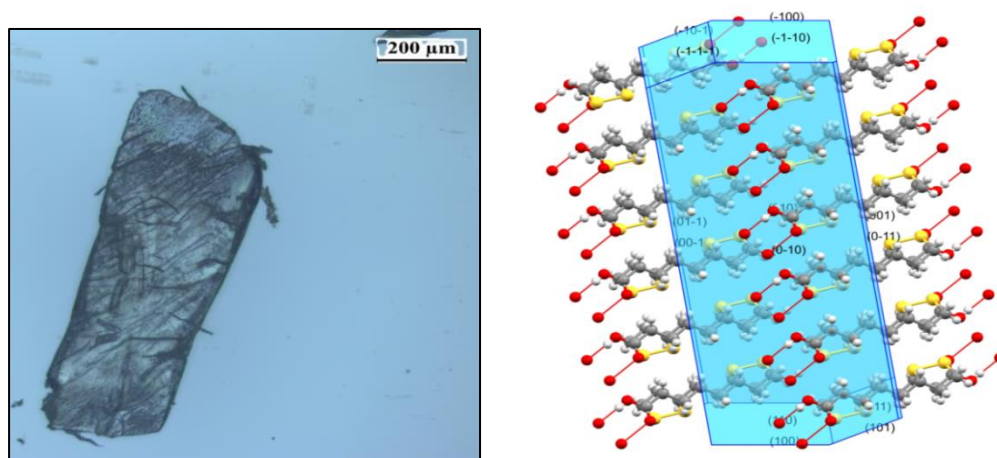
**Figure 4.11** Crystal packing of ALA II

**Table 4.3** Crystal Structure of ALA II

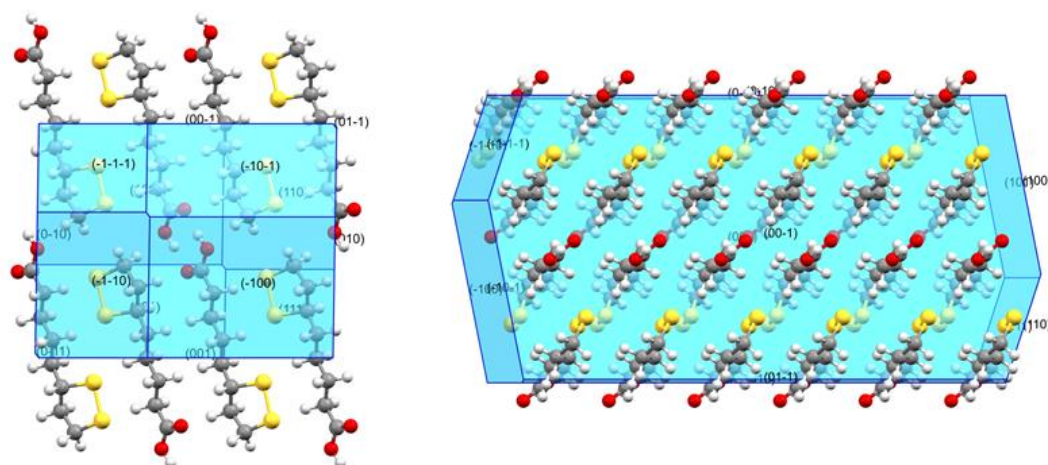
Lattice Parameters	
Formula unit	C <sub>8</sub> H <sub>14</sub> O <sub>2</sub> S <sub>2</sub>
Molecular weight (g/mol)	206.33
Crystal system	Triclinic
Space group	P-1
a (Å)	4.758 (12)
b (Å)	9.191 (3)
c (Å)	11.637 (3)
α (°)	89.101 (15)
β (°)	80.810 (13)
γ (°)	78.873 (16)
Volume (Å <sup>3</sup> )	492.9 (2)
Goodness of Fit	1.046

Based on the refined crystal structure, the morphology of ALA II was predicted using the Bravais Friedel Donnay Harker (BFDH) model using *Mercury 3.9*

incorporated within the Cambridge Crystallographic Data software package<sup>208</sup>. The BFDH approach considers the binding energy between the different crystal faces and does not account for solvent effect, supersaturation or experimental growth conditions<sup>22</sup>. However, it does provide a theoretical morphology to compare with the observed crystals produced under different conditions. The predicted morphology of ALA II produced an elongated block-like habit, in comparison to the tabular shaped ALA I<sup>209</sup>. Microscopy image of a single ALA II crystal was obtained with dimensions of 300 x 1100  $\mu\text{m}$ . A general similarity between the single crystal of ALA II and the predicted morphology shown in can be observed (Figure 4.12 and Figure 4.13).



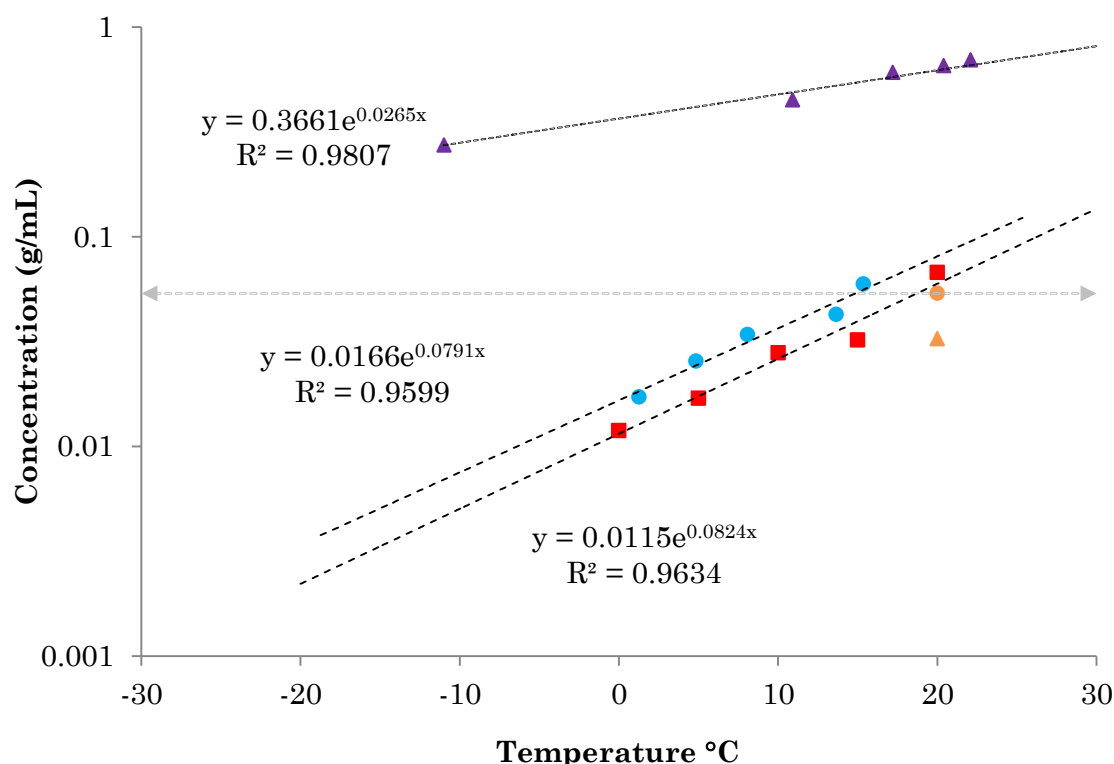
**Figure 4.12** A crystal of ALA II (left) and the predicted crystal morphology of ALA II (b-axis).



**Figure 4.13** Predicted morphology of ALA II viewing from a-axis (left) and c-axis (right).

### 4.3.2 Solubility

Solubility of ALA I, ALA II and NIC were obtained in ipa : water 9:10 v/v solvent system (Figure 4.14). ALA I and II have different temperature dependent solubilities whilst NIC has around a 12-fold higher solubility at 20 °C. The dotted lines represent extrapolated data and are based on the solubility data acquired. It is predicted that, as the solubilities of ALA I and II do not cross each other over the investigated temperature, this would indicate a monotropic relationship between ALA I and ALA II.



**Figure 4.14** Log scale solubilities of ALA I (red square), ALA II (blue circle) and NIC (black triangle) in ipa : water 9:10 v/v. Concentration of ALA and NIC used to crystallise ALA II are indicated by the orange circle and triangle, respectively.

The metastable form has a higher solubility compared to the stable form of ALA and NIC shows an order of magnitude higher solubility compared to ALA in the same solvent system. By definition hydrotropes are water soluble chemicals and it could be that this greatly enhanced solubility of NIC in the solvent system plays a critical role in the hydrotropic action of NIC. Furthermore, the concentration of NIC used in ALA II formation, is undersaturated with respect to itself and explains why NIC remains in solution at the isolation temperature.

Similarly, the co-former used to obtain the metastable form of paracetamol and mefenamic acid through the templating approach is also selected on the condition that it has a higher solubility than the API and is undersaturated at the isolation temperature meaning the co-former does not precipitate<sup>148, 210</sup>.

Enhanced solubility observed for most metastable polymorphs can be explained by the difference in the Gibbs energy where stable forms have lower free energies. However, in the case of metastable forms, more solid will dissolve as a result of higher free energy<sup>211</sup> (Equation 4.1).

$$\Delta G_{II-I} = \Delta H_{I-II} - T\Delta S_{I-II} \quad \text{Equation 4.1}$$

where:  $G$  is free energy,  $H$  is enthalpy,  $T$  is temperature and  $S$  is entropy.

Dissolution, the preceding step to solubility, is a thermodynamically favourable process. In cases where  $\Delta G_{II-I}$  is above zero, dissolution and solubility of polymorph II will be higher as its energetically unfavourable and the system will try to minimise free energy. Solubility studies between polymorphs have found the ratio of polymorph solubility to be less than two<sup>51</sup> indicating that the solubility difference observed here is plausible. The lower solubility of ALA I suggests lower free energy and an increased stability of this form compared to ALA II, is in line with the findings for the solubilities of each form and solution mediated transformation studies.

#### 4.3.3 Concentration of NIC Effect on Polymorphic Form of ALA

The effect of NIC on the outcome of polymorphic form was assessed by carrying out crystallisation experiments under identical conditions. The crystallised material was analysed by XRPD and is reported in Table 4.4 and as a schematic in Figure 4.15. These results would indicate that the quantity of NIC has an important effect on the solid form crystallised as the concentration of NIC is increased, the polymorphic outcome transitions from ALA I (stable) to ALA II (metastable) and lastly to the ALA-NIC co-crystal.

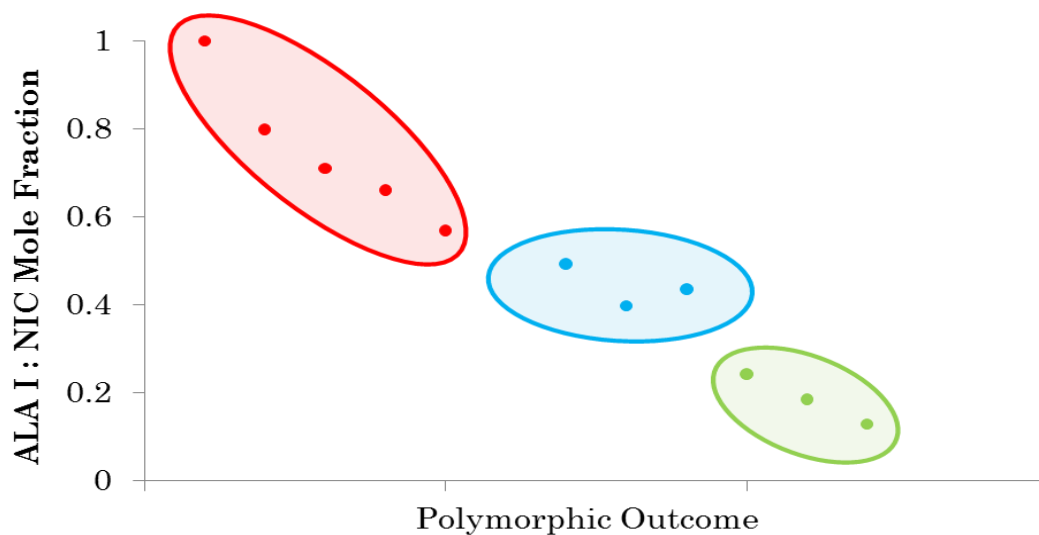
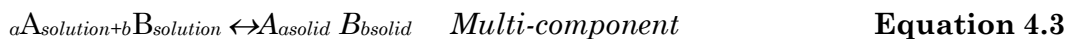
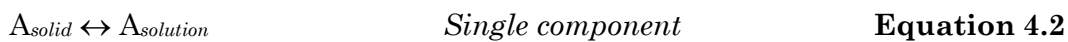
From the ratios investigated, between 0 – 0.57 mole fraction of ALA : NIC - ALA I was obtained. Whilst from 0.40 – 0.49 mole fraction ALA II and between the range of 0.13 – 0.24 ALA-NIC co-crystal resulted.

**Table 4.4** ALA-NIC experiments crystallised under identical conditions.

Mole fraction of ALA : NIC	ALA Form
1	I
0.799	I
0.710	I
0.661	I
0.569	I
0.493	II
0.399	II
0.436	II
0.243	Co-crystal
0.185	Co-crystal
0.129	Co-crystal

A similar concentration dependent effect has been reported for flufenamic acid and mefenamic acid<sup>210</sup> and acridine<sup>212</sup>. At a certain concentration, flufenamic acid allowed the crystallisation of the metastable form of mefenamic acid. This was attributed to the concentration of flufenamic acid in the solution being below the solubility limit at the isolation temperature. However, at higher concentrations, the system would be supersaturated with respect to flufenamic acid resulting in the flufenamic acid mefenamic acid co-crystal or physical mixtures of both ingredients. Similarly, for acridine crystallisation with 50 mol % of the secondary component impeded the co-crystallisation, resulting in the formation of two new metastable polymorphs. Likewise, as NIC concentration is increased, the ALA-NIC co-crystal is obtained. This could be due to the supersaturation of NIC attained at the higher concentrations, allowing NIC to be incorporated into the crystal lattice with ALA.

Solid forms outcomes resulting in a single component is represented by Equation 4.2<sup>213</sup> and for each component of a co-crystal of API (A) and co-former (B), to give co-crystal  $A_aB_b$ , is represented by Equation 4.3<sup>214</sup>:



**Figure 4.15** Polymorphic form of ALA when crystallised under identical experimental conditions with increasing NIC concentrations. ALA I (red), ALA II (blue) and ALA-NIC co-crystal (green).

**Table 4.5** Range of molar concentration used during small scale crystallisation trials with corresponding solid forms recovered and equilibria. (Average ALA concentration was 0.250 M for all experiments with a standard deviation of 0.004).

Molar Concentration of NIC (M)	Polymorphic Outcome of ALA	Solid-solution Equilibrium Equations
0-0.189	I	$ALA_{\text{solution}} + NIC_{\text{solution}} \leftrightarrow ALA(I)_{\text{solid}} + NIC_{\text{solution}}$
0.26-0.377	II	$ALA_{\text{solution}} + NIC_{\text{solution}} \leftrightarrow ALA(II)_{\text{solid}} + NIC_{\text{solution}}$
0.7-1.530	ALA-NIC Co-crystal	$ALA_{\text{solution}} + NIC_{\text{solution}} \leftrightarrow ALA-NIC_{\text{solid}}$

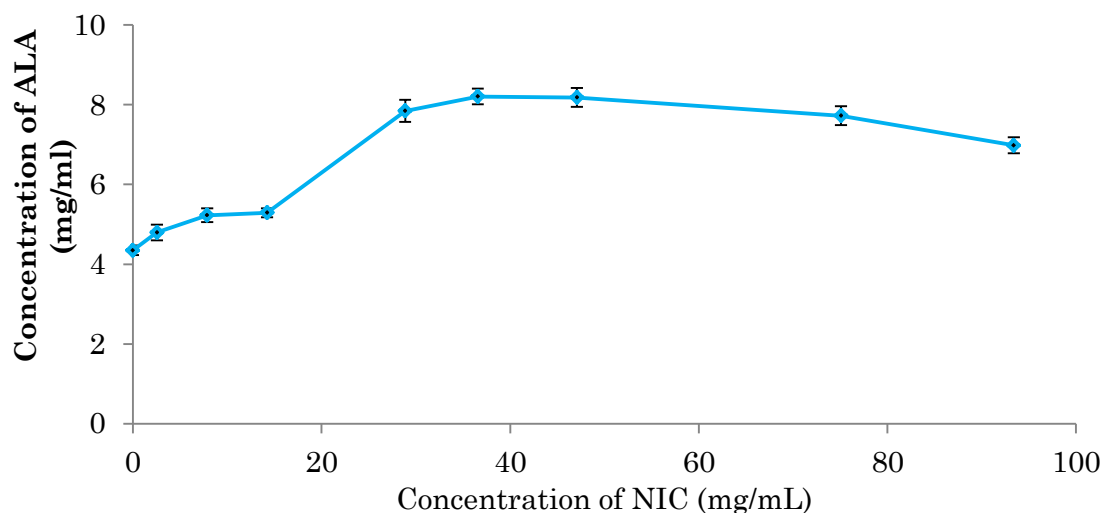
The possible effects of NIC on the resultant polymorphic form of ALA at the concentrations which resulted in ALA I or ALA II have been separately discussed below in *Section 4.3.7*.

#### 4.3.4 Determination of Hydrotropic Effect of Nicotinamide on ALA

Solubilisation of ALA through hydrotropic action of NIC was determined using a stirred tank reactor allowing measurements to be carried out at constant temperature using an in-situ ATR -UV probe. 10 °C was selected as the temperature to determine the hydrotropic effect of NIC on ALA I as the solubility was measurable using the ATR-UV probe and polymerisation of ALA was not observed.

NIC demonstrates solubilisation of ALA I as the measured concentration increases as a function of increasing NIC (Figure 4.16). On increasing the hydrotrope concentration, firstly the drug solubility increased gradually but at 5.29 mg/mL, a significant increase in the solubility of ALA I was observed. A noteworthy feature in Figure 4.16 is the presence of the flat line between NIC

concentrations 7.88 and 14.23 mg/mL. This has been observed for DENA, a structurally similar molecule to NIC with hydrotropic properties<sup>189</sup>. This was noted for all the solutes which were solubilised in the presence of DENA (suggesting it to be a feature of the hydrotrope as opposed to the solute) and was attributed to the self-aggregation behaviour of DENA.



**Figure 4.16** Concentration of ALA as a function of NIC concentration (error bars represent standard deviation).

The similar findings here allows the suggestion to be made that, the flat kink observed prior to a significant increase in solubility, is indicative of the self-aggregation of NIC previously reported<sup>174, 186</sup>. Between starting and the maximum concentration of NIC an increase of 88.7% in ALA concentration was calculated. The change in concentration was not linear, showing a sigmoidal response which has been attributed to intermolecular interactions involved in the solubilisation process<sup>185</sup>. Also, once the maximum concentration of ALA I within this system was reached ( $C_{max}$  at NIC concentration of 36.6 mg/mL), there was a reduction in the concentration of ALA irrespective of NIC addition. Within the concentrations of NIC studied, a decrease in solubility was detected when NIC reached 0.39 M (47.075 mg/mL). Increase in concentration of NIC results in NIC-NIC self-association<sup>174, 186, 193</sup> and although this self-aggregation has been considered a contributing factor to solubilisation, recently it has been demonstrated that strong NIC-NIC self-association in fact reduces hydrotrope solubilisation efficiency by up to 40%<sup>169, 173, 187</sup> leading to a reduction in












solubilisation efficiency. Furthermore, between the observed maximum solubility and the last solubility value recorded, a 15% reduction in the solubility of ALA was detected.

#### 4.3.5 Stability of ALA II in Solution

For polymorphic compounds, solution mediated transformation is an important process whereby a metastable phase converts into a more stable crystalline form. Solvent-mediated polymorphic transformation (SMPT) is induced by the difference in solubility of the metastable and stable polymorphs. Hence, the metastable form will dissolve and nucleation and growth of the stable polymorph will take place reducing the free energy of the system. A number of conditions can influence overall rate of the transformation process including; stirrer speed and type, seed size, surface interactions between polymorphs, solvent and temperature<sup>215-217</sup> and solid loading<sup>218</sup>. Within this investigation, the effect of temperature on the rate of transformation was investigated whilst keeping stirrer speed, solvent composition (ipa : water 9:10 v/v) and stirrer type constant. However, in all cases, excess ALA II was added based on the solubility data (*Section 4.3.2*) thus solid loading was not kept constant.

Ex-situ analysis via XRPD of solution mediated transformation of ALA II can be seen in Table 4.6. It is observed that the transformation of ALA II, which is in contact with aqueous solution at temperatures at 0 °C, 10 °C and 20 °C, is complete within 6 hours and at -10 °C and -15 °C ALA II had not fully transformed to ALA I within 33 hours.

**Table 4.6** Ex-situ transformation of ALA II (Blue) to ALA I (Red) at a variety of temperatures. The mixture of ALA I and ALA II are represented by the purple box.

Temperature °C	20 °C	10 °C	0 °C	-10 °C	-15 °C
Sampling Time (hours)					
6					
21	-	-	-		
33	-	-	-		

The effect of temperature on the transformation rate of piracetam (form II – metastable to form III - stable) has been investigated over the temperature range of 5–50 °C<sup>218</sup>. The appearance of the stable form of piracetam decreases from 43 h at 5 °C to 2.5 h at 50 °C, while the metastable to stable transformation time decreased from 93 h at 5 °C to 6.75 h at 50 °C, concluding that the rate of transformation increased with temperature. In this system, the time for appearance of ALA I is inversely related to temperature, in keeping with the literature example of piracetam, detailed above. This could be attributed to the increased solubility of ALA II at higher temperatures, increasing the relative supersaturation with respect to ALA I resulting in an increase in the overall rate of transformation<sup>218, 219</sup>. Based on these results, when ALA II is produced, it is expected to be stable for long enough without rapid transformation to ALA I.

#### 4.3.6 Dynamic Light Scattering

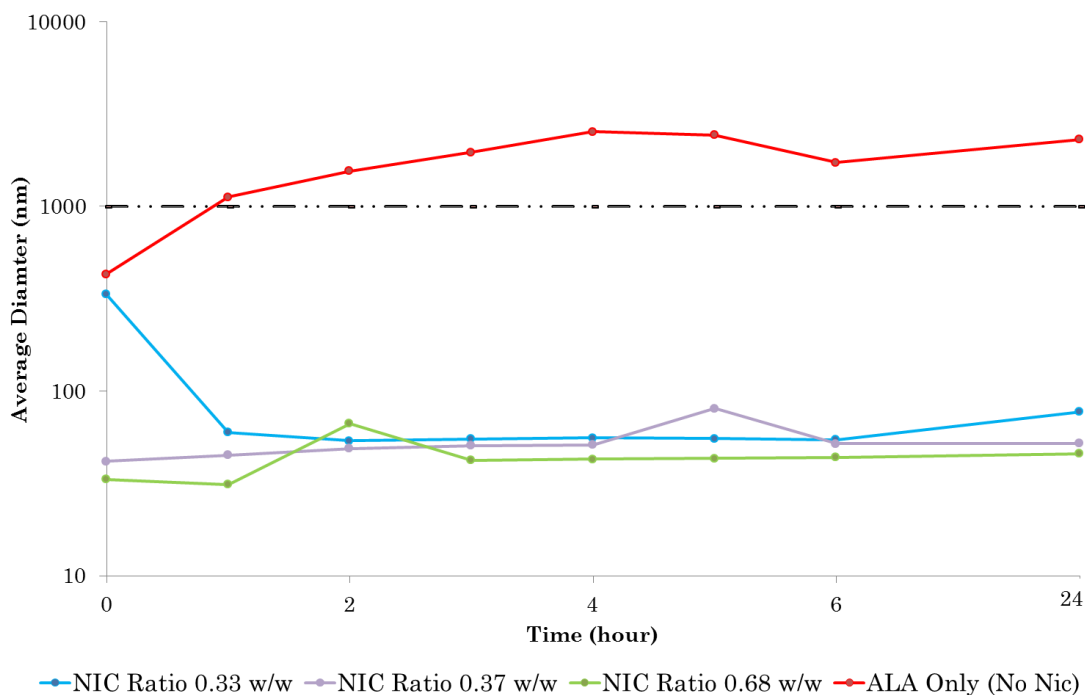
By keeping the concentration of ALA constant, the effect of NIC concentration on the intermolecular interactions in solution was investigated as it was hypothesised that NIC concentration may be leading to other solid forms of ALA (Table 4.7).

**Table 4.7** Experimental conditions used to assess the effect of NIC on solution characteristics in ipa : water 9:10 v/v

ALA (g)	NIC (mass %)	Expected ALA Form
0.268	0	ALA I
0.268	0.33	ALA I
0.268	0.37	ALA II
0.268	0.68	ALA-NIC Co-crystal

It was observed that, solutions which contained 0.33, 0.37 and 0.68 w/w of NIC reached a final average size of 77.33 nm, 52.14 nm and 45.76 nm, respectively. Samples which only had ALA I (i.e. no NIC), reached an average final size of 2303 nm. These results would suggest that the average size reached after 24 hours for the solutions containing varying concentrations of NIC, were very

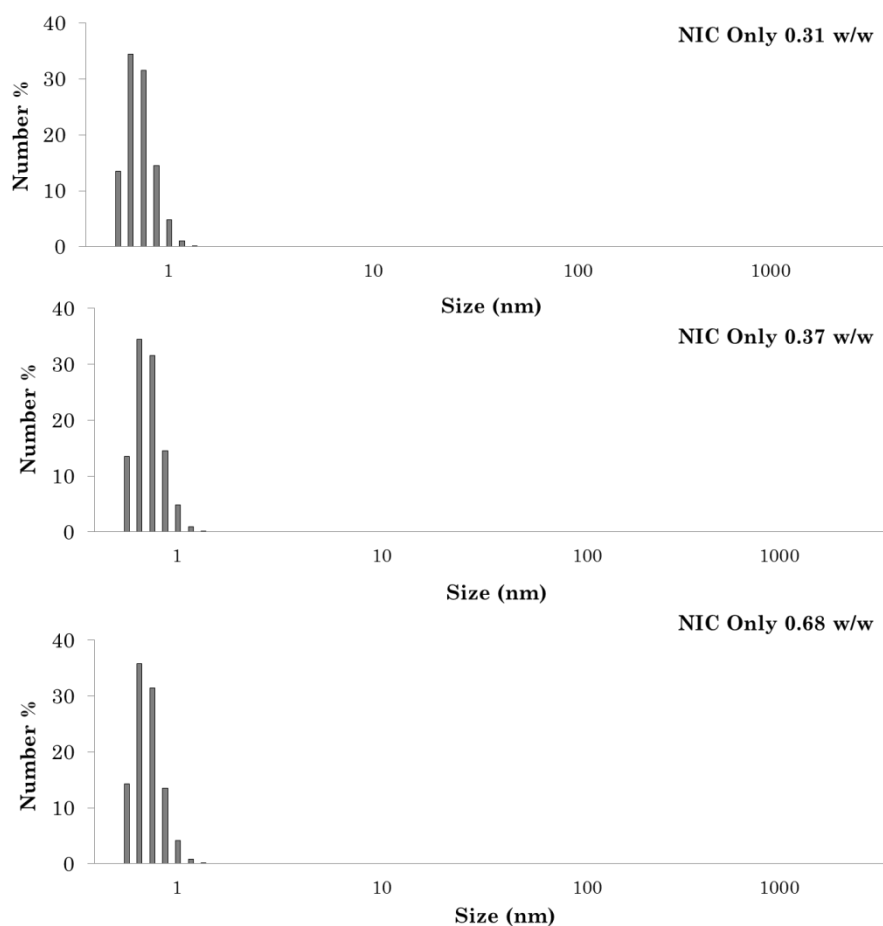
similar. The biggest difference observed was for the vial which did not contain NIC, where the final size of particles was above 2000 nm (Figure 4.17).



**Figure 4.17** Average particle size recorded (logarithmic scale) for samples with identical ALA concentration with varying NIC concentration (n=3), black dashed line indicates upper limit for definition of mesoscale. No measurements were taken between t = 6 and t = 24 the line between those times are to guide the eye only.

These results are in keeping with the findings by Robertson *et al*<sup>220</sup> who investigated mesoscale droplets for solutions of 2,6-lutidine (hydrotrope) in water with the addition of cyclohexane (poorly soluble compound). The size of the mesoscale droplets for 15%, 30%, 45% and 60% of lutidine, with addition of constant mass of cyclohexane resulted in mesoscopic droplets without any significant differences in the size of the droplets. However, the general trend noted were that, the size of the mesoscopic droplets increased with decreasing hydrotrope concentration within solution. Under the conditions examined, the presence of NIC greatly influenced the final size (final size in the ALA only solution 2303 nm and 45.67 nm in 0.68 w/w of NIC). Further to this under the experimental conditions examined, the size of the droplets decreases with increasing hydrotrope concentration which is in keeping with the results obtained for the 2,6-lutidine/water/cyclohexane system<sup>220</sup>. Although the final

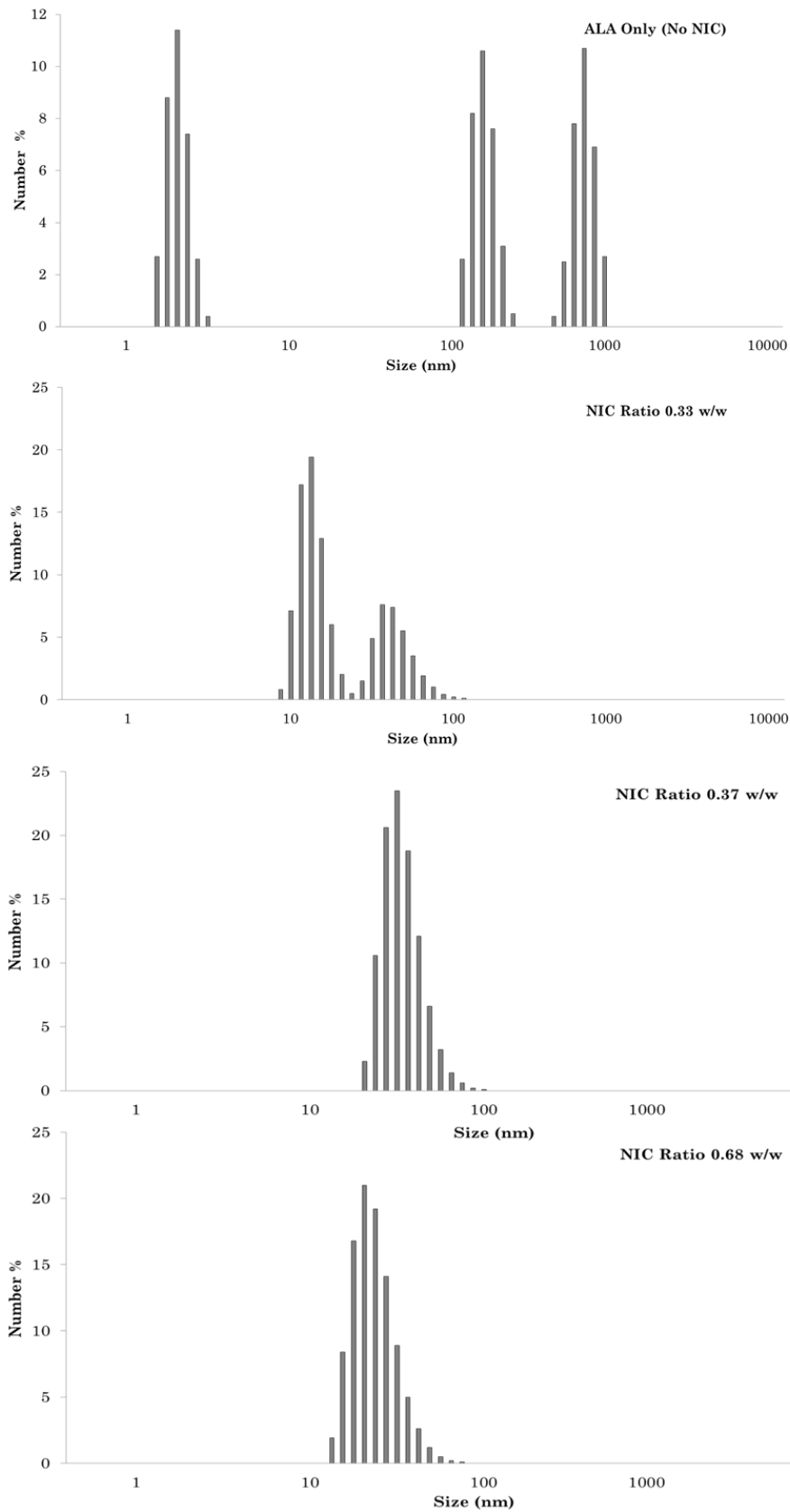
average droplet diameter was not significantly affected in the NIC containing solution, the occurrence of each size group was investigated for solutions containing only NIC (Figure 4.18) and for solutions with increasing concentrations of NIC at a constant mass of ALA (Figure 4.19).



**Figure 4.18** Average number distribution of the frequency of each size,  $t = 24$ ,  $n = 3$ .

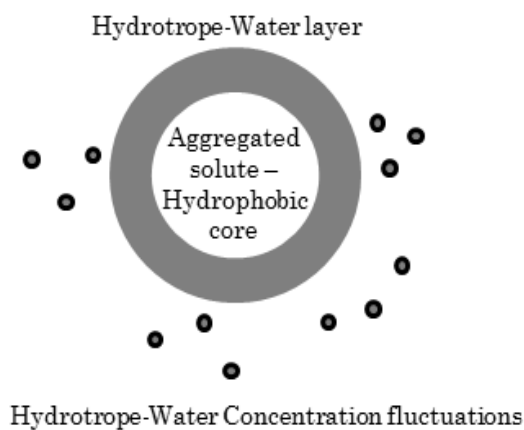
Aqueous solutions of NIC did not show any mesoscale cluster formations at any of the concentrations investigated at  $t = 24$  hours (Figure 4.18). Observations made here may be molecular clusters which are sizes in the order of 1 nm as observed by Subramanian *et al*<sup>221</sup> in hydrotrope only aqueous solutions. Upon the addition of ALA, mesoscale differences emerge and the presence of larger than previously noted particles can be seen (Figure 4.19). Formation of mesoscopic droplets only by the addition of ALA are consistent with findings by Subramanian *et al*<sup>221</sup> where only on the addition of cyclohexane to the hydrotrope-solvent system did larger particles form. This was attributed to the

stabilisation and rearrangement of the solvent–hydrotrope structures by the poorly soluble solute leading to the formation of larger droplets. In the complete absence of NIC, the solution resulted in three different size classes of particles (Figure 4.19). The concentration of ALA I was the same for all other vials studied, hence the difference was attributed to the influence of NIC and the role it plays within the solution. The solubility measurements for ALA I (*Section 4.3.2*) indicate that at the given composition and temperature, the solution is expected to be undersaturated. Therefore, it is not expected to be due to the precipitation of ALA I and no evidence for this was observed at crystallisation temperatures which may indicate this to be temperature dependant effect. Similar observations have been made and reported as; oiling out<sup>222</sup>, micro/emulsification<sup>223</sup> or the ouzo effect<sup>220</sup>. Further investigations may be helpful in allowing more definite conclusions to be made as to the composition of the solution. Solutions with 0.33 mass % of NIC produced a bimodal distribution of particles which at 0.37 mass % transition to unimodal distribution. These could be mesoscopic droplets which have been observed to range from 50nm to orders of 100 nm in diameter<sup>224</sup>. These results may serve as evidence for “mesoscale solubilisation” which has been defined as the formation of mesoscopic droplets which results in increased solubility of hydrophobic compounds in aqueous solutions as a result of non-ionic hydrotropes<sup>221</sup>. Investigations of ternary (hydrotrope-solvent-solute) solution properties revealed mesoscopic droplets formed only in the region where thermodynamic anomalies had been observed in hydrotrope-solvent composition (e.g. heat capacity, excess molar volumes, activity coefficient and excess partial molar entropies)<sup>221</sup>. Such thermodynamic changes can alter the interactions between the solvent and solute, changing the local molecular environment, influencing the crystallisation outcomes. In the presence of NIC, crystallisation occurs in the presence of mesoscopic clusters and, hence, nucleation occurs in a different molecular environment leading to a different solid form (ALA II). Similarly, during the crystallisation of acridine, 50 mol % of terephthalic acid or cis,transmuconic acid lead to the formation to metastable forms of acridine<sup>212</sup>. It was thought to result in the formation of distinct aggregates in solution prior to crystallisation and, thus, in the induction of polymorphism.



**Figure 4.19** Average number distribution of the frequency % of each size,  $t = 24$ ,  $n = 3$ .

A move to the left and a decrease in the occurrence of larger clusters are observed for NIC ratio 0.68 % w/w (Figure 4.19). Radial distribution function studies and molecular dynamic simulations of tertiary butyl alcohol (TBA) – water–cyclohexane solutions with increasing concentrations of TBA have been reported<sup>221</sup>. Both techniques showed that as the hydrotrope concentration increased, the tendency to form TBA–water–cyclohexane droplets disappeared. At the highest concentrations of hydrotrope examined, the hydrotrope and solute preferred to mix with each other and no cluster formation was detected. At concentrations above 0.68 mass % of NIC, it could be proposed that ALA-NIC do not interact to form clusters in the same manner to result in the formation of mesoscopic droplets. The clusters reported in Figure 4.19 may, therefore, be a mixture of self-aggregated clusters of NIC (NIC has been reported to undergo self-aggregation<sup>173</sup>) and the basic interaction of ALA-NIC without higher ordered interactions that would lead to clusters and mesoscopic solubilisation. The structure of the mesoscopic droplets have been investigated with molecular dynamic simulations for TBA (hydrotrope), water (solvent) and cyclohexane (hydrophobe) ternary system (Figure 4.20)<sup>221</sup>. This study has shown aggregated hydrophobic solute molecules which are surrounded by the hydrotrope.



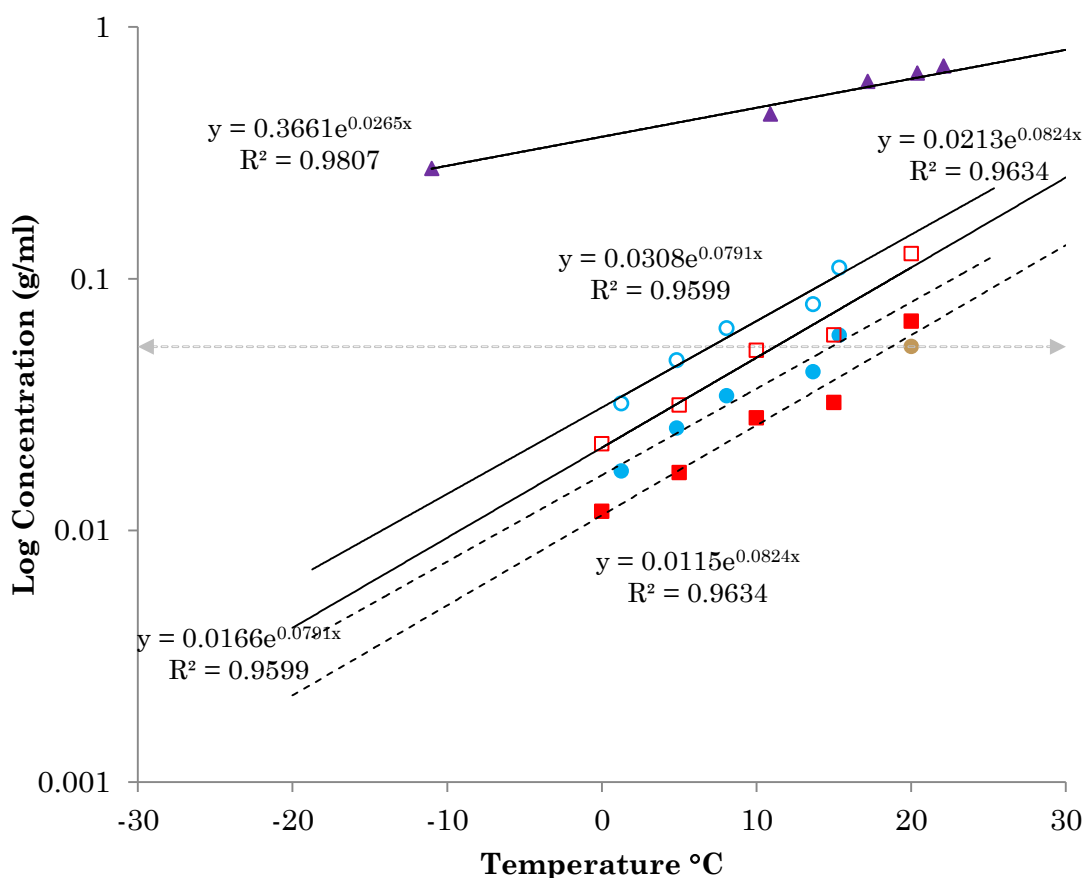
**Figure 4.20** Schematic of the mesoscopic droplets which form in solutions containing hydrotropes and a poorly water soluble solute (image adapted from reference 221).

The concentration of the hydrotrope is proposed to be denser in the layer surrounding the aggregated poorly soluble solute as opposed to the bulk

solution. Higher order interactions between the hydrotrope and water molecules that surround the solute aggregate, is proposed to lead to cluster formation.

#### 4.3.7 Nucleation of ALA II

The experimental concentration of NIC used to achieve ALA II was 32.6 mg/mL (Section 4.2.1). The average of the concentrations measured at 28.88 mg/mL and 36.58 mg/mL was taken to estimate the increase in solubility at 32.6 mg/mL (Figure 4.16). The calculated percentage increase in solubility was then applied to the experimentally obtained solubility data of ALA I and ALA II. These are referred to as estimated solubility of ALA with NIC and ALA II with NIC (Figure 4.21).

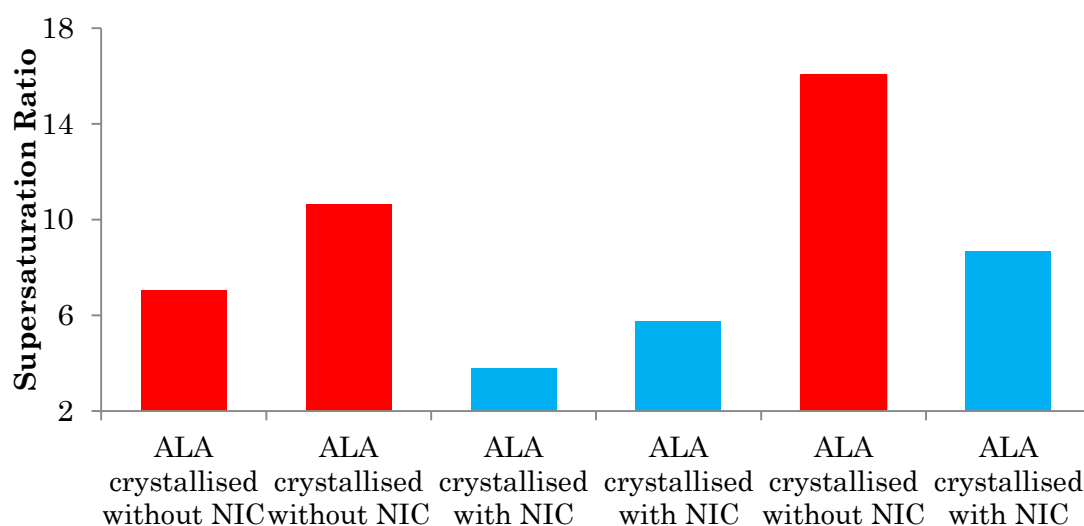


**Figure 4.21** Log scale solubilities of ALA I (red square), ALA II (blue circle) and NIC (black triangle) in ipa : water 9:10 v/v. Solid lines represent predicted solubility based on the expected increase in solubility of ALA I at experimental NIC (ALA I: red empty squares and ALA II: blue empty circles), experimental ALA concentration (orange circle).



To investigate the effect of supersaturation and to differentiate this from the role NIC may be playing in leading to ALA II, ALA was crystallised in the presence and absence of NIC at three different supersaturation ratios using the isothermal method described in detail elsewhere<sup>225</sup>. At constant mass of ALA and NIC, crash cooling crystallisation experiments were performed using the concentrations of ALA and NIC as described in *Section 4.2.1*.

The supersaturation ratios achieved were calculated using the equations fitted to the experimentally obtained solubility for ALA without NIC and the estimated ALA solubility with NIC. The polymorphic form of ALA obtained from the experiments over the range of supersaturation ratio 16.0 to 3.8 is shown in Figure 4.22. Under the experimental conditions examined, regardless of the supersaturation ratios, ALA II could not be isolated unless ALA was crystallised in the presence of NIC. On comparison of the supersaturation ratios attained, ALA II was generally isolated at lower supersaturations.



**Figure 4.22** Resultant solid state of ALA when crystallised with and without ALA. (Red: ALA I and Blue: ALA II).

An exception may be at supersaturation ratios 7.04 and 8.66 where ALA I and ALA II were obtained, respectively. However, if the formation of ALA I at supersaturation ratio 7.04 was due to insufficient driving force for the nucleation of ALA II, increasing the supersaturation (10.62 or 16.04) would be expected to result in ALA II. However, regardless of the supersaturation, ALA II

was not obtained in the absence of NIC. These results confirm that NIC is required to produce ALA II.

During these experiments it was also observed that nucleation of solutions without NIC occurred more rapidly (typically less than 1 minute) than with solutions containing NIC (5-6 minutes). As supersaturation increases, nucleation rate increases ( $J$ )<sup>25</sup> (i.e. induction time decreases,  $t_{ind}$ ). This may result from the fact that NIC increases the solubility of ALA and consequently decreases supersaturation relative to ALA I and II leading to longer induction times (Equation 4.4).

$$J = 1/t_{ind} \qquad \text{Equation 4.4}$$

With the demonstrated increase in solubility of ALA in the presence of NIC, nucleation of the metastable form is estimated to be occurring at lower supersaturations than would be the case for crystallisations from pure ALA solution. Hence, despite there being a greater driving force for the nucleation of ALA I, ALA II preferentially nucleates (Equation 4.5).

$$B = k_b \Delta S s^b \qquad \text{Equation 4.5}$$

where:  $B$  is nucleation rate,  $k_b$  is the nucleation constant,  $Ss$  is supersaturation and  $b$  is nucleation order.

The effect of supersaturation on the polymorphic content of phenylbutazone has been studied<sup>25</sup>. Similarly, as supersaturation increased, the fraction of the stable polymorph increased. It was concluded that, at low supersaturations, the relative nucleation rate of the metastable form was considerably greater (attributed to the lower interfacial tension of the metastable form which is expected to reduce the supersaturation required for nucleation<sup>226</sup>) than the relative crystal growth rates; hence, the nature of the polymorph that crystallised was determined by the relative nucleation rates. However, at higher

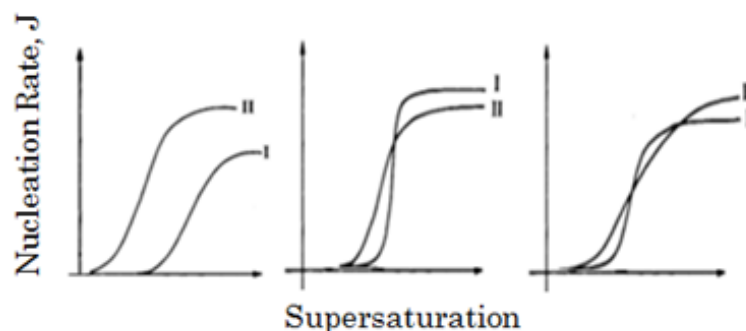
supersaturations, whilst nucleation rates of both forms were considered to be equal and the effect of supersaturation on the nucleation rate becomes more dominant compared to the interfacial tension, growth rates of the stable form were significantly higher, resulting in the formation of the stable form. Therefore, the competition between the rates of nucleation and growth rates of the two polymorphs dictates the polymorph outcome. Similar findings for L-glutamic acid have been reported where the competition of nucleation kinetics between the  $\alpha$  form (metastable) and the  $\beta$  (stable) form was shown to be a major factor in determining the polymorphic form<sup>227</sup>.

Interfacial tension,  $\gamma$ , is inversely proportional to the logarithm of solubility<sup>228</sup>, meaning as solubility increases,  $\gamma$  decreases. NIC was found to increase the solubility of ALA (*Section 4.3.4*) coupled with evidence of mesoscale solubilisation (*Section 4.3.6*). Due to the enhanced solubility of ALA in the presence of NIC, the number of solute molecules per unit volume and the frequency of molecular transport would be greater, leading to a smaller  $\gamma$ <sup>228</sup>. A reduction in  $\gamma$  would result in a smaller critical nucleus size (Equation 4.6). The data obtained from DLS experiments (*Section 4.3.6*) may serve as evidence; since solutions with NIC lead to mesoscopic clusters in solution ( $\approx 40$  nm). Thus, solubility affects the probability of intermolecular collisions and reduces  $\gamma$ , leading to larger  $J$ , resulting in a higher nucleation rate for ALA II at lower supersaturations where  $\gamma$  is more influential.

$$\Delta G_{crit} = \frac{4}{3} \pi \gamma r_c^2 \quad \text{Equation 4.6}$$

Nucleation rates of polymorphs as a function of supersaturation have been explored by Cardew and Davey<sup>229</sup> (Figure 4.23). This study concluded that the phase which has a higher nucleation rate can vary with supersaturation and depends on the surface (e.g. interfacial tension) and bulk parameters (e.g. solution composition and temperature). For the nucleation of ALA II, the fundamental role of NIC has been demonstrated. Such examples have been reported where the metastable form of tolbutamide, exclusively crystallised in

the presence of 2,6-di-*O*-methyl- $\beta$ -cyclodextrin and the stable form crystallised in the absence of the cyclodextrin<sup>230</sup>.

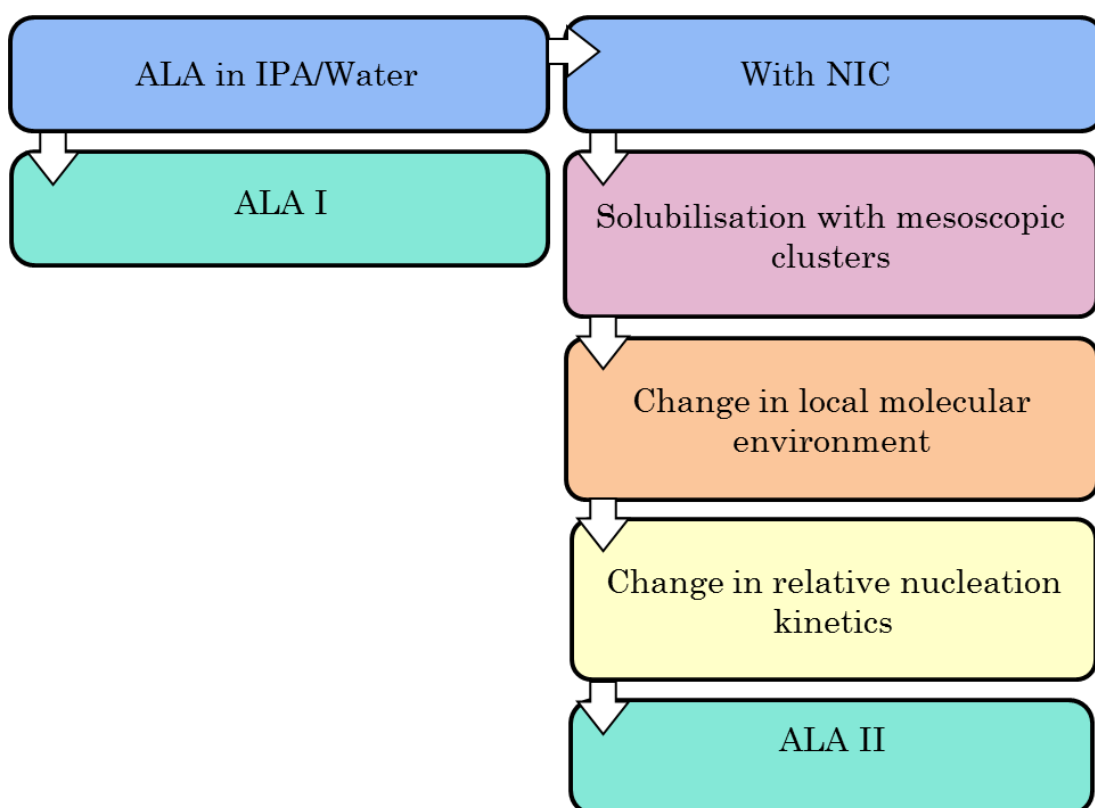


**Figure 4.23** Alternative nucleation kinetics of a polymorphic system, I (stable) and II (metastable) (image from reference 229).

Further examples include; the crystallisation of maleic acid which yielded a metastable form only in the presence of caffeine<sup>231</sup> and the cocrystallisation trials between isonicotinamide and felodipine where isonicotinamide failed to enter the lattice of felodipine, leading instead to the nucleation of the metastable form of felodipine<sup>232</sup>. In such cases, the presence of a secondary component was thought to have played a structure directing role in the formation of a metastable form. In particular, the amide group of isonicotinamide was thought to have played a structure directing role in the formation of the metastable form of felodipine. Likewise, crystallisation studies between flufenamic acid and mefenamic acid lead to the metastable form of mefenamic acid when crystallised in the presence of flufenamic acid<sup>210</sup>. The interaction between the two components, possibly by hydrogen bonding between carboxyl groups was thought to interfere with the growth of mefenamic acid, resulting in the delay of formation of the stable form and, thus, allowing competitive formation of the metastable form. Other examples where additives influence on the nucleation kinetics of polymorphs have been reported for ortho amino benzoic acid<sup>233</sup> and acridine<sup>212</sup>.

Solution phase additives have frequently been shown to have a substantial effect on the outcomes of a crystallisation process (e.g. polymorphic form). Amphiphilic molecules, such as NIC, can position themselves at the solute/solvent interface and can affect nucleation kinetics depending on their specific structure and

interactions with the solute<sup>234</sup>, influencing the packing of the emerging structure, which may promote the growth of one form over another. This is thought to occur during the nucleation phase, where solutes are associating in solution to create building units, the molecular interactions between associated solute and template create specific pre-arrangements, templating the nucleation of a specific polymorph<sup>212, 235</sup>. Here, however the results support a specific effect of NIC on the crystallisation of ALA polymorphs. The hydrotropic effect of NIC is leading to the formation of mesoscopic clusters, creating a distinct molecular environment in which nucleation of ALA occurs. This is impacting in the relative nucleation kinetics of the two polymorphs and favouring the formation of the metastable form II (Figure 4.24).



**Figure 4.24** Schematic of the effect NIC is proposed to be having in solution leading to ALA II

#### 4.3.8 Solid state Stability

ALA II was found to be stable for 12 months and for around 1 month when stored at -17 °C and at room temperature (~22 °C), respectively.

#### **4.4 Summary**

The crystallisation and crystal structure of a novel metastable polymorph of ALA, ALA II, is reported. The polymorph is obtained selectively and consistently in the presence of NIC, which has a hydrotropic effect on ALA solubility. The results presented show evidence for NIC interaction with ALA impacting on the relative nucleation kinetics for ALA that favours the formation of form II. In contrast, under all conditions tested in the absence of NIC, ALA I was always produced.

Crystallisation of metastable forms can lead to improved dissolution and solubility profiles. Hydrotropy is shown to be an alternative method of controlling solid form of ALA from a novel polymorph through to creating a cocrystal at higher NIC concentrations. This is a significant result in showing for the first time that the hydrotrope effect can have a potential role in the discovery and control of polymorphism and can be used to design strategies for selectively obtaining metastable polymorphs. Further work required to establish the specific mechanism of selecting polymorphic prediction and the transferability/general applicability to other materials and solution systems.

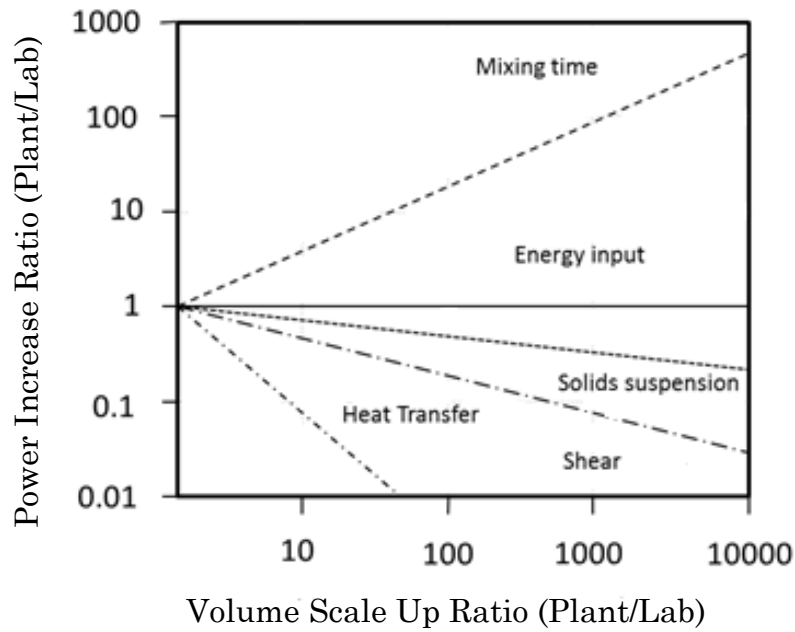
# **Chapter 5** Scale-Up of Crystallising Alpha Lipoic Acid Form II

## 5.1 Introduction

The behaviour and success of a crystallisation process is generally affected when moving from small scale to a larger scale operation. From a fluid mechanics point of view, good mixing can be easily achieved at small scale, however, inhomogeneities in mixing can readily occur at larger scale. Poor mixing leads to regions of high local supersaturation which can, in turn, drive undesirable nucleation and agglomeration. Differences in local stirrer intensity can also lead to changes in particle breakage and secondary nucleation processes<sup>48</sup>. Growth rate is also dependent on supersaturation as well as the presence and identity of any impurities, the mixing regime, particle breakage and agglomeration<sup>7</sup>. Particular difficulties affecting scale up are stirrer speed (which affects shear rate and particle breakage) and power per unit volume (which affects mixing time, particle suspension, and frequency of exposure to the high shear zones)<sup>48</sup>. The hydrodynamics present within a crystalliser at a given rpm will show variation from one position within the crystalliser to another. This can result in concentration gradients, suspension and heat transfer difficulties. Often, more homogenous mixing is achieved close to the impeller with poorer mixing in other parts of the crystalliser. This is an issue to address as crystals respond to their immediate environment<sup>236</sup>.

The difficulty around scale up of processes remains challenging as not all the parameters which vary with the dimensions of the vessel, scale in the same way (Figure 5.1). Mixing time is directly proportional to an increase in process volume to a point whereby this becomes unrealistic. Heat transfer is significantly affected, where a volume increase of 50 would need 100 times more power. The potential consequence of this in cooling crystallisation is clear given that heat transfer is the method of supersaturation generation. Consequently, the reduction in available heat transfer area combined with reduced mixing efficiency in larger scale crystallisers makes scale up process in STR scale challenging.





**Figure 5.1** Relationship between some of the parameters used for scale up (Image adapted from reference 237).

In order to address these issues, a number of approaches have been used when scaling up a process in a STR including power input<sup>238</sup>, volume average shear rate<sup>239</sup> and Computational Fluid Dynamics (CFD)<sup>240</sup>. Due to the complicated nature of scale up within a STR the most appropriate approach is often case specific<sup>10</sup>.

The numerical simulations of scaling-up are based on the inner geometry of the crystalliser, the type of mixer, presence of probes, fluid volume and properties. There are three essential principles which govern fluid flow: (1) mass is conserved; (2) Newton's second law of motion and (3) energy is conserved. These three fundamentals can be expressed and solved with the help of CFD using the Navier-Stokes equation (Equation 5.1).

$$\rho \frac{\partial u}{\partial t} + \rho(u \cdot \nabla)u = \nabla \cdot [-pI + \mu(\nabla u + (\nabla u)^T)] \quad \text{Equation 5.1}$$

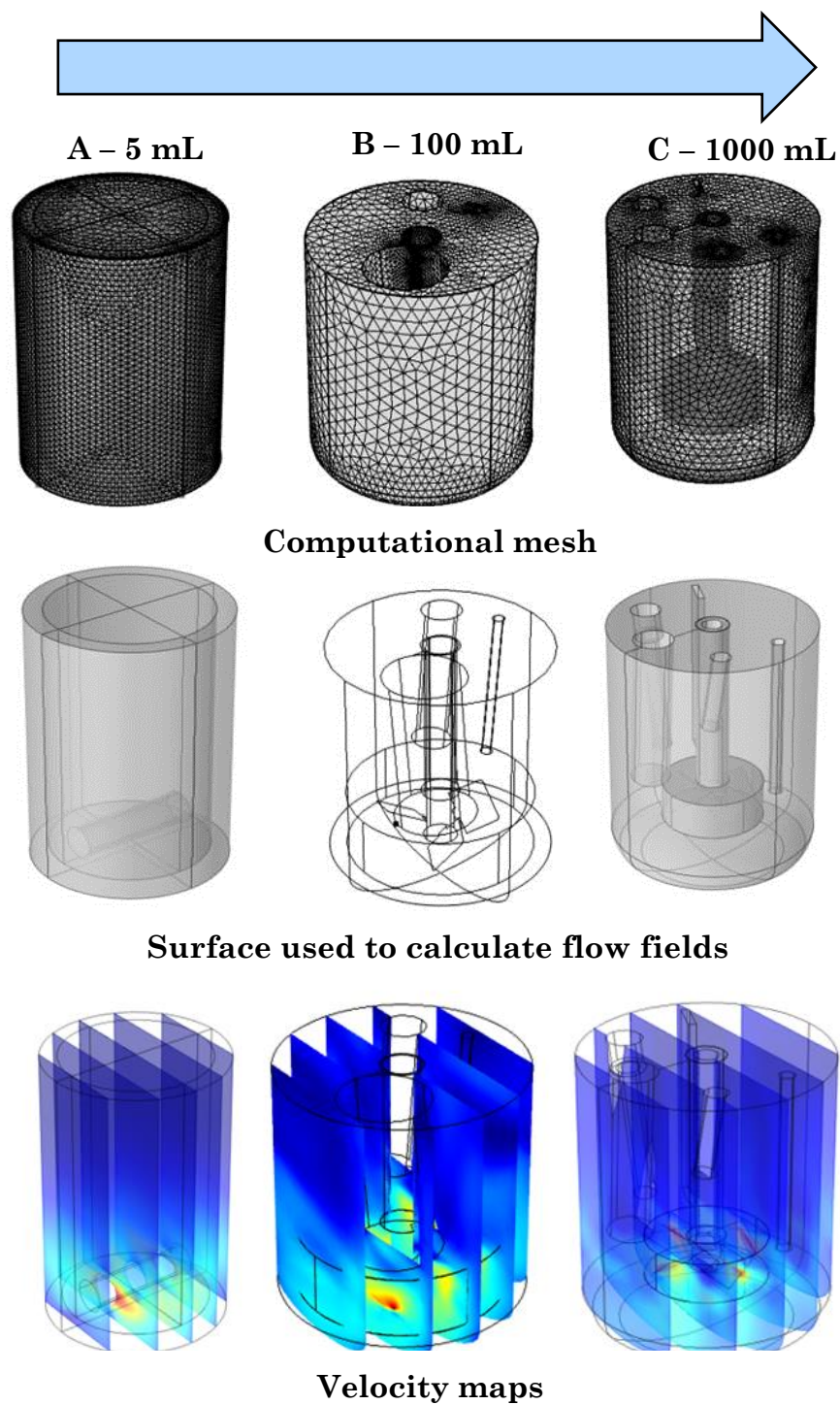
Here  $\mu$  is the dynamic viscosity kg/(m.s),  $u$  is the velocity (m/s),  $\rho$  is the fluid density (kg/m<sup>3</sup>), and  $p$  is the pressure (Pa).

Three different outcomes are produced from CFD simulations; shear rate, turbulent dissipation energy and turbulent kinetic energy. Turbulent kinetic energy and local energy dissipation rate, are micromixing performance indicators<sup>240</sup> and are important to keep constant when scaling up<sup>237</sup>. Shear rate is defined as the speed at which one layer of fluid passes another layer and this can influence the local conditions to which crystals are exposed to<sup>21</sup>. The three parameters used consider a wide range of fluid parameters as turbulent dissipation rate can be related to power density whilst turbulent kinetic energy is related to Reynolds number. As a result, these outcomes were used to investigate the scale up of the crystallisation of ALA II.

The aim of this chapter is to identify conditions with the help of CFD that would allow the scale up of material from initial discovery stage to 1000 mL in order to produce more material and gain insight into the process and parameters that affect the outcome.

## 5.2 Materials and Method

Predictions of flow fields in all three STRs shown in Figure 5.2 were obtained through simulations carried out with CFD models built in-house using *COMSOL Multiphysics 5.2.1.199*<sup>241</sup>. The scale up study was based on three-dimensional, time-independent simulations. Model information can be seen in Table 5.1. In all cases a tetrahedral mesh with normal coarseness was used. The numerical investigation of scaling up from 5 mL to 1000 mL was based on the inner geometry of the crystalliser, the type of mixer (magnetic stirrer bar for 5 mL and pitch blade turbine for 100 mL and 1000 mL), presence of probes (temperature, FBRM and PVM), fluid volume and physical properties (Figure 5.2). A table of the approach taken to scale up this process with the aid of CFD is shown in Table 5.2.



**Figure 5.2** 3D mesh used for each of the crystallisers investigated at three different scales A: 5 mL, B: 100 mL and C: 1000 mL (images not drawn to scale). Top: Computational mesh defining the geometry and boundary conditions. Middle: Surface used with agitator and PAT. Bottom: Resultant velocity maps from the CFD calculations.

**Table 5.1** The meshing used for the CFD simulations.

<b>Mesh Features</b>	<b>5 mL Crystalliser</b>	<b>100 mL Crystalliser</b>	<b>1000 mL Crystalliser</b>
Maximum element size (mm)	1.07	3.48	6.7
Number of vertex elements	27	105	147
Minimum element size (mm)	0.32	1.04	2
Number of edge elements	663	1895	1761
Maximum element growth rate	1.15	1.15	1.15
Number of boundary elements	9144	26200	13856
Curvature Factor	0.6	0.6	0.6
Number of elements	82013	328221	163516
Resolution of Narrow Regions	0.7	0.7	0.7
Free meshing time (s)	1.61	1.95	2.58
Minimum element quality	0.2427	0.0032	0.2094

**Table 5.2** A workflow approach to scale up with CFD.

Step 1	Step 2	Step 3	Step 4
Build crystalliser model	Screen experimental process conditions	Select CFD approach	Carry out experimental measurement

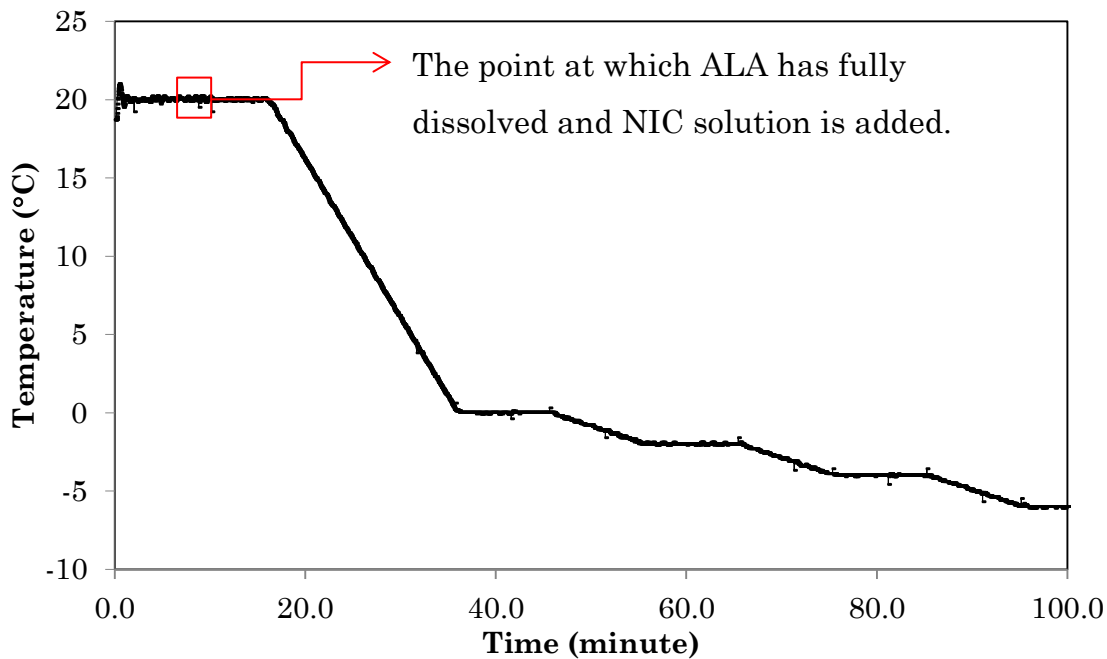
### 5.2.1 Small Scale Controlled Crystallisation Experiments

The first step was to carry out a number of small scale experiments where process conditions could be varied to identify circumstances in which ALA II could be isolated. To build a systematic understanding of the performance of the system under different process conditions as a function of scale, the most significant process parameters were identified. Whilst keeping the concentration of ALA and NIC constant, both cooling profile and stirrer speed were investigated using a benchtop multi-reactor crystalliser.

**Table 5.3** Experimental conditions tested at small scale.

	Vial A	Vial B	Vial C	Vial D	Vial E	Vial F
ALA Wt						
(g)	0.0536	0.0536	0.0536	0.0536	0.0536	0.0536
NIC Wt						
(g)	0.0326	0.0326	0.0326	0.0326	0.0326	0.0326
Cooling Rate	-5	-5	Controlled	Controlled	-0.1	-0.1
	°C/min	°C/min	staggered	staggered	°C/min	°C/min
RPM	800	400	800	400	800	400

For all experiments, NIC solution was added when transmissivity was 100%, indicating all of ALA I was dissolved (Figure 5.3). This allowed the two solutions to be mixed at room temperature before being subjected to a temperature change.



**Figure 5.3** Controlled staggered cooling rate: An initial rapid cooling rate of 1 °C/min was used which was then followed by a slower cooling rate of 0.2 °C/min where the solution was held for ten minutes between temperatures changes.

### 5.2.2 Initial Scale Up (100 mL)

Mixing conditions from the small scale (5 mL – 800 rpm) experiments were simulated using CFD to translate the appropriate mixing conditions to 100 mL (Table 5.4). Using Equation 5.2, 350 rpm was chosen at the 100 mL scale.

**Table 5.4** Mixing conditions calculated from CFD for 5 mL and 100 ml working volume.

Scale	RPM (minute)	Shear Rate (1/s)	Turbulent Dissipation Rate (m <sup>2</sup> /s <sup>3</sup> )	Turbulent Kinetic Energy (m <sup>2</sup> /s <sup>2</sup> )
5 mL	800	32.509	0.059657	0.002248
	50	9.903	0.004213	0.000401
	100	12.505	0.007252	0.000813
	150	15.391	0.011529	0.001232
	200	18.966	0.018163	0.001694
	250	22.926	0.027578	0.002177
	300	27.109	0.040225	0.002687
100 mL	350	31.432	0.056566	0.003240
	400	35.847	0.077008	0.003838
	450	40.326	0.101850	0.004478
	500	44.860	0.131230	0.005151

### 5.2.3 Final Scale Up (1000 mL)

A larger set up, with a total working volume of 1000 mL was then used as a final scale of crystallisation. CFD simulations were based on 100 mL conditions (Table 5.5). Using Equation 5.2, 600 rpm was chosen at the 1000 mL scale.

**Table 5.5** Mixing conditions simulated from small scale to 1000 mL working volume.

Scale	RPM (minute)	Shear Rate (1/s)	Turbulent Dissipation Rate (m <sup>2</sup> /s <sup>3</sup> )	Turbulent Kinetic Energy (m <sup>2</sup> /s <sup>2</sup> )
100 mL	800	32.509	0.05966	0.0022483
	50	2.9226	0.0004375	0.00017976
	155.56	7.653	0.0044813	0.00086002
	261.11	13.291	0.017465	0.0019421
	366.67	19.122	0.043525	0.0034007
	400	20.967	0.055232	0.0039497
	433.33	22.809	0.068863	0.0045418
	466.67	24.647	0.084612	0.0051804
1000 mL	472.22	24.952	0.087469	0.0052922
	500	26.481	0.10262	0.0058643
	533.33	28.31	0.12316	0.0065988
	566.67	30.135	0.14638	0.0073837
	577.78	30.742	0.15484	0.0076608
	600	31.951	0.17274	0.0082313
	633.33	33.761	0.20248	0.0091435
	666.67	35.562	0.23603	0.010128
	683.33	36.456	0.25455	0.010657
	700	37.352	0.27397	0.011199
	788.89	42.069	0.40012	0.014524
	894.44	47.6	0.60527	0.019396
1000	53.148	0.87035	0.024939	

#### 5.2.4 Experimental Conditions for Scale Up Experiments

The total difference between shear rate, turbulent dissipation rate and turbulent kinetic energy were used to identify the conditions which were most similar for both 100 mL and 1000 mL scale. Figure 5.4 displays the difference in

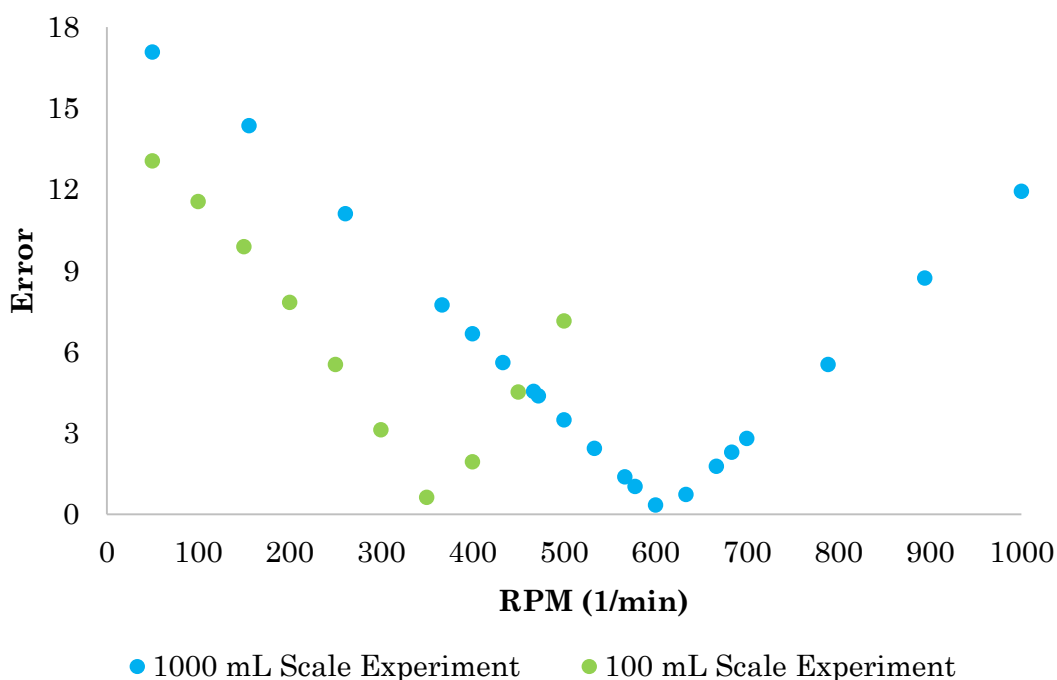


the error of the three variables used for a range of RPMs and is calculated using Equation 5.2.

$$\text{Error} = \sqrt{(x - x_1)^2 + (y - y_1)^2 + (z - z_1)^2} \quad \text{Equation 5.2}$$

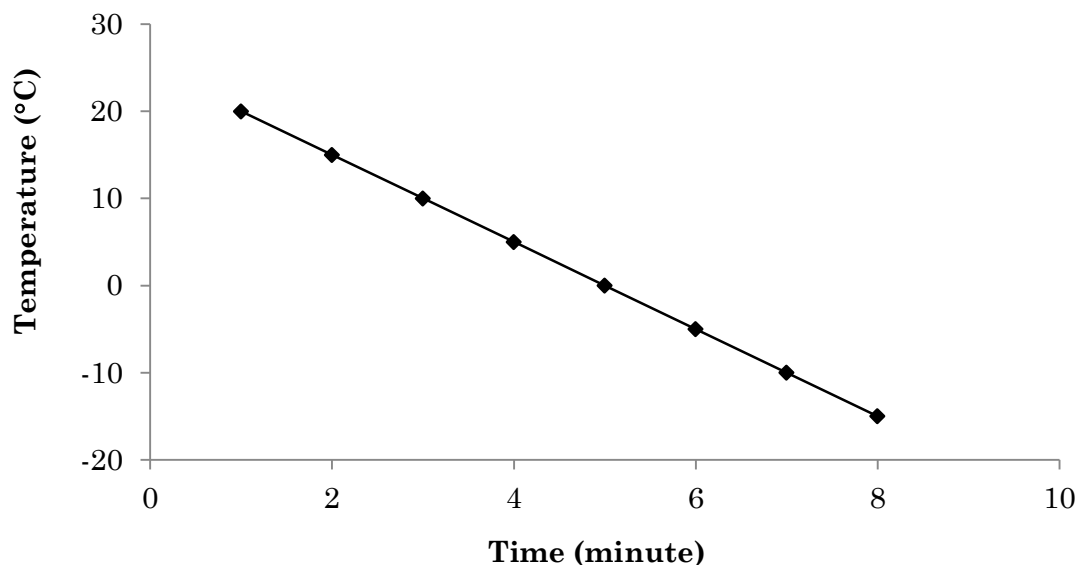
where (x is shear rate,  $x_1$  is the reference shear rate, y is turbulent dissipation rate,  $y_1$  is the reference turbulent dissipation rate, z is the turbulent kinetic energy and  $z_1$  is the reference turbulent kinetic energy).

As 350 rpm and 600 rpm had the smallest error for 100 mL and 1000 mL experiments, respectively, these RPM values were chosen. It is expected that these conditions should provide the closest conditions to the previously used conditions to successfully crystallise ALA II.



**Figure 5.4** Error for mixing conditions at both 100 mL and 1000 mL scale

The linear cooling profile programmed for 100 mL and 1000 mL experiments (Figure 5.5).



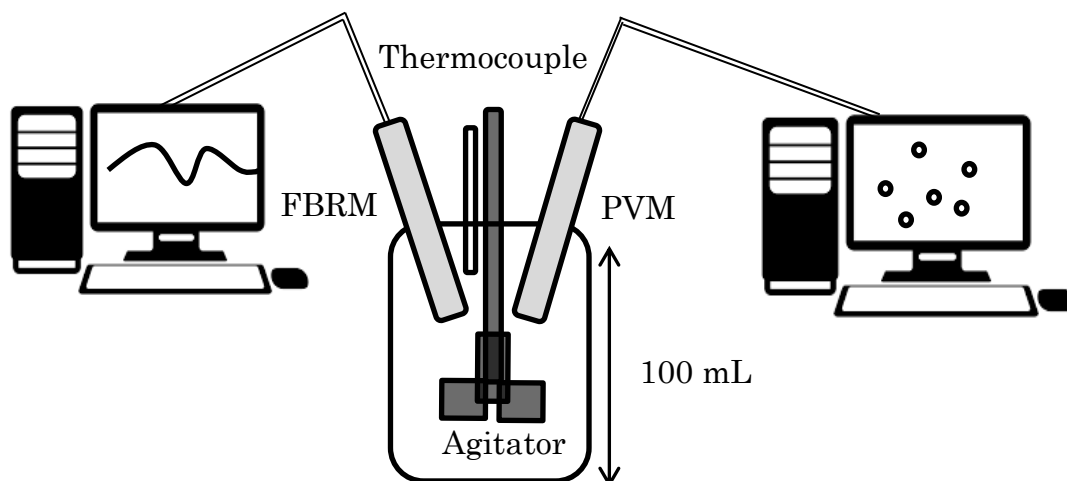
**Figure 5.5** Linear temperature profile used for both 100 mL and 1000 mL experiments.

### 5.2.5 Experimental Set-Up and Procedure (100 mL)

Using the set-up in Figure 5.6, a cooling crystallisation of ALA I in the presence of NIC, with the aim of crystallising ALA II, was carried out using the following experimental procedure and setup. Unfortunately, due to the solution becoming a slurry and blocking the imaging pane of the PVM probe, it was not possible to capture clear and meaningful images and no data from PVM is presented.

The stirrer speed was set to 350 rpm and the reactor temperature was set to 20 °C. ALA which was dissolved in IPA was added to the crystalliser and stirred for five minutes. The NIC solution was then added and stirred for a further five minutes. At the end of ten minutes, the reactor was set to cool to -15 °C at -5 °C/min and then held for 12 hours.

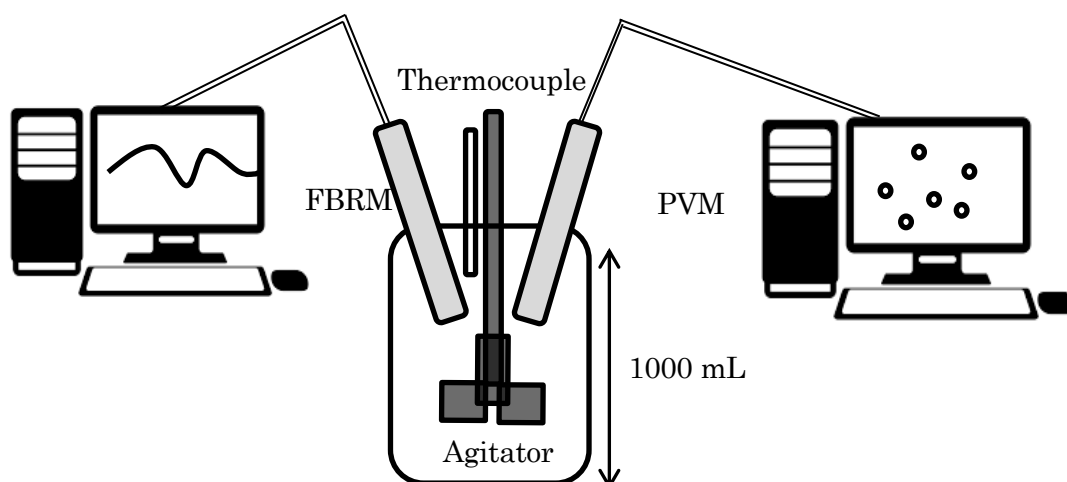
Once nucleation had taken place, a sample was taken, dried and analysed to determine which form of ALA had formed initially, at the end of the experiment a sample was also removed for XRPD analysis to identify any phase transformation.



**Figure 5.6** Experimental set-up for 100 mL.

### 5.2.6 Experimental Set-Up and Procedure (1000mL)

Based on the values obtained from the CFD model (Figure 5.4), the experimental set up (Figure 5.7) and procedure was used.



**Figure 5.7** Experimental set-up for 1000 mL.

The stirrer speed was set to 600 rpm and the reactor temperature was set to 20 °C. The ALA solution dissolved in IPA was added to the crystalliser and stirred for around five minutes. The NIC solution was then added and stirred for a further five minutes. At the end of the ten minutes, the reactor was set to cool to -15 °C at -5 °C/min and then held for 12 hours. Once nucleation had taken place, a sample was taken, dried and analysed to determine which form of ALA

had formed initially, at the end of the experiment a sample was also removed for XRPD analysis to identify any phase transformation.

## **5.2.7 Physical Characterisation**

### **5.2.7.1 SEM**

Samples were gently tapped onto sticky carbon tabs added to 10 mm diameter aluminium stubs and placed under vacuum for three minutes prior to transfer to the SEM for analysis. Beam voltage of 1000 V, with detection of backscattered electron signal, at magnifications of x2500 and x1500 was used.

### **5.2.7.2 Gas Adsorption**

A 20 point adsorption, 20 point desorption isotherm at 77 K was carried using the instrument detailed in *Section 3.2.1.7*. Approximately 1 g of material was accurately weighed into a 9 mm diameter glass cell, and degassed under vacuum for 18 h at 25 °C, prior to the sorption isotherm being conducted. Brunauer-Emmett-Teller (BET) surface area was calculated within the *Quantachrome® ASiQwin™* software version 3.01, using 6 points within the P/P<sub>0</sub> range 0.05 to 0.35. Adsorbate details were as follows: Nitrogen Temperature 77.350 K, Molecular Weight.: 28.013 g, Cross Section: 16.200 Å<sup>2</sup>, Liquid Density: 0.808 g/cc.

### **5.2.7.3 XRPD**

Solid materials were characterised off-line via XRPD using a Bruker AXS D2 Phaser 2nd generation diffractometer as described in *Section 3.2.1.9*. Data were collected at room temperature from 4-35° 2θ with a 0.01° 2θ step size and 1 s step count time. Phase purity quantification was carried out using software *Bruker AXS Topas* version 5.

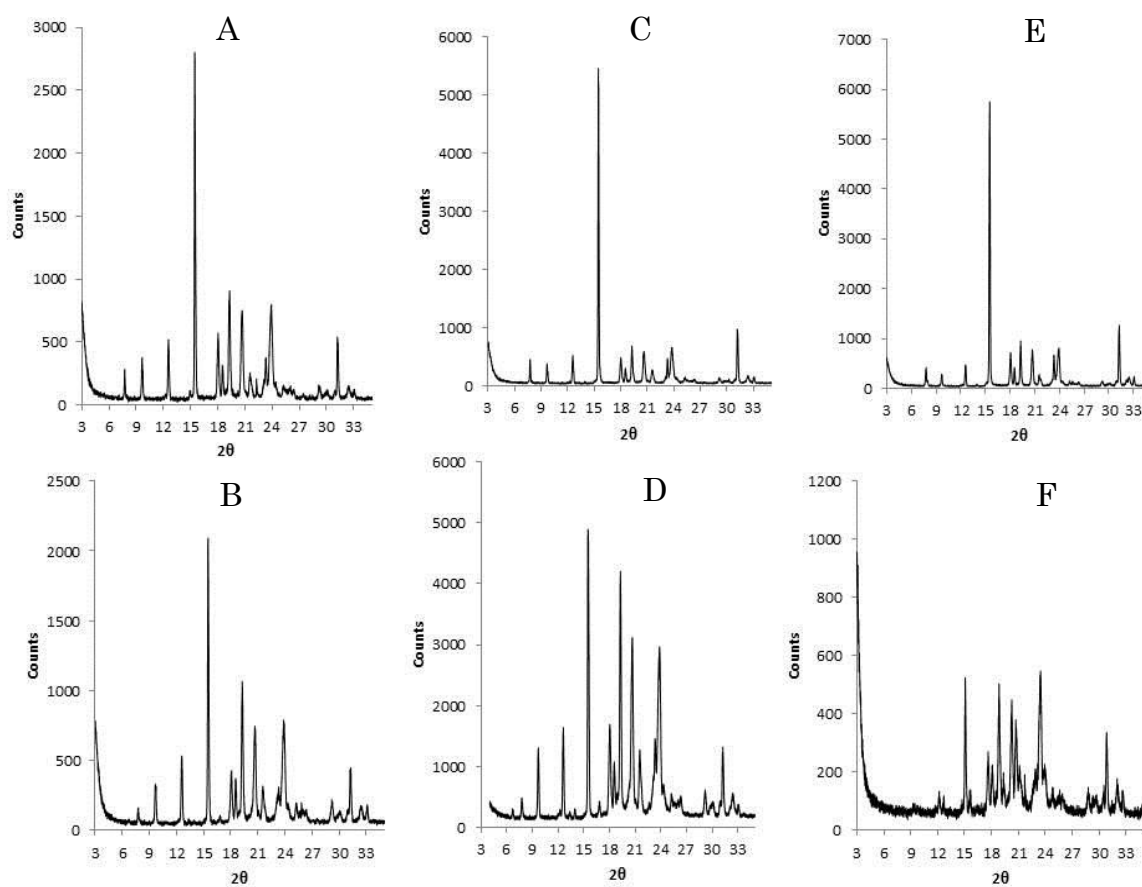
### **5.2.7.4 FBRM**

FBRM data were collected as described in *Section 3.2.1.2*.

## 5.3 Results and Discussion

### 5.3.1 Small Scale Controlled Crystallisation Experiments

The aim of this section was to discover under which crystallisation conditions ALA II would form. Three different cooling rates and two different stirrer speeds were investigated. It can be seen in Figure 5.8 under most of the hydrodynamic conditions tested ALA II was successfully isolated. However, conditions D and F produced mixed polymorphs of ALA. Conditions D and F both had slow (400 rpm) stirrer speeds, with variable and slow cooling profiles, respectively.



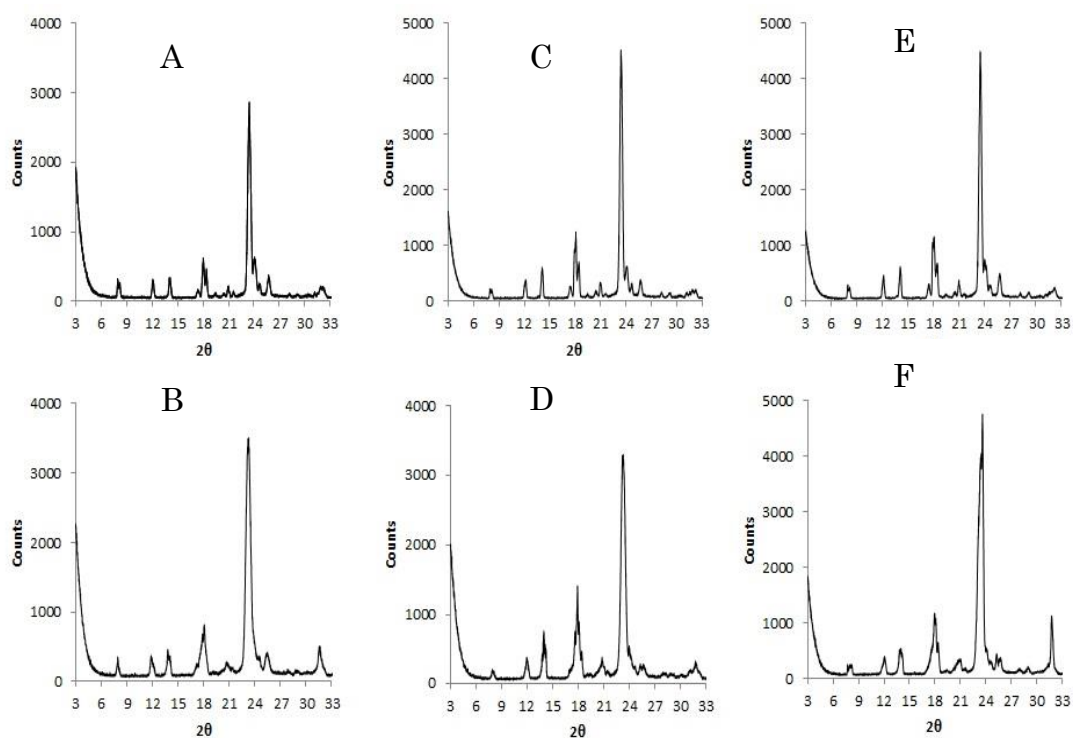
**Figure 5.8** XRPD patterns from the initial small scale experiments which investigated the effect of cooling rate and mixing on polymorphic outcome in the presence of NIC.

Condition A: 5 °C/min, 800 rpm, B: 5 °C/min, 400 rpm, C: Controlled staggered cooling rate (Figure 5.3), 800 rpm, D: Controlled staggered cooling rate (Figure 5.3), 400 rpm, E: 0.1 °C/min, 800 rpm and F: 0.1 °C/min, 400 rpm.

**Table 5.6** Polymorphic outcome of the small scale experiments.

Vial A	Vial B	Vial C	Vial D	Vial E	Vial F
ALA II	ALA II	ALA II	ALA I & II	ALA II	ALA I & II

Given that concentration, solvent and final temperature was kept constant, the difference in polymorphic outcome can be attributed to the differences in stirrer speed and cooling rate. A control experiment was performed in which NIC was excluded and other parameters (i.e. concentration, cooling profile and mixing conditions) were kept constant. This showed that when crystallised under identical conditions but in the absence of NIC, ALA I was preferentially crystallised (Figure 5.9).



**Figure 5.9** XRPD patterns from the initial small scale experiments which investigated the effect of cooling rate and mixing on polymorphic outcome without NIC.

Condition A: 5 °C/min, 800 rpm, B: 5 °C/min, 400 rpm, C: Controlled staggered cooling rate (Figure 5.3), 800 rpm, D: Controlled staggered cooling rate (Figure 5.3), 400 rpm, E: 0.1 °C/min, 800 rpm and F: 0.1 °C/min, 400 rpm

One other control experiment was carried out which investigated the effect of agitation (800 rpm) on the polymorphic outcome of ALA. The solutions prepared, contained NIC. The vials were placed in the reactor when the investigated temperature had been reached and kept until nucleation was detected. The results of these experiments can be seen in Table 5.7.

**Table 5.7** Polymorphic forms of ALA obtained crystallised under mixed and unmixed conditions.

Temperature (°C)		0	-5	-10	-15
Polymorphic Form of ALA	Mixed	ALA I	ALA I & II	ALA II	ALA II
	Unmixed	ALA II	ALA II	ALA II	ALA II

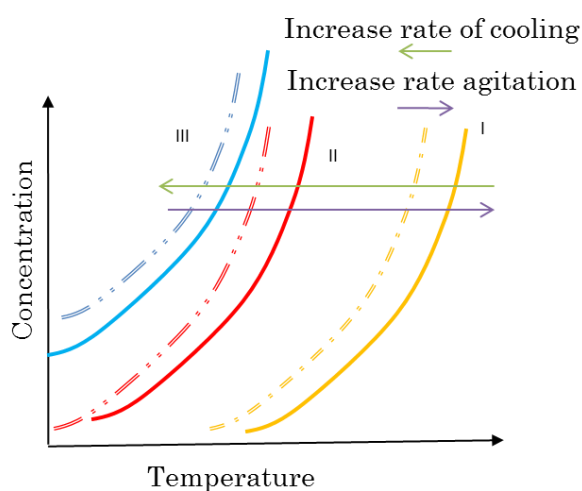
The series of control experiments confirmed NIC's critical role in isolating ALA II as, under identical and controlled experimental conditions but without NIC, ALA I was consistently obtained (Figure 5.9). Additionally, the metastable form of ALA was crystallised in the absence of mixing when the suitable isolation temperature was used (Table 5.7). This may allow the suggestion to be made that the isolation temperature/cooling rate has a fundamental role in crystallising ALA II rather than the presence/intensity of agitation. However, when ALA-NIC solution was exposed to a mixing regime and a cooling rate simultaneously, the success of being able to crystallise ALA II was influenced by both variables (Figure 5.8).

The nucleation behaviour of gestodene – ethanol system, as a result of a varying cooling rates and agitation speeds for the batch cooling crystallisation has been reported by Wang *et al*<sup>27</sup>. The MSZW was measured at four different cooling rates and whilst, the MSZW was directly proportional to the cooling rate used, it was inversely related to the agitation speed. This confirms that cooling rate and agitation speed have opposing effects on the MSZWs of systems. This has been an reported for other systems e.g. paracetamol – ethanol<sup>242</sup>, L-glutamic acid – water<sup>243</sup>.

The effect of cooling rate on MSZW has been attributed to the kinetic factor relating to the ordering of the structured crystal nuclei from molecular clusters<sup>244</sup> which leads to the widening of the MSZW. The relation between

agitation rate and MSZW has been explained by the detachment of nuclei from the stirrer's surface to the bulk solution, as a result of fluid shear, leading to surface induced heterogeneous nucleation<sup>243</sup>. An alternative explanation has also been suggested, where it is proposed that the rate of secondary nucleation increases with agitation, triggering nucleation to be detected earlier<sup>245</sup>.

The two variables discussed; cooling rate and agitation can be related to the isolation of different polymorphs by reference to the degree of supersaturation achieved, Figure 5.10.



**Figure 5.10** A hypothetical temperature concentration graph displaying the effect of cooling rate and agitation on MSZW of polymorphs I-III. Broadening or narrowing of the MSZW (represented by the dashed lines) can lead to the isolation of different polymorphs. The isolation temperature (hence supersaturation) will depict the final polymorphic form (figure adapted from reference 244).

If the MSZW is increased to the left e.g. by imposing a faster cooling rate, higher levels of supersaturations can be achieved before nucleation occurs, and the solution can become supersaturated with respect to a more soluble metastable polymorph allowing isolation of that form. The influence of the crystallisation process parameters on the polymorphic outcome of famotidine has been studied<sup>246</sup>. When higher cooling rates were used (quenching with an ice bath and 1 °C/min), the metastable form was more likely to form. This was attributed to the metastable limit of polymorph B being exceeded under those conditions allowing that form to be isolated. The same trend has been noted for other



polymorphic systems: gestodene – ethanol<sup>27</sup> (investigated up to 2 °C/min) and L-Glutamic acid – water<sup>247</sup> (investigated up to 3 °C/min). In contrast to these results, the metastable form of carbamazepine (form II) has been successfully crystallised from experimental conditions regardless of the cooling rate used (cooling rates investigated were from 0.25 °C/min to ice-cooling)<sup>248</sup>. This indicates that the desired form can be produced as long as the correct conditions are present.

Although the effect of agitation on MSZW and its subsequent outcome on supersaturation is known, relating that to polymorphic outcome has, thus far, been challenging. For the reactive crystallisation of L-glutamic acid, two different mixing speeds, 250 and 500 rpm were selected. The polymorphic composition of the crystal product was not significantly affected by the mixing intensity<sup>249</sup>. Furthermore, this has been shown in other systems such as the carbamazepine – saccharin co-crystal where form-I was preferred when the agitation speed was increased, the effect of the agitation rate on polymorphic selection was not as pronounced as the supersaturation generation method<sup>250</sup>. Sefcik *et al*<sup>248</sup> investigated the influence of agitation on the polymorphic outcome of carbamazepine, a highly polymorphic system<sup>56</sup>. This study concluded that, whilst under quiescent conditions, the metastable form II was produced however, the presence of agitation resulted in crystals which were typically form III (stable form). In that case, whilst stirring was a key factor influencing the initial polymorphic form obtained, it also influenced the rate of SMPT. This would suggest that when the metastable form is obtained, suitable conditions need to be provided to be able to preserve the polymorphic form and inhibit SMPT. The observed differences in the effect of agitation have been attributed to:

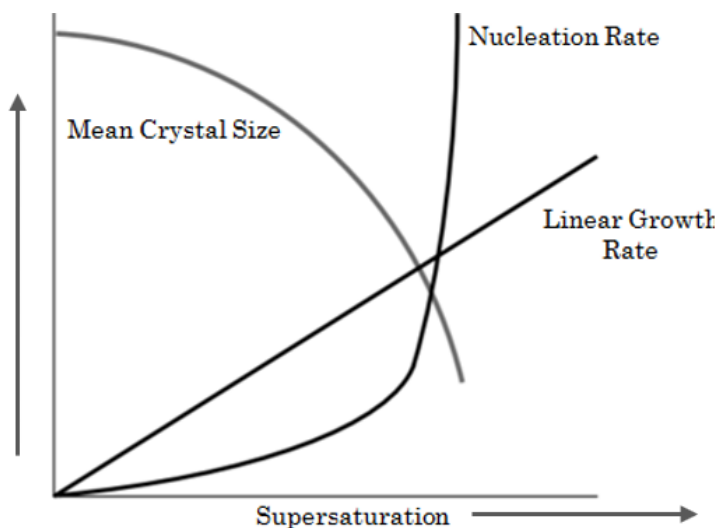
- i. *m*-hydroxybenzoic acid: differences in the crystal structures, where nucleation of one polymorph may be more sensitive to changes in shear flow conditions<sup>251</sup>.
- ii. L-glutamic acid: agitation being sufficient to disrupt nucleation of the one polymorph or lead to nuclei which lack the necessary well-formed crystallographic facets on which other forms can nucleate<sup>252</sup>.

Therefore it is challenging to predict the way in which process conditions (specifically cooling rate and agitation) will influence the polymorphic outcome as the response appears to be system dependent. It was concluded that NIC was key for ALA II to crystallise. ALA II was successfully crystallised under most conditions investigated except; where controlled staggered (initially 1 °C/min then 0.1 °C/min) and a slow cooling rate (0.1 °C/min) were used with 400 rpm stirrer speed. Thus, condition A (stirrer speed 800 rpm at a cooling rate of -5 °C/min) were taken forward and investigated at larger scale crystallisers.

### 5.3.2 Initial Scale Up (100 mL)

Changes in mixing processes, are described by the model parameters determined using CFD. Simulation results offer valuable insights for determining optimal operating conditions and equipment parameters on scale. The primary outcome of this scale up was to ensure the correct polymorphic form had been crystallised using the suitable mixing conditions determined through CFD. FBRM and PVM were applied to gain further understanding of the system.

The CSD is determined by crystal growth, nucleation, secondary nucleation, breakage and fines (Figure 5.11).



**Figure 5.11** Effect of supersaturation on nucleation rate, growth rate and particle size (Image adapted from reference 253).

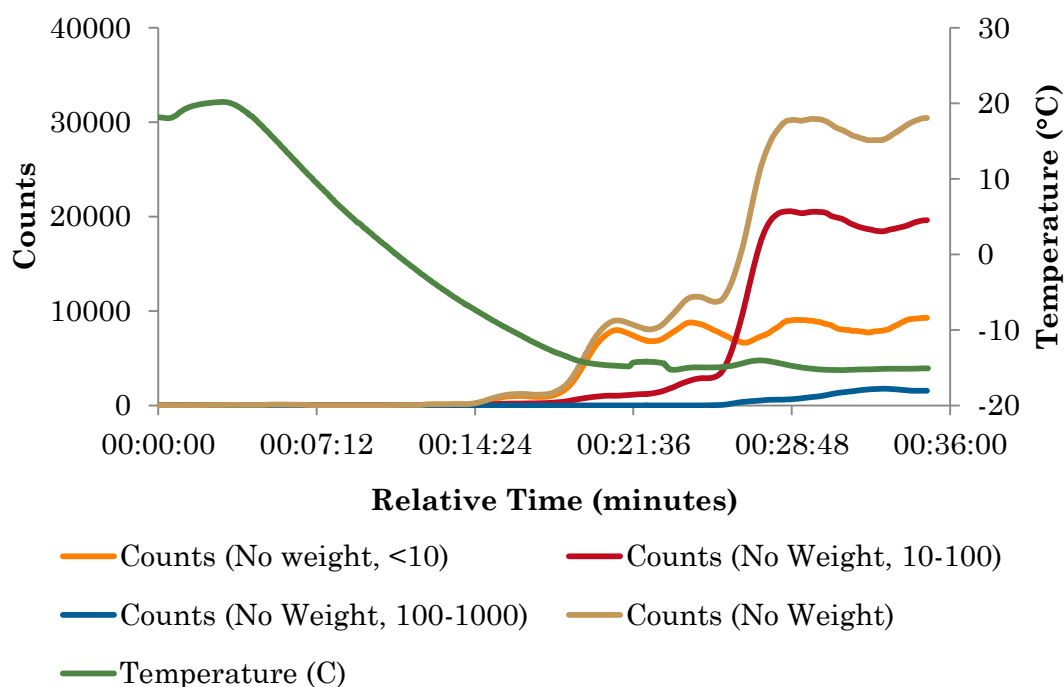
The number of nuclei formed increase exponentially as supersaturation increases. At low supersaturation, the growth process is dominant and particle size is determined by the growth process of crystals. At higher supersaturations, the nucleation rate increases. The process is controlled by nucleation with a higher number of nuclei thus limiting crystal growth

The general trend from the FBRM signal is observed in Table 5.8. Initially there are a low numbers of particles and a gradual increase in the number of particles can be observed as cooling progresses. The majority of the particles appear to be smaller than 10  $\mu\text{m}$  with very few particles larger than 100  $\mu\text{m}$ .

**Table 5.8** Trends of the various particle size bands for 100 mL scale.

<b>Trend</b>	<b>00:02:34</b>	<b>00:14:45</b>	<b>00:14:55</b>	<b>00:15:15</b>
Temperature ( $^{\circ}\text{C}$ )	20.12	-7.97	-8.26	-8.82
counts No Wt <10	29.2	346.24	445.15	660.18
counts No Wt 10-100	13.7	71.79	88.45	129.22
counts No Wt 100-1000	0.0776	0.0305	0.0305	0.0305
counts No Wt	42.98	418.06	533.63	789.44

Nucleation was identified based on total counts (no weight) when a significant increase in the number of particles was detected (Figure 5.12). The nucleation temperature was identified as -7.9  $^{\circ}\text{C}$  (total particle number above 300). It is evident that after nucleation there is a steady increase in particle count in the size range of 10-100  $\mu\text{m}$  and <10  $\mu\text{m}$ . However, the number of particles between 100-1000  $\mu\text{m}$  remained the lowest throughout the experimental time.



**Figure 5.12** FBRM data for counts of particles at all weights.

The peaks and troughs seen post-nucleation in Figure 5.12 can be due to a number of events. A similar observation has been reported in aluminium potassium sulfate - water system where the smallest size band of particles (0-20  $\mu\text{m}$ ) showed similar trends and was attributed to the presence of fines<sup>26</sup>.

In keeping with the potassium sulfate - water system, the smallest particles (0-10  $\mu\text{m}$ ) are the contributing particles to this observation. Fines can be due to multiple nucleation events taking place where, as cooling progresses through the solution further nucleation events happen. This particularly may be the case when a fast cooling regime is used as the crystalliser will not have time to reach temperature equilibrium. However, other process including; secondary nucleation or particle breakage could also be contributing to the CSD.

However, the main aim was to investigate polymorphism and as a result the effect of cooling rate or agitation on the CSD has not been further explored. Studies investigating the relationship between cooling rate and CSD for potassium dichromate showed that the crystals obtained from a cubic profile were larger; more uniform in size with fewer fines and low levels of agglomeration. The crystals obtained from a linear profile were smaller in size with more agglomeration and fines<sup>254</sup>. Similarly, studies investigating physical

properties of L-glutamic acid crystals obtained poorly formed smaller crystals at high agitation speeds<sup>252</sup>. Therefore, these experimental settings may have contributed to the small crystal size obtained for these experiments.

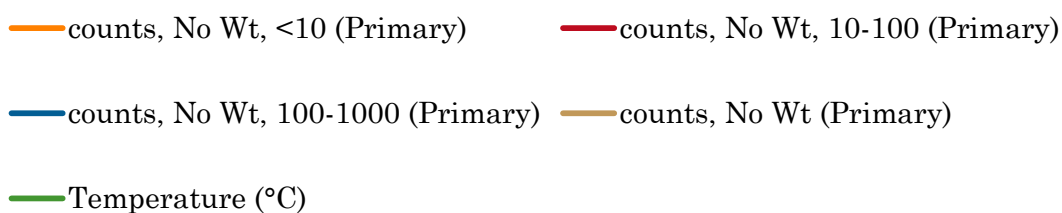
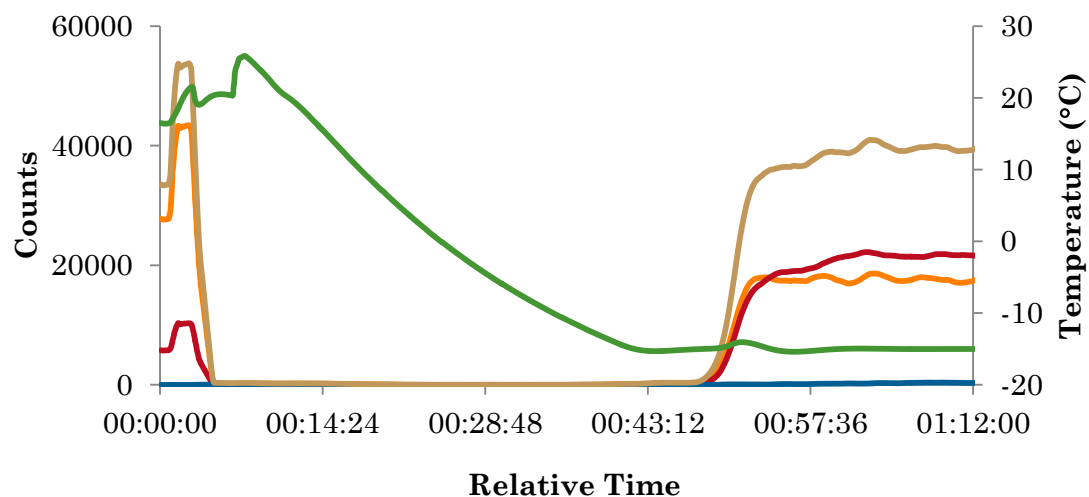
### 5.3.3 Final Scale Up (1000 mL)

When ALA II had been successfully crystallised at the 100 mL scale, the next step was to identify if this would be possible at a 1000 mL working volume. The hydrodynamic conditions at 100 mL scale were used in the CDF model to determine the mixing conditions for this experiment. The concentration of materials and experimental procedure was kept identical to the previous smaller scale experiments.

In Figure 5.13, the trends associated with particle size, which are inferred from chord length distribution, can be observed. In keeping with the previous experiments, particle size remained small and very few particles within 100-1000  $\mu\text{m}$  were detected. The possible reasons for this have been explained in *Section 5.3.2*.

**Table 5.9** Trends of the various particle size bands for 1000 mL scale.

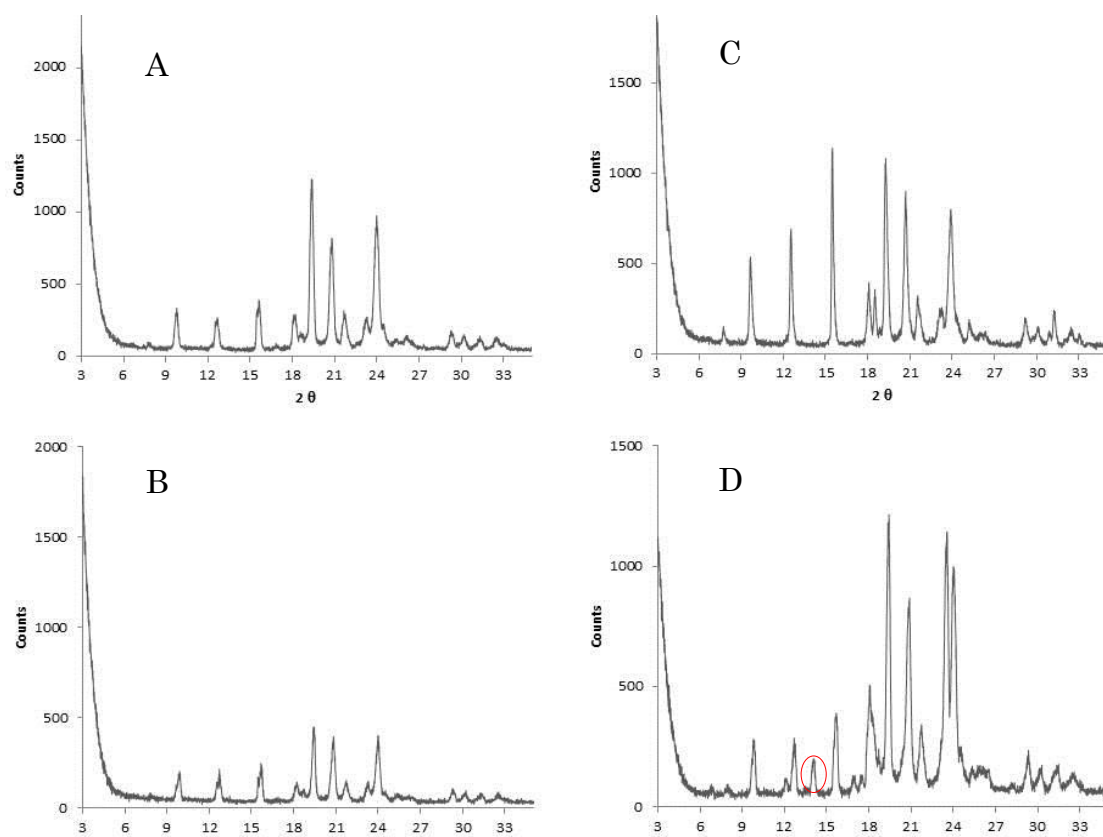
<b>Trend</b>	<b>00:27:49</b>	<b>00:42:10</b>	<b>00:47:31</b>	<b>00:49:01</b>
counts No Wt <10	3.12	148.63	360.91	1826.35
counts No Wt 10-100	1.03	22.87	80.11	1022.01
counts No Wt 100-1000	0.0317	0.0164	0.301	15.42
Counts (No Weight)	4.18	171.51	441.32	2.863.77
Temperature( $^{\circ}\text{C}$ )	-3.37	-15.05	-15.03	-14.93



**Figure 5.13** FBRM data for counts of particles at all weights.

Similarly to the 100 mL experiments, peaks and trough after the main nucleation event can be seen (Figure 5.13). However, this effect appears to be delayed compared to the previous 100 mL scale experiment (Figure 5.12). If this is due to multiple nucleation events, the delay may be due to the difference in the time each system needed to reach the desired temperature.

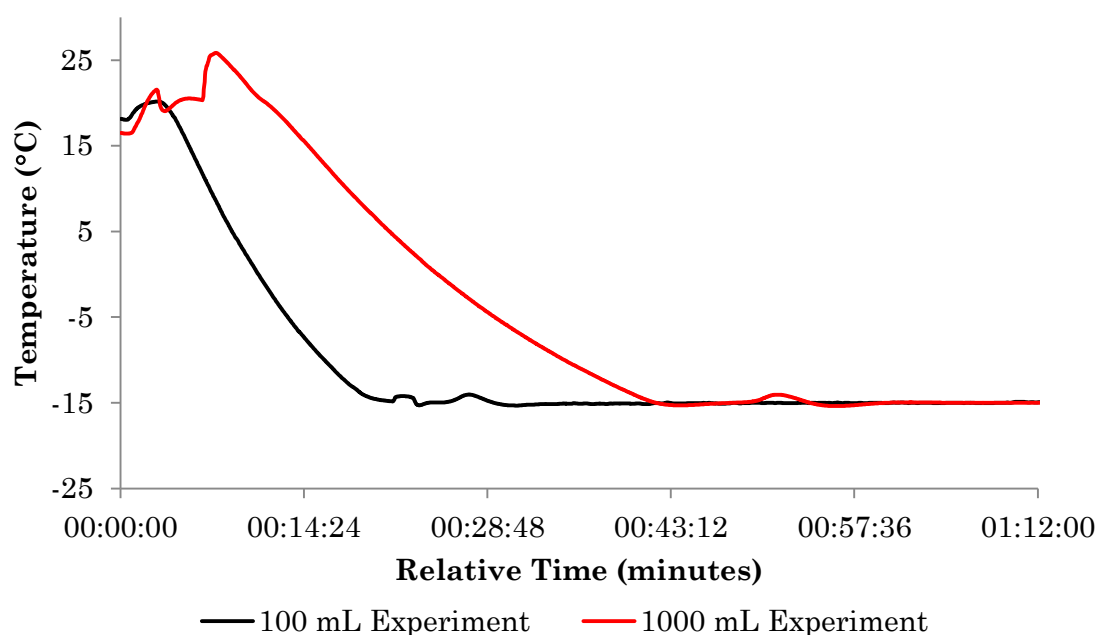
In both cases, a sample was removed at the beginning, when nucleation was observed and at the end of the experiment after the hold period. The sample was filtered, washed and dried and the solid material left was analysed by XRPD. Sampling was carried out in this way to understand if the desired polymorphic form had been obtained and whether it would convert to the stable form with time.



**Figure 5.14** Powder pattern for the 100 mL scale immediately after nucleation (A) and after 12 hours (B), 1000 mL scale immediately after nucleation (C) and after 12 hours (D).

Although the temperature data does not indicate a deviation from the desired temperature, given there is a reduced surface to volume ratio it is more difficult for the system to maintain this temperature throughout the vessel and this is a recognised challenge when scaling up in STR<sup>129</sup>. The challenges surrounding heat transfer capabilities of STRs have been shown through CFD where temperature gradients have been observed for STRs<sup>255, 256</sup> and in this case this

may have triggered SMPT. This means that cooling rates obtainable in small scale STRs are significantly higher than those achievable in larger scale crystallisers. Given the increase in volume and corresponding challenges around heat transfer, there is an expected reduction in the efficiency of the mixing which would further contribute to temperature and concentration variation throughout the vessel. This can be seen in Figure 5.15 where both 100 mL and 1000 mL experiments were set up to perform the same experimental procedure but it took the 100 mL vessel around 20 minutes to reach the desired temperature and twice as long for the 1000 mL vessel. This is a limitation of the cooling capability of the platform.



**Figure 5.15** Temperature profiles for 100 mL and 1000 mL experiments.

These points must be taken into consideration when considering why ALA II might have formed initially but the powder patterns from the end of the experiment would indicate there to be some transformation to ALA I.

### 5.3.3 Physical Characterisation

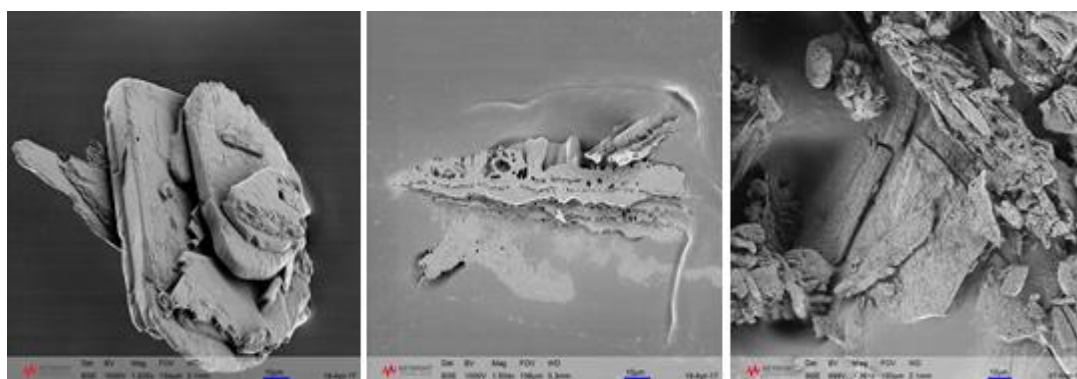
To determine the size and properties of the particles formed, SEM and gas adsorption were completed. SEM allowed the size, shape and other surface



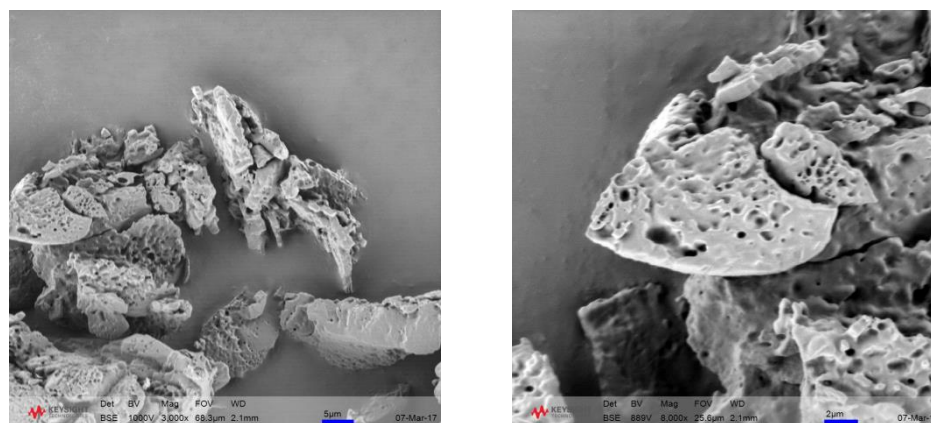
properties to be identified. Due to some observations made, the material produced was then also assessed using gas adsorption.

### 5.3.3.1 SEM

In order to characterise the solid material, SEM images were collected of the raw material, ALA I and ALA II (Figure 5.16 and Figure 5.17). Samples of ALA I and ALA II were crystallised from small scale uncontrolled conditions. Some porosity was indicated for recrystallised ALA I, however the level and consistency was not identical to that of ALA II which was considerably more porous.

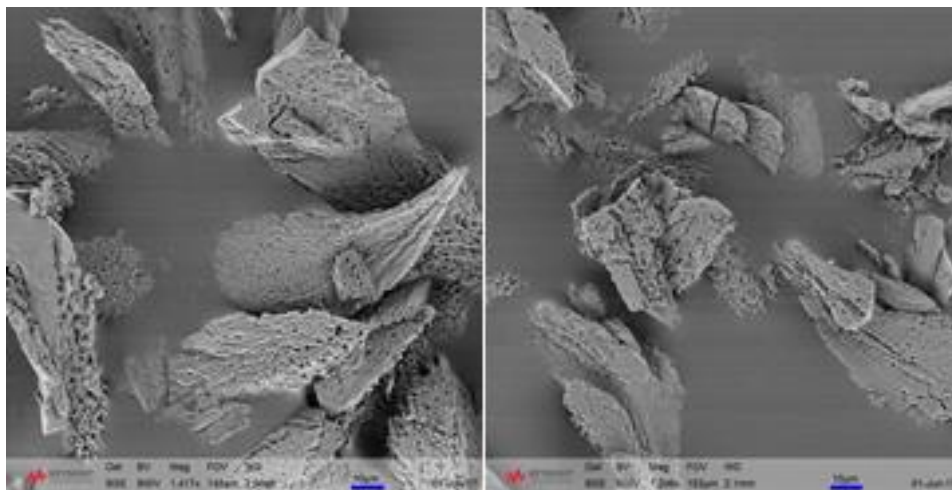


**Figure 5.16** SEM images taken of the raw material (left), recrystallised ALA I (centre) and ALA II (right). Scale bar indicates 10  $\mu\text{m}$ .



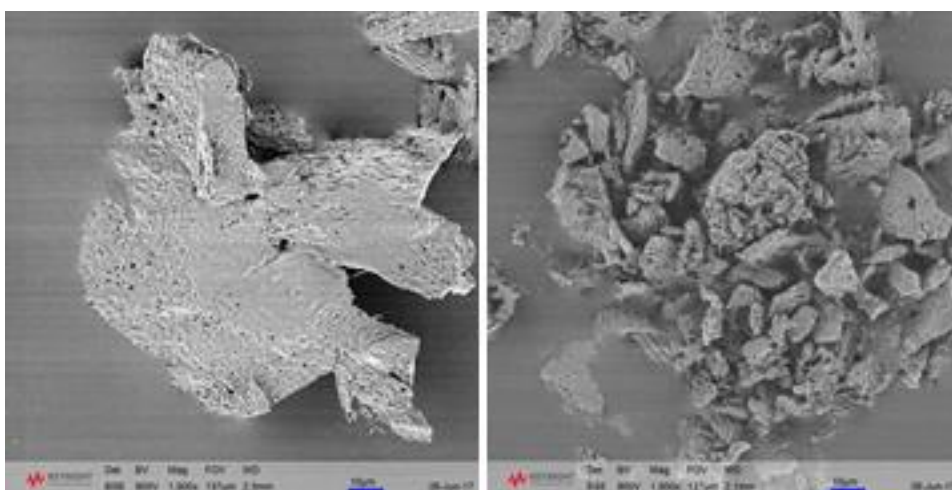
**Figure 5.17** Zoomed in SEM image of ALL II. Scale bar indicates 5  $\mu\text{m}$  (left) and 2  $\mu\text{m}$  (right).

Initially, the effect of washing was investigated to identify if this could be the cause for the porous surface obtained. This was achieved by crystallising ALA II in the presence of NIC as previously explained; however, during the filtration step one sample was washed with deionised water whilst one sample was not. From the images in Figure 5.18 both samples were identical from this perspective, thus washing was eliminated as the reason.



**Figure 5.18** ALA II unwashed (left) and washed (right).

It was of interest to see if ALA II produced from different scales had different surface properties. Thus, ALA II obtained from 100 mL and 1000 mL were also analysed by SEM. It was observed that the scale of crystallisation did not change the presence of porosity. However, images obtained from the sample crystallised at 1000 mL visually appeared to be less porous (Figure 5.19).



**Figure 5.19** ALA II crystallised at 100 mL scale (left) and 1000 mL (right).

One possible reason reported in literature responsible for the formation of porous materials prepared by a solvent-based processes, is due to removal of included solvent molecules from inside the material which has been attributed to possession of irregular shapes, or inefficient packing of crystals<sup>257</sup>. Examples of porous crystalline materials are reported though not heavily<sup>97, 98, 257, 258</sup>, as crystallising species will typically endeavour to maximise contact with each other as per thermodynamics, to reduce any void space. Therefore, the presence of porosity will often require the assembly of specifically shaped rigid structures capable of strong and directional interspecies interactions<sup>97</sup>.

Whilst the washing of crystallised material did not affect the formation of porosity the scale of crystallisation appeared to affect the level of porosity. As SEM was not able quantify the depth or type of porosity, gas adsorption studies were carried out on these samples.

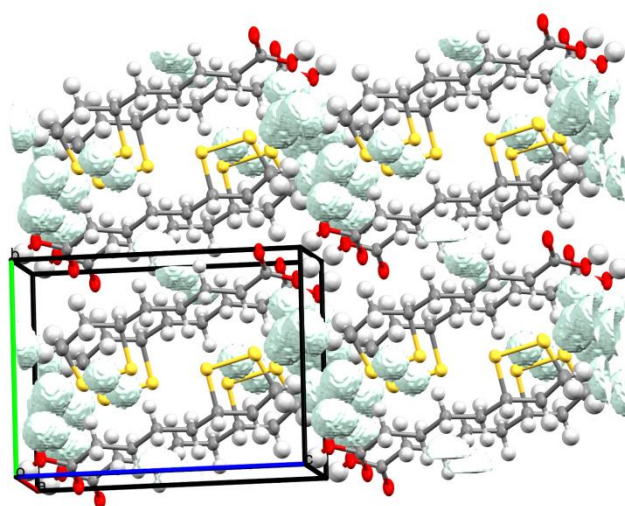
### 5.3.3.2 BET

In addition to the images obtained from SEM, gas adsorption studies were performed on samples from all crystallisation scales. Gas adsorption studies specifically provide information regarding type of porosity, specific surface area, pore size distribution and shape. N<sub>2</sub> adsorptions over a wide range of pressures can be used to acquire quantitative and qualitative information. For all three samples analysed, the surface area obtained can be seen (Table 5.10).

**Table 5.10** Surface area obtained for samples from all three scales and the raw material.

Experimental Scale	Surface Area (m <sup>2</sup> /g)	% Increase
Raw Material	0.423	-
10 mL	1.354	220.09
100 mL	1.347	218.44
1000 mL	0.775	83.22

In agreement with the SEM images, surface area was the lowest for the samples obtained from the 1000 mL scale (83.22%). Several possible reasons can be suggested as to why the crystals have formed in this way. As previously explained, porosity can be due to solvent inclusion (and the subsequent removal). The removal process would leave voids/pores during extraction of solvent during the filtration process. However, if this was the reason it would be expected for the porosity to be higher and deeper than what appears to be only present on the crystal surface. Furthermore, the void space of ALA II was calculated using Mercury<sup>208</sup>. Porosity builds from the molecular scale up and requires the presence of channels throughout, with a minimum diameter of 3 Å<sup>258</sup>. The void space calculations using a 2 Å probe radius resulted in no void space. However, using a probe radius of 0.7 Å, a void space of 4 % was calculated. Thus, whilst ALA II is less efficiently packed, the diameter is much smaller than the value required to satisfy the definition of conventional porosity (Figure 5.20).



**Figure 5.20** Packing of ALA II and the void space available using a probe radius of 0.7 Å and a grid spacing of 0.1 Å.

Nucleation and growth of crystals is heavily dependent on supersaturation. Defects and strains on the crystal may appear if there is non-uniform growth of crystals i.e. some crystals grow more rapidly in areas of higher supersaturation<sup>236</sup> or if the experimental conditions do not allow enough time for the new molecules to settle to their position<sup>259</sup>. In these experiments, voids

observed during the growth of crystals could be due to the cooling rate used as this was the method of supersaturation generation. It has been reported<sup>260</sup> that when a slow cooling rate is used defects have time to heal and when a high cooling rate is used, the defects are frozen into the lattice. However, when an intermediate cooling rate is used the defects can agglomerate leading to surface defects such as voids. The increase in surface area decreases as the scale of crystallisation increases. Highest surface area was obtained for the 10 mL experiments and the smallest change was calculated for the largest scale studied. It is known that the time taken for the system to reach the desired temperature was almost double for the 1000 mL scale (*Section 5.3.5.3*). Hence, it could be that the slower cooling rate present in the larger scale experiments allowed the molecules to arrive to their equilibrium position and any imperfections to heal, leading to a lower surface area.

Table 5.11 reports the surface area obtained for raw and processed pharmaceutically relevant chemicals. In comparison to the literature data, the increase in surface area obtained is generally lower than the other methods used to increase surface area e.g. micronisation. Although there is visual evidence of porosity, the level would not be sufficient for applications reported within literature e.g. the separation and extraction of gases and solvents<sup>258</sup>. However, it is still interesting that the material would retain this characteristic as it is not the most energy efficient form.

**Table 5.11** Surface area for raw and processed APIs.

API	Surface Area m <sup>2</sup> /g	% Increase	Processing	Reference
Deflazacort	4.2	950	Micronised	261
Deflazacort	0.4	-	Raw material	261
Deflazacort	1.9	375	Hollow crystals	261
Diclofenac	1.73	-	Raw material	262
Diclofenac Sodium	1.37	-	Raw material	262
Diclofenac	2.4	38.73	Jet milled	262
Diclofenac Sodium	11.3	724.82	Jet milled	262

## 5.4 Summary

The purpose of this work was to advance the understanding from the discovery stage of isolating ALA II. This included identifying experimental conditions under which ALA II was successfully crystallised. Once experimental conditions were established, a larger volume STR batch crystalliser was used to develop further understanding of behaviour within solution leading to the isolation of the metastable form.

ALA II was successfully isolated at both 100 mL and 1000 mL scales; some phase transformations were noted at the largest scale investigated. Transformation of ALA II to the stable polymorphic form may be attributed to the literature reported difficulties regarding scale up in STR's. Solid material obtained was noted to be porous, however, further studies of this has revealed it to be most likely a surface property and possibly due to the experimental procedure.

Previous experiments (Chapter 4) revealed the solid state outcome to be dictated by the concentration of NIC. Due to the nature of 'batch' production the composition is fixed and therefore the likelihood of being able to control the polymorphic form, by altering the concentration of NIC, would be challenging with such a set up. Furthermore, difficulties relating to heat transfer capabilities of a STR and the consequences of this resulting in SMPT have been identified. An OBR, which has improved heat transfer capabilities, may address this issue. Lastly, a continuous platform may allow the polymorphic form to be better controlled and if desired, changed from ALA I, ALA II and ALA-NIC co-crystal at any point in the process.

# Chapter 6 Design, Development and Characterisation of a Novel Continuous Oscillatory Baffled Reactor

Part of this chapter is based on:

Reference 282 L. N. Ejim, S. Yerdelen, T. McGlone, I. Onyemelukwe, B. Johnston, A. J. Florence and N. M. Reis, *Chemical Engineering Journal*, 2017, 308, 669-682.



## 6.1 Introduction

Meso scale OBRs were originally demonstrated for use in reaction engineering (ester saponification reaction<sup>124</sup>) and suspension studies of particles relevant to catalysis (silica resin, polyamine resin and ionic exchange resin<sup>263</sup>). Subsequent studies on meso OBR have used an internal diameter (I.D) of 4.4–5 mm; although, an ID up to 10 mm can be classified as meso scale<sup>264</sup>.

Complementing the range of studies regarding the characterisation<sup>263, 265, 266</sup>, inorganic<sup>267-269</sup> and biological processes<sup>270</sup> within a meso scale OBR (Table 6.1), the batch and continuous crystallisation of paracetamol<sup>66</sup> (meso scale 4.4 mm SPC OBR<sup>271</sup>) was recently investigated. The study aimed to assess the impact of process operating conditions on crystal size with the suitability for enhanced direct crystallisation of micronised powders. It was concluded that mixing intensity, supersaturation and temperature determined the crystal size properties. The continuous mode was shown to be more suitable in the production of inhalable size particles due to smaller residence times, limited crystal growth and reduced friction, breakage and aggregation of the crystals.

Platforms for crystallisation must provide conditions suitable for the formation and growth of nuclei or seeds, and the suspension and effective transport of particles. The appropriate experimental conditions will be dictated by the specifications and the performance required for the particles (e.g. size and shape of particles, flowability or compressibility). To define an operating space and the capabilities of the crystalliser which will be appropriate for the specific crystallisation process, a range of hydrodynamic conditions must be investigated and characterised.

The work presented here begins by studying a range of novel meso scale baffle geometries to identify the optimum design which was then used to construct an OBR for continuous crystallisation. This work was carried out by determining the minimum critical amplitude for suspension of particles over a range of frequencies. The novel COBR was then further characterised with the help of CFD, Residence Time Distribution (RTD) studies and preliminary heat transfer studies.

**Table 6.1** Chronological order of the design, characterisation, development and application of the meso scale OBR.

Process	Year	Reference
The fluid mechanics relating to a novel oscillatory flow micro reactor	2003	263
Fluid mechanics and design aspects of a novel oscillatory flow meso-reactor	2005	265
Application of a novel oscillatory flow micro-bioreactor to the production of gamma-decalactone in a two immiscible liquid phase medium	2006	270
Biodiesel reaction screening using oscillatory flow meso reactors	2007	272
The intensification of gas-liquid flows with a periodic, constricted oscillatory-meso tube	2007	273
The axial dispersion performance of an oscillatory flow meso-reactor with relevance to continuous flow operation	2008	274
Development and evaluation of novel designs of continuous mesoscale oscillatory baffled reactors	2010	266
Liquid backmixing in oscillatory flow through a periodically constricted meso-tube	2010	275

---

Continuous screening of base-catalysed biodiesel production using - new designs of mesoscale oscillatory baffled reactors	2011	276
Characterisation of fluid mixing in novel designs of mesoscale oscillatory baffled reactors operating at low flow rates (0.3 – 0.6 ml/min)	2011	121
Effect of geometrical parameters on fluid mixing in novel mesoscale oscillatory helical baffled designs	2011	277
Rapid determination of the reaction kinetics of an n-butylbenzaldimine synthesis using a novel mesoscale oscillatory baffled reactor	2012	267
Characterisation of mesoscale oscillatory helical baffled reactor — experimental approach	2012	278
Numerical study of the flow pattern and heat transfer enhancement in oscillatory baffled reactors with helical coil inserts	2012	279
Rapid determination of reaction order and rate constants of an imine synthesis reaction using a mesoscale oscillatory baffled reactor	2013	280
Continuous-Flow precipitation of hydroxyapatite at 37 degrees °C in a meso oscillatory flow reactor	2013	268

---

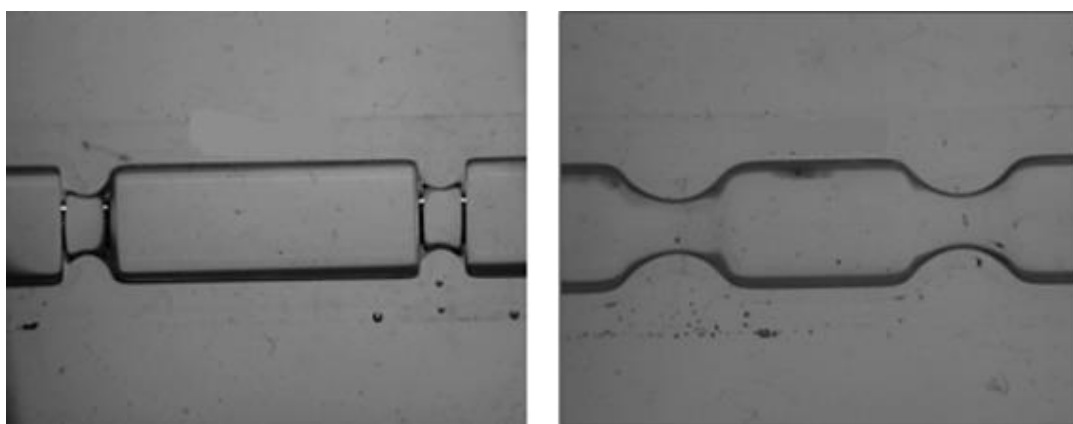
---

Precipitation of hydroxyapatite at 37 degrees °C in a meso oscillatory flow reactor operated in batch at constant power density	2013	281
Intensification of carboxylic acid esterification using a solid catalyst in a mesoscale oscillatory baffled reactor platform	2017	269
A factorial approach to understanding the effect of inner geometry of baffled meso-scale tubes on solids suspension and axial dispersion in continuous, oscillatory liquid-solid plug flows	2017	282
Effect of operating conditions on batch and continuous paracetamol crystallization in an oscillatory flow mesoreactor	2017	66

---

### 6.1.1 Mesoscale Oscillatory Baffled Reactor

The main body of OBR literature so far has been for “conventional” scale (ID>15 mm), sharp edged OBRs<sup>10, 118, 247, 283, 284</sup>. However, meso scale OBRs have been shown to have promise for pharmaceutical manufacturing<sup>66</sup>. This is attributed to their small total working volume, ability to handle solid and liquid phases and operability at low flow rates (mL/hour) with reduced starting materials, process development time, waste and man-power<sup>264, 267, 280, 282, 285</sup>. The “conventional” OBR sharp geometry was altered where the baffles were smoothed, thus reducing the high shear regions to suit bioprocess applications<sup>286</sup> and to maximise the mixing efficiency by eliminating “dead-zones” in which particles may sediment or become trapped<sup>115</sup> leading to the development of a smooth-walled, periodically constricted (SPC) tube.



**Figure 6.1** Diagram of a sharp-edged baffle (left) and smooth edged baffle (right).

Studies by Reis *et al*<sup>265</sup> on a meso scale SPC OBR, involved screening fluid oscillation conditions for suspension of solid catalysts which revealed suspension of solids to be possible up to 40 % v/v<sup>265</sup>. The degree of backmixing and mixing time was found to be controlled by the oscillatory conditions (frequency and amplitude)<sup>275, 285</sup> which have been supported by other studies on meso scale SPC OBR systems<sup>274</sup>.

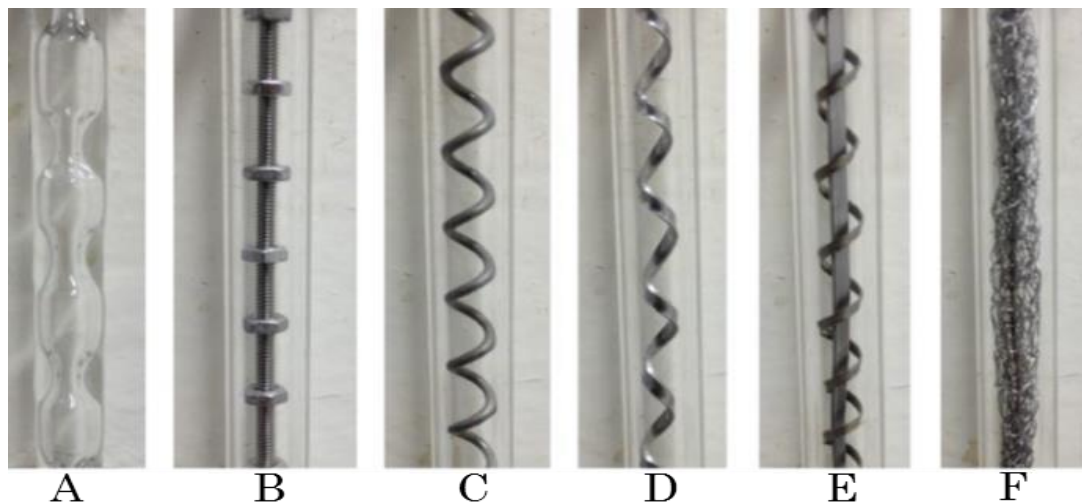
A range of other meso scale OBR with a variety of baffle configurations have been developed and characterised and some of the designs can be seen in Figure 6.2<sup>264</sup>. The integral baffle (Figure 6.2 - A) was designed as to have an I.D of 5 mm with smooth period constrictions<sup>266</sup>. The RTD profile has been studied over the flow rates from 0.3 – 8 mL/min<sup>121, 266</sup> and near plug flow was achieved at flow

rates above 1.7 mL/min. At lower flow rates from 0.3-0.6 mL/min oscillatory conditions were shown to have little influence which was attributed to the baffle thickness and diffusion process becoming more influential at the lower flow rates<sup>121</sup> due to the time scale for diffusion approaching the residence time<sup>264</sup>.

Central axial baffles (Figure 6.2 – B) comprised of 4 mm stainless steel discs, placed along a 2 mm diameter rod and have performed similar to the axial designs at flow rates from 1-8 mL/min<sup>266</sup>. Compared to the integral designs, due to the higher shear, the central baffles have been used for homogeneous liquid reactions<sup>280</sup>.

Helical baffles (Figure 6.2 – C, D, and E) have perhaps received the most interest as they have demonstrated the widest range of oscillatory conditions at which plug flow could be achieved. The helical baffled reactor reached near plug flow behaviour at higher oscillation amplitudes compared to central and integral baffles designs<sup>266</sup>. The fluid mixing inside meso scale oscillatory helical baffled reactors was investigated with a range of helical pitches, wire diameters and oscillatory conditions<sup>277</sup>. The wire diameter had little effect on the fluid mixing at amplitudes below 2 mm. A relationship between the helical pitch and amplitude was reported, where increasing the pitch required an increase in oscillation amplitude to achieve near plug flow conditions<sup>277</sup>.

RTD studies indicated that a higher degree of mixing was attributed to a stronger interaction between the two flows identified in a helical baffle<sup>278</sup> (central and swirling) which has also been confirmed with CFD and PIV<sup>279, 287</sup>. The helical designs have proven beneficial in screening processes involving immiscible liquids<sup>276, 288</sup>.



**Figure 6.2** Mesoscale baffle configurations; (A) integral baffles, (B) central axial baffles, (C) round-edged helical baffles, (D) sharp-edged helical baffles, (E) sharp-edged helical baffles with a central insert, (F) wire wool baffles. (Image taken from reference 264).

Baffle length,  $L$ , and orifice open area,  $a$ , control the size and shape of the mixing vortices within an OBR<sup>118</sup>. These have been identified as critical parameters which must be kept constant during scale up to reduce process development time and minimise scale up related setbacks<sup>115</sup>. By keeping  $L$ ,  $a$  and mixing intensity ( $Ren$ ,  $Reo$  and  $St$ ) similar, the scale-up of continuous OBRs has been studied by Smith and Mackley<sup>110</sup>. For the OBR's studied (24 mm, 54 mm and 150 mm), axial dispersion was independent of the baffle diameter. More recently, the scale-up of the meso scale OBR's has been studied<sup>266, 286</sup>. Thus far, scale up has been shown to be feasible meaning laboratory scale experiments can be used to design and optimise larger scale operations.

Applications of meso scale SPC OBR's have been shown for a number of processes. Reis *et al*<sup>289</sup> demonstrated that for the production of a flavouring agent used widely in the food industry, there was an improvement of 50% in the time needed to reach the desired concentration and productivity compared to an equivalent reaction in a 2 L STR<sup>290</sup>. The intensive mixing and low shear imposed on the bacteria were concluded as the reasons. A similar study which investigated a fermentation process, found an increase in biomass of 83%, compared with a scaled-down STR<sup>291</sup>. Thus the advantages demonstrated for biological operations, have been attributed to lower shear<sup>289, 291</sup> and enhanced

mass transfer rates which has been further confirmed with gas/liquid<sup>292</sup> and O<sub>2</sub> mass transfer studies<sup>293</sup>.

Furthermore, Zheng *et al*<sup>294</sup> compared biodiesel conversion rates between batch and continuous smooth meso scale SPC OBR which concluded that under identical experimental conditions of temperature and composition, equivalent conversion rates were obtained. The precipitation of HAp, used in bone replacement therapy, has been explored both in batch and continuous mode in a meso OBR with an ID of 4.4 mm. In both cases, improvement in production rate with enhanced crystallinity, smaller particles and narrower particle size distribution was obtained<sup>268, 281</sup>. A heterogeneously catalysed esterification process of carboxylic acid was studied by Eze *et al*<sup>269</sup> in a 5 mm meso scale OBR which concluded a significant decrease in both process development time and material use.

Mesoscale systems have successfully been demonstrated for batch and continuous crystallisation processes. However, concerns over high solid loadings and encrustation have been highlighted<sup>115</sup>. Nevertheless, literature for the meso scale OBRs have confirmed reductions in process development, control over mixing and enhanced mass transfer. A variety of mesoscale geometries have thus far been studied with different optimal flow conditions identified. Part of this study aims to establish a viable mesoscale OBR with assessment of potential implementation of PAT, automation and control. Evaluation of the axial dispersion of a meso scale SPC OBR at a range of flow conditions is reported.

## **6.1.2 Characterisation Methods**

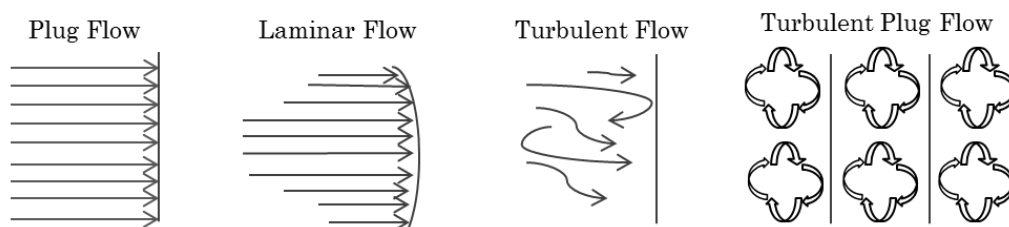
### **6.1.2.1 Residence Time Distribution (RTD)**

Mixing behaviour within an OBR depends on numerous key geometrical parameters that include the baffle spacing, baffle shape and open cross sectional area, and the importance and relationship between these geometrical parameters have been explained previously (Chapter 1).

Although difficult to achieve, plug flow is the ideal type of flow during continuous operations and can be defined as the travel of fluid through a reactor with the key features of no overtaking fluid elements in the direction of flow, perfect mixing in the radial direction and all flow elements reside for the same



length of time<sup>115</sup>. In order to attain ideal plug flow behavior, the flow must be turbulent i.e. turbulent plug flow. This is achieved by the cyclic generation and movement of vortices which results in multiple zones of turbulent mixing progressing in a plug flow manner over the length of the reactor, moving material from once baffle to another (Figure 6.3).



**Figure 6.3** Varieties of flow.

Once plug flow is achieved all elements should spend exactly the same time in the system and have a uniform process experience, producing a population of identical crystals. However, realistically, process elements can take different times to progress through the reactor. One such way of quantifying the difference in the actual and theoretical travel time and the spread of variation within species is by carrying out Residence Time Distribution experiments (RTD). These experiments are performed by introducing an inert tracer which allows its concentration to be determined as a function of time. The concentration-time profile generated from the tracer experiments are analysed, and modelled to represent overall flow behaviour and for diagnosing when there is deviation from ‘plug flow’. The experimental procedure can be conducted in a number of ways but one way in which this can be achieved is by introducing a tracer rapidly into the feed stream in as short time as possible. This technique is referred to as ‘pulse input’<sup>295</sup>. One of the main challenges with this method lies in injecting the tracer in the minimum time possible. Alternatively, the ‘imperfect pulse technique’ can be used where data is taken from two points a fixed distance apart are compared which can accommodate discrepancies due to the way the pulse is introduced. The outlet concentration is measured as a function of time generating a normalised concentration time curve.

As data is recorded from two different points, the response at the second position can be calculated by the convolution of the first position using the transfer

function (*Tr*) which can convert a given upstream response to a downstream response in the system<sup>274</sup>.

The imperfect pulse model was fitted to experimental data. A *Pipeline Pilot* protocol<sup>296</sup>, available within the electronic lab notebook, was used to automatically complete these calculations using previously reported procedures<sup>297</sup>. Concentrations were normalised using the following equation:

$$C(t) = \frac{c(t)}{\int_0^{\infty} c(t)dt} = \frac{C_{\text{pulse}}}{\frac{M}{v}} = \frac{C_i}{\sum C_i \Delta t_i} \quad \text{Equation 6.1}$$

The mass of tracer flowing through the system is equal to the area under the RTD curve (equivalent to the summation of  $C_i \Delta t_i$ ), where  $M$  is the mass of tracer (kg) and  $v$  is fluid velocity  $\text{m}^3\text{s}^{-1}$ . The model response  $C_2(t)'$  at position 2 was calculated by convolving the measured input response  $C_1(t)'$  and the model  $TR(t)$ :

$$TR(t) = \sqrt{\frac{Pe\tau}{4\pi t^3}} \exp\left\{-\frac{Pe}{4t} \left(1 - \frac{t}{\tau}\right)^2\right\} \quad \text{Equation 6.2}$$

where,  $\tau$ , is the mean residence time and  $Pe$  is the Peclet Number.

$$C_2(t)' = \int_0^t TR(t-p)C_1(p)dp. \quad \text{Equation 6.3}$$

where  $p$  is the time response downstream and  $t$  is the time response from the upstream response.

The model calculated response  $C_2(t)'$  is then compared to the experimental  $C_2(t)$  using the target function defined as:

$$\Delta C = \sum_{i=1}^N \{C_2(t_i) - C_2(t_i)'\}^2 \quad \text{Equation 6.4}$$

The  $Pe$  number is varied until the difference between the calculated and predicted responses is minimised, which is taken as the systems  $Pe$  number.

The two models reported in literature which have been applied to model meso OBRs are: Tanks in Series (TiS)<sup>121, 266, 275, 278</sup> and Axial Dispersion model<sup>274, 275, 282</sup>. The difference between these two models is that the dispersion model considers the reactor as a whole and any deviation from plug flow is due to diffusion-like process – dispersion (D)<sup>298</sup>. On the other hand, the TiS model divides the reactor into compartments ( $N$ ) and the deviation from plug flow is determined by the number of compartments. Studies for meso scale OBRs have reported that when  $N \geq 10$ , reasonable plug flow is achieved, whilst decreasing  $N$  leads to flow similar to a stirred tank reactor<sup>278</sup>. Both techniques have been considered identical<sup>299</sup> and selection of the model so far appears to be based on preference. However, more recently, the tanks-in-series mode has been found unable to represent the liquid backmixing at certain hydrodynamic conditions<sup>275</sup>. For this study the axial dispersion model with imperfect pulse method was used.

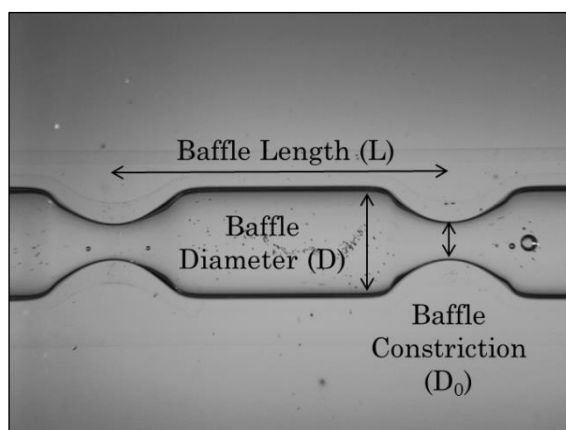
### 6.1.3 Crystallisation Control Strategies

For a given crystallisation process, appropriate design and control of the crystallisation process conditions is paramount to produce products with ideal particle properties. Two main classes of control approaches have been deployed: (i) model based and (ii) model free control techniques (direct design)<sup>300</sup>. A model predictive controller (MPC) predicts the future output and depending on the difference between the predicted and measured outputs, appropriate change in measured input can be calculated<sup>301</sup>. Plant-wide MPC of an end-to-end continuous pharmaceutical manufacturing process which included series of chemical synthesis, crystallisation and a tablet formation steps has been developed<sup>302</sup> and used for the control of a seeded cooling crystallisation of lactose<sup>303</sup>. On the other hand, model free control approaches are based on the use of PAT-based measurements and feedback control mechanisms<sup>300</sup>. Due to the advancement of PAT, measurement of solution concentration<sup>304, 305</sup>, particle count<sup>304</sup>, detection of polymorphic form<sup>306</sup> and temperature control<sup>307</sup> have made it possible for the development of advanced control strategies through model free approaches.

## 6.2 Materials and Method

### 6.2.1 Baffle Design

To assess the importance of baffle design, a range of glass straights were manufactured by Soham Scientific. In collaboration with the University of Loughborough the minimum critical amplitude required for particle suspension was compared. A number of baffle parameters (Figure 6.4) along with the shape of the baffle (smooth or sharp as shown in Figure 6.1) was investigated.



**Figure 6.4** Image showing the baffle parameters which were investigated.

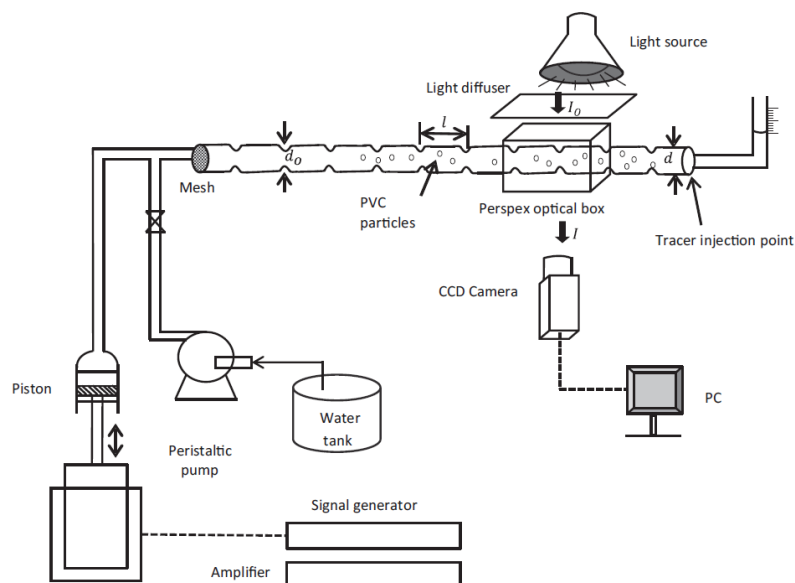
The variety of baffle designs tested can be seen in Table 6.2 and Figure 6.10. Poly-vinyl chloride (PVC) particles (with an average size of  $140\mu\text{m}$  and a density of  $1.4\text{ g/mL}$ ) were supplied from *Sigma Aldrich* (CAS number: 9002-86-2) and double distilled water was used from the laboratory. Each tube was connected horizontally to a piston-driven electromagnetic oscillator controlled by an amplifier and a signal generator. A micro mesh with a fine wire diameter made of stainless steel fibre, was fitted at this end of the tube to prevent the backflow of particles into the piston. A fixed mass of  $6.8\text{ g}$  of monodispersed PVC particles equivalent to 10% weight percentage for the slurry were homogeneously suspended in deionised water at room temperature. Once the particles were suspended in the tubes, they were allowed to completely settle after which oscillation was reapplied, and amplitude was increased until it was visually detected that all particles were fully suspended to detect the minimum critical amplitude. The minimum amplitude required to fully suspend the PVC particles was measured from the liquid level of a  $0.5\text{ mm}$  I.D. unbaffled vertical plastic

tube, connected to the other end of the tube. Thus, whilst the baffle geometry is being varied (e.g. baffle length), as the diameter remains constant (all meso tubes in this study have an internal diameter of 10 mm), changes in the liquid level can be attributed to the applied amplitude. At least three experimental repeats were carried out at values of  $f = 2, 5$  and  $7$  Hz.

**Table 6.2** Baffle parameters altered for optimum baffle design identification.

OBR reference	Constriction	Orifice open area ratio ( $\alpha$ )	Length to diameter ratio	Internal volume (mL)
A	Smooth	0.12	3	58
B	Smooth	0.25	1.5	56
C	Smooth	0.18	2.3	61
D	Smooth	0.12	1.5	48
E	Smooth	0.25	3	63
F	Sharp	0.25	1.5	69
G	Sharp	0.12	3	72
H	Sharp	0.12	1.5	54
I	Sharp	0.25	3	70
J	Sharp	0.18	2.3	65

The experimental set up for the baffle design can be seen (Figure 6.5).



**Figure 6.5** Experimental set-up used for the baffle design studies (image from reference 282).

### 6.2.2 Assessment of Oscillatory Conditions for Particle Suspension

Using the OBR reference A (Table 6.2), a mesoscale OBR reactor was built. Glass straights were manufactured by *Soham Scientific*. To determine the minimum amplitude required for particle suspension, PVC particles supplied from *Sigma Aldrich* (CAS number: 9002-86-2) were suspended in double distilled water. Particle suspension was assessed at 5, 6 and 7 Hz. Ten straights were connected to give a total reactor length of around 8 m. A fixed mass of 25 g of monodispersed PVC particles targeting 6.3 w/v % for the slurry were homogeneously suspended in deionised water at room temperature. Once the particles were homogeneously suspended in the tubes, they were allowed to completely settle after which oscillation was reapplied, and amplitude was increased until it was visually detected that all particles were fully suspended. The minimum amplitude required to fully suspend the PVC particles was measured from the liquid level of a 10 mm I.D. unbaffled vertical plastic tube, connected to the end of the reactor.

### 6.2.3 Residence Time Distribution Study of Meso scale SPC OBR

Patent Blue V sodium salt was purchased from *Sigma Aldrich* (CAS number: 20262-76-4) and double distilled water was used from the laboratory. Jackets of the glass straights which were going to be used for visualisation purposes were filled with glycerol and a perspex box also filled with glycerol was fitted around the straight. Two webcams were placed at two different positions throughout the reactor and *Yawcam* software was used to capture an image every five second.

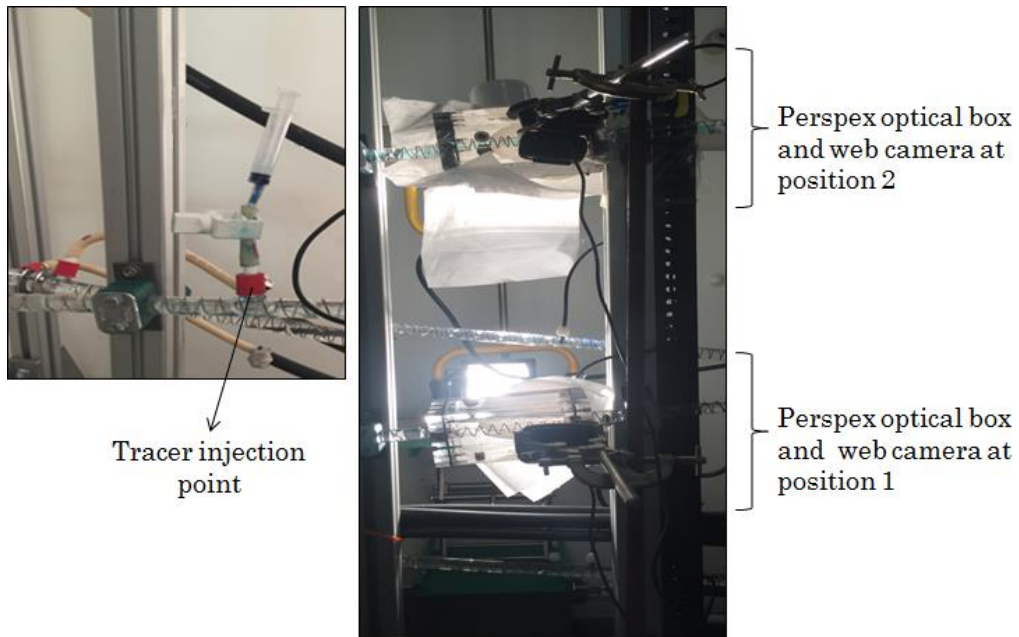
The minimum critical amplitude required for particle suspension was identified visually for each frequency with a known concentration of solids and identical oscillatory conditions were then used for liquid RTD. Furthermore, prior to beginning the experimental section of RTD determination experiments both the peristaltic pump and oscillator were calibrated to ensure the capabilities of the hardware had been pre-determined and taken into consideration for set-up and calculation.

A 0.75 mg/mL stock solution of dye was prepared and used throughout the experiments. Air bubbles were removed from the reactor and using a 5 mL syringe, 1 mL of tracer dye was injected. A web camera (Logitech 12-bit) located adjacent to the outlet of the reactor was used to measure the concentration of particles during the experiment.

A light source (230 V, 120 W Halogen, Kopp) provided illumination of the region of interest. In order to reduce optical distortions the jacket of the straight as well a rectangular Perspex optical box was filled with glycerol and fitted around the straight. A diffuser was used to spread the light and provide homogeneous illumination of the particles, minimising inaccuracy in particle concentration measurements.

Image capturing software was set to capture an image every five seconds. However, image capturing time was found to deviate between 5 to 6 seconds. The average sampling time was extracted for the second camera and this average time was used as the sampling time for the RTD calculations. Images collected were processed using *ImageJ* software version 1.51G and the mean pixel grey scale was converted to concentration of tracer (g/mL) using Beer Lambert's Law. Position and camera settings were kept identical for all experiments. Changes in background light may cause distortions in the images

captured. This was minimised by placing a black-out a curtain around the experimental set-up (Figure 6.6).

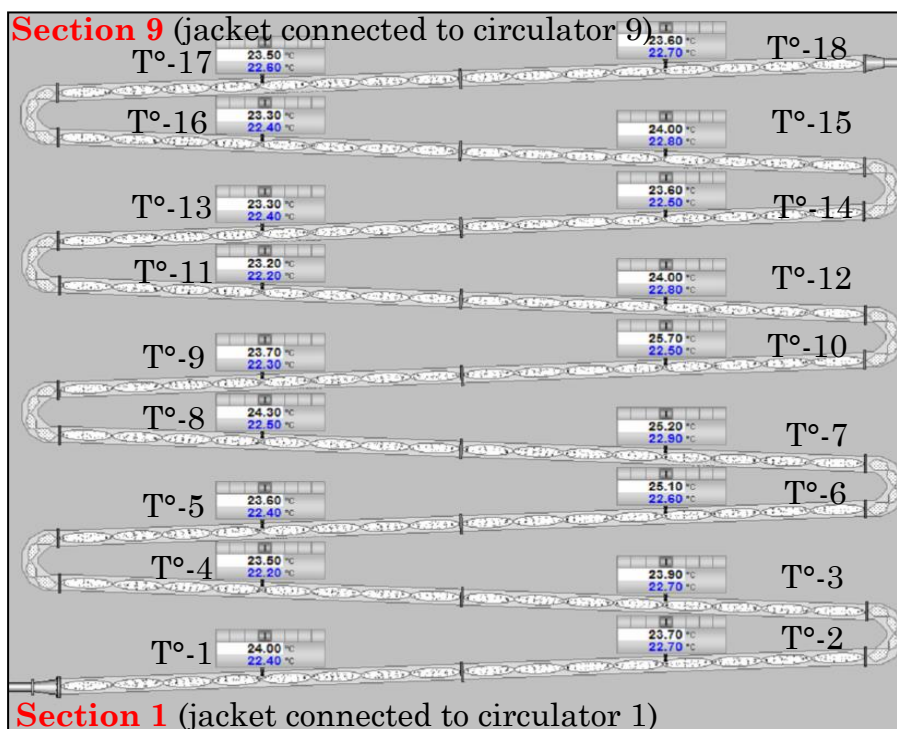


**Figure 6.6** Experimental set up for liquid RTD experiments using the imperfect pulse method.



## 6.2.4 Model Predictive Temperature Control

A PharmaMV system<sup>308</sup> was integrated with the DN10 meso scale SPC OBR to develop a model predictive temperature control as part of the initial platform development. The methodology used to develop the MPC and further details including the mathematical model and equations are detailed elsewhere<sup>303</sup>. For these studies, the reactor consisted of nine sections and each section was connected to one circulator (Figure 6.7).

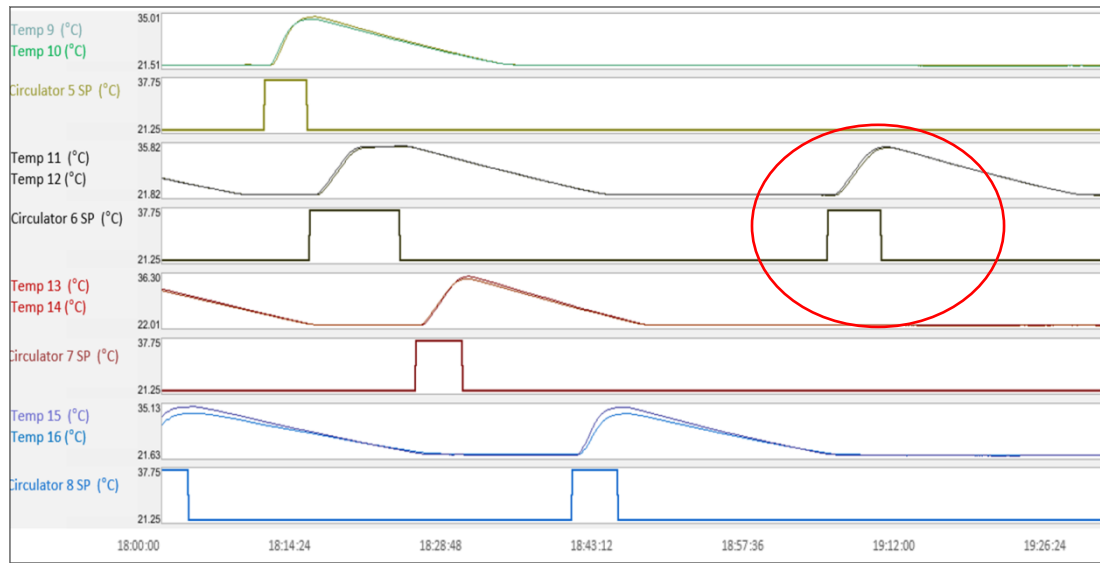


**Figure 6.7** Schematic of the reactor used to build the model predictive temperature model.

Deionised water was used both as jacket and reactor fluid. There were two temperature probes (denoted as e.g. T°1) per section to measure the reactor's temperature.

To understand the response of the circulators, the jacket fluid temperature and the reactor fluid temperature, a range of step tests were completed. Eight temperature measurements corresponding to four different sections (5th to 8th) of the reactor are shown in Figure 6.8, step tests were applied to the circulators/jacket temperature to analyse their effect on temperature. The red circle is an example of the step test and the subsequent response. Using the

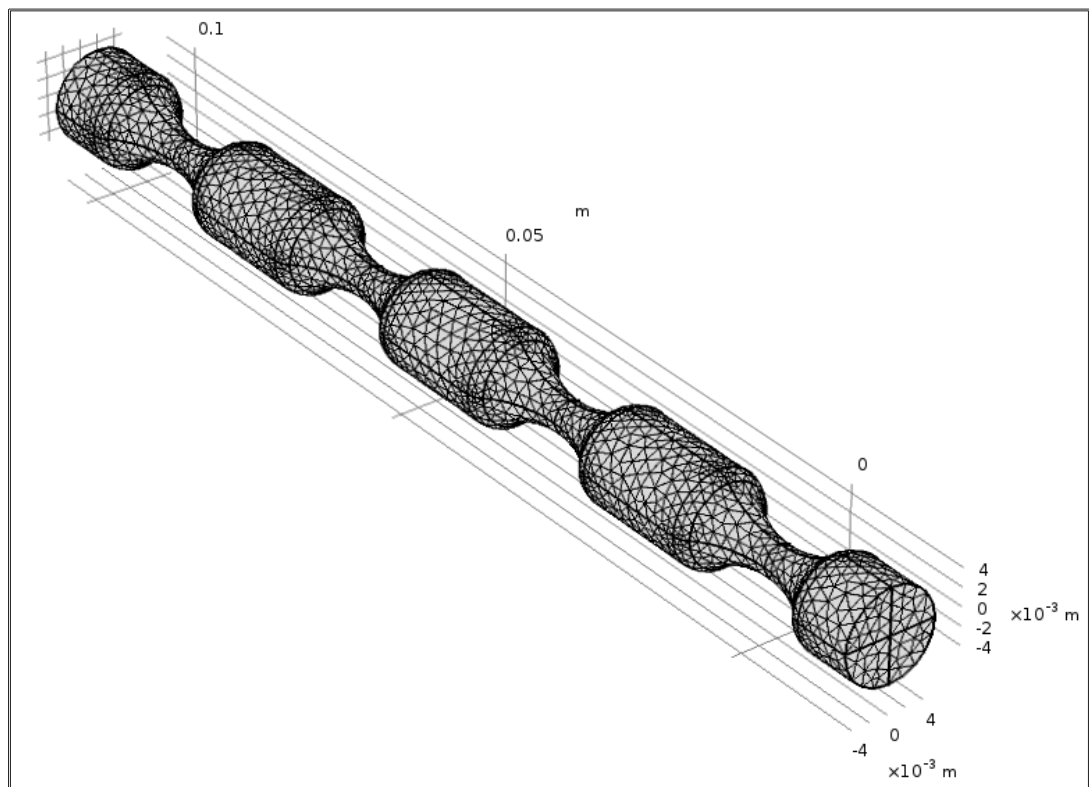
experimental data, a pseudo random binary sequence (PRBS) has been applied to each circulator to generate data for model identification which allows statistically rich data to be obtained automatically<sup>303</sup>.



**Figure 6.8** An example of the step tests carried out in sections 5 (Temperature 9 and 10), 6 (Temperature 11 and 12), 7 (Temperature 13 and 14), and 8 (Temperature 15 and 16) and their response.

### 6.2.5 CFD Analysis

CFD model was built in collaboration with a master's student and further details of the model and study can be found elsewhere<sup>309</sup>. A 3-D time dependant model was built based on geometry identified previously<sup>282</sup>. Laminar flow model has been successfully utilised to describe the fluid profile in an OBR<sup>310</sup> and the axial dispersion coefficient analysed from the Large Eddy Simulations (LES) agreed with that from the laminar simulations<sup>311</sup>. As such, whilst LES models are simulations specifically incorporating turbulent flow, since the obtained axial dispersion coefficient have been comparable to laminar flow model simulations, the latter was used for this study. All experiments were studied using a single phase laminar flow model. The fluid material chosen for the study was water and a normal mesh (167169 elements) was the most accurate mesh for the simulations as seen in Figure 6.9. Simulations were carried out for three different frequencies (5, 6 and 7 Hz) at three different flow rates (5, 10 and 20 mL/min).



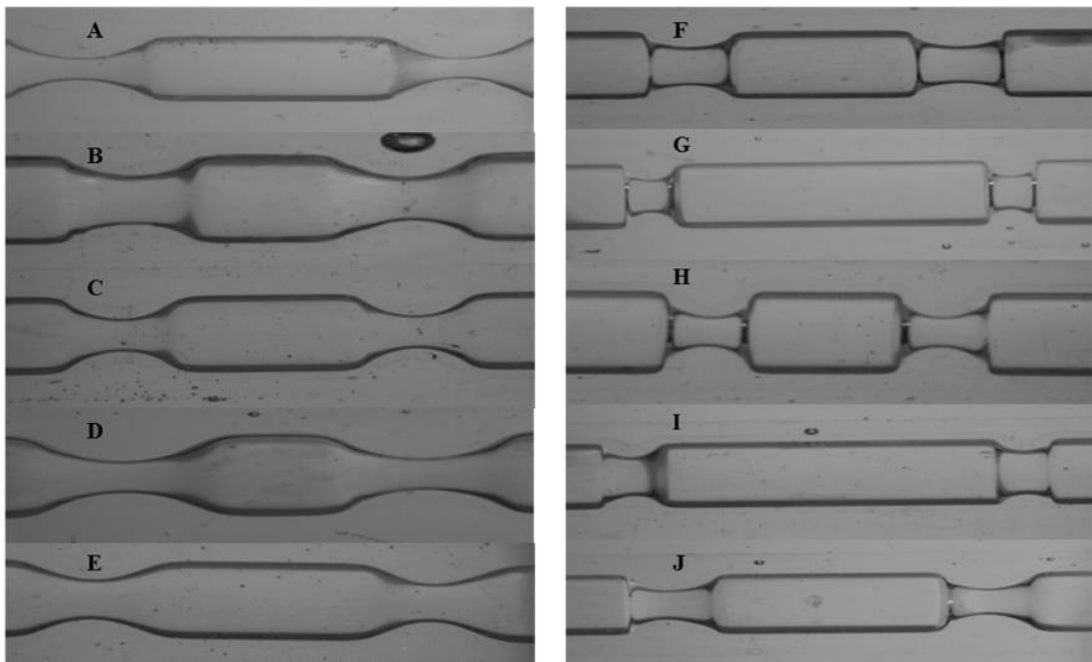
**Figure 6.9** Mesh built for smooth constricted OBR with an I.D of 10 mm.

## 6.3 Results and Discussion

### 6.3.1 Baffle Design

The effect of the straight geometry on the minimum fluid amplitude for full suspension of particles was carried out in batch mode for frequencies 2, 5 and 7 Hz as in seen Figure 6.10<sup>282</sup>. The required minimum oscillatory amplitude to fully suspend PVC particles can be considered as an indirect means of determining the extent of radial mixing generated within each baffle.

Smooth Periodic Constrictions (SPC)    Sharp Edged Periodic Constrictions (SEPC)

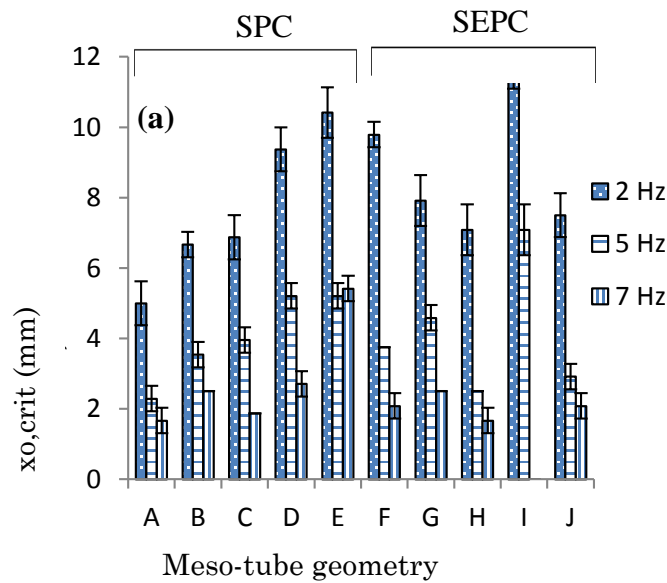


**Figure 6.10** Images of the variety of baffles investigated. (Image taken from reference 282).

The minimum critical amplitude for suspension varied according to the baffle geometry. Figure 6.11 shows the meso scale tubes with SPC geometries in general required lower critical amplitude compared to the SEPC of the same baffle length and constriction. For example, SPC tube B and SEPC tube F (both  $l = 15\text{mm}$  and  $d_0 = 5\text{ mm}$  at a fixed  $f = 2\text{ Hz}$ ), needed a minimum critical value of 6.7 mm and 9.8 mm, respectively, which represents an increase of 46 %. The need for higher amplitudes for the shape edged baffles can be related to the presence of ‘dead corners’. This is defined as stagnant regions within each baffle where the vortex strength is inadequate for full mixing resulting in small

quantities of tracer/particles becoming trapped<sup>312</sup>, which, was visually observed during the experiments.

Within the SPC geometries, minimum critical amplitude was lower for geometries with longer baffle length,  $l$ , and smaller baffle constriction,  $d_o$ . For instance, tubes A ( $l = 30$  mm,  $d_o = 3.5$  mm), B ( $l = 15$  mm,  $d_o = 5.0$  mm) and C ( $l = 22.5$  mm,  $d_o = 4.2$  mm) had the lowest amplitude requirement<sup>282</sup>. Overall, Tube A required the lowest amplitude for full PVC particle suspension at these conditions which is a linear scale up of a previously studied meso scale SPC OBR<sup>265</sup>.



**Figure 6.11** Suspension studies showing minimum amplitude ( $x_{o,crit}$ ) for full suspension of particles.

This significant variance in particle suspension is attributed to the differences in power input/dissipation and degree of radial mixing. The efficiency of particle suspension by  $f$  and  $x_o$  is linked to the settling velocity of the particles. The fluid velocity must be higher than the particles terminal velocity to achieve suspension, to allow the particles to be elevated up and over the baffled tube wall. The dominance of the radial velocity during the oscillatory flow minimises the particle settling velocity; the periodic upward motion increases the fluid drag force and helps to suspend the particles in liquids.

The settling velocity of the particles ( $u_p$ ) can be estimated using Stokes Law:

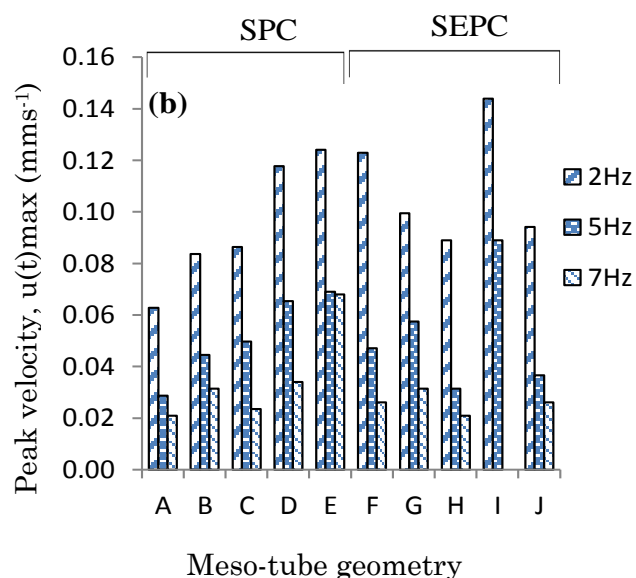
$$u_p = \sqrt{\frac{4}{3} \frac{1}{C_D} g d_p \left( \frac{\rho_p - \rho_f}{\rho_p} \right)} \quad \text{Equation 6.1}$$

Where  $\rho_p$  is the density of the particles,  $\rho_f$  is the density of water,  $d_p$  is the diameter of the particles and  $C_D$  is the drag coefficient.

The particle settling velocity distribution was calculated using Equation 6.6. The mean  $u_p$  was calculated as  $0.048 \text{ ms}^{-1}$  (the average of all the calculated  $u_p$  with the given particle size range). The peak oscillatory axial velocity ( $u(t)_{max} = 2\pi f x_0$ ) required for complete suspension of the particles should be significantly higher than  $u_p$ , to allow a high energetic efficiency of particle suspension to be achieved within the reactor (i.e where  $u(t)_{max}$  is much greater  $u_p$ ). The peak oscillatory axial velocity ( $u(t)_{max}$ ), is dependent on frequency ( $f$ ) and amplitude ( $x_0$ ) and thus is a way of determining the energetic efficiency of the particular baffle geometry with respect to particle suspension, where lower  $u(t)_{max}$  is associated with more energetically favourable conditions<sup>265</sup>.

$$u(t)_{max} = 2\pi f x_0 \quad \text{Equation 6.2}$$

For all ten meso baffle designs tested, the value of  $u(t)_{max}$  calculated ranged from  $0.021 - 0.124 \text{ m s}^{-1}$ , with tube *I* (SEPC,  $l/d = 3$ ) and *E* (SPC,  $l/d = 3$ ) having the largest values of  $0.089$  and  $0.069 \text{ ms}^{-1}$ , respectively (at  $5 \text{ Hz}$ ). The  $u(t)_{max}$  for complete suspension of particle decreases with the increase of frequency which would indicate the generation of sufficient radial mixing for suspension of particles. Whilst this has been previously observed for a similar SPC meso scale OBR<sup>265</sup> it also agrees with general operational rules for OBR's of higher frequency and lower amplitude<sup>115</sup>.



**Figure 6.12** Oscillation peak velocity,  $u(t)_{max}$  required for full suspension of particles.

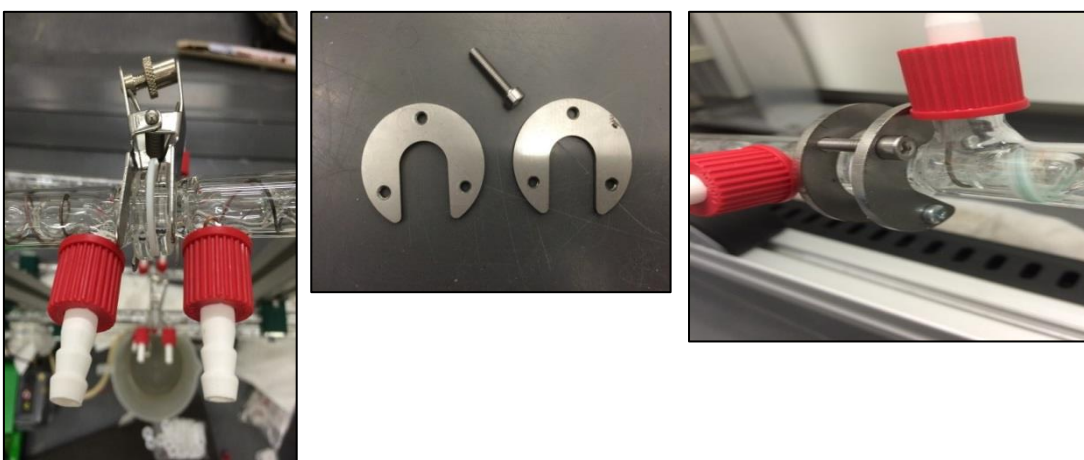
In conclusion, although the suspension of particles can be improved by changing the oscillatory conditions, the SPC geometries proved to suspend particles more efficiently than the SEPC tubes with the same dimensions under equivalent operating conditions (Figure 6.12). SPC tube A ( $l = 30$  mm,  $d_o = 3.5$  mm) appeared as the most suitable for PVC particles' suspension as it needed the lowest amplitude regardless of frequency and oscillatory peak axial velocities. For the ten meso scale straights, continuous liquid solid flow was modelled using plug flow with axial dispersion model. Both SPC and SEPC meso-tubes were capable of delivering a near plug flow behaviour and the values of axial dispersion coefficient were estimated for the solids to be in the range of  $1.0 - 2.2 \times 10^{-4} \text{ m}^2 \text{ s}^{-1}$ . Further details of this investigation can be found elsewhere<sup>282</sup>.

### 6.3.2 Development of Reactor

A meso scale SPC OBR continuous platform based on the geometry  $l = 30$  mm,  $d_o = 3.5$  mm (Tube A) was constructed and its suitability for crystallisation processes was assessed. Several challenges had to be overcome to establish an operational platform.

### 6.3.2.1 Construction: Connectors

Two types of connections to go between glass straights were tested. Below is an image of the connection. The first option was a metal clip which would go over the glass straights and can be tightened (Figure 6.13). The length of the screw part of the clip limited the degree of tightening available. This clip could not be tightened enough to provide the necessary alignment of the glass straights. An alternative was sought for which would allow more flexibility. Two metal clips which go over the glass straights and screw in three different parts was designed and tested. This configuration provided the necessary flexibility and degree of tightening which allowed the construction of a leak free reactor. Figure 6.13 shows the way in which the clips directly rested on the glass straights. Although this was a more successful method, as the metal clips were directly resting on the glass, it was very easy for the glass to crack as a result of over tightening which was overcome by small manoeuvres of tightening. This prototype equipment could be further enhanced for ease of use and flexible deployment and reconfiguration by improving the robustness and performance of the connecting straights.

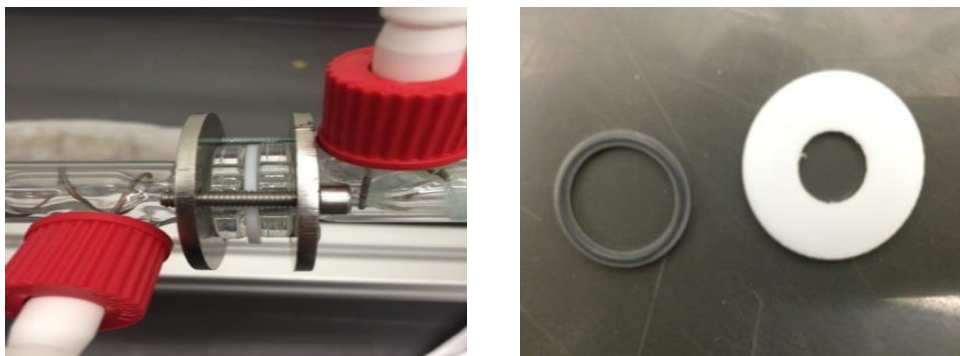


**Figure 6.13** Metal clip type one (left), metal clips type two (centre) and metal clip resting on glass (right).



### 6.3.2.2 Construction: Washers

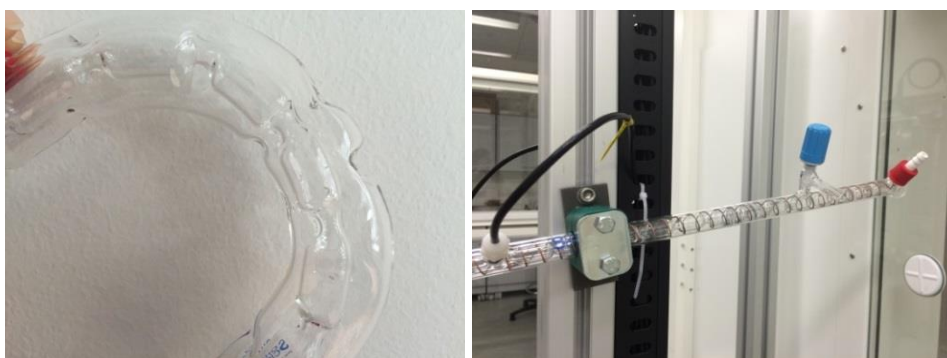
Polytetrafluoroethylene (PTFE) solid gaskets did not compensate for any irregularities which may be present on the surface of the glass which may differ from straight to straight as all were handmade (Figure 6.14). The black washers (FEP - Viton encapsulated) were more flexible and were able to compensate for any irregularities. This alternative proved to be more successful and was taken forward for the construction of the reactor.



**Figure 6.14** FEP flexible washer (left) and PTFE solid washer (right).

### 6.3.2.3 Customisation and Advanced Control Strategies

As this was a custom built crystalliser some additional features were also built-in (Figure 6.15). These included jacketed glass bends, sample removal ports and ports for PAT.



**Figure 6.15** Additional features of the crystalliser with jacketed bends (left) and sample port (right).

In an effort to reduce bubble retention the COBR was built with an upward angle of 7°. This was based on the findings that the optimum angle for a novel micro-OBR was 10° allowing all bubbles to be removed from the system in less than one minute under certain flow conditions<sup>263, 265</sup>.

A schematic of the final set up of the reactor is shown Figure 6.16. This comprised of 10 straights, 4 bends, 5 heater chillers (2 straights and bend per heater chiller), one oscillator, the required number of peristaltic pumps and feed/seed tanks. The set up was modular and can be altered in terms of total volume/sections depending on the crystallisation system under investigation.

This reactor was integrated with Perceptive Engineering Pharma MV and Siemens PCS 7 monitoring and control systems. Siemens SiPAT is a modular software solution that allows PAT-based data to be collected and integrated to enable different PAT enabled monitoring and control strategies. With the integrated PAT platform, crystallisation processes can be monitored, controlled and optimised by measuring and calculating the CQA of end products in real time. This continuous monitoring of product quality can prevent deviations from specifications<sup>313</sup>.

Perceptive Engineering provides model based Advanced Process Control (APC). PharmaMV is designed to support development and deployment of multivariable technologies for monitoring and control within the system. The PharmaMV platform provides modular tools to design, deploy and maintain advanced applications for batch and continuous processes. Perceptive's PharmaMV complements SiPAT with real-time, predictive control capabilities<sup>313</sup>.

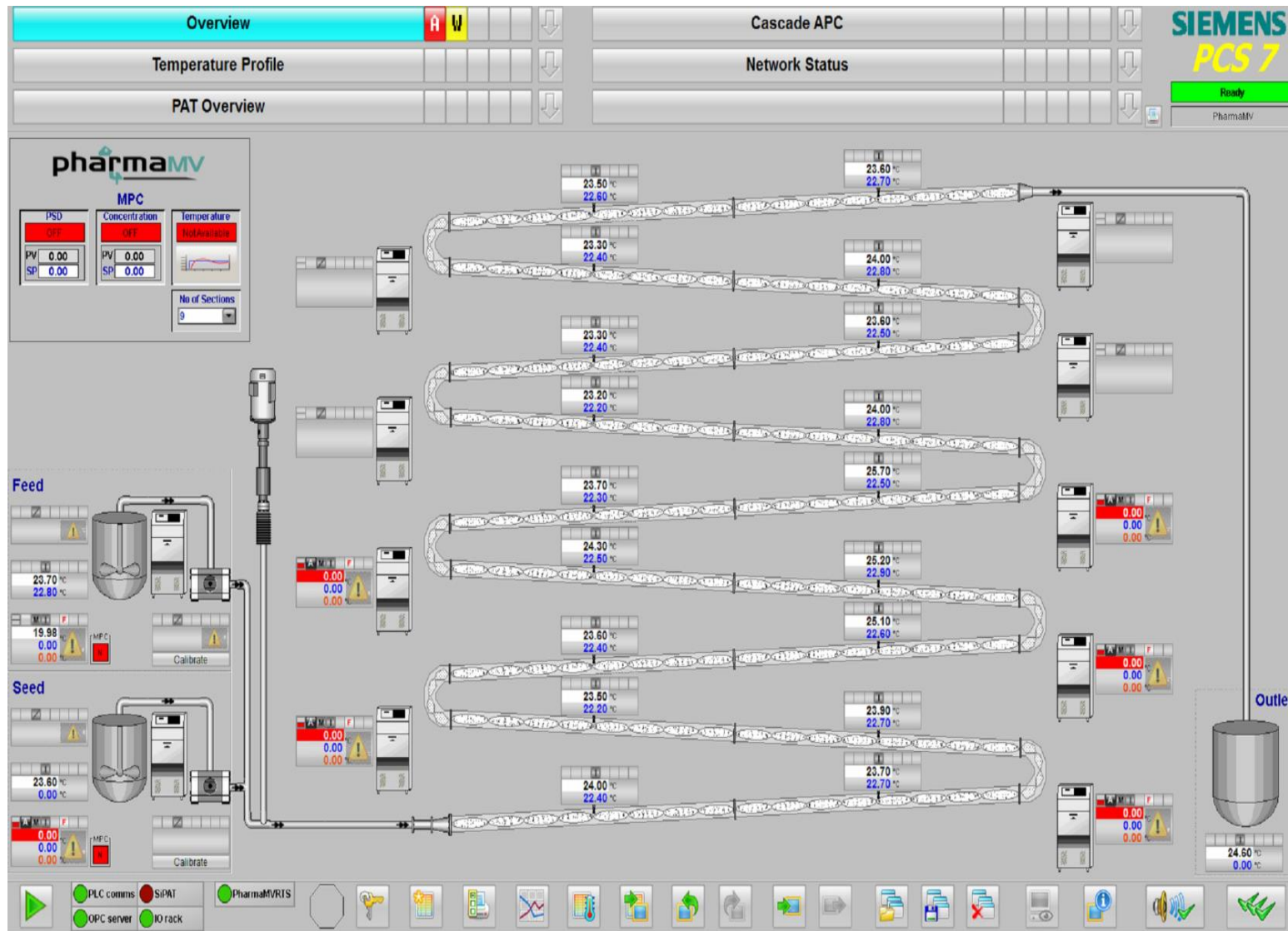


Figure 6.16 Interface allowing the monitor and control of the platform.

Control over a continuous cooling crystallisation process has been demonstrated for two COBR based processes with I.D of 69 mm and 15 mm for lactose<sup>303</sup>. Control strategies were developed for reactor temperature which allowed the solute concentration and particle size to be controlled. PAT allowed real-time monitoring and control of the crystal quality and as the need for manual sampling is eliminated (which can introduce artefacts in the solid sample e.g. due to temperature variations) PAT helps in relating OBR process conditions to the crystallisation process and consequently to the resultant product attributes. Spectral data collected from FTIR was used to build a concentration calibration model which predicted the concentration of API in the solution. The CLD was obtained from FBRM. The seed and feed flows were manipulated to remain within the desired concentration range and to achieve the target CSD.

The novel DN10 crystallisation platform integrates SiPAT, PCS7 and PharmaMV in one complete module. FBRM and UV as part of PAT technologies have been integrated which would allow crystal size and concentration to be monitored and controlled, if desired.

#### 6.3.2.4 Internal Diameter

The internal diameter of this reactor was specified as 10 mm, however due to the smooth periodic constrictions a large amount of space is 'lost', meaning only the centre of the baffle is 10 mm in diameter. In order to compensate for this the reactor was filled with water and the full length of the reactor was determined. An average diameter over 10 straights was calculated assuming it to be a straight non-baffled cylinder using Equation 6.8, herein referred to as *hydraulic diameter*.

$$V = \pi r^2 h$$

**Equation 6.3**

$$\text{Volume (V)} = 0.395 \text{ L}$$

$$\text{Length (h)} = 7.98 \text{ m}$$

$$\text{Radius (r)} = 3.969 \text{ mm} = \text{diameter (d)} = 7.939 \text{ mm}$$

From these calculations, the diameter calculated indicates a reduction of around 21 %. Also, in the baffle design studies a difference in the target and measured diameter was found<sup>282</sup>. The opposite was found for an OBR with sharp edged baffles with an internal diameter of 15 mm where it was found to be closer to 16 mm<sup>108</sup>. Therefore, not only would the hydraulic diameter compensate for the reduction of the available surface but would also any account for differences in the diameter due to the straights being individually manufactured.

### 6.3.3 Assessment of Oscillatory Conditions for Particle Suspension

The value of  $f$  had an impact on the particle suspension, since the particles were suspended at a reduced  $x_0$  when  $f$  was increased from 5 to 7 Hz (Table 6.3). Increasing  $f$  reduces the particle settling velocity, resulting in reduced  $x_0$  required for suspension. The  $u(t)_{\max}$  values for 5 and 7 Hz are in agreement with previously calculated values<sup>282</sup>. An explanation of the effect of  $f$  and  $x_0$  on suspension of particles has been explained in *Section 6.3.1*.

**Table 6.3** Oscillatory conditions tested for particle suspension.

	$u(t)_{\max}$ (ms <sup>-1</sup> )		
$f$ (Hz)	5	6	7
$x_0$ (mm)	5.5	7	4.5
	0.035	0.044	0.028

### 6.3.4 RTD

RTD analysis is a quantitative method that is typically used to understand and investigate mixing and flow. Understanding RTDs for crystallisation platforms has been used in the initial steps to characterise platform performance, optimisation and scale up of manufacturing processes. The RTD of a meso scale SPC COBR with a total length of around 8 m has been performed to develop our understanding of the mixing and flow performance of this specific COBR platform under a range of process conditions which are a practically useful range of crystallisation conditions (Table 6.4).

**Table 6.4** Parameters investigated for the liquid RTD study.

Frequency (Hz) → Flow Rate (mL/min) ↓	5	6	7
5	Residence time 80 minutes		
10	Residence time 40 minutes		
20	Residence time 20 minutes		

The change in concentration of a dye tracer solution as a function of time was modelled using the axial dispersion with a plug flow model<sup>298</sup>. Table 6.5 shows the input variables which applied to all experiments. The results are interpreted as vessel dispersion number (the reciprocal of  $Pe$  number, also referred to as dimensionless axial dispersion number in literature) to understand the effect of flow conditions on the overall RTD performance<sup>274</sup> (Equation 6.5).

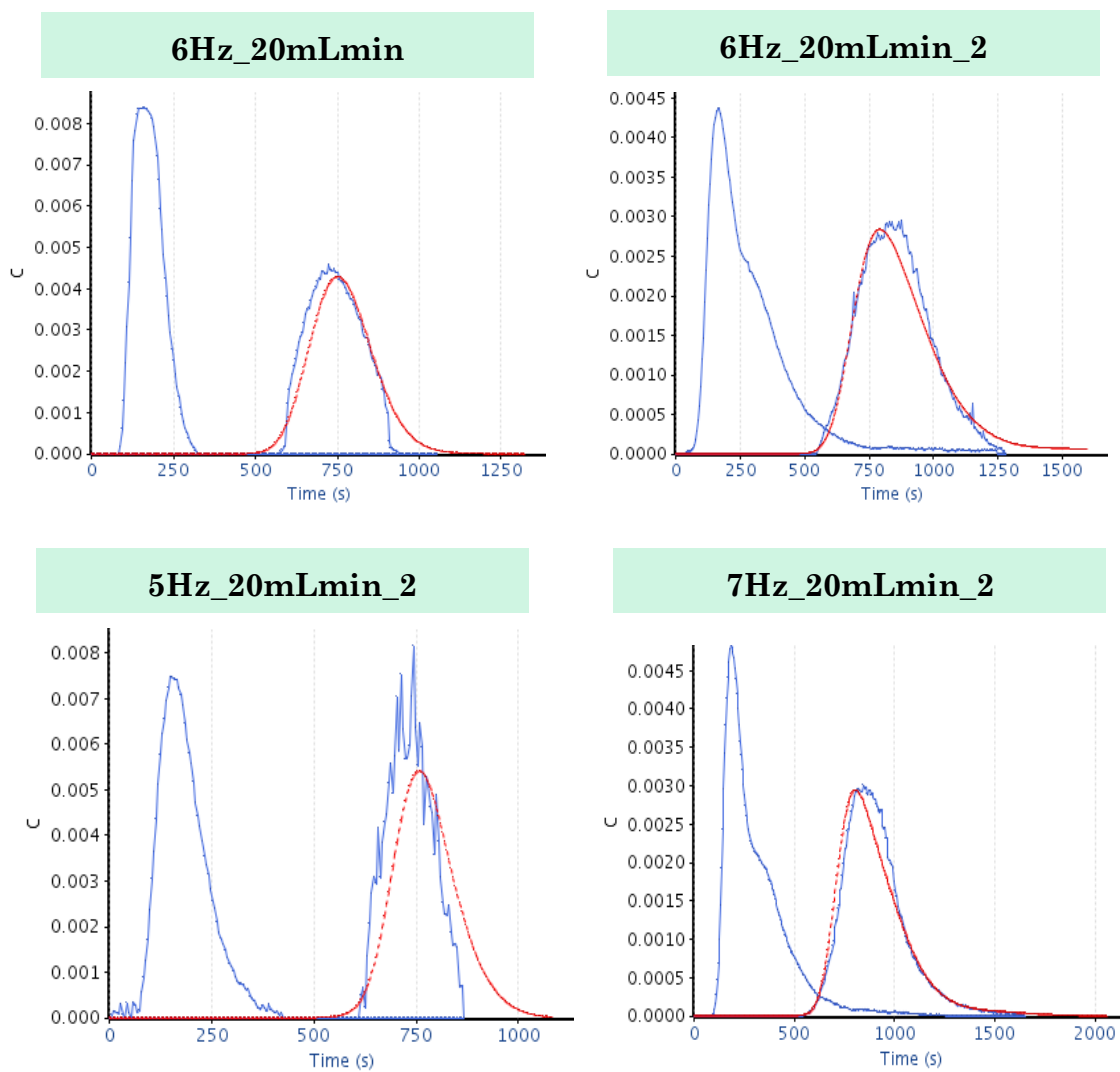
$$\text{Vessel Dispersion Number} = \frac{D}{uL} \quad \text{Equation 6.5}$$

where  $D$  is axial dispersion ( $\text{m}^2\text{s}^{-1}$ ),  $u$  is velocity of fluid ( $\text{m/s}$ ) and  $L$  is the distance between two measurement points ( $\text{m}$ ).

**Table 6.5** Constant for all calculations.

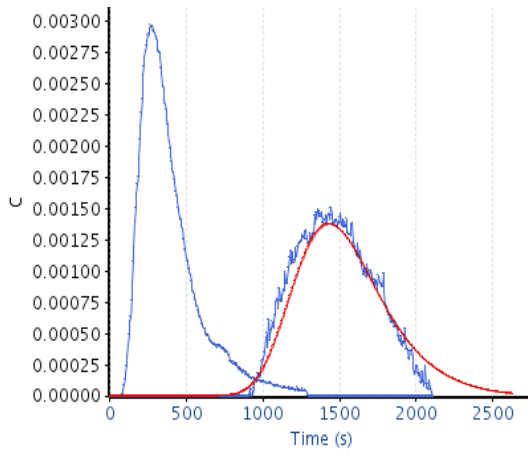
Input Variables	
Variable	Input value
Distance to camera #1 (m)	0.79
Distance to camera #2 (m)	4.01
Density of solvent ( $\text{kg/m}^3$ )	1000
Hydraulic Diameter (m)	7.94e-003

The measured tracer profile was used to estimate the vessel dispersion number at each set of conditions of flow rate and frequency. Experimental findings for all oscillatory conditions as can be seen in Figure 6.17 and Table 6.6.

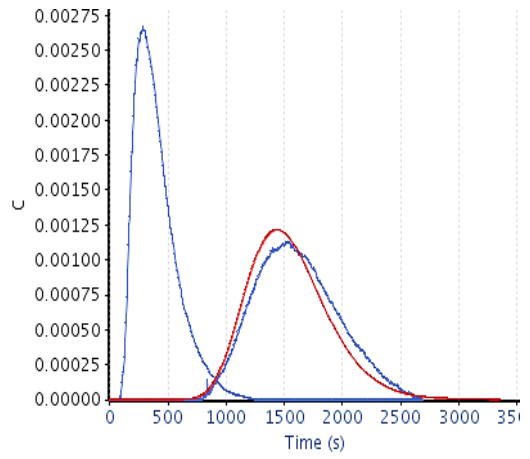


**Figure 6.17** Experimental and imperfect pulse model responses. Raw data (blue) with the model response overlaid (dotted red). Graph labelling indicates experimental frequency\_experimental flow rate\_experiment repetition number.

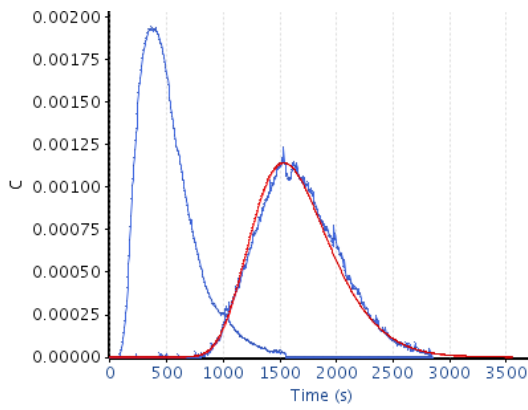
**5Hz\_10mLmin**



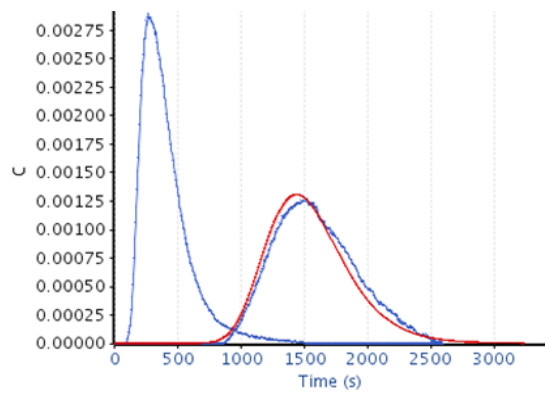
**5Hz\_10mLmin\_2**



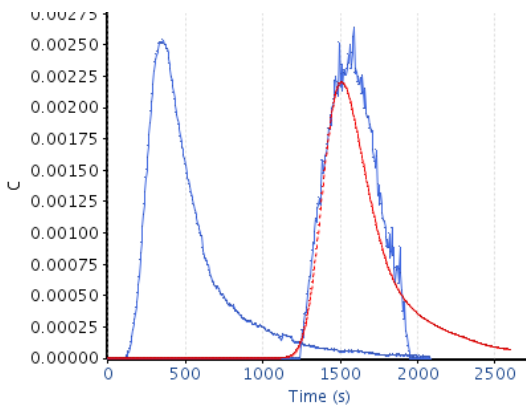
**6Hz\_10mLmin**



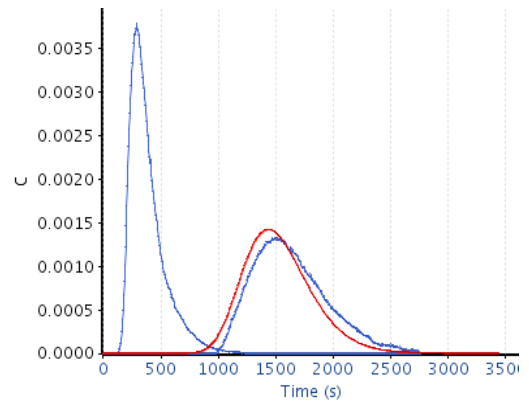
**6Hz\_10mLmin\_2**



**7Hz\_10mLmin**



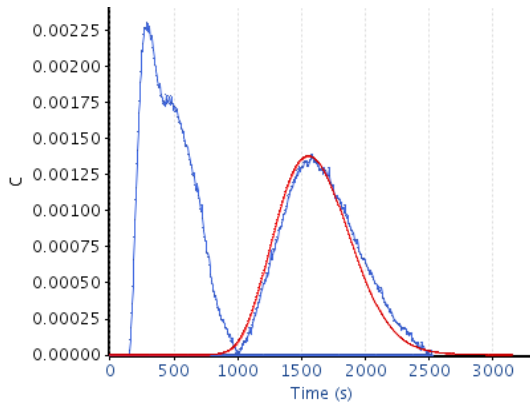
**7Hz\_10mLmin\_2**



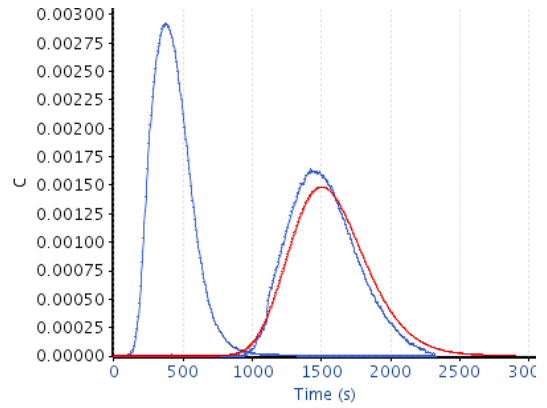
continuation of Figure 6.17



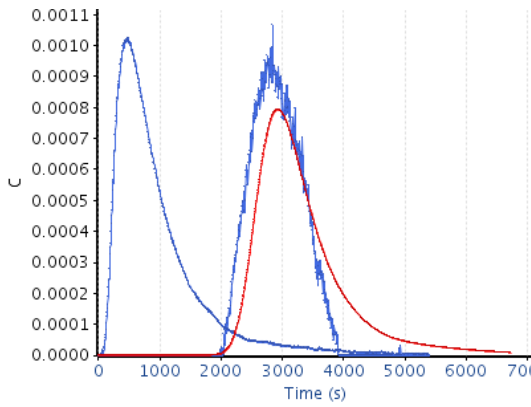
**7Hz\_10mLmin\_3**



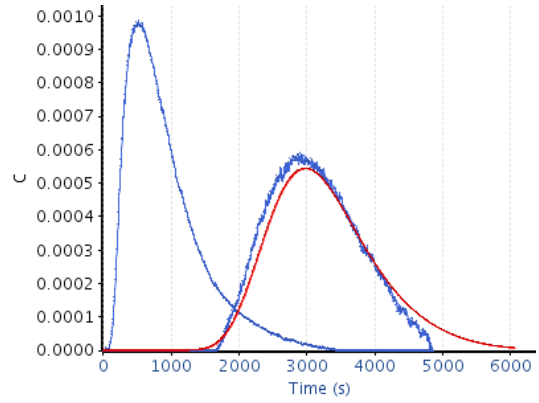
**7Hz\_10mLmin\_4**



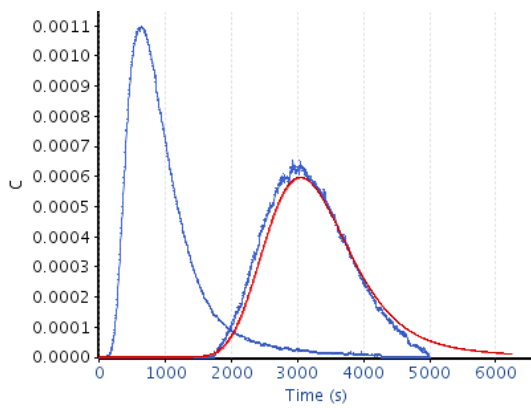
**5Hz\_5mLmin\_2**



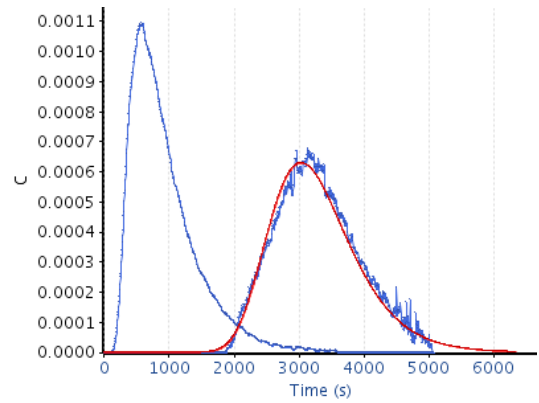
**5Hz\_5mLmin\_3**



**6Hz\_5mLmin**

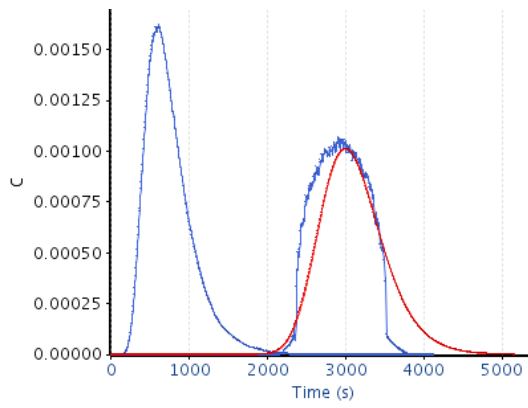


**6Hz\_5mLmin\_3**

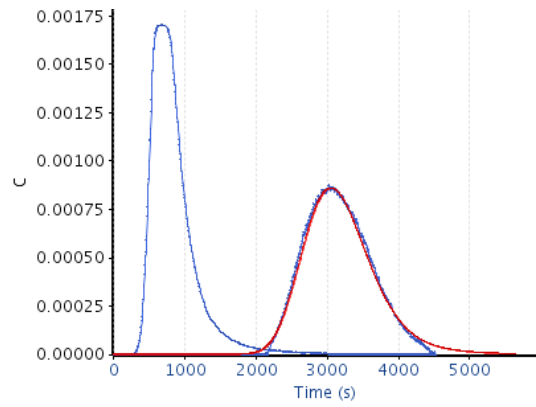


continuation of Figure 6.17

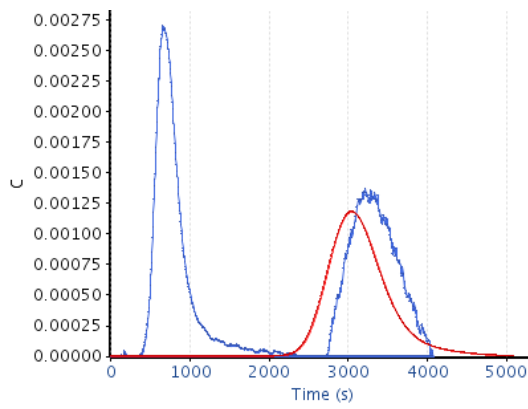
**7Hz\_5mLmin\_1**



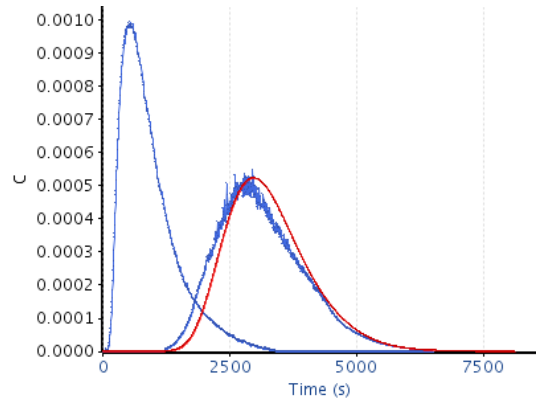
**7Hz\_5mLmin\_2**



**7Hz\_5mLmin\_3**



**5Hz\_5mLmin\_1**

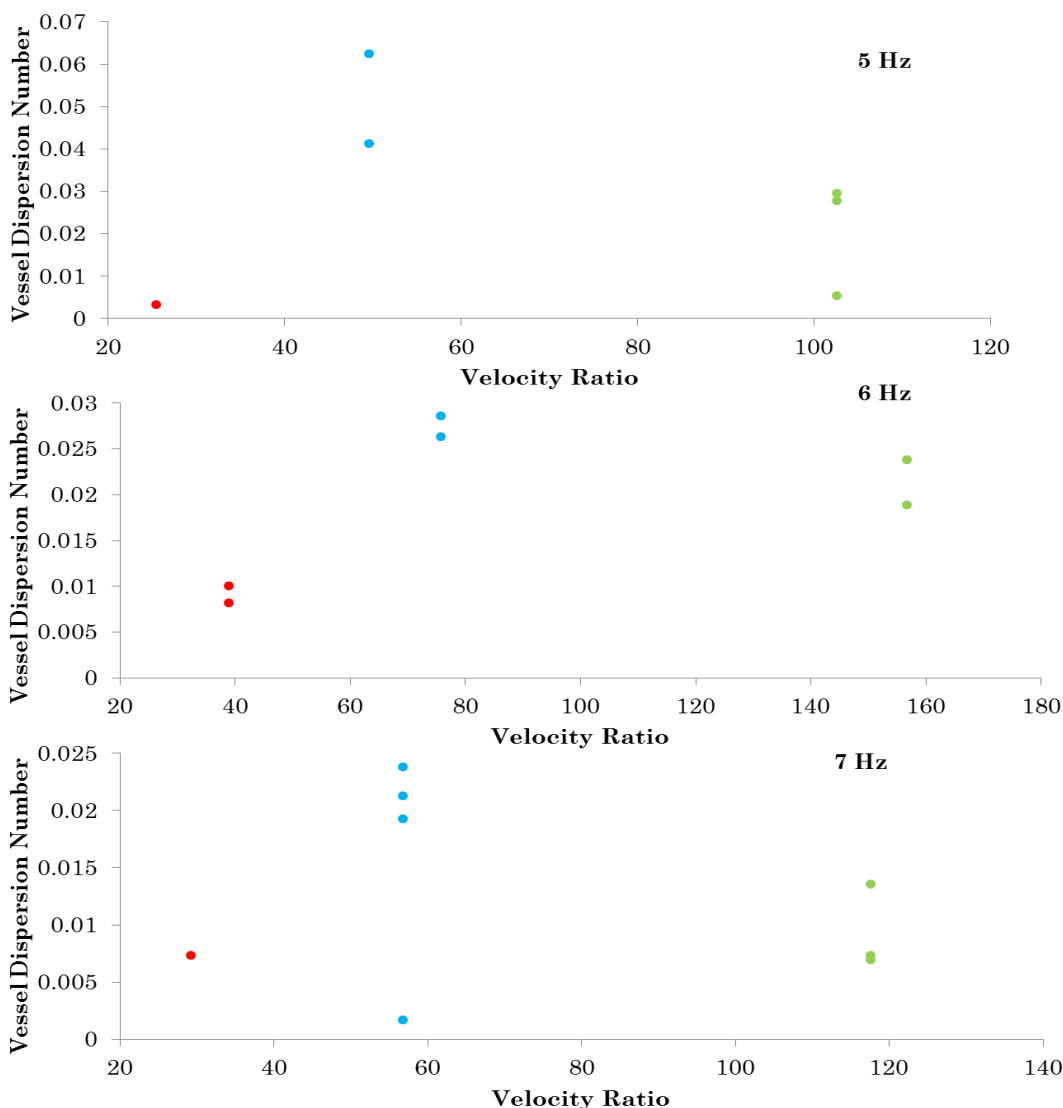


continuation of Figure 6.17

**Table 6.6** Summary of the oscillatory conditions and respective axial dispersion number.

<b>Experiment</b>	<b>f (Hz)</b>	<b>x<sub>o</sub> (mm, p-p)</b>	<b>Flow Rate (mL)</b>	<b>Peclet Number</b>	<b>Vessel Dispersion Number (-)</b>
5Hz_20mlmin_2	5	11	20.1	313	0.0032
6Hz_20mlmin_1	6	14	20.1	100	0.01
6Hz_20mlmin_2	6	14	20.1	123	0.0081
7Hz_20mlmin_2	7	9	20.1	137	0.0073
5Hz_10mlmin_1	5	11	10.34	47	0.0412
5Hz_10mlmin_2	5	11	10.34	31	0.0624
6Hz_10mlmin_1	6	14	10.34	35	0.0286
6Hz_10mlmin_2	6	14	10.34	38	0.0263
7Hz_10mlmin_1	7	9	10.34	592	0.0017
7Hz_10mlmin_2	7	9	10.34	42	0.0238
7Hz_10mlmin_4	7	9	10.34	47	0.0213
7Hz_10mlmin_3	7	9	10.34	52	0.0192
5Hz_5mlmin_2	5	11	5.051	192	0.0052
5Hz_5mlmin_3	5	11	5.051	36	0.0278
6Hz_5mlmin_1	6	14	5.051	42	0.0238
6Hz_5mlmin_3	6	14	5.051	53	0.0189
7Hz_5mlmin_2	7	9	5.051	74	0.0135
7Hz_5mlmin_1	7	9	5.051	137	0.0073
7Hz_5mlmin_3	7	9	5.051	145	0.0069
5Hz_5mlmin_1	5	11	5.051	34	0.0294

To ensure efficient mixing, the velocity ratio, which is the ratio of oscillatory to net flow velocities, must be at least greater than 1<sup>113</sup>. Here, velocity ratio's between 25 and 156 were investigated. When vessel dispersion number was plotted against the velocity ratio, Figure 6.18, the flow rate of 10 mL/min (ReN = 27.6) was determined as having the highest vessel dispersion number under all three frequencies. This difference could be as a result of the distribution of the balance between the mixing generated by the eddies and the advection by the axial flow through the baffle orifice; an observation reported for 15 mm I.D sharp edged COBR<sup>314</sup>.



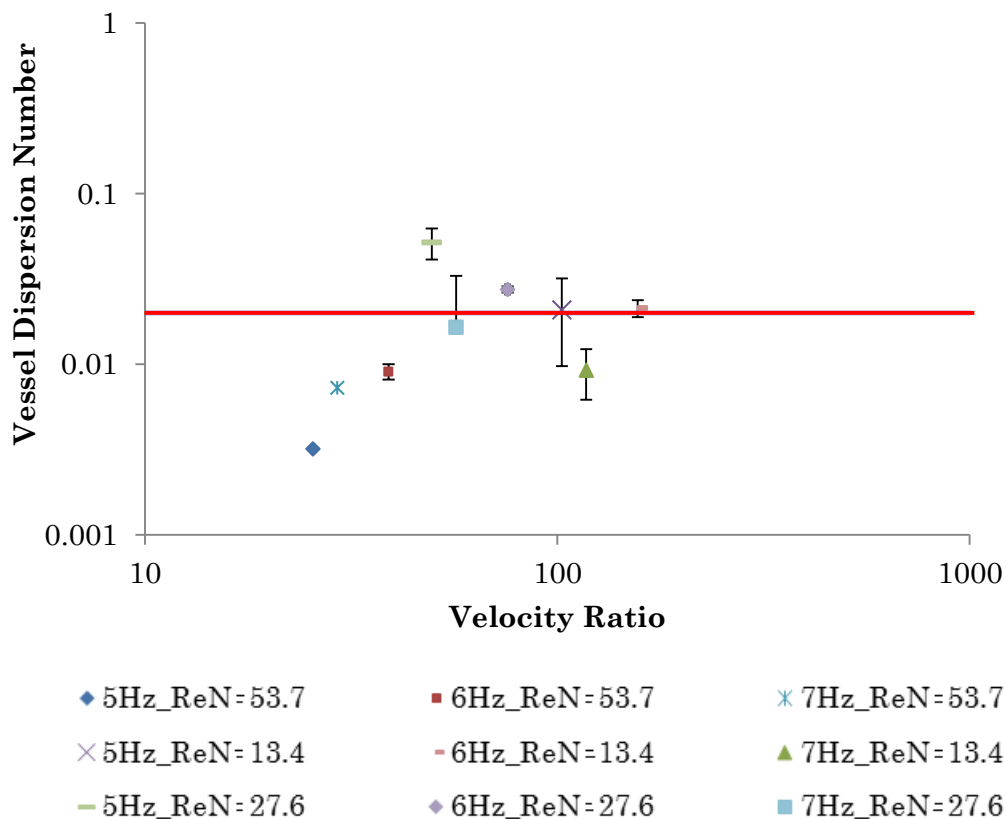
**Figure 6.18** Raw vessel dispersion number as a function of velocity ratio for all three frequencies at each flow rate (red: 20 mL/min, blue: 10 mL/min and green: 5 mL/min).

Furthermore, vessel dispersion value for 6 Hz and 20 mL/min and 6 Hz and 5 mL/min was generally than values reported for 5 Hz and 7 Hz. This may be because a higher amplitude was needed for complete particle suspension (Table 6.3). An increase in the amplitude of operation can lead to a larger dispersion due to the increased turbulence, changing the balance between the radial and the axial mixing<sup>314</sup>. Although not investigated here an increase in  $f$  (at constant  $x_0$ ) would be expected to lead to an increase in mixing intensity inside each cavity and thus not necessarily to an increase in the axial dispersion<sup>285</sup>. With the exception of the dispersion values for 10 mL/min, the remaining results are in good agreement with previous vessel dispersion values of 0.04<sup>282</sup>.

So, results are in good agreement highlighting the platform's performance in accordance with theory. A number of exceptions were seen with differences in the experimental and model responses (Figure 6.17). For example, the results for experimental conditions *7Hz\_5mLmin\_3*, show the model response to be not completely overlaid with the experimental response. This was most likely due to the use of the average sampling time for the mean residence time calculations. This observation is more pronounced for the experiments carried out at 5 mL/min where the sampling time deviation was more pronounced. Taking *5Hz\_5mLmin\_2* as an example the model response has a tail whereas the experimental response does not. This was attributed to two things. Firstly, the model response is based on the experimental C-curve from the first measurement point and so if there was a tail in the experimental data this would be reflected in the model response. Secondly, the intensity of the dye may be too low towards the end of the experiment, resulting in the contrast being too low for the software to be able to capture any differences.

In Figure 6.19 where the red line represents the upper limit of deviation for plug flow<sup>298</sup>, the lowest vessel dispersion number were achieved with the highest flow rate of 20 mL/min for all frequencies investigated. These conditions represent the closest to plug flow. However, the largest deviation from plug flow were observed for conditions of 5 Hz and 6 Hz at 10 mL/min, and at 5 Hz and 6 Hz at 5 mL/min. The greater interaction of the baffles and promotion of turbulence and radial mixing as a result of the higher flow rates may explain these observations. However, at the lower frequencies and lowest flowrate (5 mL/min),

the wider spread of the tracer and hence, enhanced dispersion in the axial direction, may be attributed to the hold-up of the tracer as a result of less efficient mixing. These results are in keeping with the previous observation where high flow rates provide the best ‘close to plug flow’ conditions<sup>314</sup>.

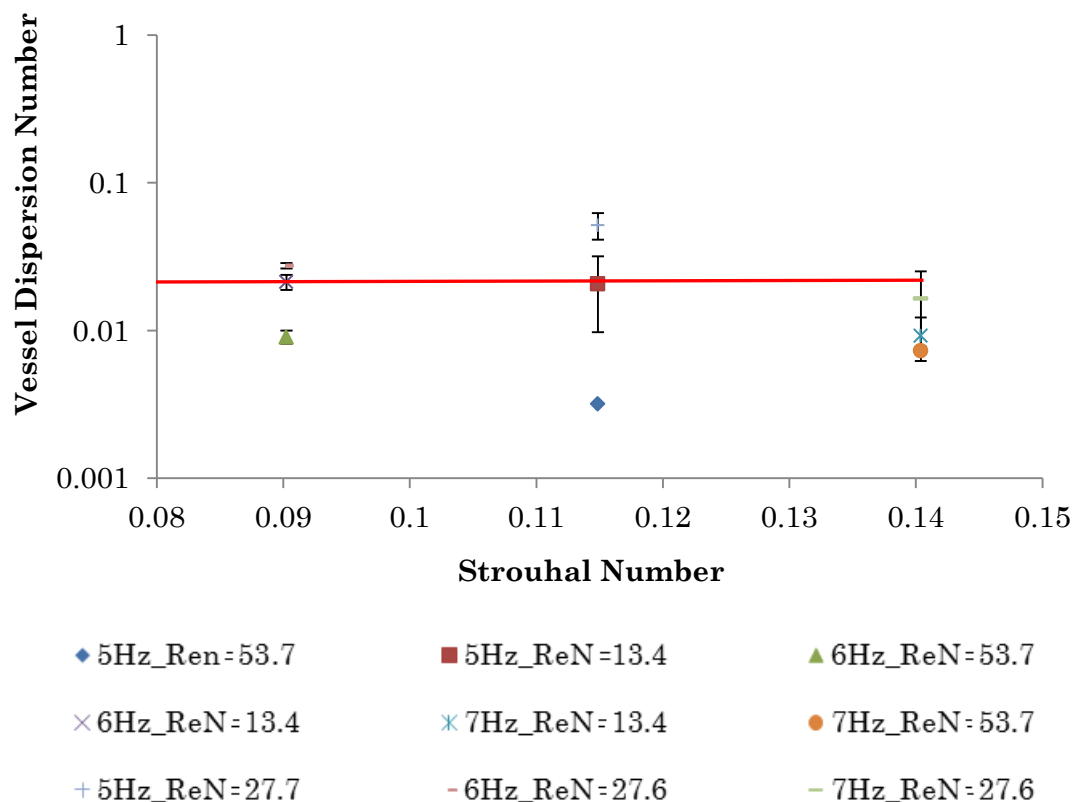


**Figure 6.19** Vessel dispersion number plotted as a function of Velocity Ratio for 5, 6 and 7 Hz for high and low flow rates (Log-log scale). Red line represents upper limit of plug flow. Error bars represent standard deviation.

Within the conditions examined, velocity ratios ranged from 25 to 117 have provided near plug flow conditions. Studies characterising different meso scale OBR's have identified the highest degree of plug flow to be achieved at velocity ratios of 4–10<sup>266</sup>, 39–40<sup>121</sup> and 25–90<sup>278</sup>. Although the variation amongst meso scale OBR which may be due to different baffle designs, the variation between conventional OBR's and meso scale OBR has been attributed to diffusion being more prominent in meso scale OBR's, which may explain why in general higher values of velocity ratio have been needed to achieve near plug flow<sup>264</sup>. Therefore, although higher velocity ratio values are required in the smaller geometries to

provide near plug flow conditions, these are achievable confirming the potential suitability of the platform for continuous processing as a PFR.

The relationship between Strouhal number (St) on vessel dispersion was also examined (Figure 6.20). St value describes the eddy propagation and is inversely proportional to the oscillation amplitude. As a general trend, as St is increased, vessel dispersion number decreases. The St numbers investigated were between 0.09 and 0.14 and the lowest vessel dispersion number was obtained for St 0.11. For conventional OBR's St values below 0.2 indicate insufficient eddy generation to generate effective mixing within the baffle region. However, results obtained here are in keeping with the findings relating to a meso SPC OBR with an I.D of 5 mm which provided near plug flow conditions within a St value of 0.08 and 0.4<sup>274</sup>. For other meso scale structures, St between 0.2 and 0.13, has been found to improve mixing significantly<sup>121</sup>.



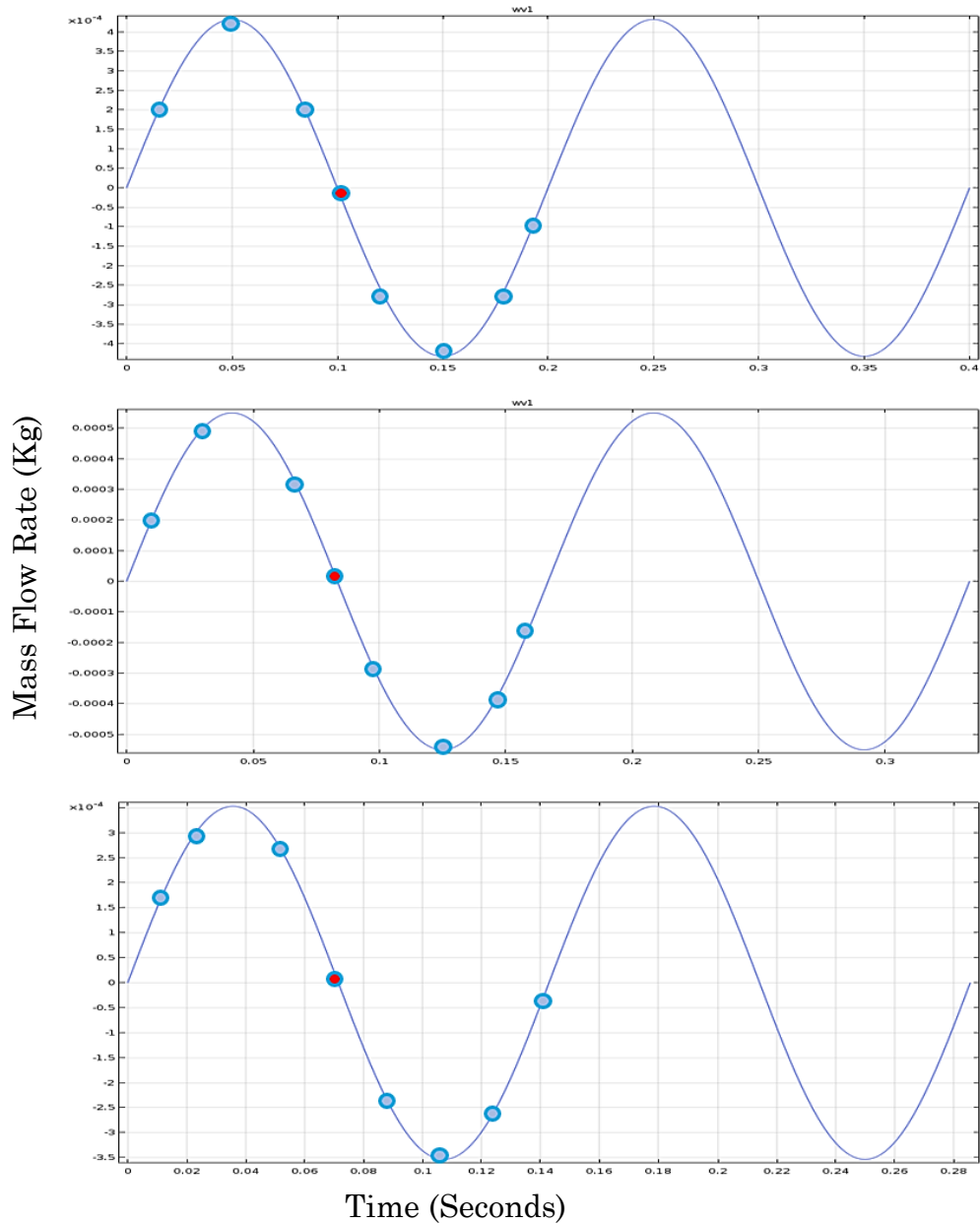
**Figure 6.20** Vessel Dispersion Number plotted as a function of Strouhal number for 5, 6 and 7 Hz for high, medium and low flow rates. Error bars represent standard deviation. Red line represents upper limit of plug flow.

To summarise, higher  $x_0$  resulted in higher levels of axial dispersion. On examination of the velocity ratio, higher flow rates improved mixing thereby minimising axial dispersion and lower values of vessel dispersion were calculated. Vessel dispersion number reduced with increasing  $f$ . This can indirectly be related to amplitude, as higher  $f$  required lower  $x_0$  for particle suspension thereby reducing the amount of axial dispersion. Several optimal numbers have been identified in literature for meso scale OBR's. The relationship between flow behaviour and different flow descriptors (e.g. Strouhal number and velocity ratio) is complex, and depends upon the baffle design<sup>121</sup>. This study largely complements the wealth of data available within literature for meso scale OBR's.



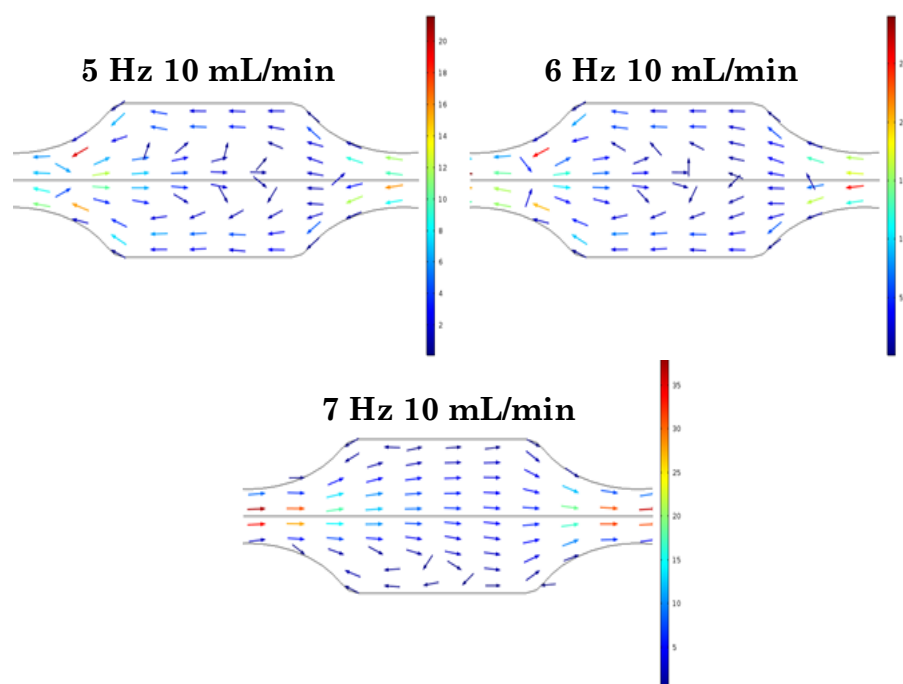
### 6.3.5 CFD Analysis

In order to understand if the findings from experimental RTD could be further explained, CFD was used to simulate the flow under the experimental conditions. The suitable time interval can be calculated using the sinusoidal velocity time function which is the motion of the piston per oscillation cycle.

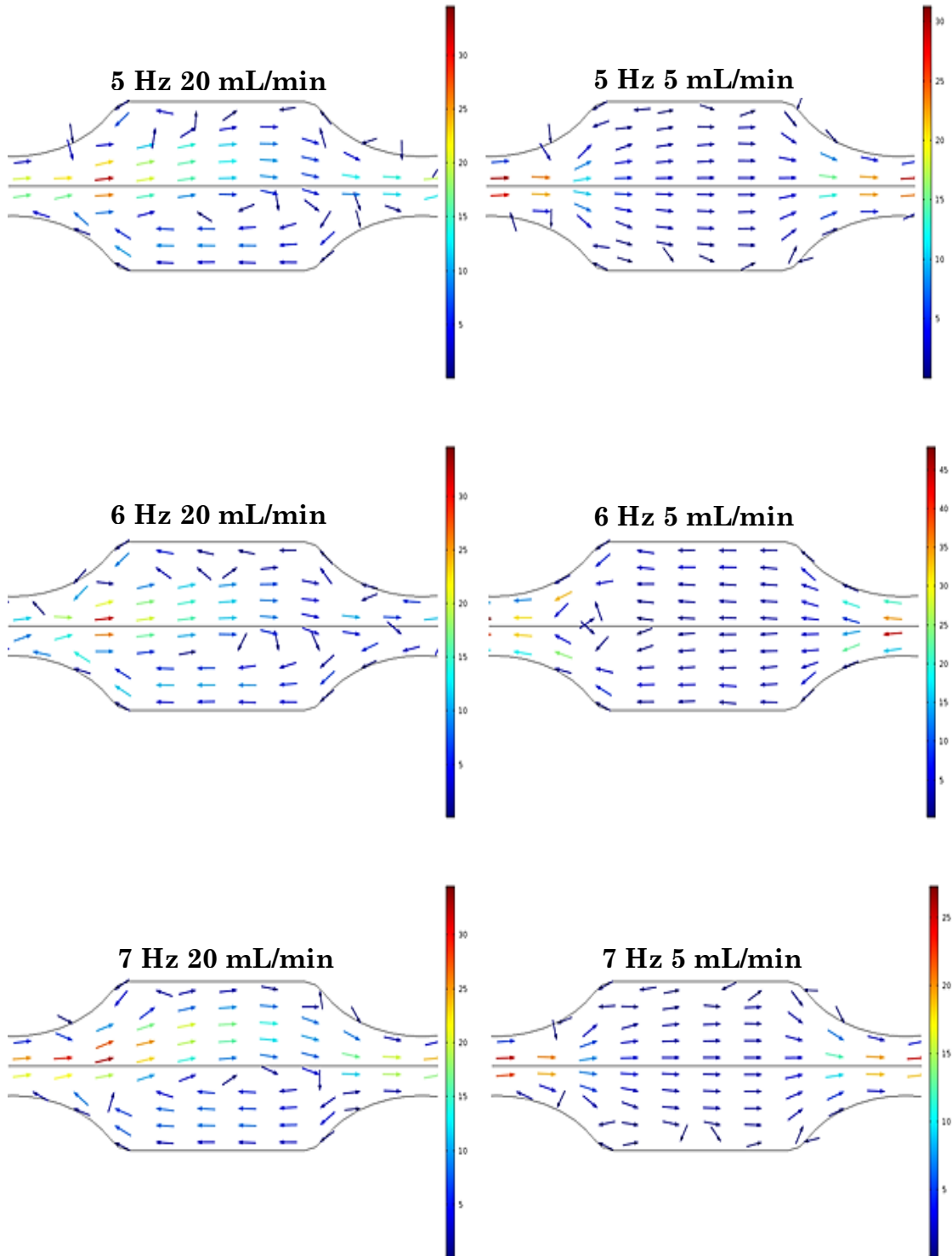


**Figure 6.21** Start and end point of phase positions for 5 Hz (Top), 6 Hz (Middle) 7 Hz (Bottom) and sampling points of an oscillation cycle- indicated by the blue circles, red circle indicates the time of simulations in Figure 6.22.

Parametric sweep of  $f$ ,  $x_0$  and flow rate was completed and the velocity (m/s) and direction of flow was plotted (Figure 6.22). The snapshots represent the point just before the flow will begin to reverse (the half way point in an oscillation cycle) and is the highest point of turbulence. For all experiments, the highest velocity is around the baffle constrictions. This is in keeping with reported CFD models of OBR in which the presence and impact of the baffles on velocity profiles was observed<sup>315</sup>. CFD simulations of a variety of baffle designs found at the point of flow reversal, disc-and-donut geometry created three zones of circular flow whilst the flow with an integral baffles was characterised as parallel streamlines which coincides with the observations made in this study<sup>315</sup>. In contrast to the simulations for 5 mL/min and 10 mL/min, there appears to be a higher degree of mixing present in 20 mL/min simulations (larger eddies which occupy most of the baffle). 20 mL/min conditions experimentally (*Section 6.3.4*) resulted in near plug flow mixing, whilst this was not the case for the other conditions examined. Whilst this is a very straightforward comparison of the conditions within the baffle, it does confirm that there is a difference in the size/shape/number of eddies formed which may contribute towards the experimental findings.



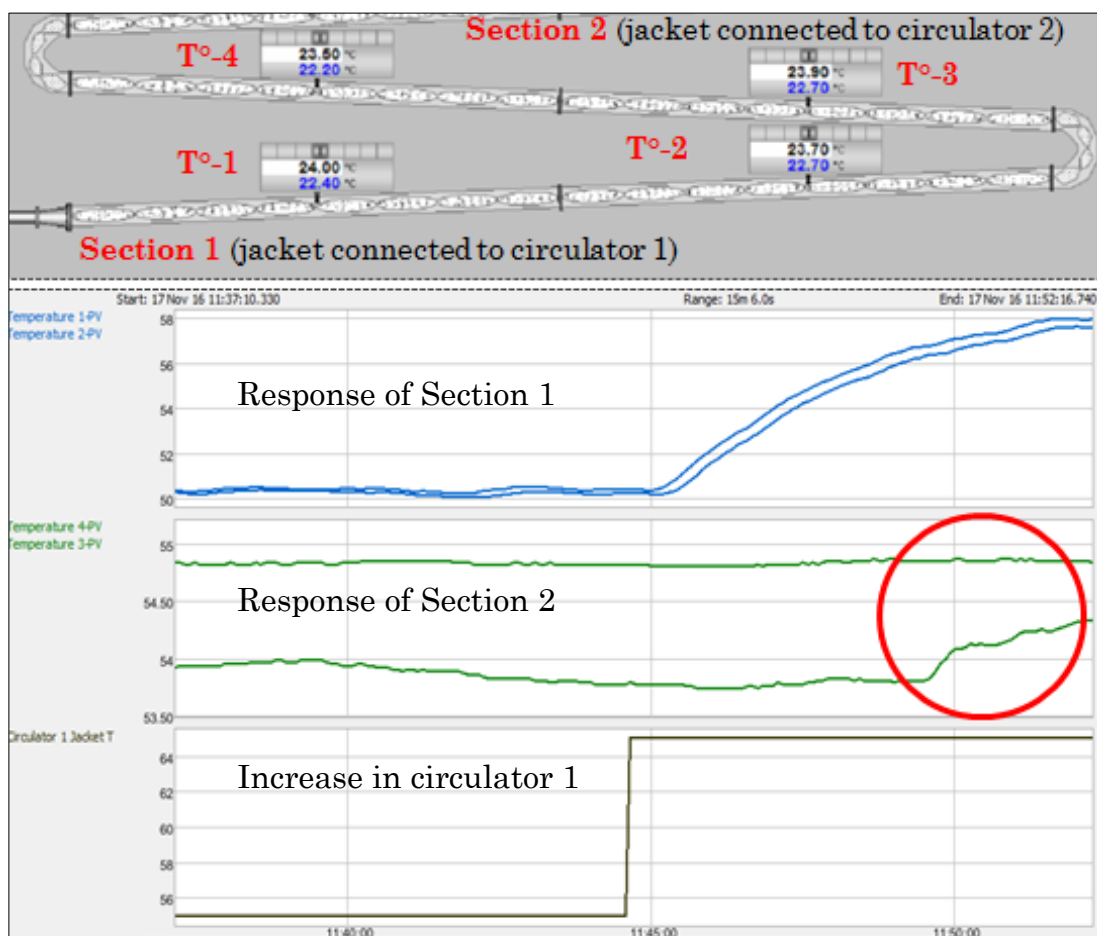
**Figure 6.22** Velocity and direction of fluid at flow rate at each  $f$  and  $x_0$ .



continuation of Figure 6.22.

### 6.3.6 Model Predictive Temperature Control

MPC is a receding horizon technique in which the current control action is obtained by solving on-line at each sampling instant<sup>303</sup>. In the series of experiments carried out one circulator was considered for each section (where a section was two straights and one bend). After a temperature change, each circulator has a noticeable effect on the corresponding section within the reactor. An interaction was observed where a change in circulator one, caused a small change in the temperature in section two indicated by an increase in temperature reported by “*Temperature 3-PV*” (highlighted in red) (Figure 6.23).

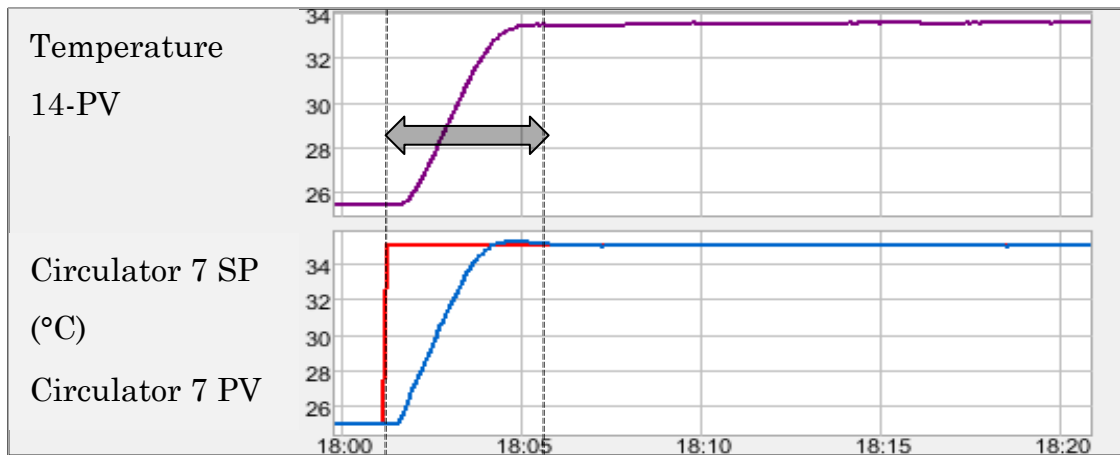


**Figure 6.23** Response of a change in temperature where a small interaction between circulator one and section two (temp probes 3 & 4) of the reactor can be seen which is highlighted in red.

Similar findings were reported for a COBR with an I.D of 15 mm, where a change in one circulator created disruption to the cooling profile further down the reactor<sup>303</sup>. As a result, changes to the temperature within a single straight may

require several circulators to be adjusted to compensate for this effect. In the DN10, this interaction is resolved rapidly and is not observed by the fourth thermocouple, which is part of Section 2.

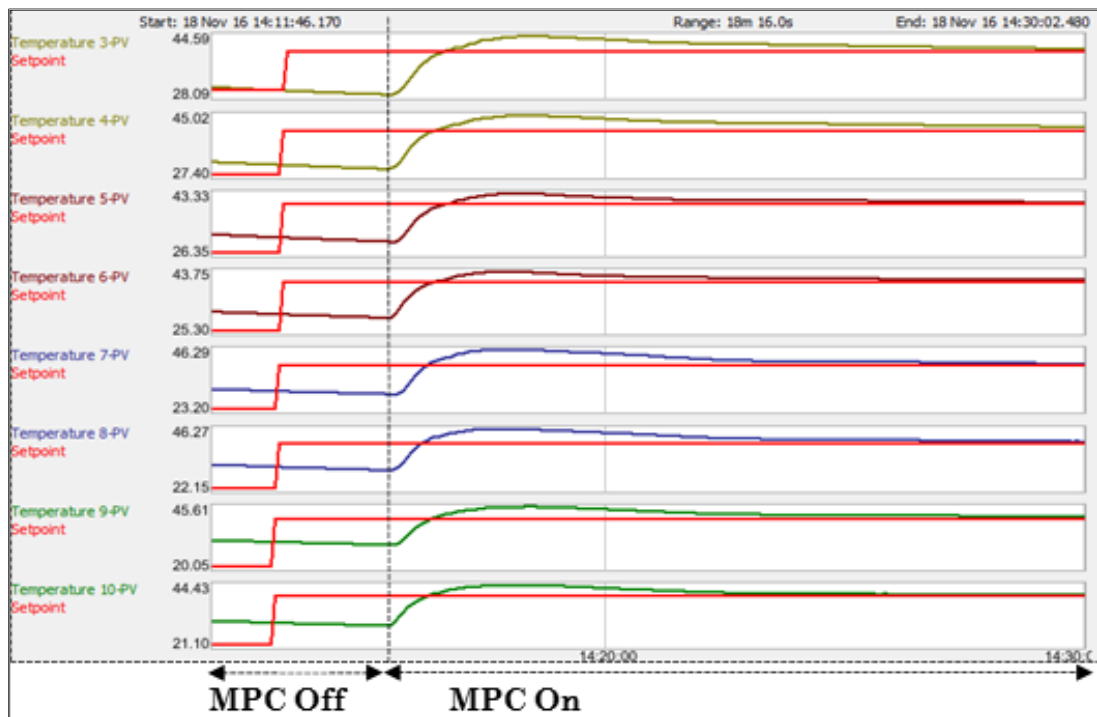
Circulators responded to a change in temperature of 10 °C in approximately 3 minutes and system temperature stabilised in around 5 minutes (Figure 6.24) which is three times quicker than a COBR with an I.D of 15 mm studied elsewhere<sup>108</sup>.



**Figure 6.24** Response of DN10 system to a step change in the temperature of one circulator and corresponding temperatures observed in the system.

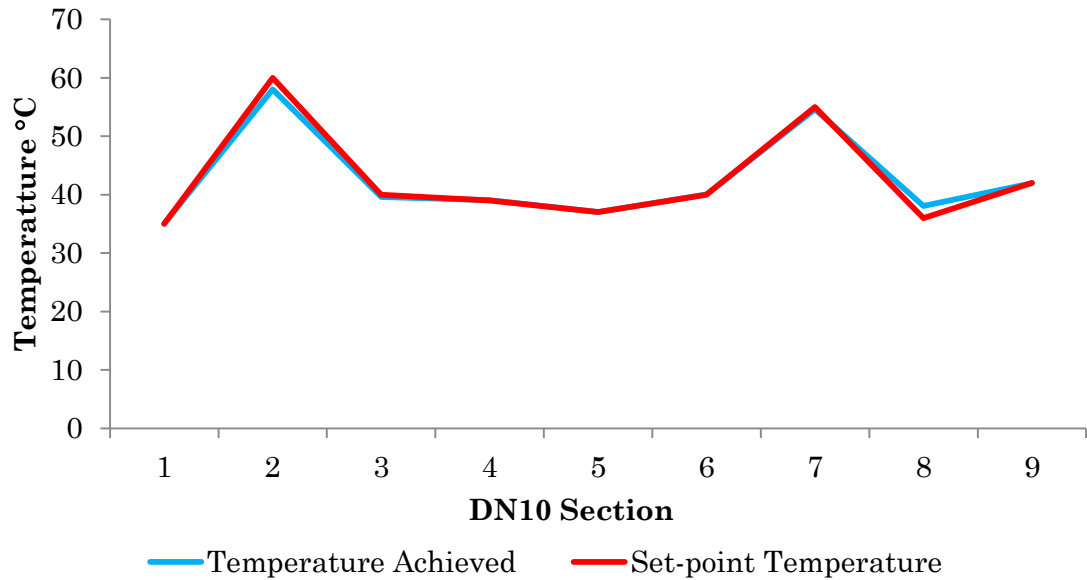
The reduction in the response time to a temperature change in the circulators and the rectification of the interaction noted in Figure 6.23 can be considered as initial indications of the enhanced heat transfer capabilities of this system.

The performance of the MPC model can be visualised, where when the MPC is activated the system effectively controls the circulators to reach the target temperature within the system (Figure 6.25).



**Figure 6.25** MPC effectively controlling the temperature over DN10 sections to achieve the target profile.

The performance of the model was tested by activating and deactivating the temperature control model. Once the MPC was activated, after the system had stabilised, the target temperatures were successfully reached with a maximum deviation of 1.04 °C (Figure 6.26). This shows the MPC ability to effectively control the circulators and account for any interactions between the sections. This will enable the desired cooling profile to be reached throughout the reactor.



**Figure 6.26** Temperature achieved in each section of DN10 when MPC is active.

## 6.4 Summary

The overall aim of this study was to design, develop and characterise a novel meso scale OBR capable of continuous operation at reduced scale. Initial investigations showed that baffle shape and geometry strongly influenced the amplitude needed to suspend particles, with smooth periodic constrictions requiring lower amplitudes than sharp edged baffles.

With the optimised baffle design, the mixing characteristics in the novel COBR with an I.D of 10 mm (DN10) was determined. Within the hydrodynamic range examined, several mixing conditions have been identified which exhibited low axial dispersion thus operating close to plug flow. However, higher amplitudes and flow rates of 5 mL/min and 10 mL/min demonstrated a deviation from plug flow. The differences in the results were attributed to the difference in the eddy formations and mixing in each cell.

Simulations of flow at different frequencies, amplitudes and flow rates have confirmed differences in the mixing regime in each baffle. With the identification of operational parameters suitable for the purposes of a crystallisation process, the system has been further enhanced with the implementation of model predictive temperature control that promotes an effective means of ensuring consistent temperature control, a key process parameter in certain crystallisation processes.

The new system, therefore, has the potential to be used to deliver continuous crystallisation processes under near plug flow operation and with accurate temperature control.



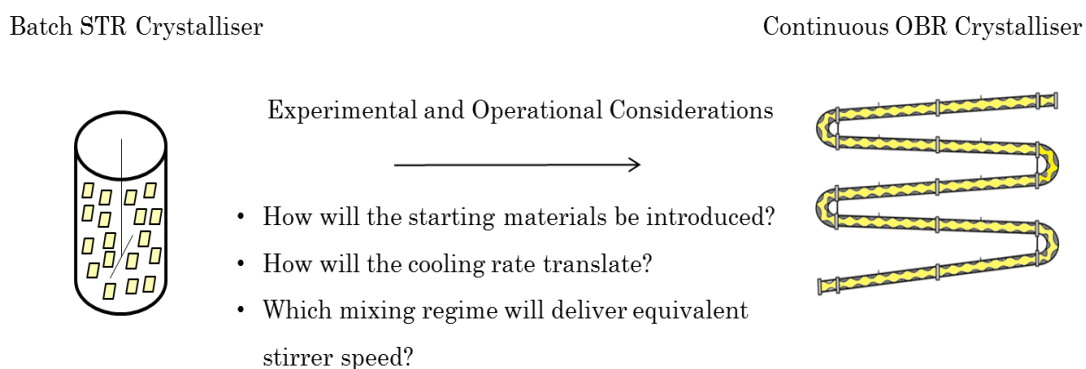
# **Chapter 7** Continuous Crystallisation of ALA Polymorphs

## 7.1 Introduction

Crystallisation is a complex process, featuring a number of phenomena such as primary nucleation, growth, secondary nucleation, agglomeration, and particle breakage<sup>60</sup>. The success of a crystallisation process is determined by its ability to reach predefined quality targets reproducibly. These targets may include a combination of crystal size, polymorphic form, yield, purity or crystal habit<sup>17</sup>. However, the process is sensitive to variation such as cooling rate or mixing. Understanding how experimental changes may influence process outcomes and the potential implications of this for downstream processing is, therefore, of considerable interest.

### 7.1.1 Technology Transfer between Crystallisers

Transferring from a batch STR to a continuous OBR presents novel design considerations in addition to operational and experimental challenges. Some of the factors to be considered are shown in Figure 7.1.



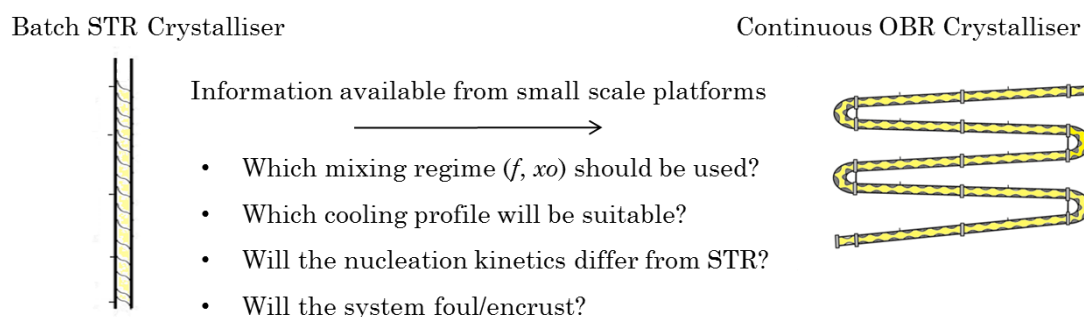
**Figure 7.1** Process and experimental design considerations when transferring between different crystallisation technologies.

Process conditions have a direct effect on outcomes, such as crystal size distribution or polymorphism<sup>20, 129, 284</sup>. As a result, such aspects need to be considered early on since, for example; high solid loading can lead to blockages<sup>115</sup> and different mixing regimes can change the kinetics of the system<sup>108</sup>.

The transfer challenges of batch to continuous operation can be minimised by utilising small scale platforms which are similar to the final crystalliser<sup>113</sup>. This

allows the system under investigation to be exposed to a similar environment, providing valuable information on process parameters which can then be used to design larger scale operations (Figure 7.2).

Small scale platforms have been utilised successfully as a starting point towards developing continuous processes<sup>107-109</sup>. The importance of reactor design is recognised as mechanisms of nucleation have been shown to vary with the configurations<sup>316</sup> resulting in different crystallisation outcomes<sup>20, 108, 316</sup>. Two OBR designs (moving fluid (MF) and moving baffle (MB)) were compared for the enantiotropic purity of sodium chlorate crystals obtained through a cooling seeded crystallisation<sup>316</sup>. Under otherwise identical experimental conditions, it was found that the MB produced higher levels of pure enantiomeric crystals compared to the MF set-up. On examination of the effect of mixing intensity, it was concluded that purity of material was largely unaffected by a change in mixing intensity in MB but the opposite was observed in MF experiments. Trends obtained were attributed to differences in shear rate, axial dispersion and deposition of a thin layer of liquid at the top of the reactor in the MF set-up which can create areas of higher local supersaturation and influence nucleation behaviour. Other studies have complemented these findings<sup>21, 317</sup>.

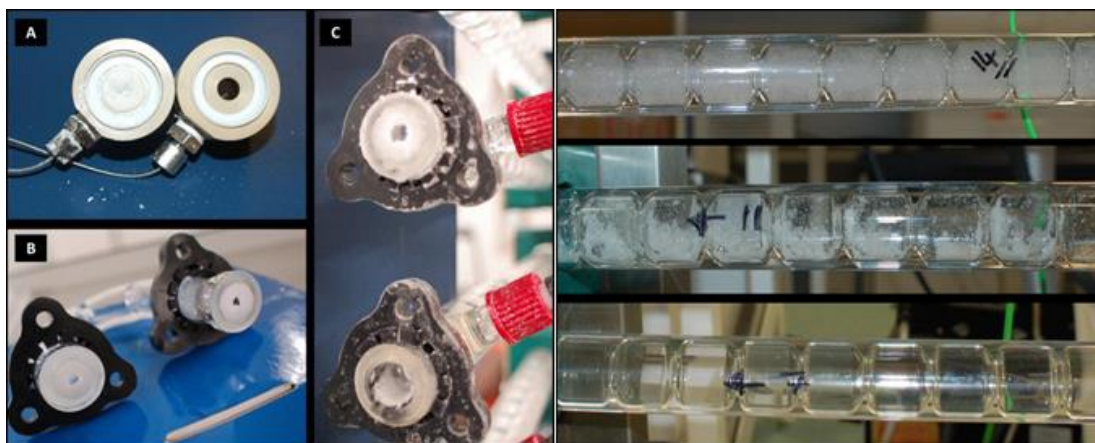


**Figure 7.2** Examples of the type of information which can be acquired from small scale experiments.

The tendency of the system to foul/encrust which is a potential challenge particularly where higher supersaturation conditions may be used to drive nucleation can be determined from small scale experiments. Fouling can be defined as the unwanted accumulation of material on surfaces including walls of the crystalliser and/or temperature/PAT probes<sup>318</sup> (Figure 7.3). Fouling can

prevent the system from achieving steady state, reduce available heat transfer surfaces, affect probe windows and possibly cause blockages<sup>319</sup>.

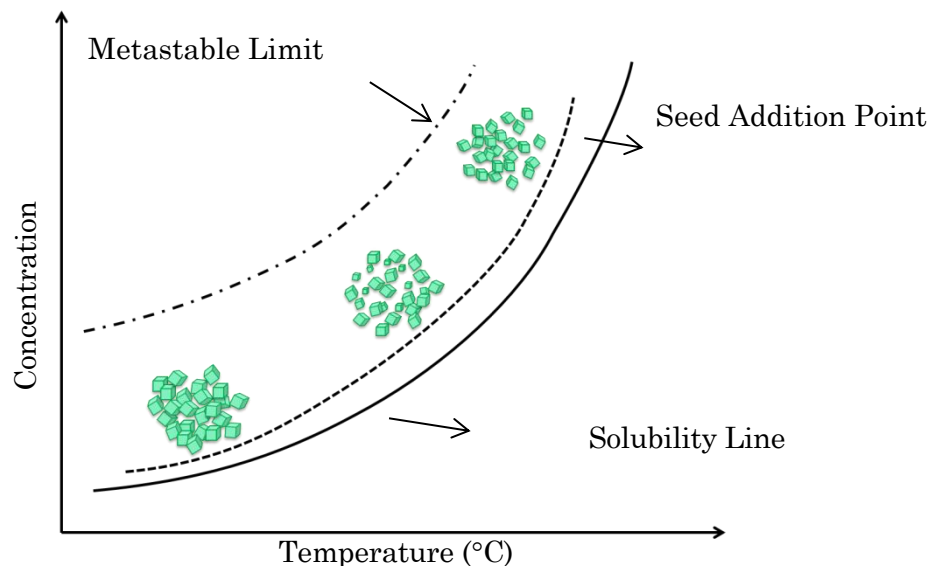
Surface properties and a range of process conditions can promote fouling including; solvent choice, supersaturation, mixing efficiency and impurities<sup>320, 321</sup>. The primary nucleation event, with respect to secondary nucleation, is thought to be a major contributor to the fouling process<sup>322</sup>. Although, fouling is a hindrance to both batch and continuous operation and in-process detection can be incorporated, it is more of an operational challenge in the latter.



**Figure 7.3** Examples of fouling (images acquired reference 108).

### 7.1.2 Experimental Considerations

Crystallisation experiments can be performed “seeded” or “unseeded”. Seeding is the deliberate addition of small crystals after which the supersaturation can be depleted through their growth (Figure 7.4).



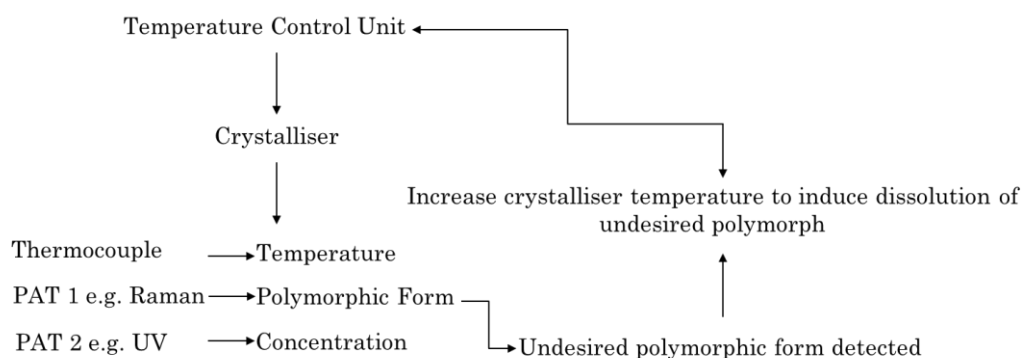
**Figure 7.4** Schematic illustrating the principle of a seeded crystallisation process. The growth of seed crystals are shown as a function of the supersaturation (the dashed line between solubility line and seed crystals) generated by means of cooling.

Growth of the seed crystals is encouraged as the outcomes of the crystallisation process (e.g. crystal size, polymorphic form and likelihood of fouling) can be better anticipated and controlled<sup>323</sup>. The ideal seed addition point should be near the solubility line and within the midpoint of the metastable zone limit<sup>323</sup>. If these conditions are not met, seeding may not be feasible, in which case unseeded crystallisation may be an option.

Unseeded crystallisation is the creation of nuclei through the generation of supersaturation in-situ. Spontaneous nucleation and growth take place simultaneously. Operationally, unseeded crystallisation processes can often lead to a metastable form<sup>324</sup> as at sufficiently high levels of supersaturation the metastable forms may have higher nucleation rate kinetics and will appear first<sup>249,229</sup>. Whilst seeding allows greater control over particle properties and operation at lower supersaturation, crystallisers also need to have ports to feed the seed material in to the crystalliser. These need to be designed and managed

in order to ensure consistent flow of feed/seed material to ensure the necessary experimental procedures can be executed to deliver crystals with the desired qualities.

Several CQA control mechanisms have been developed. Some of the control strategies include; manipulation of seed and feed pumps<sup>303</sup>, temperature cycling<sup>306</sup> and concentration control<sup>303, 305, 325</sup>. A strategy for polymorphic control using feedback control techniques based on PAT tools has been developed<sup>306</sup> and is shown below (Figure 7.5).



**Figure 7.5** Diagram of a feedback control method (figure adapted from reference 306).

The approach consists of detecting the desired polymorphic form and upon detection of the undesired form; a temperature cycle is triggered causing dissolution. This is complemented by supersaturation control which maintains the solution concentration within appropriate levels to obtain the correct polymorphic form. These strategies seek to control the nucleation and growth processes and inhibit the formation of crystals which are out of specification (e.g. CSD or polymorphic form). Continuous crystallisation can offer benefits such as; reduced downtime between batches, less batch-to-batch variation, greater control over particle attributes such as particle size distribution and solid state and incorporation of control strategies<sup>10, 107, 303</sup>. Lawton *et al*<sup>10</sup> has demonstrated the successful continuous isolation of an API in a COBR with reduced operational time from 9 hours to 12 minutes. The COBR has also been shown to be beneficial in the synthesis of vanisal sodium and aspirin with the addition of effective cleaning protocols to demonstrate the flexibility and efficiency in

cleaning with minimal waste production<sup>326</sup>. Further advantages have been highlighted and include; isolation of metastable form of API like compounds e.g. L-glutamic acid<sup>20</sup>, reduction in production time of lactose from 13 to 20 h in batch down to 4 h by continuous crystallisation<sup>107</sup> and control over particle size making it possible to directly crystallise paracetamol particles suitable for pulmonary drug delivery<sup>66</sup>.

Control and optimal operation of a crystallisation process is made significantly more complicated by the addition of a second component. However, multicomponent crystallisation in a continuous environment on a large scale has been reported<sup>109, 130</sup>. One such example is the urea and barbituric acid (UBA) system with three known polymorphs<sup>109</sup>. A COBR with I.D 15 mm was shown to consistently deliver crystallisation of UBAI (most stable). However, selective crystallisation of either UBAAII (least stable) or UBAAIII (metastable) was challenging. Dampening of oscillation, sedimentation of material and fouling were identified as possible causes. One other example is the continuous cooling crystallisation of paracetamol form II in the presence of metacetamol<sup>130</sup>. Whilst paracetamol form II was produced at a large scale COBR, phase purity was not achievable with varying amounts of metacetamol hydrate present in the final product. To obtain phase pure paracetamol form II, addition of sections to the COBR to increase the residence time was suggested.

The aim of this work was to design a continuous cooling crystallisation process to successfully control the polymorphic form of ALA purely by the addition of NIC solution. The strategy was to introduce streams of ALA and NIC separately and this is referred to as multiple streams in flow. The term multi-component crystallisation is only referred to the experiments resulting in the ALA-NIC co-crystal.

## 7.2 Experimental

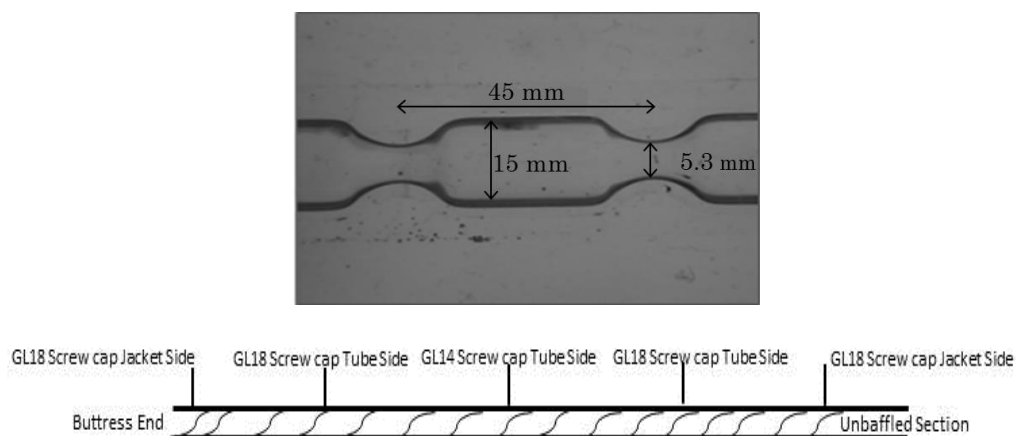
### 7.2.1 Materials

Alpha Lipoic Acid (ALA I, CAS: 1077-28-7) and Nicotinamide (NIC, CAS: 98-92-0) were obtained from Sigma Aldrich and used without further purification. Isopropanol was acquired from VWR and double distilled water was available in the laboratory.

### 7.2.2 Experimental Method

#### 7.2.2.1 Batch Cooling Crystallisation Experiments

Based on previous batch crystallisation studies (Chapter 4) there was an understanding that the ratio of ALA to NIC had a critical role in determining the solid form of ALA. However, the impact of the platform on nucleation kinetics was still to be defined. A batch SPC system with an I.D of 15 mm was designed (Figure 7.6) which was scaled up by keeping  $\alpha$  (orifice open area) equivalent between the DN10 meso scale OBR and SPC batch OBR (Table 7.1).



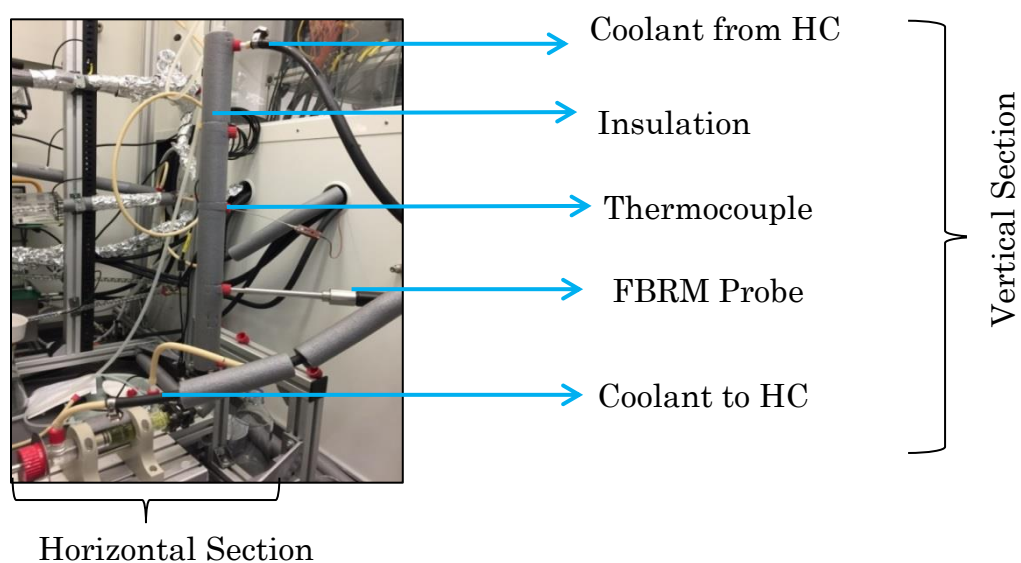
**Figure 7.6** Baffle geometry of the batch system (above) and schematic of the batch SPC platform (below).

This platform enabled the integration of a FBRM probe which allowed detection of nucleation and a thermocouple to monitor temperature. To allow greater temperature control the platform was thermally insulated (Figure 7.7).



**Table 7.1** Geometrical design features of the SPC batch DN15 platform.

	DN10 Continuous Platform	SPC Batch Platform
Diameter (mm)	10	15
$L$ (mm)	30	45
$D_o$ (mm)	3.5	5.3
$\alpha$	12%	12%



**Figure 7.7** Final set-up of the batch OBR used to determine the nucleation kinetics of ALA II.

Based on the previous small scale results (Chapter 4 and 5) the compositions in Table 7.2 had shown to successfully yield ALA II (where concentration is expressed as weight per volume of solvent). These conditions were taken forward to test the potential of the OBR to control the polymorphic form by the addition of NIC acting as a hydrotrope. The heater/chiller (HC) was set to cool automatically at the fastest rate possible which was around 1.1 °C/min.

**Table 7.2** List of experimental conditions used in STR batch experiments.

<b>STR Experiment</b>	<b>Batch OBR Experiment</b>	<b>STR Experiment</b>	<b>Batch OBR Experiment</b>
Total volume of solvent (mL) 9.5	Total volume of solvent (mL) 120	Total volume of solvent (mL) 9.5	Total volume of solvent (mL) 120
Concentration of ALA (g/100 mL) 5.37	Concentration of ALA (g/100 mL) 5.37	Volume of IPA (mL/100 mL) 47.37	Volume of IPA (mL/100 mL) 47.37
Concentration of NIC (g/100 mL) 3.27	Concentration of NIC (g/100 mL) 3.27	Volume of H <sub>2</sub> O (mL/100 mL) 52.63	Volume of H <sub>2</sub> O (mL/100 mL) 52.63

Once nucleation was detected a small amount of sample was removed, filtered, washed with double distilled water and left to dry before being analysed with XRPD to determine the polymorphic form.

### 7.2.2.2 Continuous Crystallisation of ALA Polymorphs

Previous batch experiment had successfully yielded ALA II and thus demonstrated the OBR to be a suitable platform for the crystallisation of ALA (*Section 7.2.2.1*).

The aim of these experiments would be to test if the meso scale COBR can provide a novel approach to enable the form of ALA to be selected or “dialled up”. The conditions taken forward were designed to test the potential to control the polymorphic form purely by stopping or starting the addition of dissolved NIC as a hydrotrope. Compositions chosen covered a variety of ALA:NIC ratio’s which corresponded to the three polymorphic forms of ALA so far obtained; ALA I, ALA II and ALA-NIC co-crystal.

### 7.2.2.3 Continuous Experimental Set-Up

The experimental set-up consisted of the DN10 COBR (described in Chapter 6), five heater chillers, one oscillator, two peristaltic pumps, two feed tanks and a simple filtration and collection setup Figure 7.8 and Figure 7.10.



**Figure 7.8** Y-piece to flow streams (left), stock solutions of individual streams ALA in IPA and NIC in water (centre) and filtration set up (right).

A summary of ALA and NIC conditions and their corresponding polymorphic outcomes obtained from previous batch STR cooling crystallisation experiments (Chapter 4) are shown in Table 7.3.

**Table 7.3** A summary of the compositions and respective polymorphic outcomes.

Mass of Ala (g)	Mass of NIC (g)	ALA:NIC Mass Ratio	Polymorphic Form
0.245	0	-	I
0.245	0.0365	6.712	I
0.255	0.155	1.645	II
0.245	0.5778	0.424	Co-crystal

### 7.2.2.3.1 Determination of Flow Rate

In order to determine a suitable flow rate, the theoretical cooling rate was calculated for 40 mL/min, 50 mL/min and 60 mL/min (Table 7.4). These flow rates were selected as they would provide an acceptable balance between achievable cooling rate and the residence time. The difference between the starting temperature and the isolation temperature was -27 °C. The total length of the reactor was 8 m resulting in a temperature difference of -3.38 °C/m.

**Table 7.4** Comparison of flow rates and respective theoretical cooling rates.

Flow Rate mL/min	Area (m <sup>2</sup> )	Volumetric flow rate (m <sup>3</sup> /s)	Velocity (m/s)	Cooling Rate/min
40	7.85x10 <sup>-5</sup>	6.67x10 <sup>-7</sup>	8.493x10 <sup>-3</sup>	-1.72
50	7.85x10 <sup>-5</sup>	8.33x10 <sup>-7</sup>	1.062x10 <sup>-2</sup>	-2.15
60	7.85x10 <sup>-5</sup>	1x10 <sup>-6</sup>	1.274x10 <sup>-2</sup>	-2.58

From the theoretical calculations, 50 mL/min was expected to deliver an appropriate cooling rate to produce all ALA polymorphs with a suitable residence time. 50 mL/min would give a residence time of eight minutes which, based on the previous work, is also consistent with the RT needed to produce the metastable form of ALA. The system was aimed to be operational for a minimum of four residence times assuming no significant fouling/blockage issues.

### 7.2.2.3.2 Determination of mixing conditions

Powder density ( $P/V$ ) is used to estimate the power required to achieve the desired mixing regime and is expressed in terms of power per unit volume ( $W/m^3$ ) (Equation 7.1).  $P/V$  and  $St$  number of the conditions which provided the narrowest axial dispersion from Chapter 5 were used as a target with the aim to select the appropriate  $f$  and  $x_o$  in order to achieve similar mixing conditions to the batch SPC OBR and the continuous platform<sup>264</sup> (Table 7.5).

$$P/V = \frac{2\rho N_b}{3\pi C_D^2} \left(\frac{1-\alpha^2}{\alpha^2}\right) \chi_o^3 (2\pi f)^3 \quad \text{Equation 7.1}$$

where  $N_b$  = number of baffles per unit length of OBR ( $m^{-1}$ ),  $C_D$  = the coefficient of discharge of the baffles (typically 0.7)<sup>286</sup>,  $x_o$  = oscillation amplitude, centre-to-peak (m),  $f$  = oscillation frequency (Hz).

**Table 7.5** Oscillatory condition used for batch and continuous OBR set-up.

Oscillatory Conditions for DN15			
Diameter (mm)	Frequency (Hz)	Amplitude (c-p, mm)	St
15	4.9	2	0.597
Oscillatory Conditions for DN10			
Diameter (mm)	Frequency (Hz)	Amplitude (c-p, mm)	St
10	6.3	1.33	0.597

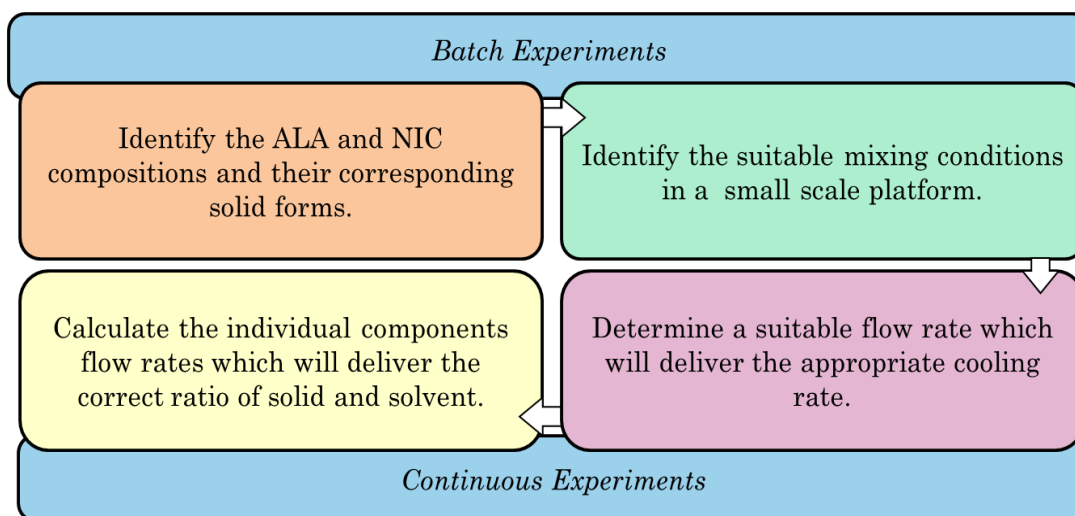
### 7.2.2.3.3 Determination of final experimental set up

A stock solution of ALA at 0.11 g/mL was prepared based on the studies carried out in Chapter 4. The concentration of NIC stock solution was varied to deliver the correct mass ratio of ALA and NIC. Comparing Table 7.3 and Table 7.6 the mass ratios of ALA and NIC agree and are expected to deliver the corresponding polymorphs of ALA.

**Table 7.6** Initial experimental conditions for ALA I (2), ALA II (3) and ALA-NIC Cocrystal (4).

Experiment	ALA Stream mL/min	NIC Stream mL/min	ALA g/min	NIC g/min	Mass Ratio
2	23.70	26.30	2.581	0.384	6.721
3	23.70	26.30	2.581	1.369	1.885
4	23.70	26.30	2.581	5.309	0.486

The experimental approach taken can be summarised as shown in Figure 7.9.



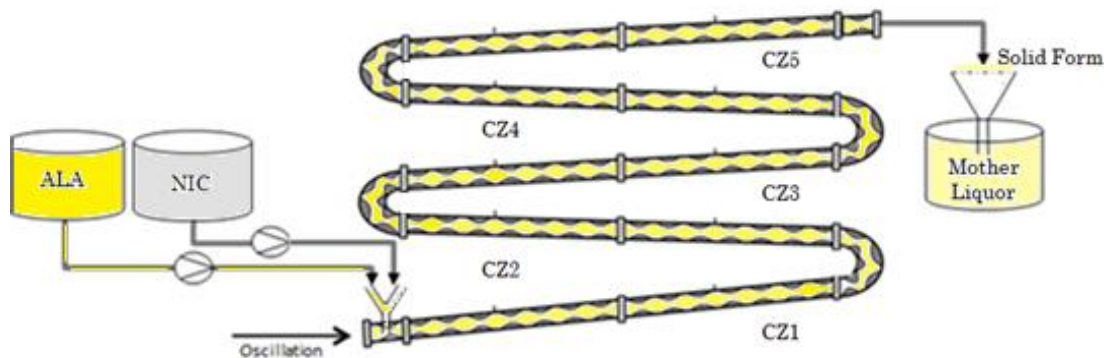
**Figure 7.9** Workflow to design the continuous crystallisation experiments.

#### 7.2.2.4 Continuous Crystallisation of the ALA-NIC Co-Crystal

The previous experiments in *Section 7.2.2.2* had ended prematurely due to fouling and subsequent blockages. The fouling and encrustation problems were most likely due to the primary nucleation<sup>322</sup> and thus, a new strategy was to reduce the concentration of ALA stock solution and increase the isolation temperatures. ALA stock solution with a concentration of 0.095 g/mL and NIC stock solution of 0.2019 g/mL was prepared (Table 7.7). These steps allowed the process to be operated for a longer period, allowing more experimental data to be collected. Findings from Chapter 4 had shown ALA II to be successfully isolated at lower temperatures. Consequently, the likelihood of being able to obtain pure ALA II would be more challenging. Hence, the multiple stream crystallisation process was tailored for the continuous production of the multi-component co-crystallisation of ALA-NIC.

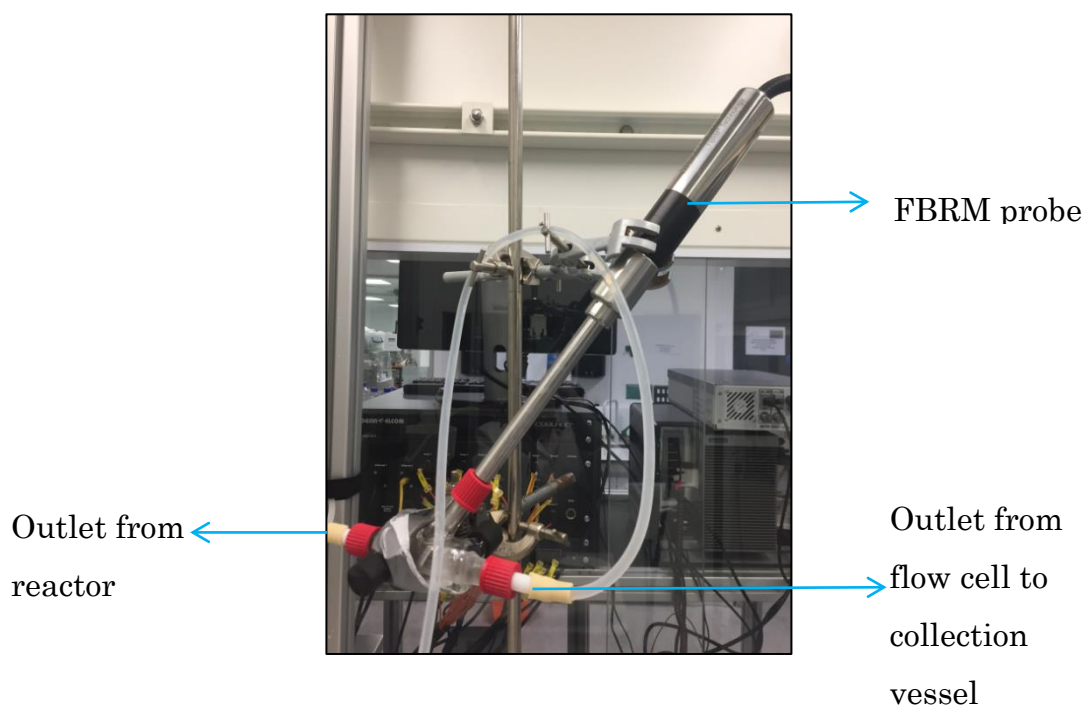
**Table 7.7** Crystallisation conditions of ALA-NIC co-crystal (Exp-7-1 and Exp-7-2).

ALA Stream mL/min	NIC Stream mL/min	ALA (g/min)	NIC (g/min)	Mass Ratio
23.70	26.30	2.2512	5.3091	0.4240



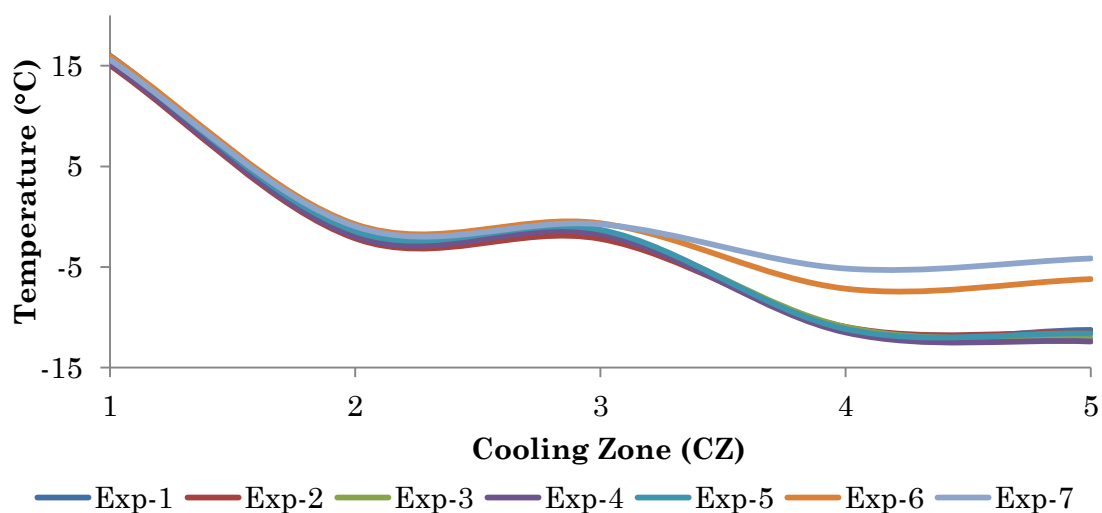
**Figure 7.10** Experimental set-up for continuous experiments. Individual streams of feed ALA-IPA and NIC-Water were introduced into the reactor using a Y-piece.

A flow cell with a total volume of 12 mL was connected to the outlet of the reactor to determine if and when steady state had been reached Figure 7.11. This flow cell, which has a low volume, in combination with the high flow rate, was used to avoid settling of product.



**Figure 7.11** Flow cell with FBRM probe connected to the outlet point of DN10.





**Figure 7.12** Temperature profiles achieved for each experiment (average of two temperature probes per cooling zone (CZ)). The first CZ was kept at 15 °C to allow the solution to mix and reach homogeneity before being cooled. The solution is assumed to have mixed homogeneously before reaching CZ 2.

#### 7.2.2.5 SEM

Samples were gently tapped onto sticky carbon tabs added to 10 mm diameter aluminium stubs, and placed under vacuum for three minutes for analysis using equipment detailed in *Chapter 3 Section 3.2.1.5*. A beam voltage of 1000 V, with detection of backscattered electron signal, at magnifications of x2500 and x1500 was used.

#### 7.2.2.6 XRPD

Solid materials were characterised off-line via XRPD using a Bruker AXS D2 Phaser 2<sup>nd</sup> generation diffractometer as detailed in *Chapter 3 Section 3.2.1.9*. Data were collected at room temperature from 4-35° 2θ with a 0.01° 2θ step size and 1 s step count time. Sample was also analysed, at room temperature, by XRPD on a Bruker D8 Advance (*Chapter 3 Section 3.2.1.9*). The range and count time are shown in Table 7.8.

**Table 7.8** Variable count time scan parameters.

<b>2<math>\theta</math>-range</b>	<b>Step size</b>	<b>Seconds/step</b>
3° to 30°	0.017°	2s
30° to 43°	0.017°	8s
43° to 56°	0.017°	16s
56° to 70°	0.017°	24s

#### **7.2.2.7 FBRM**

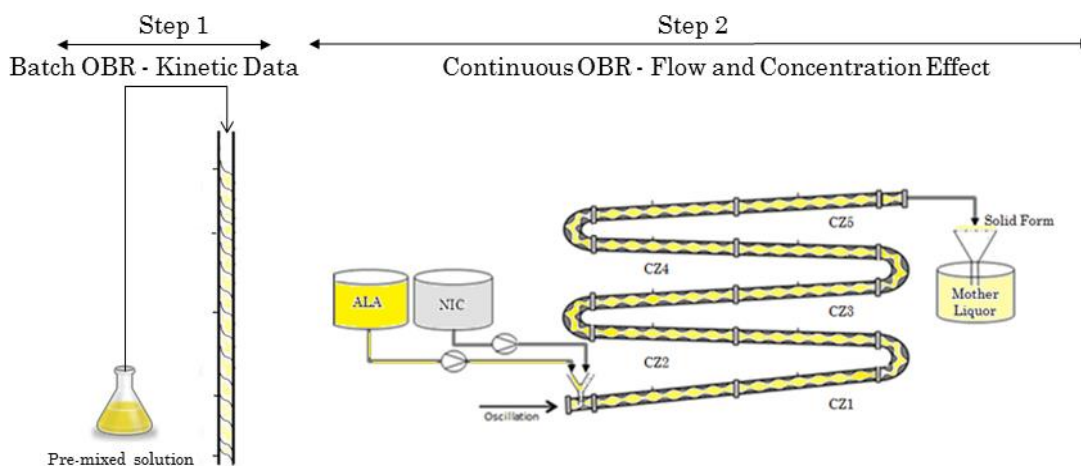
Using the equipment as detailed in *Chapter 3 Section 3.2.1.2*. A moving average of 11 points with the primary distribution function was used to detect nucleation and the data was analysed using *iC FBRM* software version 4.4.29.

#### **7.2.2.8 Particle Size Distribution**

Particle size was measured using a Malvern Morphologi G3 (Malvern Instruments). Analysis was done in triplicate, and mean results are presented as D<sub>50</sub>, average and standard deviation. Data analysis was carried out using *Malvern Morphologi* Software Version 8.20.

## 7.3 Results & Discussion

This section will describe the findings from the experiments carried out and is divided into two parts (Figure 7.13). The first part will describe the results from the batch OBR experiment. The multiple streams in flow continuous crystallisation experiments will be presented in the second part.



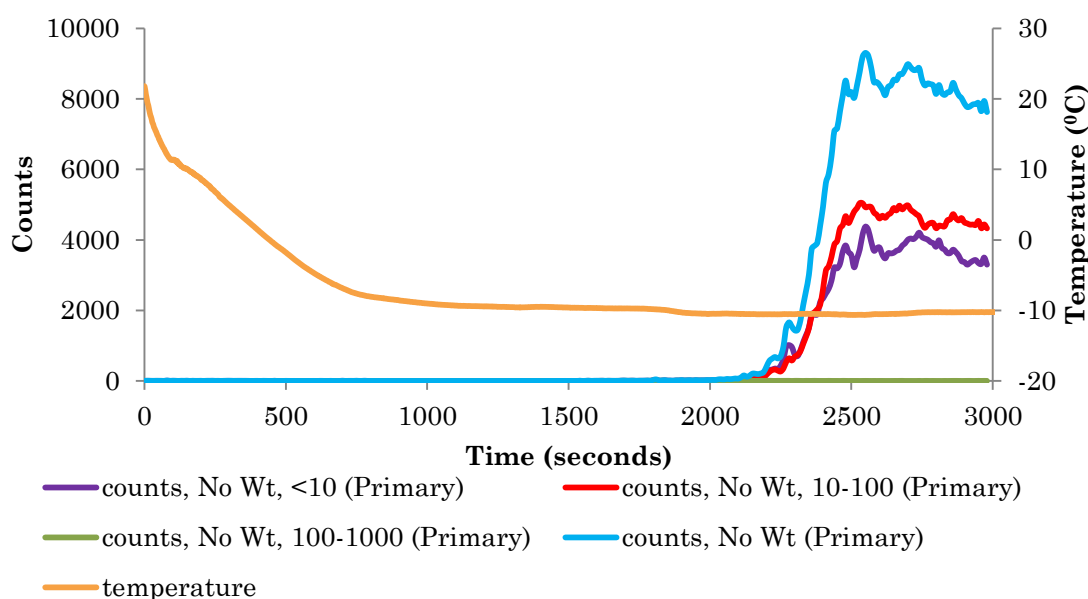
**Figure 7.13** Schematic of the experimental approach.

### 7.3.1 Batch Cooling Crystallisation Experiment

Isolation of ALA II was previously carried out in a STR from 5 mL up to 1000 mL (Chapter 5). Due to a change in platform, prior to running continuous crystallisation experiments, suitable mixing conditions and nucleation temperature which could deliver ALA II in an OBR had to be determined. This was the first step in converting a batch experimental run a continuous procedure.

Powder diffraction analysis of sample from the batch OBR experiment confirmed the polymorphic form to be ALA II with a small amount of ALA I (13 %). The concentration and ratios of ALA and NIC were based on small scale experiments which consistently produced ALA II (Chapter 4 and 5). Both ALA and NIC solution were prepared and mixed before being introduced to the reactor (pre-mixed). Therefore, a mixture of polymorphs would be unlikely due to the concentration of materials. However, there was a slight difference in both the mixing performance and the cooling efficiency between the horizontal and vertical sections of the batch OBR (Figure 7.7). The horizontal section was less

efficiently mixed which was evident as some sedimentation of solid was observed. Due to the physical limitations of the setup it was not possible to fully insulate around the horizontal glass section. This may have affected the final temperature that was obtained within the reactor. Thus, the occurrence of ALA I may be due to primary nucleation of ALA I or transformation of ALA II to ALA I. Furthermore, the CLD from the batch cooling crystallisation experiment is shown in Figure 7.14. The nucleation temperature was identified to be around -10 °C which was comparable to the nucleation temperature identified in STR (Chapter 4 and 5).



**Figure 7.14** FBRM data presented with the cooling profile used during the experiment.

No fouling on the reactor walls or PAT probes was observed. This was a positive result, as fouling can lead to difficulties with regards to heat transfer and monitoring product quality. Furthermore, the suspension of crystallised solid material was checked on the vertical section of the setup and no suspension problems were noted.

In summary, this experiment identified a nucleation temperature (around -10 °C) for ALA II to base the design of the continuous process. It also allowed suitable oscillatory conditions to be confirmed. This was achieved by

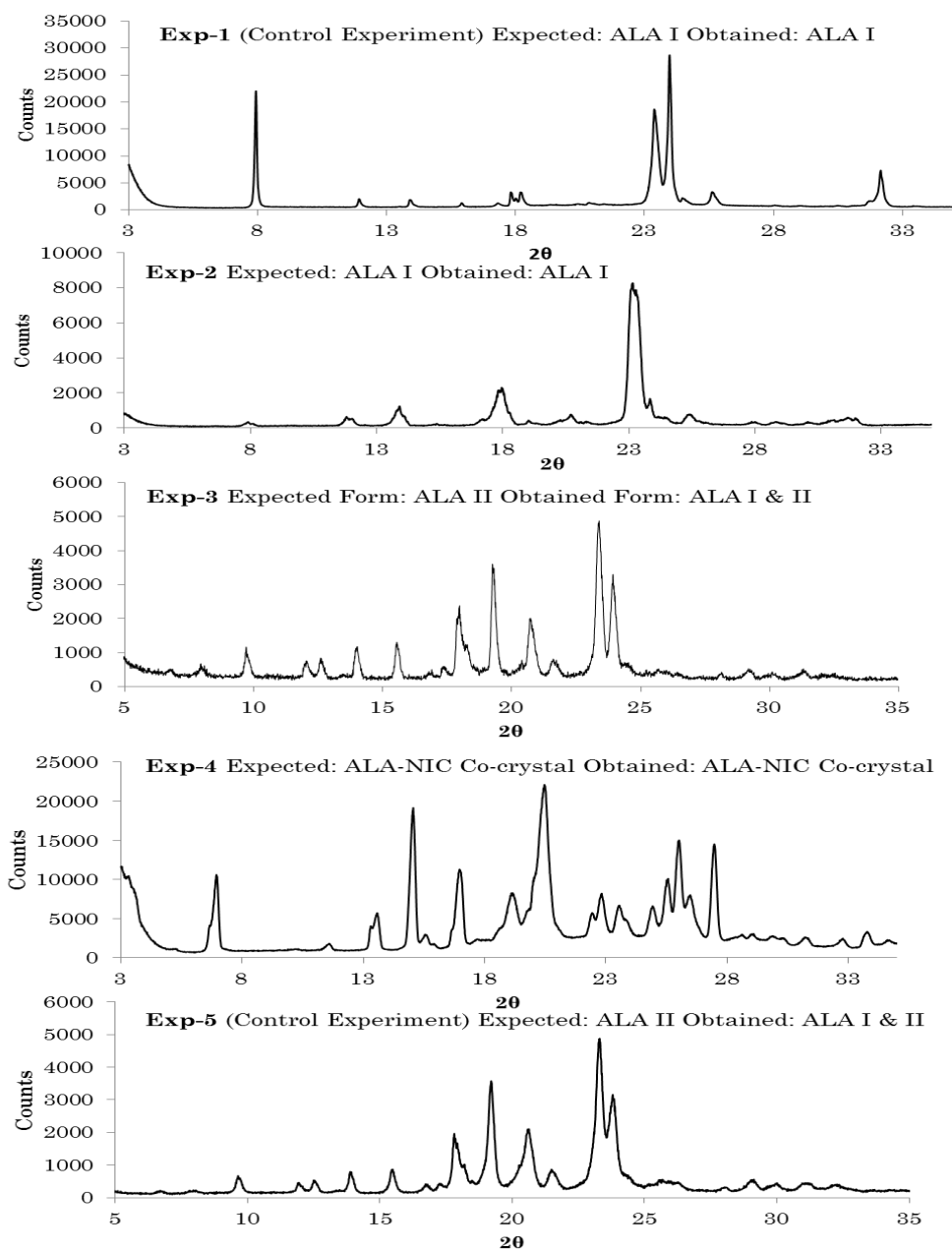
approximating the fluid mechanics within a meso reactor to those within the scaled-up batch SPC OBR.

### 7.3.2 Continuous Crystallisation Experiments of ALA Polymorphs

To transition from batch experiments to a continuous process there was an interesting challenge in being able to design experiments whereby the polymorphic outcome was controlled by the concentration of NIC. Whilst seeding is commonly used to control polymorphic outcome<sup>129, 327, 328</sup>, in this case the hydrotropic effect of NIC would be exploited in a continuous crystallisation environment. Exp-1 and Exp-5 were carried out as control experiments. Exp-1 contained no NIC and the crystalliser and the cooling profile were checked to confirm which form of ALA crystallised under those experimental conditions. Exp-5 used a pre-mixed solution of ALA and NIC (suitable to crystallise ALA II) which was then fed into the crystalliser. This experiment was able to confirm that the system and experimental procedure were suitable for the crystallisation of ALA II, independent of the method of mixing. Exp-2, Exp-3 and Exp-4 used multiple streams to assess the impact of NIC on the solid state of ALA solely through the hydrotropic effect of NIC. The experimental approach, results and the corresponding XRPD powder patterns are shown in Table 7.9 and Figure 7.15.

**Table 7.9** Summary of the experimental crystallisation conditions and results

	Exp-1	Exp-2	Exp-3	Exp-4	Exp-5
Expected Form	ALA I	ALA I	ALA II	ALA-NIC co-crystal	ALA II
Pre-mixed (Control Experiment)	√	-	-	-	√
Multiple Streams	-	√	√	√	-
Obtained Form	ALA I	ALA I	Mixed forms of ALA	ALA-NIC co-crystal	Mixed forms of ALA



**Figure 7.15** XRPD patterns for crystallisation of ALA polymorphs (Exp1-5).

Exp-1 proved that in the absence of NIC, ALA II did not form and pure ALA I was obtained. This is in line with previous results observed in batch STR (Chapter 4 and 5). Exp-2, which had both ALA and NIC components, produced the phase pure ALA I. This supports the findings in Chapter 4 where only above a certain NIC concentration ALA II formed. Exp-4 successfully demonstrated the formation of the ALA-NIC co-crystal which was also in agreement with previous experimental results where higher NIC concentrations resulted in the ALA-NIC co-crystal (Chapter 4). The experiments designed for the

crystallisation of ALA II (Exp-3 and Exp-5) produced a mixture of ALA I (major) and II (minor). Isolation of mixed polymorphs of ALA has been observed previously in experiments which were aiming to identify suitable crystallisation conditions (Chapter 5). A number of possible reasons, more specific to this set-up, which may have contributed to the mixed polymorphs are considered.

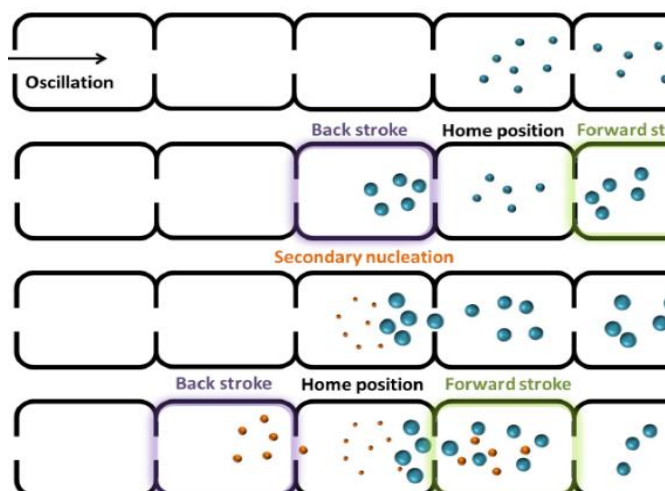
### **7.3.2.1 Experimental Conditions Impacting on Polymorphic Form (e.g. Frequency, Amplitude)**

Briggs *et al*<sup>108</sup> and Palmer *et al*<sup>20</sup> studied the effect of mixing intensity and cooling rate on the polymorphic outcomes of L-glutamic acid and L-glutamic acid/D-mannitol, respectively.

Amplitude and frequency have been reported to influence the purity of crystal material<sup>20</sup>. Increasing oscillation frequency showed a mixture of l-glutamic acid polymorphs with a higher frequency (3 Hz) resulting in slightly higher levels of the stable  $\beta$  form. The same observation was made when amplitude was increased. These findings are in keeping with the results from Ni *et al*<sup>129</sup>. Conversely to the findings for l-glutamic acid where more intensive oscillatory conditions lead to a higher content of the stable form, the opposite was observed for D-mannitol<sup>20</sup>. Experiments completed at lower amplitudes (10 mm) lead to the formation of the stable form of d-mannitol. However, an increase in amplitude to 30 mm (same frequency) resulted in only the metastable form, but increasing frequency alone led to a higher content of the stable form. This indicated that the higher amplitudes were necessary to isolate the metastable form and that the higher frequencies increased the rate of transformation to the stable form.

Observations noted during unseeded cooling crystallisation of L-glutamic acid specifically in oscillatory PFRs revealed back propagation of nucleation under near plug flow conditions following the onset of primary nucleation<sup>108</sup>. The proposed mechanism suggests that due to the oscillatory motion within the system, the crystals move against the direction of net flow towards the inlet, prompting secondary nucleation during each oscillatory back stroke (Figure 7.16). With the experimental setup used during the continuous crystallisation of ALA, this statement cannot be exclusively made as all the straight sections were

thermally insulated, preventing visual observations being made. However, if this effect is present, it can be hypothesised that the new nuclei formed due to secondary nucleation transform to the stable form as the temperature in CZ 3 ( $\sim 0\text{ }^{\circ}\text{C}$ ) is much higher than CZ 4 and CZ 5 ( $\sim -12\text{ }^{\circ}\text{C}$ ). This may have contributed to the mixed polymorphs of ALA.



**Figure 7.16** Schematic of the proposed secondary nucleation propagation mechanism (figure taken from reference 108).

A single set of oscillatory conditions were used during the experiments investigating the cooling crystallisation of ALA polymorphs (Table 7.5). The examples above highlight the potential effects of experimental conditions on polymorphic purity, particularly as the interaction of frequency and amplitude was more influential on phase purity than each component individually meaning both attributes contribute significantly to final solid form obtained<sup>20</sup>.

The polymorphic outcome of varying the experimental conditions have been examined for ALA II in small scale STR experiments (Chapter 5). Both mixing regime and cooling profile have shown to affect the phase purity. SMPT has been observed in the OBR<sup>108, 284</sup> therefore initially phase pure ALA II may have formed but experimental conditions may have resulted in both ALA I and II. The cooling profile achieved during these experiments consistently resulted in a gentler cooling rate (Figure 7.12) which from previous experiments (Chapter 5) demonstrated to often lead to mixed polymorphic forms (e.g. the temperature change between CZ 2 and 3). Higher cooling rates and gentler agitation levels may therefore aid in obtaining phase pure ALA II.



The experimental plan also aimed to continuously filter the solution. If there was a reduction in the efficiency of this process, ALA II may have transformed to ALA I during the final filtration step. Although inline sampling was not incorporated into this experimental set up, future experiments could include samples to be removed during the experiment rather than waiting until the material has eluted from the crystalliser. This may help shed light on the origin of ALA I.

### **7.3.2.2 Final Reactor Temperature**

To examine the effect of the final temperature on polymorph purity, the isolation temperature during the crystallisation of L-glutamic acid were varied from 5 to 40 °C<sup>129</sup>. Final isolation temperature was identified as another parameter influencing crystal polymorphism as the isolation of the metastable form of L-glutamic acid was more noticeable at lower temperatures. This result was explained by the dissolution of crystals being more favourable at higher temperature, accelerating SMPT. However, these results are in contrast to the findings by Palmer *et al*<sup>20</sup> who found that the polymorphic compositions were similar for experiments carried out at isolation temperatures of 40 °C and 10 °C. Phase pure ALA II has been consistently obtained at temperatures below -5 °C under mixed conditions and below 0 °C under quiescent conditions (Chapter 5). Although the final isolation temperature was higher than -5 °C during the continuous experiments, under the mixing conditions present in the COBR, lower isolation temperatures may be needed to isolate phase pure ALA II and inhibit SMPT.

### **7.3.2.3 Effects of pre-seeding**

The pre-seeding effect in OBRs has been defined as the retention of miniscule fragments of crystals present from previous experiments and has been examined by Ni *et al*<sup>284</sup>. The crystal material from previous experiments can lodge within the walls, baffles or other parts of the experimental set-up to which the process fluid is exposed to. These parent crystals then act as seeds for any subsequent experiments, affecting the physical purity of the final material.

Cooling crystallisation of l-glutamic acid was seeded with the metastable form allowing the  $\alpha$  form to be the dominant phase. However, in subsequent unseeded experiments the  $\alpha$  form crystallised under conditions which previously had only produced the stable  $\beta$  form. This was attributed to the retention of  $\alpha$  L-glutamic acid crystals around 1-10  $\mu\text{m}$  (acting as seed crystals) which had remained despite the cleaning procedure.

Although this observation has not been made, experiments resulting in ALA I were carried out first. Therefore, in this case, miniscule ALA I crystals from previous experiments may have deposited on the glass surface, the thermocouples or O-rings allowing ALA I to detach and act as seeds leading to the growth of ALA I crystals at the expense of ALA II. In the literature this has been related to the materials of construction which has been shown to promote/inhibit the nucleation of different polymorphs under identical experimental conditions<sup>129</sup>. During these experiments, the COBR was cleaned using pure IPA (without any water) since ALA has a very high solubility in this solvent ( $\sim 960$  g/L). Also, as no water was used for the cleaning process, the risk of polymerisation (which forms a difficult to clean, very stick gum like residue) was eliminated. Therefore, further work to investigate the effect of different surfaces or the implementation of more efficient cleaning strategies between experiments is highlighted.

#### 7.3.2.4 Fouling

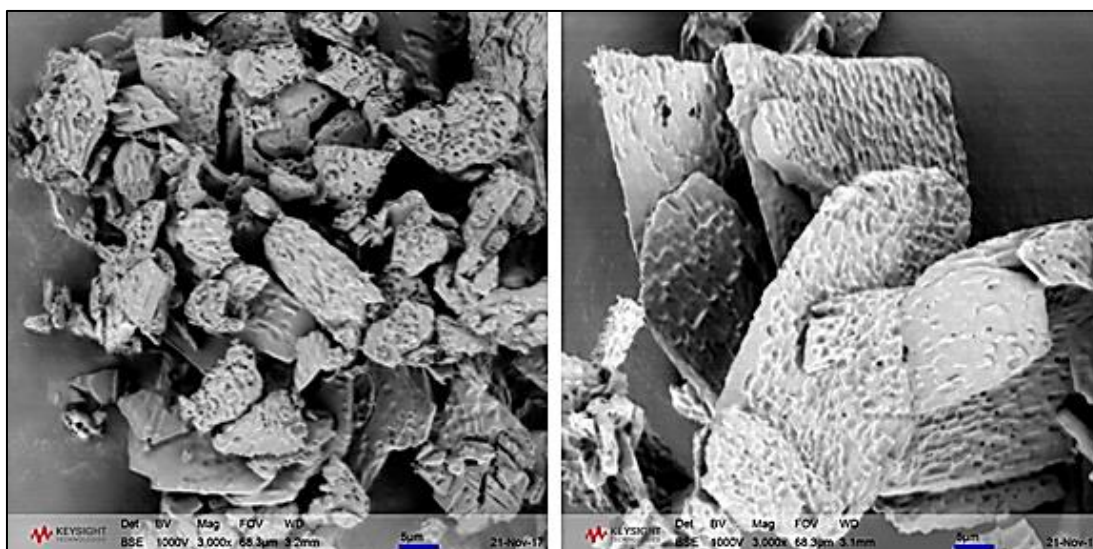
Fouling was observed during the continuous crystallisation of ALA polymorphs. Briggs *et al's*<sup>108</sup> efforts to obtain control of L-glutamic acid highlighted persistent fouling during unseeded experiments in COBR. Fouling arose due to the high supersaturation levels within the system in order to achieve primary nucleation resulting in uncontrolled nucleation and growth and impaired heat transfer<sup>329</sup>. Growth of an unwanted form or retention of unwanted crystals can lead to SMPT. The methodology taken relies on the primary nucleation event. This may be addressed by eliminating the need for primary nucleation and reducing supersaturation attained within the COBR through seeding.

To summarise, evidence has been presented for the consistent formation of a L-glutamic acid indicating that when the system and the experimental procedure is well understood and designed it is possible to isolate a metastable form in COBRs<sup>20</sup>. However, for systems containing more than one component isolating phase pure metastable forms in COBR's have thus far proven challenging (Paracetamol form II<sup>130</sup> and UBA form III<sup>109</sup>).

Experiments aiming to isolate ALA II resulted in a mixture of ALA I and II. While this was not the desired output, several possible reasons which may have contributed to this have been identified. Suggestions have been made which can be further investigated to determine their effect on the purity of the physical form. As there is evidence that ALA II was present, with an improved experimental set-up and further understanding of the system phase pure ALA II may be isolated.

### 7.3.2.5 Crystal Morphology

SEM images of ALA I and ALA II were obtained from the continuous trials (Figure 7.17). This allowed comparison of the crystal surface between experimental conditions used for continuous operation and during the cooling crystallisation in STRs (Chapter 5). An aliquot of solution from the outlet was filtered, washed with double distilled water then left to air dry overnight before being transferred to the refrigerator for storage.



**Figure 7.17** SEM images of recrystallised ALA I (left) and ALA II (right) from the continuous crystallisation experiments. Scale bar on images represents 5  $\mu\text{m}$ .

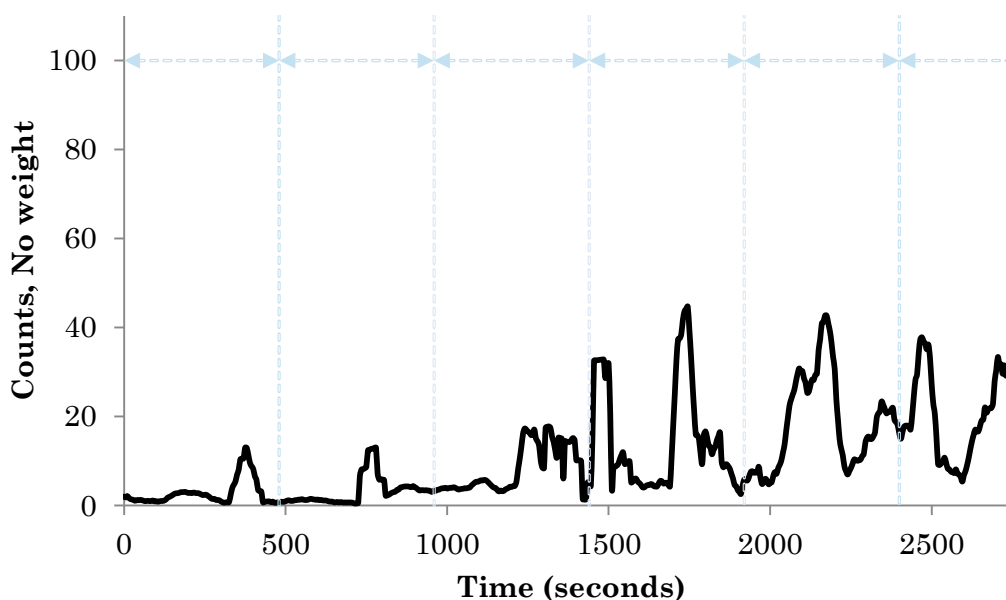
It was concluded that the crystallisation technique (batch STR studied in Chapter 5 or the continuous OBR) and the different hydrodynamic environments had little effect on the somewhat unusual surface topology and porosity. This feature was attributed to the experimental procedure used where cooling rates may not allow the growth steps to be fully completed resulting in such surface defects (Chapter 5).

ALA II crystals appear to be larger in comparison to the ALA I crystals. The growth kinetics of ALA I and ALA II have not been investigated in detail. However, there were indications (Chapter 4) that ALA II nucleates at lower supersaturations. The number of nuclei formed increase as supersaturation increases. At low supersaturation, the growth process is dominant whilst at higher supersaturations, the process is dominated by nucleation with a higher

number of nuclei formed, consuming supersaturation, thus, limiting crystal growth<sup>253</sup>. As such, it may be hypothesised that if ALA II does nucleate at a lower supersaturation, the growth process is mainly governing the size distribution of particles.

### 7.3.3 Continuous Crystallisation Experiments of ALA-NIC Co-crystal

The feasibility of continuous crystallisation was assessed with respect to ALA-NIC co-crystal. During continuous operation, FBRM has been used as a means of determining the point of nucleation and when steady state has been reached<sup>107, 108</sup>, in respect to the point at which the chord length or particle count do not change with time<sup>330</sup>. As the particle count was very low at the start of the experiment, nucleation was detected when particle count was around 100 (Figure 7.18).

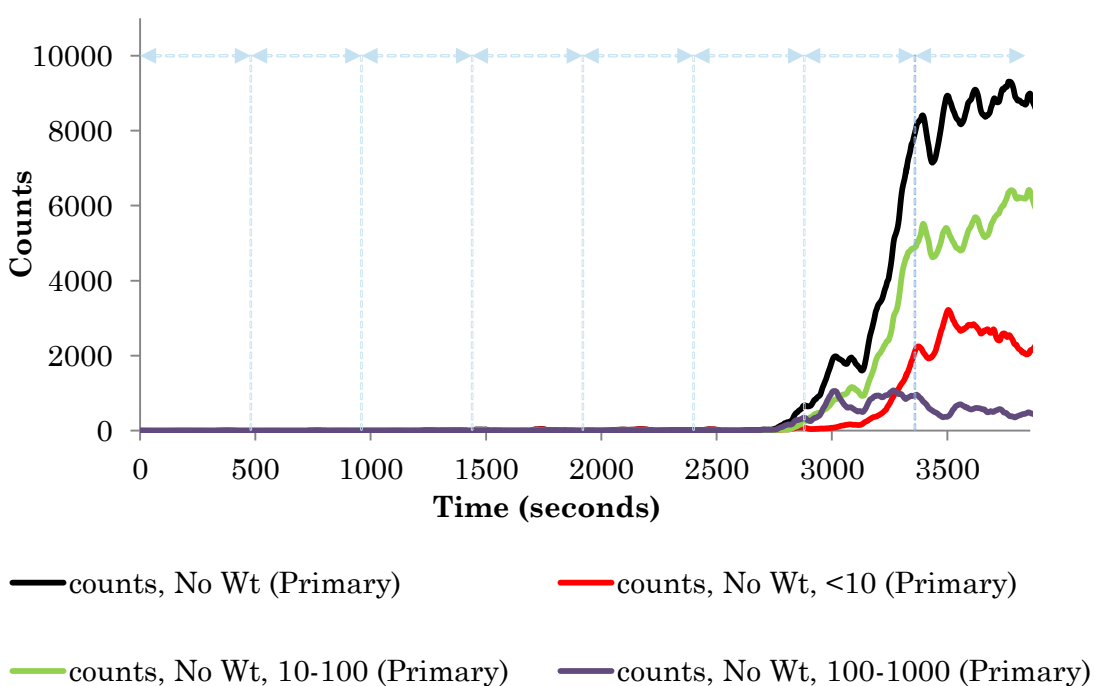


**Figure 7.18** CLD data collected from the flow cell between residence times (RT) 1-5, each segment represents one residence time (480 seconds).

The first 5 RT can be seen in Figure 7.19 and nucleation was confirmed to have taken place during the 5<sup>th</sup> RT with the system reaching steady-state within 1.5 RT's of nucleation. The results obtained here are in keeping with previously reported findings for cooling crystallisation performed in COBR's<sup>20, 107, 108</sup>. During continuous processing, there is a start-up period where system adjusts before reaching steady-state. The material produced under steady-state

operation should then be consistent and lie within the specified attributes. To achieve steady state, up to two RTs have been reported for unseeded crystallisation processes<sup>108</sup> and 1-1.5 RTs for seeded crystallisation processes<sup>107, 108</sup>. This difference has been attributed to the unseeded experiments relying upon a nucleation event prior to the appearance of crystals. Conversely, during seeded experiments, desupersaturation of the feed solution will begin as soon as seeds are introduced and these will grow as long as the process operates within the MSZW without fouling or product settling.

The CLD data for all the particle size bands is shown in Figure 7.19. The majority of the particles were between 10-100  $\mu\text{m}$  and particles between 100-1000  $\mu\text{m}$  contributed the least to the total particle count. This may be due to the experimental set up which is designed to induce nucleation and soon after nucleation the crystals leave the reactor, limiting subsequent growth. The abundance of smaller particle agrees with the batch STR crystallisation of ALA II at both 100 mL and 1000 mL scales (Chapter 5).



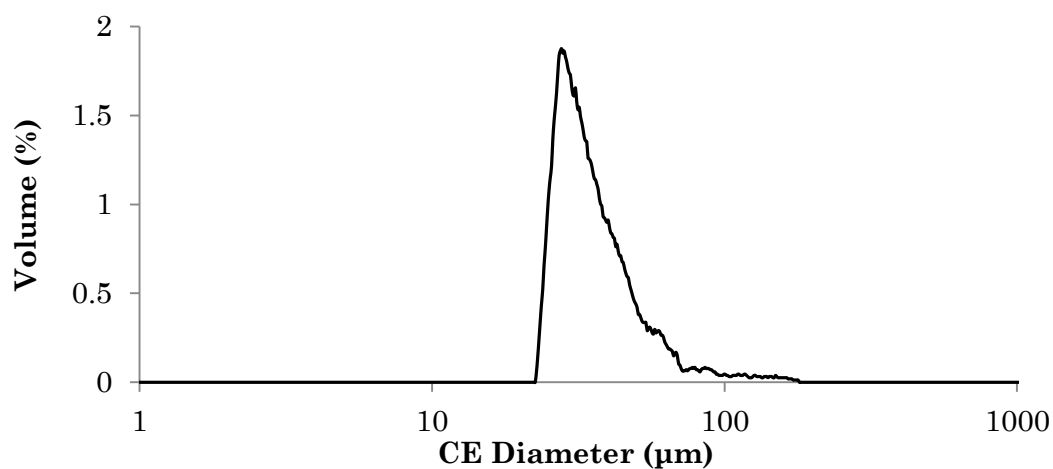
**Figure 7.19** FBRM data collected from the flow cell, each segment represent one RT (480 seconds) with a total run of 8 RT's.

Some peaks and troughs in the particle count can be seen (Figure 7.19). This has been reported in literature during the use of FBRM within an OBR

crystallisers<sup>107</sup>. This observation was attributed to the forward and backward motion provided by the oscillator and the subsequent movement of particles within the crystalliser. Also, ALA-NIC co-crystals appear to be plate like, intergrown and agglomerated and these crystal features may also contribute to some of the noise that is observed in the CLD (Figure 7.18 and Figure 7.19). Whilst this pulsing effect and crystal features do complicate interpretation of FBRM data, clear trends can be observed e.g. when steady state was reached.

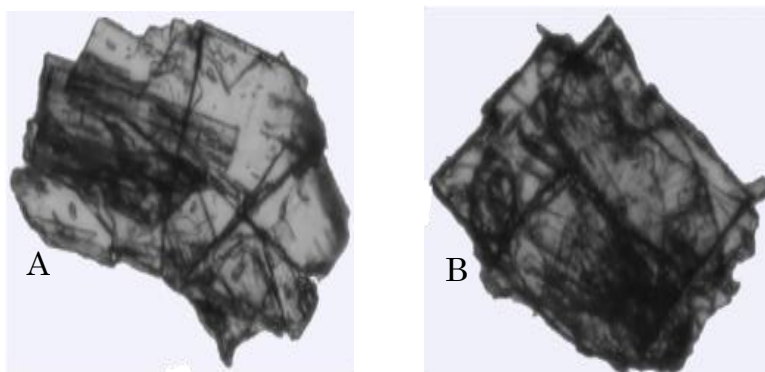
### 7.3.3.1 Particle Size Distribution

Off-line particle size analyses of the product from the continuous crystallisation experiments was carried out in triplicate. The average of three samples is shown in Figure 7.20. The crystals obtained from the COBR had a unimodal PSD with a  $D_{50}$  of 32.74  $\mu\text{m}$ ,  $D_{90}$  of 54.17  $\mu\text{m}$  and a standard deviation of 17.47  $\mu\text{m}$ . These results are in line with the FBRM result (Figure 7.19) where the largest contribution to the size distribution of particles came from particles between 10-100  $\mu\text{m}$ .



**Figure 7.20** Off-line PSD of ALA-NIC co-crystal.

A slight spread of the PSD to right can be seen (Figure 7.20). This is most likely due to agglomeration which is the clustering of crystals to form larger sized particles<sup>331</sup> (Figure 7.21).



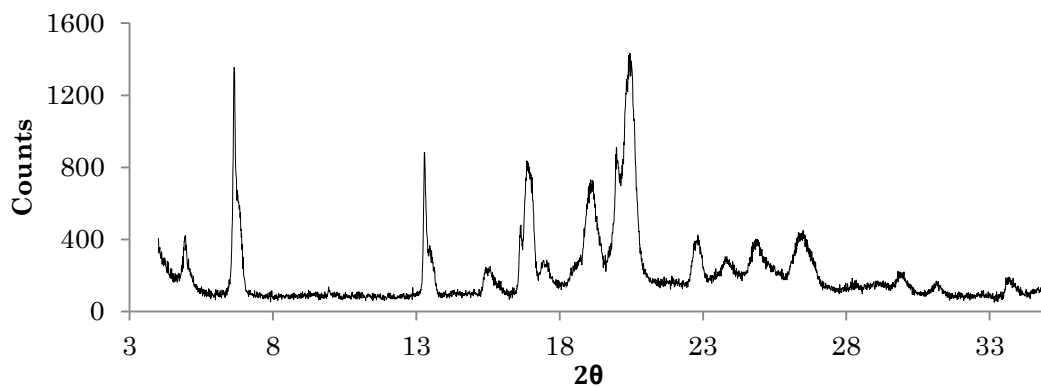
**Figure 7.21** Microscopy images of ALA-NIC co-crystals with evidence of agglomeration. CE diameter of crystal A: 164  $\mu\text{m}$  and B: 137  $\mu\text{m}$ .

Cooling rate, concentration, solvent and agitation rate have shown to impact likelihood for a system to agglomerate<sup>331</sup>. Whilst controlled agglomeration has shown to be a useful way of modifying particle properties<sup>332</sup>, it is often an undesirable process, especially for modelling of processes. It can affect achieving target CQAs by impacting growth rates<sup>42</sup> and reduce washing and drying efficiency downstream<sup>319</sup> and incorporation of ultrasonic irradiation has shown to reduce the amount of agglomerates<sup>333</sup>.

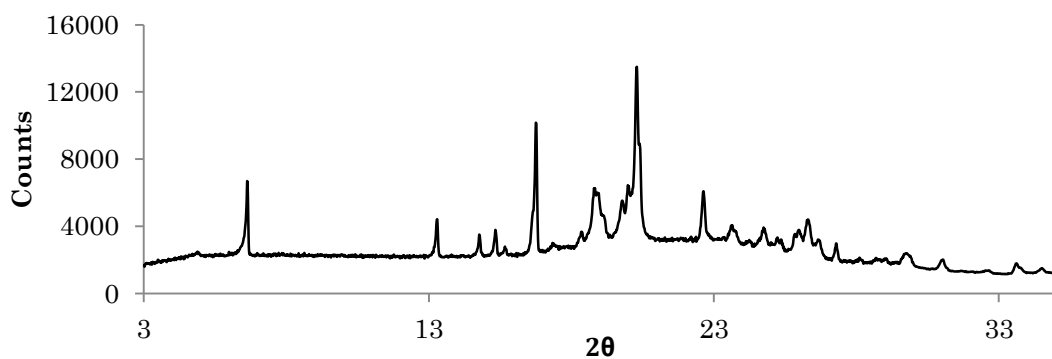


### 7.3.3.2 Solid Form

Samples obtained from the ALA-NIC co-crystal experiments were analysed with XRPD to confirm the solid form obtained (Figure 7.22 and Figure 7.23). Both patterns are comparable with each other and to the previously reported ALA-NIC co-crystal<sup>53</sup>, indicating the ALA-NIC co-crystal was successfully crystallised.



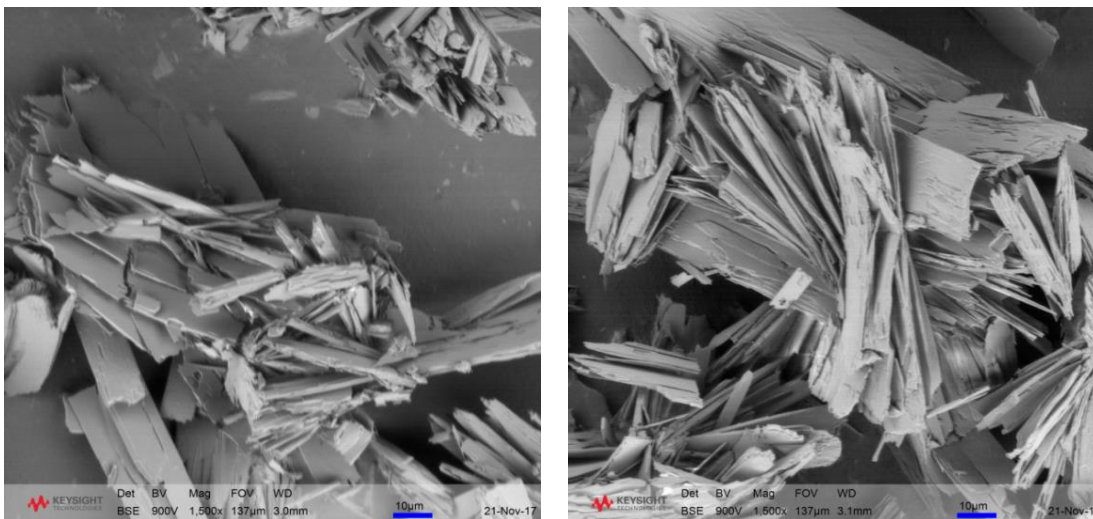
**Figure 7.22** Powder pattern ALA-NIC co-crystal (Exp-7-1).



**Figure 7.23** Powder pattern ALA-NIC co-crystal (Exp-7-2).

### 7.3.3.3 Crystal Morphology

Samples collected from the continuous experiments were examined also with SEM (Figure 7.24). They can be seen to be agglomerated, plate like crystals in keeping with the previous findings of the ALA-NIC co-crystal<sup>53</sup>.



**Figure 7.24** SEM images of ALA-NIC co-crystal obtained from the optimised continuous crystallisation experiments.

ALA-NIC co-crystal images appear to be solid, non-porous crystals, in contrast to the observations made for ALA I and ALA II. It was previously mentioned in Chapter 5 that, cooling rate can lead to surface irregularities; and in this case the final isolation temperature was increased. This would reduce the overall cooling rate and may have allowed the crystals to grow, completing each growth step fully.

Summary of the resultant solid form and yield obtained ((Equation 7.2) for all experiments are reported in Table 7.10.

$$\text{Yield (\%)} = \frac{\text{total mass obtained (g)}}{\text{mass flow rate } \left(\frac{\text{g}}{\text{min}}\right) \times \text{residence time (min)}} \times 100 \quad \text{Equation 7.2}$$

Whilst the potential application of hydrotrophy in a continuous environment has been effectively demonstrated for polymorphic control; further optimisation of this process would be necessary to allow phase pure isolation of ALA II. This should be possible as long as a suitable hydrodynamic environment for the

nucleation of ALA II is provided and SMPT is inhibited. Low yield may be due to the short residence time used during these experiments. To increase yield/productivity; a seeded crystallisation approach could be developed, RT could be increased, or the temperature profile in the reactor could be optimised.

**Table 7.9** Summary of results.

Exp	Expected	Obtained	Yield	Notes
1	ALA I	ALA I	33%	Control Experiment
2	ALA I	ALA I	48%	-
3	ALA II	ALA II & I	36%	-
4	ALA-NIC Cocrystal	ALA-NIC Cocrystal	12%	-
5	ALA II	ALA II & I	42.5%	Control Experiment
6	ALA-NIC Cocrystal	ALA-NIC Cocrystal	35%	Feasibility study (1)
7	ALA-NIC Cocrystal	ALA-NIC Cocrystal	32.6%	Feasibility study (2)

## 7.4 Challenges

This section provides a summary of some of the challenges faced during this work and how they were resolved.

### 7.4.1 Temperature Control

One of the first challenges faced was obtaining the desired temperature within the COBR. This was a major issue as if the desired temperature profile could not be achieved then the prospect of a successful crystallisation was at risk. It was identified that this was due to the lack of insulation around both the COBR and the piping from heater/chiller to COBR. The visual evidence of condensation and subsequent ice confirmed this. Thus, the first step was to insulate the COBR and piping with polyethylene, a form of thermoplastic insulation and aluminium. In addition to this, heater/chillers with a higher cooling capacity were used for CZ 4 and 5 (*Lauda RP 855*). These steps helped considerably and

much more realistic conditions were achieved within the crystalliser. However, the heater/chillers were controlled manually and some fluctuations between experiments can be seen. Temperature control in CZ 3 was particularly challenging as the straight was partially covered with the perspex box (used during the RTD experiments in Chapter 6) and thus could not be fully thermally insulated. Also, for CZ 1-3 HC with a smaller cooling capacity were used (*Lauda Eco RE 630*). For future works, implementation of real time control and use of higher specification HC for all CZ would likely allow tighter control of crystalliser temperature.

#### **7.4.2 Flow and Concentration Adjustment**

The aim was to allow both streams to be mixed in the first temperature zone before being subjected to cooling profile. However, it was also the ratio of each flow which controlled the polymorphic outcome. If the NIC stream had a significantly higher flow rate, it was exposed to the cooling before being mixed with IPA leading to formation of ice and subsequently blocking of the reactor. To overcome this, the stock concentration of NIC solution was increased without increasing the flow rate. This enabled both streams to be mixed and the freezing point of the solid was lowered sufficiently to continue with the experiment.

#### **7.4.3 Isolation and Wash Step**

The aim of this work was to isolate the metastable form of ALA as previously detailed. However, conditions of isolation meant there was a danger of the form dissolving or converting once the slurry left the temperature controlled environment. To minimise this, firstly the outlet was kept as short as possible and a continuous filtration set up was attached. This allowed the slurry to be filtered and washed as soon as it left the crystalliser therefore minimising the likelihood of dissolution or other phenomena.

## 7.5 Summary

Overall, the concentration of NIC was confirmed to have a strong impact on the solid state of ALA crystallised in continuous mode. Three different concentrations of NIC were used with the aim of producing the previously studied three different solid state forms. All ALA polymorphs were produced which represents a systematic study of the continuous crystallisation of both single and multi-component systems through exploitation of hydrotrophy.

Whilst the continuous isolation experiments revealed fouling and subsequent blockages this was partially addressed by lowering stock solution concentrations and increasing isolation temperatures.

Phase pure isolation of ALA II was not possible and several contributing factors have been identified. To attain both higher yield and pure ALA II in the continuous crystallisation processes, increasing the residence time and increasing the number of cooling stages should be considered.

This work is the first reporting the feasibility of this mesoscale OBR for the purposes of crystallisation. Overall, the mesoscale OBR has shown significant potential as a lab scale continuous crystalliser. In this case study, the experimental set-up has allowed the polymorphic form to be tailor made which thus far has not been possible for batch crystallisation techniques.

# **Chapter 8 Conclusions and Future Work**

## 8.1 Conclusions

This thesis reports the design and development of a novel meso scale OBR capable of continuous operation. Key conclusions for each of the chapters are summarised in the section below.

### 8.1.1 Chapter 4

A novel metastable polymorph of ALA (referred to as ALA II) which was previously obtained during co-crystallisation trials of ALA I and NIC was initially investigated at small scale (working volume < 10 mL).

- i. Crystal structure of ALA II has been determined and the theoretical morphology calculated. Comparison with experimental findings shows reasonable agreement although interesting topology of crystals was noted.
- ii. When crystallised under identical conditions, ALA II was obtained only in the presence of NIC. The hydrotropic action of NIC was confirmed by UV analysis.
- iii. The solid state outcome of ALA II is dictated by the presence and concentration of NIC, final temperature reached and process conditions.
- iv. ALA II, the metastable form, is isolated at lower supersaturation levels whereas at higher supersaturations the stable form formed. These observations suggest NIC has a structure directing or templating role in the solution, affecting the relative nucleation kinetics of ALA I and II in favouring the formation of ALA II.

### 8.1.2 Chapter 5

The controlled process conditions (temperature, stirrer speed) were identified at small scale (5 mL). The scale up of the crystallisation of ALA II was explored in 100 mL and 1000 mL STR to investigate the effect of process parameters on the polymorphic form. This allowed FBRM to be used to enhance process understanding.

- i. Experimental conditions under which ALA II was successfully crystallised have been characterised using CFD. CFD was used to compare the process conditions with respect to each crystallisation scale and select conditions.
- ii. ALA II was successfully taken from the discovery/screening stage (5 mL) and produced at both 100 mL and 1000 mL scales.
- iii. ALA II formation is relatively insensitive to mixing environment and is critically dependent upon NIC concentration and crystallisation temperature.

### 8.1.3 Chapter 6

A novel meso-scale COBR with an internal diameter of 10 mm (mesoscale) was designed, developed and characterised.

- i. The effect of baffle design on minimum amplitude required for full suspension of particles was studied. The work highlighted the reduction of minimum amplitude required in SPC compared to sharp edged baffles to achieve full particle suspension.
- ii. Liquid RTD along with CFD simulations have enhanced our understanding of the mixing regime within the COBR and indicated a range of oscillator conditions at which near plug-flow can be achieved. This provides a clear understanding of the prevailing process conditions during operation of continuous crystallisation.
- iii. The platform was integrated with a model predictive temperature control enabling automated setup and control of a key crystallisation parameter.



#### 8.1.4 Chapter 7

The feasibility of this novel OBR for the purposes of continuous crystallisation was investigated with the previously studied ALA-NIC system (Chapter 4 and 5). The goal was to control a key pharmaceutical attribute, specifically crystal form.

- i. Three different concentrations of NIC were used to isolate the three known solid-states of ALA (namely; ALA I, ALA II and ALA-NIC co-crystal) confirming the NIC role in controlling the solid state of ALA and is translated to a continuous flow environment.
- ii. The continuous experiments encountered fouling and blockages which was addressed by lowering stock solution concentrations and isolation temperatures. Further optimisation of the process could be achieved.
- iii. Meso scale COBR can control the polymorphic form of ALA, providing access to a wide range of material properties in a highly controlled and scalable manner.

## **8.2 Recommendations for Future Work**

The experimental work reported here suggests firstly; that polymorphic control is possible through the use of hydrotropes and secondly; that the meso scale OBR system is showing significant potential as a lab scale continuous crystalliser. However, scope for more experimentation in this area of research in order to enhance application of this technology and optimisation of processes is required. Some recommendations for future work are considered in the following sections.

### **8.2.1 Hydrotropes and Crystallisation**

Progression of this work would be to identify further hydrotrope API systems to determine if polymorphic control can be achieved as demonstrated with the ALA system. Crucially, this would highlight the potential transferability of this approach. This will also enable the development of a database of hydrotrope-API interactions which will complement the existing literature. Solubilisation through hydrotropy has been predicted using machine learning algorithms based on considerations of molecular properties<sup>184</sup>. Using the database created and machine learning methods the possibility of rapid and suitable hydrotrope selection may be possible and process development can take place without material/time consuming screening procedures. Application of hydrotropes to form screening would provide access to novel forms potentially.

### **8.2.2 Lipoic Acid and Hydrotropes**

A basic phase diagram of ALA as a function of NIC concentration (at constant solvent composition and temperature) has been investigated. It will be important to develop a comprehensive understanding of ALA-NIC phase behaviour as a function of e.g. cooling profile, mixing regime and isolation temperature using techniques including UV (concentration data) and Raman (information regarding solid form). This will be the base for effective continuous processes to be established to control the crystallisation of ALA.

An understanding of the phase diagram will allow systematic approaches to be taken for the development of crystallisation processes as recently reported for the continuous cooling crystallisation of paracetamol<sup>319</sup>. However, crystallisation

processes are further complicated by the presence and effects of additives and the approaches need to account for this. Building a systematic method through the use of workflows, the main areas identified for control and optimisation of the crystallisation processes of ALA in the presence of NIC are; process parameters (e.g. supersaturation, temperature, concentration of NIC and fouling), the quality attributes (e.g. purity, crystal size, size distribution and solid form) and modelling of process parameters with the final crystal attributes. Further work is required also to understand the cause of the porous and pitted crystal morphology. Studying the nucleation and growth of ALA II using Atomic force microscopy (AFM) may allow the surface of the crystals to be analysed and allow further information to be gathered.

### **8.2.3 Platform and Predictive Capabilities**

Building upon the work described in chapters 4, 6 and 7, first principle and empirical modelling provides a way towards the fundamental understanding of crystallisation behaviour of APIs in the presence of hydrotropes. In combination with MPC, the success of in-line PAT in allowing target attributes to be reached rapidly has been demonstrated for the crystallisation of lactose<sup>303</sup>. In the reported example, reactor temperature, solution concentration and crystal size were monitored and adjusted to reach the desired crystal attributes. Such workflows will provide the basis for multicomponent crystallisations or crystallisation of APIs in the presence of additives e.g. where the concentration of hydrotrope additives is the control variable.

Initial indicators of enhanced heat transfer have been identified for a meso-scale OBR (Chapter 6). Further investigation is needed to understand and control this property to be able to design the suitable controlled cooling profiles. Such studies will complement the RTD findings. A further extension of the RTD work (Chapter 6) would be to combine RTD profiles with other predictive modelling tools (population balance modelling which will describe phenomena including nucleation, growth, attrition and agglomeration), allowing the crystal properties to be modelled as a function of different mixing regimes accessed within the meso COBR.

To advance the capabilities of the meso scale COBR, the current materials of construction (glass) and the way in which the straights are connected can be improved to allow a more robust plug-play set-up. If the neck of the straights could be strengthened with the aid of a plastic sheath, this may act as a cushion and reduce the contact and pressure generated during tightening of the metal clips which rest on the glass straight. This will allow the platform to be quickly modified to suit other types of crystallisation processes including; anti-solvent or API's with different nucleation/growth kinetics. This is a key aim in enabling flexible, modular processing.

#### **8.2.4 Continuous Processing**

This work has illustrated the application of combining two individual continuous feed streams to control the solid form of ALA with the basic integration of a filtration set up (Chapter 7). To further demonstrate the possibility of end-to-end continuous manufacturing, the current experimental procedure can be improved to mitigate the persistent fouling observed during the continuous crystallisation experiments. Different materials of construction<sup>334</sup>, ultrasound<sup>335</sup> or seeding approaches<sup>108</sup> have so far demonstrated to reduce the risk of fouling.

The basic filtration set up, which was directly connected to the outlet of the reactor, can be improved and additional processes can be integrated. Achieving these goals, coupled with close-loop feedback to control, allows the ability to have on-demand, controlled manufacture of materials, with tight control of material attributes. The goal is to enable this, quickly, inexpensively and robustly.

# Chapter 9 Publications

- i. A factorial approach to understanding the effect of inner geometry of baffled meso-scale tubes on solids suspension and axial dispersion in continuous, oscillatory liquid-solid plug flows.

Ejim, LN, Yerdelen, S, McGlone, T, Onyemelukwe, I, Johnston, B, Florence, AJ & Reis, NM 2017, 'A factorial approach to understanding the effect of inner geometry of baffled meso-scale tubes on solids suspension and axial dispersion in continuous, oscillatory liquid-solid plug flows'. *Chemical Engineering Journal*, vol 308, pp. 669–682. DOI: 10.1016/j.cej.2016.09.013

- ii. Enabling precision manufacturing of active pharmaceutical ingredients: workflow for seeded cooling continuous crystallisations

Brown, CJ, McGlone, T, Yerdelen, S, Srirambhatla, V, Mabbott, F, Gurung, R, Briuglia, ML, Ahmed, B, Polyzois, H, McGinty, J, Perciballi, F, Fysikopoulos, D, Macfhionnghaile, P, Siddique, H, Raval, V, Harrington, TS, Vassileiou, A, Robertson, M, Prasad, E, Johnston, A, Johnston, B, Nordon, A, Srail, J, Halbert, G, Ter Horst, JH, Price, CJ, Rielly, CD, Sefcik, J & Florence, AJ, 2018, 'Enabling precision manufacturing of active pharmaceutical ingredients: workflow for seeded cooling continuous crystallisation' *Molecular Systems Design & Engineering*. 2018, **3**, pp518-549 DOI: 10.1039/C7ME00096K

## **Chapter 10** References

## 10.1 References

1. C. Badman and B. L. Trout, *J Pharm Sci*, 2015, **104**, 779-780.
2. K. Plumb, *Chemical Engineering Research and Design*, 2005, **83**, 730-738.
3. P. McKenzie, S. Kiang, J. Tom, A. E. Rubin and M. Futran, *AIChE Journal*, 2006, **52**, 3990-3994.
4. M. Mousazadeh, S. A. Torabi and B. Zahiri, *Computers & Chemical Engineering*, 2015, **82**, 115-128.
5. L. X. Yu, R. A. Lionberger, A. S. Raw, R. D'Costa, H. Wu and A. S. Hussain, *Advanced Drug Delivery Reviews*, 2004, **56**, 349-369.
6. B. S. Riley and X. Li, *AAPS PharmSciTech*, 2011, **12**, 114-118.
7. P. Kleinebudde, J. Khinast and J. Rantanen, *Continuous Manufacturing of Pharmaceuticals*, John Wiley & Sons, 2017.
8. J. Vercruyse, U. Delaet, I. Van Assche, P. Cappuyns, F. Arata, G. Caporicci, T. De Beer, J. P. Remon and C. Vervaet, *Eur J Pharm Biopharm*, 2013, **85**, 1031-1038.
9. M. M. Nasr, M. Krumme, Y. Matsuda, B. L. Trout, C. Badman, S. Mascia, C. L. Cooney, K. D. Jensen, A. Florence, C. Johnston, K. Konstantinov and S. L. Lee, *J Pharm Sci*, 2017, **106**, 3199-3206.
10. S. Lawton, G. Steele, P. Shering, L. Zhao, I. Laird and X.-W. Ni, *Organic Process Research & Development*, 2009, **13**, 1357-1363.
11. S. Mascia, P. L. Heider, H. Zhang, R. Lakerveld, B. Benyahia, P. I. Barton, R. D. Braatz, C. L. Cooney, J. M. B. Evans, T. F. Jamison, K. F. Jensen, A. S. Myerson and B. L. Trout, *Angewandte Chemie International Edition*, 2013, **52**, 12359-12363.
12. S. D. Schaber, D. I. Gerogiorgis, R. Ramachandran, J. M. B. Evans, P. I. Barton and B. L. Trout, *Industrial & Engineering Chemistry Research*, 2011, **50**, 10083-10092.
13. Q. Su, Z. K. Nagy and C. D. Rielly, *Chemical Engineering and Processing: Process Intensification*, 2015, **89**, 41-53.
14. M. Poliakoff and P. Licence, *Nature*, 2007, **450**, 810-812.
15. G. S. Calabrese and S. Pissavini, *AIChE Journal*, 2011, **57**, 828-834.



16. N. G. Anderson, *Organic Process Research & Development*, 2001, **5**, 613-621.
17. D. Zhang, S. Xu, S. Du, J. Wang and J. Gong, *Engineering*, 2017, **3**, 354-364.
18. D. J. Ende, *Chemical Engineering in the Pharmaceutical Industry: R&D to Manufacturing*, Wiley, 2010.
19. C. M. Chew and R. I. Ristic, *AIChE Journal*, 2005, **51**, 1576-1579.
20. L. Palmer, University of Strathclyde, 2013.
21. C. J. Callahan and X.-W. Ni, *CrystEngComm*, 2014, **16**, 690-697.
22. R. Davey and J. Garside, *From Molecules to Crystallizers*, Oxford University Press, 2000.
23. M. Fujiwara, Z. K. Nagy, J. W. Chew and R. D. Braatz, *Journal of Process Control*, 2005, **15**, 493-504.
24. G. He, A. B. H. Wong, P. S. Chow and R. B. H. Tan, *J Cryst Growth*, 2011, **314**, 220-226.
25. S. Datta and D. J. W. Grant, *Crystal Research and Technology*, 2005, **40**, 233-242.
26. P. Barrett and B. Glennon, *Chemical Engineering Research and Design*, 2002, **80**, 799-805.
27. L.-y. Wang, L. Zhu, L.-b. Yang, Y.-f. Wang, Z.-l. Sha and X.-y. Zhao, *J Cryst Growth*, 2016, **437**, 32-41.
28. J. Atherton, I. Houson and M. Talford, in *Process Understanding*, Wiley-VCH Verlag GmbH & Co. KGaA, 2011, DOI: 10.1002/9783527637140.ch4, pp. 87-125.
29. M. Lenka and D. Sarkar, *J Cryst Growth*, 2014, **408**, 85-90.
30. B. Marciniak, *J Cryst Growth*, 2002, **236**, 347-356.
31. S. Boyd, K. Back, K. Chadwick, R. J. Davey and C. C. Seaton, *J Pharm Sci*, 2010, **99**, 3779-3786.
32. N. Lyczko, F. Espitalier, O. Louisnard and J. Schwartzentruber, *Chemical Engineering Journal*, 2002, **86**, 233-241.
33. L. L. Simon, Z. K. Nagy and K. Hungerbuhler, *Chemical Engineering Science*, 2009, **64**, 3344-3351.

34. S. Karthika, T. K. Radhakrishnan and P. Kalaichelvi, *Cryst Growth Des*, 2016, **16**, 6663-6681.
35. J. W. Mullin, in *Crystallization (Fourth Edition)*, Butterworth-Heinemann, Oxford, 2001, DOI: <http://dx.doi.org/10.1016/B978-075064833-2/50007-3>, pp. 181-215.
36. A. S. Myerson, *Faraday Discussions*, 2015, **179**, 543-547.
37. J. Litster, *Design and Processing of Particulate Products*, Cambridge University Press, Cambridge, 2016.
38. D. Erdemir, A. Y. Lee and A. S. Myerson, *Accounts of Chemical Research*, 2009, **42**, 621-629.
39. D. Zahn, *Chemphyschem*, 2015, **16**, 2069-2075.
40. D. Gebauer and H. Cölfen, *Nano Today*, 2011, **6**, 564-584.
41. M. Liiri, T. Koironen and J. Aittamaa, *J Cryst Growth*, 2002, **237-239**, **Part 3**, 2188-2193.
42. P. H. Karpinski and J. S. Wey, in *Handbook of Industrial Crystallization (Second Edition)*, Butterworth-Heinemann, Woburn, 2002, DOI: <http://dx.doi.org/10.1016/B978-075067012-8/50008-2>, pp. 141-160.
43. J. W. Mullin, in *Crystallization (Fourth Edition)*, Butterworth-Heinemann, Oxford, 2001, DOI: <http://dx.doi.org/10.1016/B978-075064833-2/50008-5>, pp. 216-288.
44. C. F. Abegg, J. D. Stevens and M. A. Larson, *AIChE Journal*, 1968, **14**, 118-122.
45. T. Vetter, M. Iggländ, D. R. Ochsenein, F. S. Hänseler and M. Mazzotti, *Cryst Growth Des*, 2013, **13**, 4890-4905.
46. D. E. Horgan, L. M. Crowley, S. P. Stokes, S. E. Lawrence and H. A. Moynihan, in *Advanced Topics in Crystallization*, ed. Y. Mastai, InTech, Rijeka, 2015, DOI: 10.5772/59715, p. Ch. 03.
47. J. Liu, Z. Chang, X. Sun, S. Shen, C. Lei and H. Liu, *J Cryst Growth*, 2006, **291**, 448-454.
48. N. Variankaval, A. S. Cote and M. F. Doherty, *AIChE Journal*, 2008, **54**, 1682-1688.
49. E. H. Lee, *Asian Journal of Pharmaceutical Sciences*, 2014, **9**, 163-175.

50. A. J. Aguiar, J. Krc, A. W. Kinkel and J. C. Samyn, *J Pharm Sci*, 1967, **56**, 847-853.
51. M. Pudipeddi and A. T. M. Serajuddin, *J Pharm Sci*, 2005, **94**, 929-939.
52. Food and Drug Administration Center for Drug Evaluation and Research (CDER), Regulatory Classification of Pharmaceutical Co-Crystals, U.S. Department of Health and Human Service, 2013, 5.
53. L. Zhao, V. Raval, N. E. B. Briggs, R. M. Bhardwaj, T. McGlone, I. D. H. Oswald and A. J. Florence, *Crystengcomm*, 2014, **16**, 5769-5780.
54. K. Wittering, J. King, L. Thomas and C. Wilson, *Crystals*, 2014, **4**, 123.
55. S. Agharkar, S. Lindenbaum and T. Higuchi, *J Pharm Sci*, 1976, **65**, 747-749.
56. A. L. Grzesiak, M. Lang, K. Kim and A. J. Matzger, *J Pharm Sci*, 2003, **92**, 2260-2271.
57. M. R. Abu Bakar, Z. K. Nagy, A. N. Saleemi and C. D. Rielly, *Cryst Growth Des*, 2009, **9**, 1378-1384.
58. D. Winn and M. F. Doherty, *AIChE Journal*, 2000, **46**, 1348-1367.
59. R. H. Braatz, Shinhi., 2002.
60. J. H. ter Horst, C. Schmidt and J. Ulrich, in *Handbook of Crystal Growth (Second Edition)*, Elsevier, Boston, 2015, DOI: <http://doi.org/10.1016/B978-0-444-63303-3.00032-8>, pp. 1317-1349.
61. T. Vetter, C. L. Burcham and M. F. Doherty, *Chemical Engineering Science*, 2014, **106**, 167-180.
62. R. Liu, *Water-Insoluble Drug Formulation, Second Edition*, CRC Press, Boca Raton, FL, 2008.
63. H. Choi, W. Lee, J. Lee, H. Chung and W. S. Choi, *Metals and Materials International*, 2007, **13**, 353-358.
64. V. K. Sharma, Preparation of micron-size pharmaceutical particles by microfluidization, 2003.
65. G. G. Liversidge and K. C. Cundy, *Int J Pharm*, 1995, **125**, 91-97.
66. P. Cruz, F. Rocha and A. Ferreira, *Crystengcomm*, 2016, **18**, 9113-9121.
67. European Medicines Agency, ICH Topic Q4B Annex 12 Analytical Sieving General Chapter, 2009.

68. P. A. Meenan, S. R. Anderson and D. L. Klug, in *Handbook of Industrial Crystallization (Second Edition)*, Butterworth-Heinemann, Woburn, 2002, DOI: <http://doi.org/10.1016/B978-075067012-8/50005-7>, pp. 67-100.
69. A. Nokhodchi, N. Bolourtchian and R. Dinarvand, *Int J Pharm*, 2003, **250**, 85-97.
70. S. Watterson, S. Hudson, M. Svård and Å. C. Rasmuson, *Fluid Phase Equilibria*, 2014, **367**, 143-150.
71. R. E. Gordon and S. I. Amin, Crystallization of ibuprofen, *Google Patents*, 1984.
72. D. Cheuk, M. Svard, C. Seaton, P. McArdle and A. C. Rasmuson, *Crystengcomm*, 2015, **17**, 3985-3997.
73. S. Banga, G. Chawla, D. Varandani, B. R. Mehta and A. K. Bansal, *The Journal of pharmacy and pharmacology*, 2007, **59**, 29-39.
74. M. Guo, Q. Fu, C. Wu, Z. Guo, M. Li, J. Sun, Z. He and L. Yang, *Colloids and Surfaces B: Biointerfaces*, 2015, **128**, 410-418.
75. H. Schiweck, M. Clarke and G. Pollach, in *Ullmann's Encyclopedia of Industrial Chemistry*, Wiley-VCH Verlag GmbH & Co. KGaA, 2000, DOI: 10.1002/14356007.a25\_345.pub2.
76. G. Westphal, G. Kristen, W. Wegener, P. Ambatiello, H. Geyer, B. Epron, C. Bonal, G. Steinhauser and F. Götzfried, in *Ullmann's Encyclopedia of Industrial Chemistry*, Wiley-VCH Verlag GmbH & Co. KGaA, 2000, DOI: 10.1002/14356007.a24\_317.pub4.
77. P. Sriamornsak and K. Burapapadh, *Asian Journal of Pharmaceutical Sciences*, 2015, **10**, 230-238.
78. H. J. M. Kramer, S. K. Bermingham and G. M. van Rosmalen, *J Cryst Growth*, 1999, **198-199, Part 1**, 729-737.
79. J.-P. Astier and S. Veessler, *Cryst Growth Des*, 2008, **8**, 4215-4219.
80. G. J. Witkamp, J. P. Vrijenhoef, J. de Graauw and F. van der Ham, Crystallisation of materials from aqueous solutions, *Google Patents*, 2006.
81. Z. K. Nagy, M. Fujiwara and R. D. Braatz, *Journal of Process Control*, 2008, **18**, 856-864.

82. M. Knox, M. Trifkovic and S. Rohani, *Chemical Engineering Science*, 2009, **64**, 3555-3563.
83. M. Trifkovic, M. Sheikhzadeh and S. Rohani, *J Cryst Growth*, 2009, **311**, 3640-3650.
84. A. N. Saleemi, C. D. Rielly and Z. K. Nagy, *Chemical Engineering Science*, 2012, **77**, 122-129.
85. S. C. Barthe, M. A. Grover and R. W. Rousseau, *Cryst Growth Des*, 2008, **8**, 3316-3322.
86. X. Liu, D. Sun, F. Wang, Y. Wu, Y. Chen and L. Wang, *J Pharm Sci*, 2011, **100**, 2452-2459.
87. P. Tipduangta, K. Takiuddin, L. Fábíán, P. Belton and S. Qi, *Cryst Growth Des*, 2015, **15**, 5011-5020.
88. S. L. Childs, L. J. Chyall, J. T. Dunlap, D. A. Coates, B. C. Stahly and G. P. Stahly, *Cryst Growth Des*, 2004, **4**, 441-449.
89. S. G. Antonio, C. O. Paiva-Santos and V. D. N. Bezzon, *Journal of Pharmaceutical Sciences*, 2014, **103**, 3567-3575.
90. KeySight. Technologies, Using a Compact Low Voltage FE-SEM in Evaluating Materials Nano-Porosity: Preliminary Study, 2015.
91. Malvern, Dynamic Light Scattering (DLS), <https://www.malvern.com/en/products/technology/dynamic-light-scattering>, (accessed 11/02/2018, 2018).
92. A. Jawor-Baczynska, J. Sefcik and B. D. Moore, *Cryst Growth Des*, 2013, **13**, 470-478.
93. W. I. Goldburg, *American Journal of Physics*, 1999, **67**, 1152-1160.
94. C. Xu, X. Cai, J. Zhang and L. Liu, *Particuology*, 2015, **19**, 82-85.
95. L. Liu, X. Cai, J. Zhang and C. Xu, *Procedia Engineering*, 2015, **102**, 904-910.
96. R. Shaw, Dynamic Light Scattering Training, DOI: <http://149.171.168.221/partcat/wp-content/uploads/Malvern-Zetasizer-LS.pdf>.
97. R. Natarajan, L. Bridgland, A. Sirikulajorn, J.-H. Lee, M. F. Haddow, G. Magro, B. Ali, S. Narayanan, P. Strickland, J. P. H. Charmant, A. G.

- Orpen, N. B. McKeown, C. G. Bezzu and A. P. Davis, *J Am Chem Soc*, 2013, **135**, 16912-16925.
98. J. Tian, P. K. Thallapally and B. P. McGrail, *Crystengcomm*, 2012, **14**, 1909-1919.
99. J. R. Holst, A. Trewin and A. I. Cooper, *Nat Chem*, 2010, **2**, 915-920.
100. J. C. Groen, L. A. A. Peffer and J. Pérez-Ramírez, *Microporous and Mesoporous Materials*, 2003, **60**, 1-17.
101. D. Giron, *Journal of Thermal Analysis and Calorimetry*, 2002, **68**, 335-357.
102. M. M. Knopp, K. Löbmann, D. P. Elder, T. Rades and R. Holm, *European Journal of Pharmaceutical Sciences*, 2016, **87**, 164-173.
103. J. F. Gamble, A. P. Ferreira, M. Tobyn, L. DiMemmo, K. Martin, N. Mathias, R. Schild, B. Vig, J. M. Baumann, S. Parks and M. Ashton, *International Journal of Pharmaceutics*, 2014, **465**, 210-217.
104. H. Kinnunen, G. Hebbink, H. Peters, D. Huck, L. Makein and R. Price, *International Journal of Pharmaceutics*, 2015, **478**, 53-59.
105. S. C. Das, S. R. B. Behara, D. A. V. Morton, I. Larson and P. J. Stewart, *Powder Technology*, 2013, **249**, 297-303.
106. A. Krupa, R. Jachowicz, M. Kurek, W. Figiel and M. Kwiecień, *Powder Technology*, 2014, **266**, 329-339.
107. H. Siddique, C. J. Brown, I. Houson and A. J. Florence, *Organic Process Research & Development*, 2015, **19**, 1871-1881.
108. N. E. B. Briggs, University of Strathclyde, 2015.
109. K. Wittering, University of Bath, 2015.
110. K. B. Smith and M. R. Mackley, *Chemical Engineering Research and Design*, 2006, **84**, 1001-1011.
111. P. Stonestreet and P. M. J. Van Der Veeke, *Chemical Engineering Research and Design*, 1999, **77**, 671-684.
112. A. W. Dickens, M. R. Mackley and H. R. Williams, *Chemical Engineering Science*, 1989, **44**, 1471-1479.
113. P. Stonestreet and A. P. Harvey, *Chemical Engineering Research and Design*, 2002, **80**, 31-44.

114. J. Hofinger, The University of Birmingham, 2012.
115. T. McGlone, N. E. B. Briggs, C. A. Clark, C. J. Brown, J. Sefcik and A. J. Florence, *Organic Process Research & Development*, 2015, **19**, 1186-1202.
116. M. S. Abbott, A. P. Harvey, G. V. Perez and M. K. Theodorou, *Interface focus*, 2013, **3**, 20120036.
117. C. R. Brunold, J. C. B. Hunns, M. R. Mackley and J. W. Thompson, *Chemical Engineering Science*, 1989, **44**, 1227-1244.
118. X. Ni, G. Brogan, A. Struthers, D. C. Bennett and S. F. Wilson, *Chemical Engineering Research and Design*, 1998, **76**, 635-642.
119. X. Ni and S. Gao, *The Chemical Engineering Journal and the Biochemical Engineering Journal*, 1996, **63**, 157-166.
120. X. Ni, Y. Zhang and I. Mustafa, *Chemical Engineering Science*, 1998, **53**, 2903-2919.
121. A. N. Phan, A. Harvey and J. Lavender, *Chemical Engineering and Processing*, 2011, **50**, 254-263.
122. Y. Zhang, X. Ni and I. Mustafa, *Journal of Chemical Technology & Biotechnology*, 1996, **66**, 305-311.
123. P. Gough, X. Ni and K. C. Symes, *Journal of Chemical Technology & Biotechnology*, 1997, **69**, 321-328.
124. A. P. Harvey, M. R. Mackley and P. Stonestreet, *Industrial & Engineering Chemistry Research*, 2001, **40**, 5371-5377.
125. X. Ni and P. Gough, *Chemical Engineering Science*, 1997, **52**, 3209-3212.
126. N. E. B. Briggs, U. Schacht, V. Raval, T. McGlone, J. Sefcik and A. J. Florence, *Organic Process Research & Development*, 2015, **19**, 1903-1911.
127. C. J. Brown, J. A. Adelokun and X. Ni, *Chemical Engineering and Processing: Process Intensification*, 2015, **97**, 180-186.
128. H. McLachlan and X.-W. Ni, *J Cryst Growth*, 2016, **442**, 81-88.
129. X. Ni and A. Liao, *Chemical Engineering Journal*, 2010, **156**, 226-233.
130. L. R. Agnew, T. McGlone, H. P. Wheatcroft, A. Robertson, A. R. Parsons and C. C. Wilson, *Cryst Growth Des*, 2017, DOI: 10.1021/acs.cgd.6b01831.

131. Zeiss, MCS 600,  
<https://www.zeiss.com/spectroscopy/products/spectrometer-systems/mcs-600.html>).
132. Mettler. Toledo, ParticleTrack G400,  
[https://www.mt.com/gb/en/home/products/L1\\_AutochemProducts/FBRM-PVM-Particle-System-Characterization/FBRM/fbrm-g400.html](https://www.mt.com/gb/en/home/products/L1_AutochemProducts/FBRM-PVM-Particle-System-Characterization/FBRM/fbrm-g400.html)).
133. Bruker, TENSOR II FTIR Spectrometer,  
<https://www.bruker.com/products/infrared-near-infrared-and-raman-spectroscopy/ft-ir-routine-spectrometers/tensor/overview.html>).
134. Netzsch, DSC 214 Polyma, <https://www.netzsch-thermal-analysis.com/en/products-solutions/differential-scanning-calorimetry/dsc-214-polyma/>).
135. KeySight Technologies, Using a Compact Low Voltage FE-SEM in Evaluating Materials Nano-Porosity: Preliminary Study, 2000-2018.
136. Malvern Panalytical, Zetasizer Nano ZS,  
<https://www.malvernpanalytical.com/en/products/product-range/zetasizer-range/zetasizer-nano-range/zetasizer-nano-zs>).
137. M. Instruments, Dynamic Light Scattering: An Introduction in 30 Minutes,  
[https://warwick.ac.uk/fac/cross\\_fac/sciencecity/programmes/internal/themes/am2/booking/particlesize/intro\\_to\\_dls.pdf](https://warwick.ac.uk/fac/cross_fac/sciencecity/programmes/internal/themes/am2/booking/particlesize/intro_to_dls.pdf), (accessed 11/02/2018, 2018).
138. Q. Instruments, AUTOSORB SURFACE AREA AND PORE SIZE BY GAS SORPTION,  
[http://www.quantachrome.com/gassorption/autosorb\\_iq.html](http://www.quantachrome.com/gassorption/autosorb_iq.html)).
139. L. Microsystems, Fixed Stage Microscope for Electrophysiology Leica DM6000 FS, <https://www.leica-microsystems.com/products/light-microscopes/upright-microscopes/details/product/leica-dm6000-fs/>).
140. Bruker, The D8 ADVANCE Family.
141. Bruker, D2 Phaser, <https://www.bruker.com/products/x-ray-diffraction-and-elemental-analysis/x-ray-diffraction/d2-phaser/overview.html>).
142. Mettler Toledo.
143. Technobis Crystallization Systems, 2018.



144. Mettler Toledo, PVM V819 Technology, [https://www.mt.com/gb/en/home/products/L1\\_AutochemProducts/FBRM-PVM-Particle-System-Characterization/PVM/Lasentec\\_PVM\\_V819.html](https://www.mt.com/gb/en/home/products/L1_AutochemProducts/FBRM-PVM-Particle-System-Characterization/PVM/Lasentec_PVM_V819.html)).
145. G. R. Desiraju, *Chemical Communications*, 1997, DOI: 10.1039/A607149J, 1475-1482.
146. N. Blagden, M. de Matas, P. T. Gavan and P. York, *Advanced Drug Delivery Reviews*, 2007, **59**, 617-630.
147. A. O. Surov, K. A. Solanko, A. D. Bond, G. L. Perlovich and A. Bauer-Brandl, *Cryst Growth Des*, 2012, **12**, 4022-4030.
148. L. R. Agnew, D. L. Cruickshank, T. McGlone and C. C. Wilson, *Chemical Communications*, 2016, **52**, 7368-7371.
149. M. Lang, A. L. Grzesiak and A. J. Matzger, *J Am Chem Soc*, 2002, **124**, 14834-14835.
150. C.-H. Gu, K. Chatterjee, V. Young and D. J. W. Grant, *J Cryst Growth*, 2002, **235**, 471-481.
151. R. Thakuria and A. Nangia, *Acta Crystallogr C*, 2011, **67**, O461-O463.
152. C. Guillonneau, Y. Charton, Y.-M. Ginot, M.-V. Fouquier-d'Hérouël, M. Bertrand, B. Lockhart, P. Lestage and S. Goldstein, *European Journal of Medicinal Chemistry*, 2003, **38**, 1-11.
153. E. Dozio, M. Ruscica, L. Passafaro, G. Dogliotti, L. Steffani, A. Pagani, G. Demartini, D. Esposti, F. Frascini and P. Magni, *European Journal of Pharmacology*, 2010, **641**, 29-34.
154. M. D. Coleman, R. C. Eason and C. J. Bailey, *Environmental Toxicology and Pharmacology*, 2001, **10**, 167-172.
155. K. P. Shay, R. F. Moreau, E. J. Smith, A. R. Smith and T. M. Hagen, *Biochimica et Biophysica Acta (BBA) - General Subjects*, 2009, **1790**, 1149-1160.
156. H. S. Lee, M. H. Na and W. K. Kim, *Nutrition Research*, 2010, **30**, 403-409.
157. S.-J. Zhang, Q.-F. Ge, D.-W. Guo, W.-X. Hu and H.-Z. Liu, *Bioorganic & Medicinal Chemistry Letters*, 2010, **20**, 3078-3083.

158. M. J. Torres, A. Fierro, C. D. Pessoa-Mahana, J. Romero-Parra, G. Cabrera and M. Faúndez, *European Journal of Pharmacology*, DOI: <http://dx.doi.org/10.1016/j.ejphar.2017.01.038>.
159. Y. Kangawa, T. Yoshida, H. Abe, Y. Seto, T. Miyashita, M. Nakamura, T. Kihara, S.-m. Hayashi and M. Shibutani, *Experimental and Toxicologic Pathology*, DOI: <http://dx.doi.org/10.1016/j.etp.2016.12.004>.
160. L. Packer, E. H. Witt and H. J. Tritschler, *Free Radical Biology and Medicine*, 1995, **19**, 227-250.
161. I. L. Karle, J. A. Estlin and K. Britts, *Acta Crystallographica*, 1967, **22**, 567-573.
162. C.-P. Racz, S. Santa, M. Tomoaia-Cotisel, G. Borodi, I. Kacso, A. Pirnau and I. Bratu, *Journal of Inclusion Phenomena and Macrocyclic Chemistry*, 2013, **76**, 193-199.
163. A. F. Wagner, E. Walton, G. E. Boxer, M. P. Pruss, F. W. Holly and K. Folkers, *J Am Chem Soc*, 1956, **78**, 5079-5081.
164. R. C. Thomas and L. J. Reed, *J Am Chem Soc*, 1956, **78**, 6148-6149.
165. N. Ikuta, H. Sugiyama, H. Shimosegawa, R. Nakane, Y. Ishida, Y. Uekaji, D. Nakata, K. Pallauf, G. Rimbach, K. Terao and S. Matsugo, *International Journal of Molecular Sciences*, 2013, **14**, 3639.
166. H. Takahashi, Y. Bungo and K. Mikuni, *Bioscience, Biotechnology, and Biochemistry*, 2011, **75**, 633-637.
167. J. Zhang, L. Dang and H. Wei, *Journal of Chemical & Engineering Data*, 2010, **55**, 4025-4028.
168. P. Bauduin, A. Renoncourt, A. Kopf, D. Touraud and W. Kunz, *Langmuir*, 2005, **21**, 6769-6775.
169. J. J. Booth, S. Abbott and S. Shimizu, *The Journal of Physical Chemistry B*, 2012, **116**, 14915-14921.
170. C. V. Subbarao, I. P. K. Chakravarthy, A. V. S. L. S. Bharadwaj and K. M. M. K. Prasad, *Chem Eng Technol*, 2012, **35**, 225-237.
171. H. Suzuki and H. Sunada, *Chem Pharm Bull*, 1998, **46**, 125-130.
172. R. E. Coffman and D. O. Kildsig, *J Pharm Sci*, 1996, **85**, 951-954.

173. J. J. Booth, M. Omar, S. Abbott and S. Shimizu, *Physical Chemistry Chemical Physics*, 2015, **17**, 8028-8037.
174. Y. Cui, C. Y. Xing and Y. Q. Ran, *J Pharm Sci*, 2010, **99**, 3048-3059.
175. A. A. Rasool, A. A. Hussain and L. W. Ditter, *J Pharm Sci*, 1991, **80**, 387-393.
176. A. K. Jain, *Eur J Pharm Biopharm*, 2008, **68**, 701-714.
177. R. Sanghvi, D. Evans and S. H. Yalkowsky, *Int J Pharm*, 2007, **336**, 35-41.
178. N. Ahuja, O. P. Katare and B. Singh, *Eur J Pharm Biopharm*, 2007, **65**, 26-38.
179. L.-Y. Lim and M.-L. Go, *European Journal of Pharmaceutical Sciences*, 2000, **10**, 17-28.
180. A. M. Saleh and L. K. El-Khordagui, *Int J Pharm*, 1985, **24**, 231-238.
181. B. Haddou, J. P. Canselier and C. Gourdon, in *The Role of Colloidal Systems in Environmental Protection*, Elsevier, Amsterdam, 2014, DOI: <https://doi.org/10.1016/B978-0-444-63283-8.00005-3>, pp. 97-142.
182. G. A. Abdelbary, M. M. Amin and M. Abdelmoteleb, *Journal of Drug Delivery Science and Technology*, 2016, **33**, 98-113.
183. S. Agrawal, S. S. Pancholi, N. K. Jain and G. P. Agrawal, *Int J Pharm*, 2004, **274**, 149-155.
184. S. A. Damiati, L. G. Martini, N. W. Smith, J. M. Lawrence and D. J. Barlow, *Int J Pharm*, 2017, **530**, 99-106.
185. D. Balasubramanian, V. Srinivas, V. G. Gaikar and M. M. Sharma, *The Journal of Physical Chemistry*, 1989, **93**, 3865-3870.
186. W. Kunz, K. Holmberg and T. Zemb, *Current Opinion in Colloid & Interface Science*, 2016, **22**, 99-107.
187. S. Shimizu and N. Matubayasi, *The Journal of Physical Chemistry B*, 2014, **118**, 10515-10524.
188. J. Lee, S. C. Lee, G. Acharya, C.-j. Chang and K. Park, *Pharmaceut Res*, 2003, **20**, 1022-1030.
189. J. Y. Kim, S. Kim, M. Papp, K. Park and R. Pinal, *J Pharm Sci*, 2010, **99**, 3953-3965.

190. R. C. da Silva, M. Spitzer, L. s. H. M. da Silva and W. Loh, *Thermochimica Acta*, 1999, **328**, 161-167.
191. D. E. Guttman and M. Y. Athalye, *Journal of the American Pharmaceutical Association (Scientific ed.)*, 1960, **49**, 687-691.
192. R. A. Kenley, S. E. Jackson, J. S. Winterle, Y. Shunko and G. C. Visor, *J Pharm Sci*, 1986, **75**, 648-653.
193. R. E. Coffman and D. O. Kildsig, *J Pharm Sci*, 1996, **85**, 848-853.
194. S. Das and S. Paul, *The journal of physical chemistry. B*, 2016, **120**, 173-183.
195. S. Feldman and M. Gibaldi, *J Pharm Sci*, 1967, **56**, 370-375.
196. R. Schmid, *Monatshefte für Chemie / Chemical Monthly*, 2001, **132**, 1295-1326.
197. R. Breslow, in *Structure and Reactivity in Aqueous Solution*, American Chemical Society, 1994, vol. 568, ch. 20, pp. 291-302.
198. R. E. Coffman and D. O. Kildsig, *Pharmaceut Res*, 1996, **13**, 1460-1463.
199. R. Breslow and T. Guo, *Proceedings of the National Academy of Sciences of the United States of America*, 1990, **87**, 167-169.
200. W. Loh, A. E. Beezer and J. C. Mitchell, *Thermochimica Acta*, 1995, **255**, 83-91.
201. M. Hopkins Hatzopoulos, J. Eastoe, P. J. Dowding, S. E. Rogers, R. Heenan and R. Dyer, *Langmuir*, 2011, **27**, 12346-12353.
202. V. Srinivas and D. Balasubramanian, *Langmuir*, 1998, **14**, 6658-6661.
203. D. Subramanian, J. B. Klauda, J. Leys and M. A. Anisimov, *Herald of St. Petersburg University*, 2013.
204. Bruker, Apex3 Software, <https://www.bruker.com/products/x-ray-diffraction-and-elemental-analysis/single-crystal-x-ray-diffraction/overview/sc-xrd-software/apex3.html>).
205. G. M. Sheldrick, SADABS, Programs for Scaling and Absorption Correction of Area Detector Data).
206. O. V. Dolomanov, Bourhis, L. J., Gildea, R. J., Howard, J. A. K. & Puschmann, H. , *Journal of Applied Crystallography*, 2009, **42**, 339-341.

207. L. J. Reed, I. C. Gunsalus, G. H. F. Schnakenberg, Q. F. Soper, H. E. Boaz, S. F. Kern and T. V. Parke, *J Am Chem Soc*, 1953, **75**, 1267-1270.
208. CCDC, Cambridge Structural Database, Mercury).
209. R. M. Stroud and C. H. Carlisle, *Acta Crystallographica Section B*, 1972, **28**, 304-307.
210. E. H. Lee, S. R. Byrn and M. T. Carvajal, *Pharmaceut Res*, 2006, **23**, 2375-2380.
211. D. R. Grant and P. Myrdal, in *Polymorphism in Pharmaceutical Solids, Second Edition*, CRC Press, 2009, DOI: doi:10.3109/9781420073225-13 10.3109/9781420073225-13, pp. 436-480.
212. X. Mei and C. Wolf, *Cryst Growth Des*, 2004, **4**, 1099-1103.
213. R. R. Schartman, *Int J Pharm*, 2009, **365**, 77-80.
214. S. J. Nehm, B. Rodríguez-Spong and N. Rodríguez-Hornedo, *Cryst Growth Des*, 2006, **6**, 592-600.
215. X. Yang, J. Lu, X. Wang and C. B. Ching, *Journal of Raman Spectroscopy*, 2008, **39**, 1433-1439.
216. R. Bobrovs, L. Seton and A. Actins, *Crystengcomm*, 2014, **16**, 10581-10591.
217. D. M. Croker, R. J. Davey, A. C. Rasmuson and C. C. Seaton, *Crystengcomm*, 2013, **15**, 2044-2047.
218. A. Maher, D. M. Croker, Å. C. Rasmuson and B. K. Hodnett, *Cryst Growth Des*, 2012, **12**, 6151-6157.
219. A. Maher, D. M. Croker, C. C. Seaton, Å. C. Rasmuson and B. K. Hodnett, *Cryst Growth Des*, 2014, **14**, 3967-3974.
220. A. E. Robertson, D. H. Phan, J. E. Macaluso, V. N. Kuryakov, E. V. Jouravleva, C. E. Bertrand, I. K. Yudin and M. A. Anisimov, *Fluid Phase Equilibria*, 2016, **407**, 243-254.
221. D. Subramanian, C. T. Boughter, J. B. Klauda, B. Hammouda and M. A. Anisimov, *Faraday Discussions*, 2013, **167**, 217-238.
222. P. Bonnett, K. Carpenter, S. Dawson and R. Davey, *Chemical communications*, 2003, 698-699.
223. S. A. Vitale and J. L. Katz, *Langmuir*, 2003, **19**, 4105-4110.

224. Y. Georgalis, A. M. Kierzek and W. Saenger, *The Journal of Physical Chemistry B*, 2000, **104**, 3405-3406.
225. S. Jiang and J. H. ter Horst, *Cryst Growth Des*, 2011, **11**, 256-261.
226. N. Rodríguez-hornedo and D. Murphy, *J Pharm Sci*, 1999, **88**, 651-660.
227. T.-T. C. Lai, S. Ferguson, L. Palmer, B. L. Trout and A. S. Myerson, *Organic Process Research & Development*, 2014, **18**, 1382-1390.
228. C.-H. Gu, V. Young and D. J. W. Grant, *J Pharm Sci*, 2001, **90**, 1878-1890.
229. P. T. Cardew and R. J. Davey, presented in part at the Symposium on the Tailoring of Crystal Growth, Institution of Chemical Engineers, London, 1982.
230. Y. Sonoda, F. Hirayama, H. Arima, Y. Yamaguchi, W. Saenger and K. Uekama, *Cryst Growth Des*, 2006, **6**, 1181-1185.
231. G. M. Day, A. V. Trask, W. D. S. Motherwell and W. Jones, *Chemical Communications*, 2006, DOI: 10.1039/B513442K, 54-56.
232. B. Lou, D. Boström and S. P. Velaga, *Cryst Growth Des*, 2009, **9**, 1254-1257.
233. E. Simone, M. V. Cenzato and Z. K. Nagy, *J Cryst Growth*, 2016, **446**, 50-59.
234. J. Anwar, P. K. Boateng, R. Tamaki and S. Odedra, *Angew Chem Int Edition*, 2009, **48**, 1596-1600.
235. S. A. Kulkarni, C. C. Weber, A. S. Myerson and J. H. ter Horst, *Langmuir*, 2014, **30**, 12368-12375.
236. D. Green, in *Handbook of Industrial Crystallization (Second Edition)*, Butterworth-Heinemann, Woburn, 2002, DOI: <https://doi.org/10.1016/B978-075067012-8/50010-0>, pp. 181-199.
237. I. N. Houson and Dawsonera, *Process understanding for scale-up and manufacture of active ingredients*, Wiley-VCH, Weinheim, 2011.
238. M. Kraume and P. Zehner, *The Canadian Journal of Chemical Engineering*, 2002, **80**, 1-8.

239. F. W. J. M. M. Hoeks, L. A. Boon, F. Studer, M. O. Wolff, F. van der Schot, P. Vrabél, R. G. J. M. van der Lans, W. Bujalski, Å. Manelius, G. Blomsten, S. Hjorth, G. Prada, K. C. A. M. Luyben and A. W. Nienow, *Journal of Industrial Microbiology and Biotechnology*, 2003, **30**, 118-128.
240. M. Li, G. White, D. Wilkinson and K. J. Roberts, *Chemical Engineering Journal*, 2005, **108**, 81-90.
241. Comsol, Understand, Predict, and Optimize Engineering Designs with the COMSOL Multiphysics® Software).
242. N. A. Mitchell and P. J. Frawley, *J Cryst Growth*, 2010, **312**, 2740-2746.
243. K. Liang, G. White, D. Wilkinson, L. J. Ford, K. J. Roberts and W. M. L. Wood, *Industrial & Engineering Chemistry Research*, 2004, **43**, 1227-1234.
244. H. G. Brittain, *Polymorphism in pharmaceutical solids*, New York : M. Dekker, ©1999., 1999.
245. N. Kubota, *J Cryst Growth*, 2008, **310**, 629-634.
246. J. Lu, X. J. Wang, X. Yang and C. B. Ching, *J Pharm Sci*, 2007, **96**, 2457-2468.
247. X. Ni and A. Liao, *Cryst Growth Des*, 2008, **8**, 2875-2881.
248. K. Sypek, I. S. Burns, A. J. Florence and J. Sefcik, *Cryst Growth Des*, 2012, **12**, 4821-4828.
249. H. Qu, H. Alatalo, H. Hatakka, J. Kohonen, M. Louhi-Kultanen, S.-P. Reinikainen and J. Kallas, *J Cryst Growth*, 2009, **311**, 3466-3475.
250. M.-J. Lee, I.-C. Wang, M.-J. Kim, P. Kim, K.-H. Song, N.-H. Chun, H.-G. Park and G. J. Choi, *Korean Journal of Chemical Engineering*, 2015, **32**, 1910-1917.
251. J. Liu, M. Svärd and Å. C. Rasmuson, *Cryst Growth Des*, 2014, **14**, 5521-5531.
252. C. Cashell, D. Corcoran and B. K. Hodnett, *J Cryst Growth*, 2004, **273**, 258-265.
253. H.-H. Tung, E. L. Paul, M. Midler and J. A. McCauley, in *Crystallization of Organic Compounds*, John Wiley & Sons, Inc., 2008, DOI: 10.1002/9780470447796.ch4, pp. 77-100.

254. E. Aamir, Z. K. Nagy and C. D. Rielly, *Chemical Engineering Science*, 2010, **65**, 3602-3614.
255. E. Kougoulos, A. G. Jones and M. W. Wood-Kaczmar, *Org Process Res Dev*, 2006, **10**, 739-750.
256. C. D. Rielly and A. J. Marquis, *Chem Eng Sci*, 2001, **56**, 2475-2493.
257. N. B. McKeown, *Journal of Materials Chemistry*, 2010, **20**, 10588-10597.
258. L. J. Barbour, *Chemical Communications*, 2006, DOI: 10.1039/B515612M, 1163-1168.
259. J. D. Wright, *Molecular Crystals*, Cambridge University Press, 1987.
260. A. W. Vere, *Crystal Growth: Principles and Progress*, Springer US, 1 edn., 1987.
261. A. S. Paulino, G. Rauber, C. E. M. Campos, M. H. P. Maurício, R. R. de Avillez, G. Capobianco, S. G. Cardoso and S. L. Cuffini, *European Journal of Pharmaceutical Sciences*, 2013, **49**, 294-301.
262. A. K. Yazdi and H. D. C. Smyth, *Int J Pharm*, 2016, **502**, 170-180.
263. A. P. Harvey, Mackley, M.R., Reis, N., Vicente, A.A., Teixeira, J.A., presented in part at the The 4th European Congress of Chemical Engineering., 2003.
264. J. R. McDonough, A. N. Phan and A. P. Harvey, *Chemical Engineering Journal*, 2015, **265**, 110-121.
265. N. Reis, A. P. Harvey, M. R. Mackley, A. A. Vicente and J. A. Teixeira, *Chemical Engineering Research and Design*, 2005, **83**, 357-371.
266. A. N. Phan and A. Harvey, *Chemical Engineering Journal*, 2010, **159**, 212-219.
267. F. R. M. Rasdi, A. N. Phan and A. P. Harvey, *Procedia Engineering*, 2012, **42**, 1527-1539.
268. F. Castro, A. Ferreira, F. Rocha, A. Vicente and J. A. Teixeira, *Industrial & Engineering Chemistry Research*, 2013, **52**, 9816-9821.
269. V. C. Eze, J. C. Fisher, A. N. Phan and A. P. Harvey, *Chemical Engineering Journal*, 2017, **322**, 205-214.
270. N. Reis, C. N. Goncalves, M. Aguedo, N. Gomes, J. A. Teixeira and A. A. Vicente, *Biotechnol Lett*, 2006, **28**, 485-490.



271. D. E. O. S. V. A. A. MARTINS, F. A. M. AZEVEDO, D. A. R. F. A. NOGUEIRA and T. J. A. COUTO, *Google Patents*, 2015.
272. M. Zheng, R. L. Skelton and M. R. Mackley, *Process Safety and Environmental Protection*, 2007, **85**, 365-371.
273. N. Reis, P. C. Mena, A. A. Vicente, J. A. Teixeira and F. A. Rocha, *Chemical Engineering Science*, 2007, **62**, 7454-7462.
274. M. Zheng and M. Mackley, *Chemical Engineering Science*, 2008, **63**, 1788-1799.
275. N. Reis, A. A. Vicente and J. A. Teixeira, *Chemical Engineering and Processing: Process Intensification*, 2010, **49**, 793-803.
276. A. N. Phan, A. P. Harvey and M. Rawcliffe, *Fuel Processing Technology*, 2011, **92**, 1560-1567.
277. A. N. Phan and A. P. Harvey, *Chemical Engineering Journal*, 2011, **169**, 339-347.
278. A. N. Phan and A. P. Harvey, *Chemical Engineering Journal*, 2012, **180**, 229-236.
279. J. P. Solano, R. Herrero, S. Espin, A. N. Phan and A. P. Harvey, *Chemical Engineering Research & Design*, 2012, **90**, 732-742.
280. F. R. M. Rasdi, A. N. Phan and A. P. Harvey, *Chemical Engineering Journal*, 2013, **222**, 282-291.
281. F. Castro, A. Ferreira, F. Rocha, A. Vicente and J. A. Teixeira, *Aiche Journal*, 2013, **59**, 4483-4493.
282. L. N. Ejim, S. Yerdelen, T. McGlone, I. Onyemelukwe, B. Johnston, A. J. Florence and N. M. Reis, *Chemical Engineering Journal*, 2017, **308**, 669-682.
283. X. Ni, M. R. Mackley, A. P. Harvey, P. Stonestreet, M. H. I. Baird and N. V. Rama Rao, *Chemical Engineering Research and Design*, 2003, **81**, 373-383.
284. X.-W. Ni, A. Valentine, A. Liao, S. B. C. Sermage, G. B. Thomson and K. J. Roberts, *Cryst Growth Des*, 2004, **4**, 1129-1135.
285. N. Reis, A. A. Vicente, J. A. Teixeira and M. R. Mackley, *Chemical Engineering Science*, 2004, **59**, 4967-4974.

286. N. Reis, University of Minho, 2006.
287. J. R. McDonough, S. M. R. Ahmed, A. N. Phan and A. P. Harvey, *Chemical Engineering Science*, 2017, **171**, 160-178.
288. A. N. Phan, A. P. Harvey and V. Eze, *Chem Eng Technol*, 2012, **35**, 1214-1220.
289. N. Reis, C. N. Gonçalves, M. Aguedo, N. Gomes, J. A. Teixeira and A. A. Vicente, *Biotechnology Letters*, 2006, **28**, 485-490.
290. M. Aguedo, N. Gomes, E. E. Garcia, Y. Waché, M. Mota, J. A. Teixeira and I. Belo, *Biotechnology Letters*, 2005, **27**, 1617-1621.
291. N. Reis, C. N. Gonçalves, A. A. Vicente and J. A. Teixeira, *Biotechnology and Bioengineering*, 2006, **95**, 744-753.
292. N. Reis, R. N. Pereira, A. A. Vicente and J. A. Teixeira, *Industrial & Engineering Chemistry Research*, 2008, **47**, 7190-7201.
293. A. Ferreira, J. A. Teixeira and F. Rocha, *Chemical Engineering Journal*, 2015, **262**, 499-508.
294. M. Zheng, R. L. Skelton and M. R. Mackley, *Process Safety and Environmental Protection*, 2007, **85**, 365-371.
295. S. Fogler, in *Elements of Chemical Reaction Engineering*, Michigan, 2008, vol. 4th Edition, ch. 13, pp. 867-944.
296. BIOVIA Pipeline Pilot, <http://accelrys.com/products/collaborative-science/biovia-pipeline-pilot/>).
297. M. Z. Zheng and M. Mackley, *Chem Eng Sci*, 2008, **63**, 1788-1799.
298. O. Levenspiel, in *Chemical Reaction Engineering* 1999, ch. 13, pp. 293-317.
299. O. Levenspiel, in *Chemical Reaction Engineering*, 3rd edn., 1999, ch. 14, pp. 321-338.
300. Z. K. Nagy, G. Fevotte, H. Kramer and L. L. Simon, *Chemical Engineering Research and Design*, 2013, **91**, 1903-1922.
301. S. K. Jha, S. Karthika and T. K. Radhakrishnan, *Resource-Efficient Technologies*, 2017, **3**, 94-100.
302. A. Mesbah, J. A. Paulson, R. Lakerveld and R. D. Braatz, 2015.

303. F. Tahir, K. Krzemieniewska-Nandwani, J. Mack, D. Lovett, H. Siddique, F. Mabbott, V. Raval, I. Houson and A. Florence, *Control Engineering Practice*, 2017, **67**, 64-75.
304. N. Doki, H. Seki, K. Takano, H. Asatani, M. Yokota and N. Kubota, *Cryst Growth Des*, 2004, **4**, 949-953.
305. N. C. S. Kee, R. B. H. Tan and R. D. Braatz, *Cryst Growth Des*, 2009, **9**, 3044-3051.
306. E. Simone, A. N. Saleemi, N. Tonnon and Z. K. Nagy, *Cryst Growth Des*, 2014, **14**, 1839-1850.
307. M. W. Hermanto, M.-S. Chiu, X.-Y. Woo and R. D. Braatz, *AIChE Journal*, 2007, **53**, 2643-2650.
308. P. Engineering, <http://www.perceptiveapc.com/>).
309. N. Belkaid, Master's, University of Strathclyde, 2017.
310. X. Ni, H. Jian and A. W. Fitch, *Chemical Engineering Science*, 2002, **57**, 2849-2862.
311. M. Manninen, E. Gorshkova, K. Immonen and X. W. Ni, *Journal of Chemical Technology & Biotechnology*, 2013, **88**, 553-562.
312. K. B. Smith, University of Cambridge 1999.
313. P. E. Limited, Siemens and Perceptive Engineering combining software solutions for the Pharmaceutical Industry, [http://www.perceptiveapc.com/news/latest\\_news/siemens/](http://www.perceptiveapc.com/news/latest_news/siemens/) 2018).
314. R. Kacker, S. I. Regensburg and H. J. M. Kramer, *Chemical Engineering Journal*, 2017, **317**, 413-423.
315. A. Mazubert, D. F. Fletcher, M. Poux and J. Aubin, *Chemical Engineering and Processing: Process Intensification*, 2016, **108**, 78-92.
316. C. J. Callahan and X.-W. Ni, *The Canadian Journal of Chemical Engineering*, 2014, **92**, 1920-1925.
317. C. J. Callahan and X.-W. Ni, *Cryst Growth Des*, 2012, **12**, 2525-2532.
318. J. S. Wey and P. H. Karpinski, in *Handbook of Industrial Crystallization (Second Edition)*, Butterworth-Heinemann, Woburn, 2002, DOI: <https://doi.org/10.1016/B978-075067012-8/50012-4>, pp. 231-248.

319. C. J. Brown, T. McGlone, S. Yerdelen, V. Srirambhatla, F. Mabbott, R. Gurung, M. L. Briuglia, B. Ahmed, H. Polyzois, J. McGinty, F. Perciballi, D. Fysikopoulos, P. MacFhionnghaile, H. Siddique, V. Raval, T. S. Harrington, A. D. Vassileiou, M. Robertson, E. Prasad, A. Johnston, B. Johnston, A. Nordon, J. S. Srail, G. Halbert, J. H. ter Horst, C. J. Price, C. D. Rielly, J. Sefcik and A. J. Florence, *Molecular Systems Design & Engineering*, 2018, DOI: 10.1039/C7ME00096K.
320. T. Geddert, I. Bialuch, W. Augustin and S. Scholl, *Heat Transfer Engineering*, 2009, **30**, 868-875.
321. B. O. Hasan, G. J. Nathan, P. J. Ashman, R. A. Craig and R. M. Kelso, *Applied Thermal Engineering*, 2012, **36**, 210-218.
322. T. A. Hoang, H. M. Ang and A. L. Rohl, *Powder Technology*, 2007, **179**, 31-37.
323. O. Narducci, A. G. Jones and E. Kougoulos, *Organic Process Research & Development*, 2011, **15**, 974-980.
324. M. Boukerche, D. Mangin, J. P. Klein, O. Monnier and C. Hoff, *Chemical Engineering Research and Design*, 2010, **88**, 1474-1478.
325. N. C. S. Kee, P. D. Arendt, R. B. H. Tan and R. D. Braatz, *Cryst Growth Des*, 2009, **9**, 3052-3061.
326. C. Ricardo and N. Xiongwei, *Organic Process Research & Development*, 2009, **13**, 1080-1087.
327. N. Doki, M. Yokota, K. Kido, S. Sasaki and N. Kubota, *Cryst Growth Des*, 2004, **4**, 103-107.
328. W. Beckmann, K. Nickisch and U. Budde, *Organic Process Research & Development*, 1998, **2**, 298-304.
329. X. Zhao and X. D. Chen, *Heat Transfer Engineering*, 2013, **34**, 719-732.
330. A. S. Myerson, M. Krumme, M. Nasr, H. Thomas and R. D. Braatz, *J Pharm Sci*, 2015, **104**, 832-839.
331. E. M. Ålander and Å. C. Rasmuson, *Industrial & Engineering Chemistry Research*, 2005, **44**, 5788-5794.
332. Y. Kawashima, M. Imai, H. Takeuchi, H. Yamamoto, K. Kamiya and T. Hino, *Powder Technology*, 2003, **130**, 283-289.

333. O. Narducci, A. G. Jones and E. Kougoulos, *Chemical Engineering Science*, 2011, **66**, 1069-1076.
334. F. Mabbott, University of Strathclyde, 2017.
335. C. Tachtatzis, R. Sheridan, C. Michie, R. C. Atkinson, A. Cleary, J. Dziewierz, I. Andonovic, N. E. B. Briggs, A. J. Florence and J. Sefcik, *Chemical Engineering Science*, 2015, **133**, 82-90.